A Spin-Parity Analysis of the Reaction $\bar{p}p \to \pi^+\pi^-\pi^\circ\omega$

by

Rodney C. McCrady

A dissertation submitted in partial fulfillment of the
requirements for the degree of

Doctor of Philosophy

in the Department of Physics

Carnegie Mellon University

October 5, 1998

Abstract

An analysis of the reaction $\bar{p}p \to \pi^+\pi^-\pi^\circ\omega$ is presented. The annihilations took place at rest in liquid hydrogen. This measurement finds that $\pi^+\pi^-\pi^\circ\omega$ is produced in $16.1 \pm 1.0\%$ of such annihilations. A prominent signal of $\bar{p}p \to \omega\omega$ is observed. The rate for this process was measured using a technique which is practically background free; the measured rate is $BR(\bar{p}p \to \omega\omega) = 3.23 \pm 0.25\%$. This rate is important in calculations concerning $\bar{p}p$ annihilation dynamics. A partial wave analysis was also performed. New results include possible observation of $\omega\pi\pi$ decay modes for the $a_1(1260)$, $h_1(1170)$ and $a_1(1700)$. These results need confirmation. Also, the $b_1\pi$ decay mode of the $\omega(1600)$ is found to be stronger than the $\omega(\pi\pi)_s$ decay mode: $BR(\omega(1600) \to b_1\pi)/BR(\omega(1600) \to \omega(\pi\pi)_s) = 1.6 \pm 0.2$.

Contents

Chapter 1

Introduction

Throughout the history of physical science, people have endeavored to find the fundamental constituents of the universe: those indivisible, immutable objects of which all matter is composed. Currently, this field of study is known as particle physics.

The components of atoms, electrons and nucleons, are members of families of such particles. The family of *leptons* includes the electron (e), and two similar particles called the muon (μ) and the tau (τ). They are similar to each other in the fundamental ways in which they interact with other matter. The μ and τ are quite different from the electron, though, in that they exist for a very short time after being created before decaying into other particles. Each of these has a partner particle called a neutrino (ν_e, ν_μ and ν_τ). Each lepton has associated with it an antiparticle, which is identical except that some of its attributes are of the opposite sign (see Table 1.1.) All of the leptons have half-integer spin. They participate in the electromagnetic and weak interaction, but do not interact via the strong force.

Attribute	leptons						antileptons					
	e	ν_e	μ	ν_μ	τ	ν_τ	$\bar{e}$	$\bar{\nu_e}$	$\bar{\mu}$	$\bar{\nu_\mu}$	$\bar{\tau}$	$\bar{\nu_\tau}$
Electric charge	-1	0	-1	0	-1	0	$+1$	0	$+1$	0	$+1$	0
Helicity		-1		-1		-1		$+1$		$+1$		$+1$

Table 1.1: The leptons and antileptons.

The proton and neutron are composed of quarks. The quark family, like the leptons, has three generations. In the first generation are the constituents of the proton and neutron and are called *up* (u) and *down* (d). The members of the other two generations are called *strange*, *charm*, *bottom*, and *top* (s, c, b and t). Their properties are shown in Table 1.2. As with the leptons, each quark has an associated antiquark. The quarks also have half-integer spin. They interact via the strong, weak and electromagnetic forces.

A bizarre feature of quarks is that they seem to not exist in isolation; they always occur as constituents of other composite systems, such as protons and neutrons. This is known as *confinement*.

Attribute	Quark					
	d	u	s	c	b	t
Electric charge	$-\frac{1}{3}$	$+\frac{2}{3}$	$-\frac{1}{3}$	$+\frac{2}{3}$	$-\frac{1}{3}$	$+\frac{2}{3}$
Isospin z-component	$-\frac{1}{2}$	$+\frac{1}{2}$	0	0	0	0

Table 1.2: The quarks.

Quantum field theories, which have met with spectacular success in describing the electromagnetic and weak interactions, model the forces of the fundamental interactions as being carried by virtual gauge bosons: the photon (γ) for the electromagnetic force, $W^{\pm}$ and Z° particles for the weak force, and *gluons* (g) for the strong force. In the electromagnetic interaction, a photon couples to particles with a strength determined by the particles' *electric* charge; the photon itself does not possess an electric charge. The strength of the strong force depends on a charge dubbed *color*. The gluons do carry this kind of charge and can therefore interact directly with one another via the strong force. This feature leads to an increase in the apparent strength of the strong force with increasing separation of the interacting quarks. This gives rise to the phenomenon of confinement, which prohibits quarks from existing in isolation; they always occur as elements of composite systems called hadrons.

At the time of its proposal, the quark model required only three quarks (up, down and strange) to explain the known particle spectrum. The quark contents of the proton and neutron are (uud) and (udd). Such objects which are composed of three quarks are called baryons. Combinations of three quarks of various flavors in different dynamical configurations leads to a spectrum baryons, many of which have been observed. Examples include the Λ (uds), Δ^{++} (uuu) and Σ^{-} (dds). Another class of particles, *mesons*, can be formed from the combination of a quark and an antiquark. The positively charged pion (π^{+}) is composed of an up and an anti-down quark ($u\bar{d}$), for example. The meson spectrum consists of particles composed of $q\bar{q}$ pairs in various combinations of flavor, spin, isospin, orbital angular momentum, and radial excitations (see Figure 2.1.)

The mathematical models which describe the interactions of the quarks and gluons also allow for the existence of other types of hadrons. Among these are *hybrid* mesons and baryons ($q\bar{q}g$ and $qqqg$), *dibaryons* and *pentaquarks* ($qqqqqq$ and $qqqq\bar{q}q$) and *glueballs* (gg). At this time, the existence of such objects is still in question.

Finding and characterizing mesons is known as meson spectroscopy. The first true mesons discovered were the pions. The charged pions decay via the weak interaction, and have a lifetime of about $26ns$, allowing them to be observed easily using electronic methods. Most mesons, though, decay via the strong interaction and have lifetimes of around 10^{-24} seconds. The Heisenberg uncertainty principle relating energy and time, $\Delta E \Delta t \sim \hbar$, shows that such a short lived particle has an uncertainty in its energy, or mass, on the order of hundreds of MeV. That is, a given meson can exist with a wide range of masses. This short lifetime also means that such mesons cannot

travel any appreciable distance before decaying, making them virtually impossible to detect directly. Their presence is inferred from measurements of their decay products, usually pions and photons. These mesons are referred to as *resonances* rather than particles. Other factors making detection of the resonances difficult are their relatively large masses and the fact that they are not produced in the laboratory as copiously as are pions. These mesons' masses also lie rather close to one another, making it difficult to determine which type of meson produced the detected decay products.

The first of the short lived mesons were discovered by examining the *invariant mass* distributions of their decay products. The invariant mass of a particle is defined by

$$m = \sqrt{E^2 - \vec{p}^2}.$$

Since energy (E) and momentum ($\vec{p}$) must be conserved in the decay of a meson, the combination of its N decay products must have the same invariant mass:

$$m = \sqrt{(\sum_{i=1}^{N} E_i)^2 - (\sum_{i=1}^{N} \vec{p}_i)^2}.$$

So by adding up the energies and momenta of three pions produced in high energy collisions of pions and protons, for example, one may observe that many events produce invariant masses near $550 MeV/c^2$, indicating that η mesons had been produced. The lowest lying mesons, such as the η, ω and ϕ produce invariant mass distributions which span a relatively narrow range ($< 20 MeV$) of energies. The angular distribution of the decay products relative to the direction of flight of the meson can indicate some of its characteristics, such as its spin and intrinsic parity. This is a consequence of conservation of angular momentum and parity.

Some mesons' mass distributions overlap to such a degree that the decay products' energy and angular distributions are a quantum-mechanical mixture of those expected for the individual mesons. In such cases, searching invariant mass distributions is not an effective method for discovery and characterization of the decaying mesons. In these regimes, one must accumulate many thousands of events and use sophisticated analysis procedures in order to determine which mesons were produced and in what quantities. Such is the goal of the Crystal Barrel experiment.

This dissertation presents the results of an analysis of data collected by the Crystal Barrel experiment in which a proton and an antiproton annihilate to produce a final state consisting of three pions and an omega meson ($\pi^+\pi^-\pi^\circ\omega$.) The conjecture is that the annihilations first produce meson resonances which then decay into $\pi\pi$, $\omega\pi$, $\pi\pi\pi$, and $\omega\pi\pi$. Many of the known resonances are expected to be observed, and the possibility exists to observe previously unknown ones, such as a hybrid meson known as $\hat{\rho}$. Observation of new decay modes of known resonances is also expected.

1.1 Summary of the Analysis

In this section a brief summary of the measurement technique is presented. Details of each aspect of the experiment are given in subsequent chapters.

The analysis involves study of an experiment in which protons and antiprotons annihilated at rest to produce four mesons in the final state: $\bar{p}p \to \pi^+\pi^-\pi^\circ\omega$. The analysis will determine what happened between the initial and final states. The model supposes that the $\bar{p}p$ annihilation first produces meson resonances; these intermediate states then decay to yield the four final state mesons. A *spin parity analysis* determines the spin and parity quantum numbers of the intermediate meson resonances. Which resonances occurred and in what quantities will be determined by the energy and angular distributions of the final state mesons. Spin parity analysis is also known as *Partial Wave Analysis* (PWA.) Motivations for study of these processes are given in Chapter 2.

In order to observe $\bar{p}p$ annihilation at rest, a beam of low energy antiprotons is used. Each antiproton enters a liquid hydrogen target where it quickly loses energy through ionization. When it has slowed sufficiently, the antiproton ejects the electron from a hydrogen atom and is captured to form a $\bar{p}p$ atom. The atom is initially formed in a high angular momentum state ($L \sim 20$,) but due to strong Stark mixing in liquid hydrogen, the atom rapidly cascades to an S-orbital (L=0) [2]. Because of the large overlap of the wave functions of the proton and antiproton in the S-orbitals, annihilation occurs. The entire process of slowing, capture, cascade and annihilation takes place typically in less than $1ns$.

Usually mesons decay, ultimately, into charged pions ($\pi^\pm$) and photons (γ.) This may occur in several steps, as shown here for the particular channel which is the subject of this dissertation:

$$\bar{p}p \to \text{Resonances} \to \pi^+\pi^-\pi^\circ\omega \begin{cases} \to \gamma\gamma \\ \to \pi^\circ\gamma \begin{cases} \to \gamma\gamma \end{cases} \end{cases} = \pi^+\pi^-5\gamma$$

These decays occur with lifetimes of 10^{-16} to 10^{-24} seconds. The detector system detects charged pions and photons. The charged pions are detected by a drift chamber situated in a magnetic field; the direction and curvature of the measured track gives a measurement of the momentum vector for the pion. The photons are detected by cesium iodide scintillating crystals, yielding a measurement of the energy of the photon and the direction in which it is emitted. A computer program reconstructs photons into the π°'s and ω's, so ultimately and measurement of the energies and momenta of the four final state mesons is derived. Details of the detector system are presented in Chapter 3.

Chapter 10 discusses the measurement of the total rate of production of the final state to be analyzed. It is found that $\pi^+\pi^-\pi^\circ\omega$ is produced in $16.1 \pm 1.0\%$ of $\bar{p}p$

annihilations at rest. This is a large rate; for a sense of scale, consider that $\pi^\circ\pi^\circ\pi^\circ\omega$ is produced in less than 2% of annihilations [3]. This high rate has implications for the anticipated complexity of the PWA. For example, the process $\bar{p}p \to \pi a_2(1320)$, with the a_2 decaying to $\omega\pi\pi$, accounts for about 0.3% of annihilations. This is known from the analysis of other final states (with the a_2 in other decay modes) where $\pi a_2(1320)$ production is clearly seen. This process results in $\pi + \omega\pi\pi$ so $\pi a_2(1320)$ should be one of the intermediate states present in the $\pi^+\pi^-\pi^\circ\omega$ final state, but only as a small contribution ($(0.3\%)/(16.1\%) \simeq 1.8\%$.) This indicates that many intermediate states may be needed to describe this final state. Also, the sensitivity of the analysis to processes which occur with small rates will probably be weak, since the fitting procedure and the availability of computing resources limit the PWA to about ten processes.

Study of this particular final state was chosen because of the possibility of observing a $J^{PC} = 1^{-+}$ hybrid meson (the $\hat{\rho}$) decaying to $b_1(1235)\pi$:

$$\begin{array}{lll} \bar{p}p \to \hat{\rho}\pi & & = \omega\pi\pi\pi \\ \quad \hookrightarrow b_1(1235)\pi & & \\ \quad\quad \hookrightarrow \omega\pi & & \end{array}$$

The $b_1\pi$ decay mode for hybrids is favored in many theoretical models. Production of exotic states such as the $\hat{\rho}$ is probably not a strong process, and such a process would constitute a very small contribution to the $\pi^+\pi^-\pi^\circ\omega$ final state. This analysis was not able to draw any conclusions concerning the $\hat{\rho}$.

The large rate of production of $\pi^+\pi^-\pi^\circ\omega$ also fits in to a trend in $\bar{p}p$ annihilation: that ω's are produced quite copiously (See Section 2.3.1.) ω's are produced in at least 30% of $\bar{p}p$ annihilations at rest. The $\pi^+\pi^-\pi^\circ\omega$ final state is important in establishing this trend.

The technique for partial wave analysis is described in detail in Chapter 11; a brief summary is given here. The fitting function is determined by proposing that a particular set of processes occur, each with a given strength and phase. These processes are the productions and decays of the meson resonances, such as $\bar{p}p \to \pi a_2(1320)$, $a_2 \to \omega\pi\pi$. For each event, the probability that the proposed set of processes would produce that event is computed; the probabilities for all of the events are multiplied together to get the joint probability of producing the data set. The strengths and phases of the processes are then varied to maximize the joint probability. This method of fitting is known as the unbinned maximum likelihood method. One could, in principle, bin the data, (i.e. divide the function space into bins, and count the number of events falling into each bin,) but this is not suitable in this analysis for the following reasons: the function describing a four-particle final state is 5-dimensional. Even with only 10 bins per dimension, there would be 10^5=100,000 bins, and with only about 50,000 events in the data sample, there would be a very small number of events per bin, making the interpretation of the fit quality difficult.

The major assumptions made in the analysis model are those which are typical in this type of analysis:

- The $\bar{p}p$ annihilations occur when the $\bar{p}p$ atom is an S-orbital ($^{2s+1}L_J = {}^1S_0$ or ${}^3S_1$.)

- The annihilation and resonance decays proceed via two-body modes. This is the basic assumption in the "Isobar Model." See Figure 1.1. Specifically, the $\bar{p}p$ annihilation can occur in three ways: production of an $\omega\pi$ resonance plus a $\pi\pi$ system, production of an ω plus a $\pi\pi\pi$ resonance, or production of a pion plus an $\omega\pi\pi$ resonance. Decays of $\pi\pi\pi$ resonances are modeled as decays to $\rho\pi$, with the ρ decaying to $\pi\pi$. The $\omega\pi\pi$ resonances can decay to $\omega\rho$, $\omega(\pi\pi)_s$ or $b_1(1235)\pi$. The $(\pi\pi)_s$ state is an empirical description of two pions in an S-wave; its interpretation in terms of resonances is not well understood. The $b_1(1235)$ is a well known $\omega\pi$ resonance.

- Resonances' mass distributions are described by Breit-Wigner functions. For example, the probability that a $\pi\pi$ pair formed a ρ is given by a Breit-Wigner function centered at $770MeV$ with a width of $\Gamma = 150MeV$.

- The helicity formalism is used in computing angular distributions associated with the annihilations and decays. The helicity formalism is based on conservation of angular momentum and transformation laws. The distributions depend on the spin of the initial state, and the spins and orbital angular momentum of the daughter particles.

- The intermediate states from each of the two initial states ($^1S_0$ and $^3S_1$) interfere with one another. The processes originating from $^1S_0$ are added incoherently to those originating from $^3S_1$. That is, the two initial states do not interfere.

As an initial hypothesis for the PWA, a set of processes involving known resonances in known decay modes was used. There were indications that some process was missing from this fit; for example, some of the angular distributions were poorly described. The addition to this initial hypothesis of one particular process resulted in great improvement: $\bar{p}p \to h_1(1170)\pi$, $h_1 \to \omega\pi\pi$. The $h_1(1170)$ is a well known resonance, but has been reported only in its $\rho\pi$ decay mode [1]; the $\omega\pi\pi$ decay mode has not been ruled out however. Addition of this process to the PWA dramatically improves the angular distributions.

Other processes were also added to the PWA fit, with the hope of observing $\omega\pi\pi$ decay modes of other resonances. Most were fit as small contributions to the final state, but two particular resonances produced an interesting result: the $a_1(1260)$ and the $a_1(1700)$. The $a_1(1260)$ is a well known resonance, and has been observed primarily in the $\rho\pi$ decay mode. The $a_1(1700)$ has only been reported in the last couple of years, also in the $\rho\pi$ decay mode. No search for $\omega\pi\pi$ decay modes has been reported in the particle physics literature. When these resonances are included *individually* in the PWA fits (in $\omega\pi\pi$ decay modes), they are fit as small ($< 5\%$)

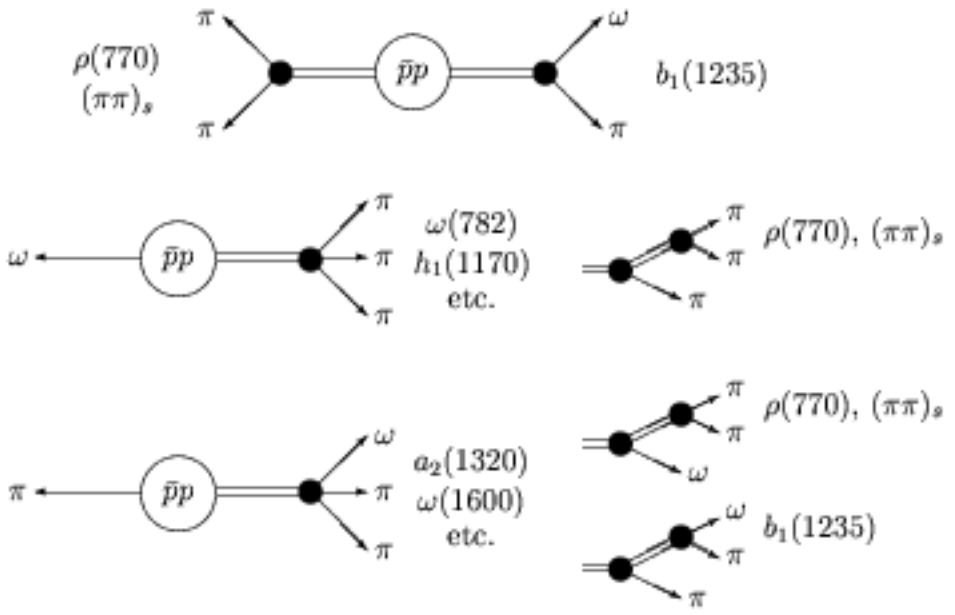

Figure 1.1: The three modes of annihilation into two mesons which are modeled in this analysis. The two body decay modes of the resonances are also shown.

contributions to the final state. However, when *both* are included, they are each fit as larger (8-9%) contributions and a quantitative improvement to the fit results. The $\omega\pi\pi$ decay modes of the $h_1(1170)$, $a_1(1260)$ and $a_1(1700)$ are new results, and certainly require confirmation. Suggestions on how to confirm that production of these resonances occurs, and that they decay to $\omega\pi\pi$, are presented in Chapter 13.

Also among the interesting results of the partial wave analysis are:

- The $b_1\pi$ decay mode of the $\omega(1600)$ resonance is 1.5 to 2 times stronger than the $\omega(\pi\pi)_s$ mode.
- A large rate of production of ω plus heavy $\rho\pi$ resonances.
- A large rate of production of $b_1(1235)\rho$.

The latter two of these, along with a some results from analyses of other final states, suggest a trend involving large rates of production of a vector meson plus a P-wave meson (P-wave mesons are composed a a $q\bar{q}$ pair in an $L = 1$ state; see Chapter 2.) This trend also is discussed in Chapter 13.

Unfortunately, the large production rate of the $\pi^+\pi^-\pi^\circ\omega$ final state has limited the sensitivity of the analysis to processes which are not produced copiously. There is great interest in observation of certain resonances in $\omega\pi\pi$ decay modes: the $\hat{\rho}$ hybrid meson, the $a_0(1470)$, and $\pi(1800)$ among them. As with other high-rate final states,

simultaneous analysis of several related final states will be needed in order to constrain the PWA of $\pi^+\pi^-\pi^\circ\omega$. Suggestions for such further studies are made in Chapter 13.

Chapter 2

Meson Spectroscopy and $\bar{p}p$ Annihilation

In this Chapter, results of calculations of mesons' properties and of $\bar{p}p$ annihilations will be discussed, with particular emphasis on those aspects which analysis of $\pi^+\pi^-\pi^\circ\omega$ may be able to address. First, the quark model of mesons is discussed. Calculations of mesons' properties (masses, widths, and decay modes) are presented. Last, some calculations and observations concerning $\bar{p}p$ annihilations are discussed.

The $\pi^+\pi^-\pi^\circ\omega$ final state is of interest in meson spectroscopy because of the possibility of observing $\omega\pi\pi$ decay modes of certain resonances. These modes can determine (in the context of some models) the structure of these resonances. This final state is of interest in the study of $\bar{p}p$ annihilation dynamics for two reasons: 1) it allows measurement of the rate for $\bar{p}p \to \omega\omega$, and 2) it helps to demonstrate that ω mesons are produced in a large fraction of $\bar{p}p$ annihilations.

2.1 The Quark Model of Mesons

As mentioned briefly in Chapter 1, mesons can be thought of as a quark and an antiquark bound by the strong force into a composite object. The various configurations of the $q\bar{q}$ pairs give rise to a spectrum of mesons. Consider first the quark flavors, of which there are six known. As this dissertation concerns the reaction $\bar{p}p \to \pi^+\pi^-\pi^\circ\omega$, which has a total energy of $< 2GeV$ and no residual strangeness, the discussion can be limited to those mesons composed of up (u) and down (d) quarks, and the lightest $s\bar{s}$ mesons. (Mesons containing c, b and t quarks are known to be too massive to be of concern here.) The u and d quarks carry the isospin quantum number and may couple to form mesons with isospin $I = 0$ or 1. The intrinsic spins of the quarks can combine into total spin $s = 0$ or 1. There may be orbital angular momentum, L, between the $q\bar{q}$ pair; this will combine with the spins to yield total angular momentum J of the meson. Finally, the principal (radial) quantum number, N, takes on integral values from $N = 1$ and up.

Given the intrinsic quantum numbers of the quarks and the characteristics of their

configurations (such as the parity associated with the orbital angular momentum), the quantum numbers of the mesons can be determined: isospin (I), G-parity (G), angular momentum (J), parity (P), and charge conjugation parity (C). Figure 2.1 shows how the various $q\bar{q}$ configurations give rise to the meson spectrum. The $q\bar{q}$ configurations are specified in spectroscopic notation: $N\,^{2s+1}L_J$, where $L = 0$, 1, 2 and 3 are represented by S, P, D and F.

A collaboration known as the Particle Data Group (PDG) publishes biennially a review a particle physics, including a compilation of experimental measurements of hadrons' properties. In the following sections, where known or widely accepted values are quoted, heavy reliance is made on the averages and estimates provided by the PDG [1].

2.2 Calculations of Mesons' Properties

In this section, some theoretical descriptions and predictions of mesons' characteristics are presented. These are valuable to experimental meson spectroscopy because they can provide a description of mesons which are detected (that is radial excitations vs. orbital excitations vs. hybrid mesons), and that they can guide one's expectations for what mesons may be detected in particular decay modes.

As will be demonstrated in the following sections, experimental measurements of the masses and widths of resonances, and observing and comparing their decay modes, provides valuable information on the interpretation of the resonances in terms of their structure. In particular, observation of $\omega\pi\pi$ ($=b_1\pi$ or $\omega\rho$) decay modes of certain resonances can distinguish whether they are radial excitations, orbital excitations, or hybrid mesons.

The current consensus is that quantum chromodynamics (QCD) is the theory which describes the strong force, which binds quarks into hadrons. QCD is a field theory, and thus has the advantage that it is based on fundamental physical principals. Field theories have been successful in describing other phenomena, most notably quantum electrodynamics (QED), and in the unified description of QED and the weak force. The quark model of hadrons provided the basis for QCD: quarks are fermions with a color quantum number, which are bound into hadrons which are colorless. Isospin and strangeness correspond to valence quarks in QCD, but the quark model does not account for gluons and sea quarks, which arise naturally from the mathematics of QCD. As yet, the equations of QCD cannot be solved analytically to describe physical phenomena, but its structure can guide models and phenomenological descriptions of the mesons. For instance, in the same way that knowledge of how a magnetic dipole interacts with the magnetic field induced by a circulating electric charge, a spin-orbit interaction arising from the strong force is also predicted by the structure of QCD. Additionally, the possibility of the presence of valence gluons in hadrons is expected.

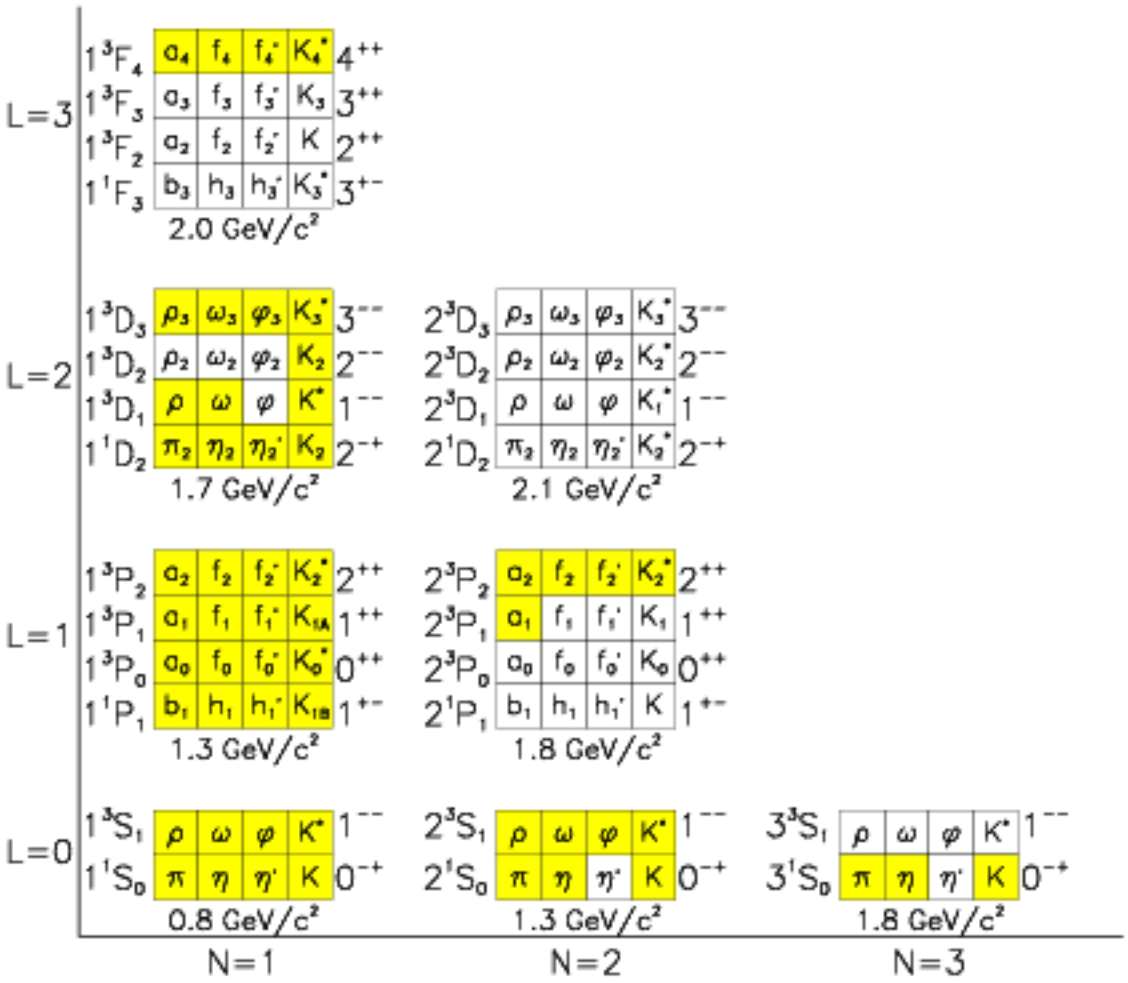

Figure 2.1: The lowest lying light quark mesons predicted by the quark model. For each combination of N and L, a table shows the names of the mesons. Those in shaded boxes are states for which a candidate has been observed. The quark configurations, $N\,^{2s+1}L_J$, are shown along the left sides of the tables, and the J^{PC} quantum numbers are shown along the right sides. Each table has four columns: 1) the $I = 1$ $n\bar{n}$ mesons, 2,3) the $I = 0$ $n\bar{n}$ and $s\bar{s}$ mesons (assuming ideal mixing) and 4) the $n\bar{s}$ mesons. For each table, an approximate mass scale of the mesons is shown. Only the lightest states are shown here; both N and L can increase without bound.

2.2.1 Mass Spectrum

A paper by Godfrey and Isgur [5] presents a prediction of the meson mass spectrum. The predictions are made using a quark model with phenomenological treatments of confinement motivated by QCD. This model describes the masses and decays of all mesons, from π to Υ, in a single consistent framework. The model is based on constituent quarks in a Coulombic potential plus the linear confinement potential expected from QCD. That is, the interactions of the valence quarks are dominated by one gluon exchange at short distances, and confinement is imposed by a flavor independent Lorentz scalar interaction. Other interactions include the color spin-orbit coupling and color hyperfine interaction. Relativistic effects are included in a unified, physically motivated way, including quark smearing effects, relativistic kinematics, and relativistic modifications of the potentials. The mass spectra for the isovector and isoscalar mesons are shown in Figures 2.2 and 2.3.

Below are comments on the calculations concerning mesons which are germane to the analysis of $\bar{p}p \to \pi^+\pi^-\pi^\circ\omega$.

The calculated masses of the well known isovector mesons, π, ρ, $b_1(1235)$, $a_1(1260)$ and $a_2(1320)$, agree well with the measured values. The $1\,^3P_0$ (0^{++}) state's mass is calculated to be $1.09 GeV$. (This value was influenced by the data available at the time.) Which resonance corresponds to this state is unclear, but the $a_0(1450)$ is favored. Its mass, $1470\pm25 MeV$ [52] is in apparent conflict with the calculation. The agreement with the known states is good overall, so the predictions for the higher states can provide guidance to experimenters: The $2\,^3P_{0,1,2}$ states ($a_{0,1,2}$ resonances) are expected in the mass range 1.78 to $1.82 GeV$. Recent observations of a_1 and a_2 resonances at masses of 1.70 and $1.66 GeV$ indicate that the a_0 excitation may be lighter than calculated. The $1\,^1D_2$ (2^{-+}) state is predicted at $1.68 GeV$; the $\pi_2(1670)$ resonance, detected primarily in 3π decay modes, probably corresponds to this state.

The calculated masses of the known isoscalar η, η', $\omega(782)$, $\phi(1020)$ and $h_1(1170)$ mesons agree well with the measured values. The model also makes predictions on their radial and orbital excitations: An additional h_1 resonance (the $2\,^1P_1$ state) is predicted at $1.78 GeV$. An h_1 resonance was recently reported at a mass of $1542\pm13 MeV$ [57]. This resonance has not been confirmed, and could be a hybrid meson or a $q\bar{q}$-hybrid mixture.

There is currently some uncertainty in regard to the orbital and radial excitations of the ω meson. The $2\,^3S_1$ state is predicted at a mass of $1.46 GeV$. The $\omega(1420)$, with a mass of $1419\pm31 MeV$, is widely believed to correspond to this state. The $1\,^3D_{1,2,3}$ states ($\omega_{1,2,3}$) resonances are expected in the mass range 1.66 to $1.70 GeV$. The confirmed existence of the $\omega(1600)$ and $\omega_3(1670)$ point to the probable existence of an $I^G J^{PC} = 0^-2^{--}$ resonance near this mass.

Unfortunately, the analysis presented in this dissertation does not result in observation of new resonances, nor does it make improved measurements of the masses of the known resonances. The predicted masses for some resonance were used, however, in partial wave analysis where attempts were made to observe new states. This model

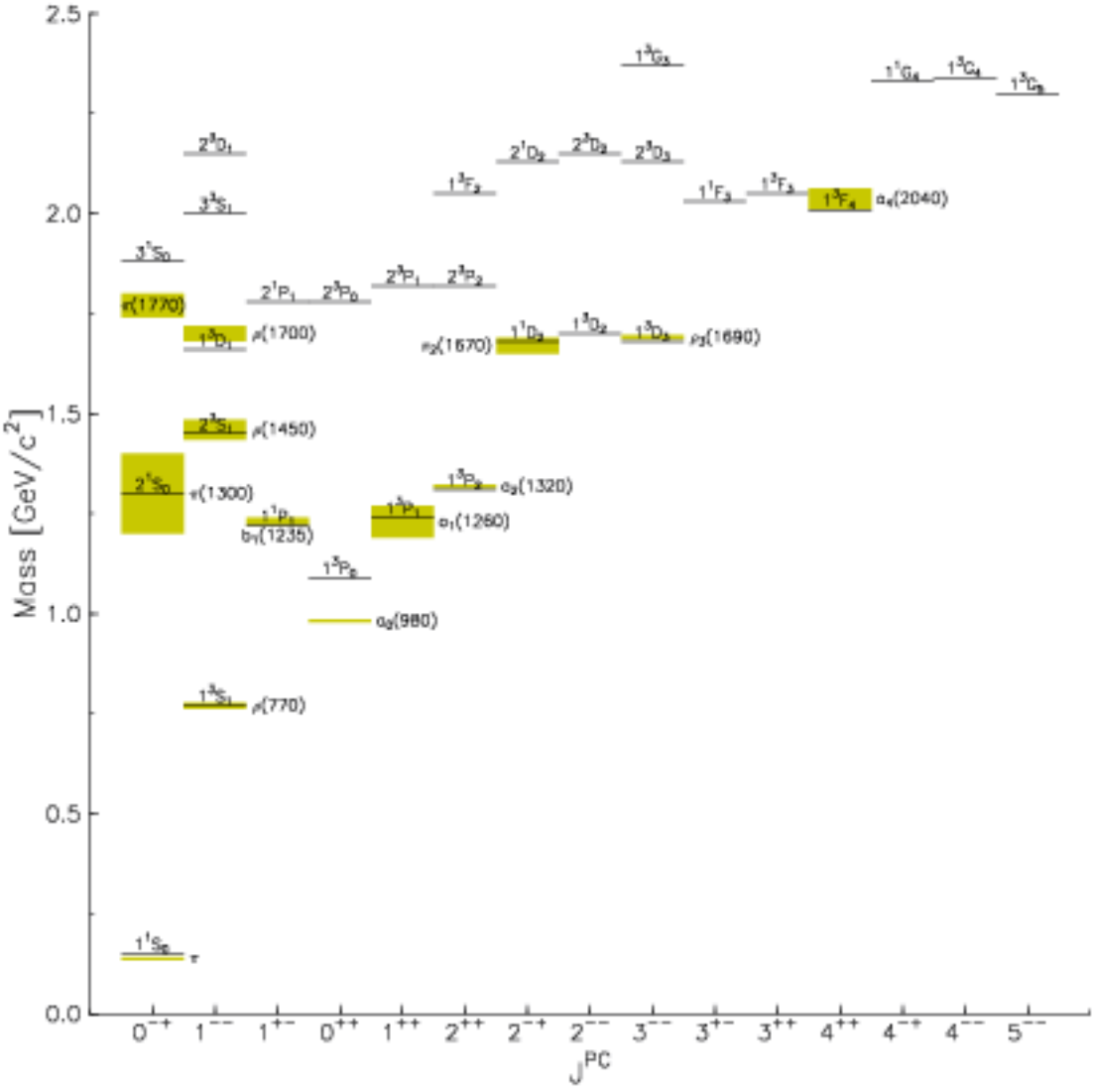

Figure 2.2: The predictions by Godfrey and Isgur of the masses of isovector mesons. Also shown are the experimental measurements, where such exist, as shaded bars representing the uncertainties in the masses of the detected states. The assignment of the $a_0(980)$ as the $1\ ^3P_0$ $J^{PC} = 0^{++}$ state is no longer widely accepted.

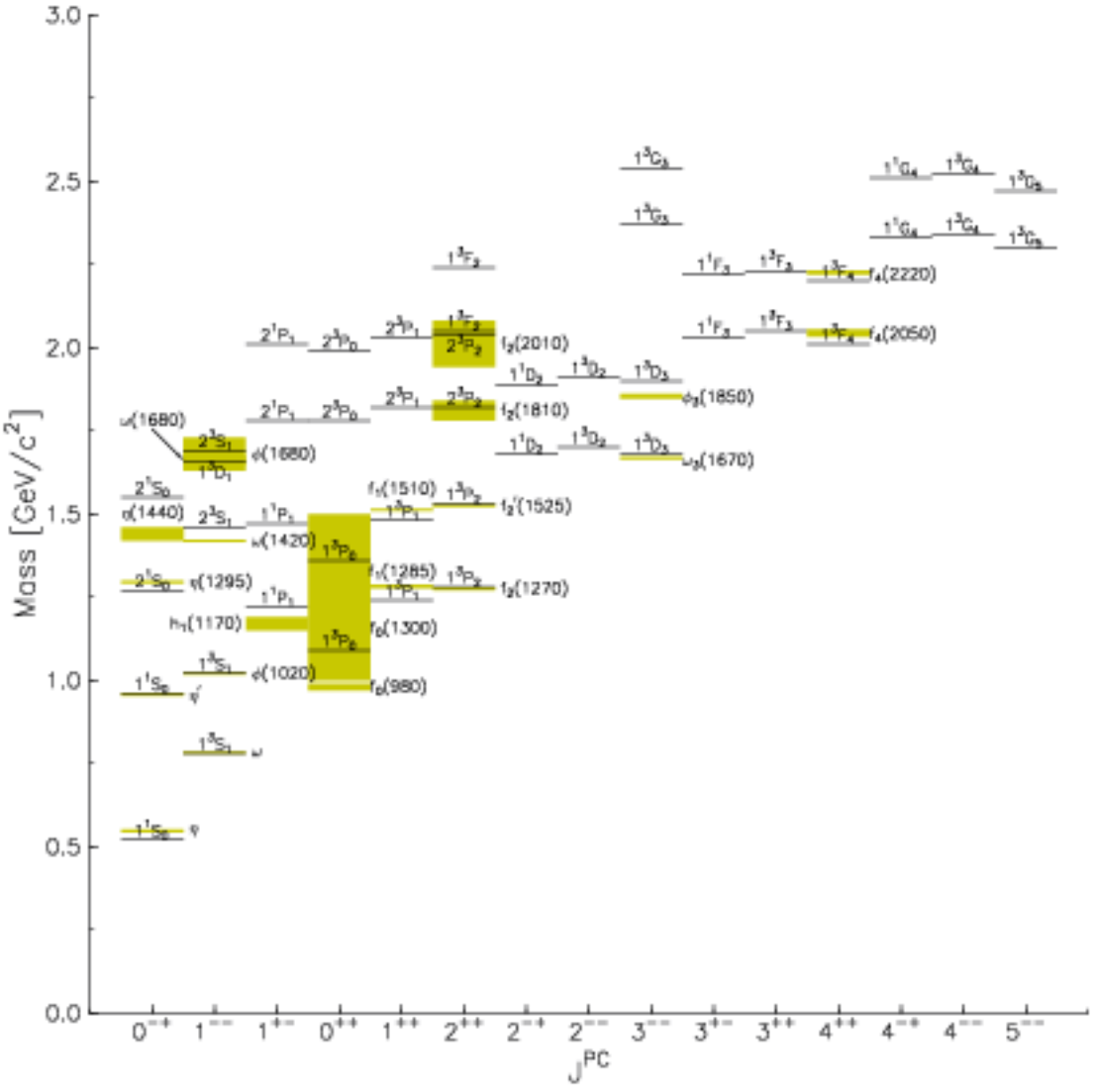

Figure 2.3: The predictions by Godfrey and Isgur of the masses of isoscalar mesons. Also shown are the experimental measurements, where such exist, as shaded bars representing the uncertainties in the masses of the detected states. The assignment f_0 states, particularly the $f_0(980)$, as pure $q\bar{q}$ mesons, is controversial.

also provided the input (to some extent) to the models for meson decays presented in the following sections.

2.2.2 Decays

2.2.2.1 Decays by Flux Tube Breaking

Meson decays by flux tube breaking were calculated by Kokoski and Isgur [7]. The flux tube model was developed by Isgur and Paton [8]. This model is extracted from the lattice formulation of QCD, but its basic degrees of freedom are quarks and flux tubes, rather than quarks and gluons. The flux tubes arise in the strong coupling limit of QCD, where the gluonic degrees of freedom condense into string-like structures. A $q\bar{q}$ meson is then modeled as a $q\bar{q}$ pair at arbitrary lattice points connected by all allowed configurations of chromoelectric flux along the links connecting the lattice points. The decays of these mesons are generated by an operator which creates a $q\bar{q}$ pair on a link. As a result of the symmetries involved, this $q\bar{q}$ pair is created with vacuum quantum numbers ($J^{PC} = 0^{++}$.) (Since the quark and antiquark have opposite intrinsic parities, one unit of orbital angular momentum is needed in order to make the overall parity positive. The spins of the $q\bar{q}$ pairs must couple to $s = 1$, in order to couple with the orbital angular momentum to make a total angular momentum of zero. So, for the $q\bar{q}$ pair, $^{2s+1}L_J = {}^3P_0$.) The decay products are mesons consisting of the newly created quark paired with the original antiquark, and vice versa. To compute the amplitudes for the decays, the wave functions of all of the mesons must be known (in order to compute the overlap integrals.) In this work two different sets of wave functions were used: 1) those from the work of Godfrey and Isgur described above, and 2) a set of harmonic oscillator wave functions. The lack of strong dependence on the chosen set of wave functions leads to the conclusion that the main systematics of the decays are due to the flux tube breaking mechanism, and not on the wave functions of the mesons. The main parameter in the model, the pair creation constant, is fitted to the decay $\rho(770) \to \pi\pi$.

This model calculates (with RMS deviation of less than 25%) nearly 100 well known decay amplitudes. Results of the calculations which are relevant to the analysis of $\bar{p}p \to \pi^+\pi^-\pi^\circ\omega$ are shown in Tables 2.1 and 2.2.

Note that no $\omega\pi\pi$ decay modes are given for a_2's, a_1's, h_1's nor π_0's. For $\omega\epsilon$ decays, the ϵ is the $1\,^3P_0$ ($I^GJ^{PC} = 0^+0^{++}$) state predicted by Godfrey and Isgur at a mass of $1.09\,GeV$; it loosely corresponds to what is now referred to as $(\pi\pi)_s$.

In comments concerning the vector mesons, the authors conclude that the $2\,^3S_1$ and $1\,^3D_1$ nonets are near 1.45 and $1.66\,GeV$, which is consistent with the currently accepted experimental interpretations of the $\rho(1450)$, $\omega(1420)$, $\rho(1650)$ and $\omega(1600)$. (At the time of this publication, only single broad states were believed to exist in this mass region.) They expect these mesons to be quite broad ($\Gamma \sim 500\,MeV$) and to overlap and mix. The isoscalar states which have been detected in experiments, however, are rather narrow, with widths of about $170\,MeV$ (see Table 2.1.) Measurement

Resonance	Predicted Decay Widths (MeV)			Γ_{expt} (MeV)
	$b_1\pi$	$\omega\epsilon$	$\rho\pi$	
$\omega(1460)\ 2\ ^3S_1$	2.25	.64	289, 225	174±59
$\omega(1660)\ 1\ ^3D_1$	441		64, 81	220±35
$\omega_3(1670)\ 1\ ^3D_3$	16 $(b_1\pi)_{L=2}$ .16 $(b_1\pi)_{L=4}$		38, 41	168±10
$\omega_2(1700)\ 1\ ^3D_2$	25		100,144 $(\rho\pi)_{L=1}$ 34,32 $(\rho\pi)_{L=3}$	220±35
$h_1(1780)\ 2\ ^1P_1$			1.7,224 $(\rho\pi)_{L=0}$ 144,884 $(\rho\pi)_{L=2}$	-

Table 2.1: Predictions by Kokoski and Isgur of the partial decay widths, in MeV, of some isoscalar mesons. Two sets of values are given, corresponding to the two sets of wave functions used in the calculations. Where only one value is shown, the two results were equal.

Resonance	Predicted Decay Widths (MeV)				Γ_{expt}
	$b_1\pi$	$\omega\rho$	$\rho\pi$	$\eta\pi$	(MeV)
$\pi_2(1670)\ 1\ ^1D_2$	0	0 $(\omega\rho)_{L=1\,s=2}$ 4, 7 $(\omega\rho)_{L=1\,s=1}$ 0 $(\omega\rho)_{L=3\,s=2}$ 1, 1 $(\omega\rho)_{L=3\,s=1}$	42, 59 $(\rho\pi)_{L=1}$ 31, 31 $(\rho\pi)_{L=3}$	-	258±18
$\pi(1800)\ 3\ ^1S_0$					212±37
$a_0(1780)\ 2\ ^3P_0$			-	6.8, 32	-
$a_1(1820)\ 2\ ^3P_1$			4.8, 32 $(\rho\pi)_{L=0}$ 50, 35 $(\rho\pi)_{L=2}$		- -
$a_2(1820)\ 2\ ^3P_2$			88, 16	20, .01	-

Table 2.2: Predictions by Kokoski and Isgur of the partial decay widths, in MeV, of some isovector mesons. The two sets of values shown correspond to the two sets of wave functions used in the calculations. Where only one value is shown, the two sets were yielded equal results.

of the masses and decay modes of these isoscalar 1^{--} resonances can provide information which would be useful in determining the amount of mixing and on the quark configurations of these states. In the analysis presented in this dissertation, evidence for the $b_1\pi$ decay mode of the $\omega(1600)$ is found; this supports its interpretation as the $1\ ^3D_1$ state.

Note that the isovector $2\ ^3P_1$ state is predicted to decay to $(\rho\pi)_{D-\text{wave}}$ more strongly than to $(\rho\pi)_{S-\text{wave}}$. This is consistent with a recent measurement of the $a_1(1700)$ by E852 [6]. This model makes no prediction concerning $\omega\pi\pi$ decay modes of this state.

2.2.2.2 The $^3P_0$ Model for Meson Decays

The BCPS collaboration published results of calculations of partial widths of radially and orbitally excited mesons, based on the $^3P_0$ model [9]. In this model, a $q\bar{q}$ pair is created with vacuum quantum numbers ($^3P_0 = 0^{++}$), which then combine with the q and $\bar{q}$ of the decaying meson to form the decay products. (This is to say that the $q\bar{q}$ pair is not formed from a one-gluon vertex, since in that case the $q\bar{q}$ pair would have the 1^{--} quantum numbers of the gluon.) This model, in fact, is obtained in a particular limit of the flux tube model described above. The validity of the $^3P_0$ model is established by calculations of decay widths of ground state mesons, especially D/S ratios in $b_1(1235) \to \omega\pi$ and $a_1(1260) \to \rho\pi$ [11]. The model is limited to decays into 2 mesons; no direct $\omega\pi\pi$ modes are accounted for, for example. Also, decays into $X(\pi\pi)_s$ are not computed, nor are decays into two mesons the sum of whose central masses is greater than the central mass of the decaying resonance. Specifically, for a resonance of mass m_R:

- $m_R > 1370 MeV$ for the $b_1\pi$ mode.
- $m_R > 1550 MeV$ for the $\omega\rho$ mode.

This excludes calculation of $\omega\pi\pi$ modes for $a_1(1260)$, $h_1(1170)$, $\pi(1300)$ and $a_2(1320)$. (Despite the fact that $a_2(1320) \to \omega\pi\pi$ has been observed.)

They use harmonic oscillator wave functions for the mesons, as these yield analytical results, and are known to give reasonable empirical approximations. Masses of the states are taken as those determined experimentally, where known, or those of other members of the same meson multiplet.

In several cases, the authors compare their predictions of decays of a $q\bar{q}$ meson to predictions for decays of a hybrid meson with similar properties. The comparisons are made against calculations based on the flux tube model, as implemented by two of the authors (Close and Page) of the BCPS paper; the details of their method of calculation are published in reference [10]. As has been typical in models of hybrid decays, there is a selection rule against decays into two mesons both of which consist of $q\bar{q}$ pairs in $L = 0$ states. In this model, though, the selection rule is weakened by accounting for the different spatial wave functions of the two decay products,

Resonance	Calculated Decay Widths (MeV)			Γ_{expt}
	$b_1\pi$	$\rho\pi$	Total	MeV
$\omega(1420)\ 2\ ^3S_1$	1	328	378	174±59
$\omega(1900)\ 3\ ^3S_1$	75	14	292	-
$\omega(1600)\ 1\ ^3D_1$	371	101	542	220±35
$\omega_2(1670)\ 1\ ^3D_2$	8	221	300	-
$\omega_3(1670)\ 1\ ^3D_3$	7	50	69	168±10
$h_1(1700)\ 2\ ^1P_1$	0	173	252	360±40
$\omega_1(1500)$ Hybrid	0	20	∼20	-

Table 2.3: BCPS calculations of partial decay widths for some orbital and radial excitations of isoscalar mesons. Decay widths are given in MeV. The experimental values in the last column are taken from the PDG.

Resonance	Calculated Decay Widths (MeV)					Γ_{expt}
	$b_1\pi$	$\omega\rho$	$\rho\pi$	$\eta\pi$	Total	MeV
$\pi(1800)\ 3\ ^1S_0$	-	73	31	-	228	212±37
$\pi_2(1670)\ 1\ ^1D_2$	0	41	118	-	250	258±18
$\pi(1800)$ Hybrid	-	0	30	-	∼240	-
$\pi_2(1800)$ Hybrid	15	0	8	-	80	-
$a_0(1700)\ 2\ ^3P_0$	165	46	-	5	293	-
$a_1(1700)\ 2\ ^3P_1$	41	15	58	-	246	-
$a_2(1700)\ 2\ ^3P_2$	28	109	104	23	336	-
$a_1(1700)$ Hybrid	0	0	30	-	∼300	-

Table 2.4: BCPS calculations of partial decay widths for some orbital and radial excitations of isovector mesons. Decay widths are given in MeV. The experimental values in the last column are taken from the PDG.

assuming that they are not identical mesons. Another selection rule plays a role in this model; it is called the *singlet selection rule*, and states that a hybrid whose $q\bar{q}$ pair is in a spin singlet ($S = 0$) state cannot decay to two mesons both of which consist of $q\bar{q}$ pairs in spin singlet states.

Concerning the vector isoscalar mesons: The PDG masses are used in the calculations. The calculated total widths are quite large, 378 and $542 MeV$ for the $\omega(1420)$ and $\omega(1600)$ respectively. The large partial width to $b_1\pi$ for the $\omega(1600)$ is interesting because neither the $2\,^3S_1$ nor hybrid $J^{PC} = 1^{--}$ state couples strongly to this channel. Thus, observation of a $b_1\pi$ decay mode for a 1^{--} resonance in this mass region would "tag" it as the likely $1\,^3D_1$ state. Evidence for this decay mode is one of the results of the partial wave analysis presented in Chapter 12. The authors comment that the physical states are probably mixtures of the $2\,^3S_1$, $1\,^3D_1$ and hybrid basis states, due to their proximity in mass and their large widths. The observed widths of about $170 MeV$ for the $\omega(1420)$ and $\omega(1600)$ may be indicative of significant mixing.

For the as yet undiscovered $1\,^3D_2$ ω_2 state, a mass of $1670 MeV$ is assumed, as this is similar to that of the $\omega(1600)$ and $\omega_3(1670)$ which are believed to be the $1\,^3D_1$ and $1\,^3D_3$ states. The $\omega_2(1670)$ is calculated to decay predominantly to $\rho\pi$, with a small partial width for $b_1\pi$.

For the $1\,^3D_3$ $\omega_3(1670)$, the calculated total width is $69 MeV$, apparently in conflict with the observed width of $168 MeV$. The $b_1\pi$ decay mode has a calculated partial width of $7 MeV$.

For the $2\,^1P_1$ (h_1) state, whose mass is predicted to be $1.7 GeV$, the calculated width to $b_1\pi$ is zero; its dominant mode is predicted to be $\rho\pi$.

The $\pi(1800)$ resonance has been reported in several decay modes, but is not seen in $\rho\pi$ [1]. The calculation for the 3^1S_0 state at this mass yields a partial width of $31 MeV$ for the $\rho\pi$ decay mode. The authors discuss the possibility that this resonance is at least in part a hybrid meson. The $\omega\rho$ decay mode can help to clarify this issue: the $q\bar{q}$ state is predicted to have a sizable branching fraction into this mode (about 30%), but the hybrid is predicted to not decay into $\omega\rho$.

There are similar concerns about the $a_1(1700)$ resonance: is it the $2\,^3P_1$ $q\bar{q}$ state or a hybrid? Close and Page predict a width of $300 MeV$ for a hybrid with these quantum numbers [9, 10]. BCPS predict a similar total width of $250 MeV$ for the $2\,^3P_1$ $q\bar{q}$. The $q\bar{q}$ state couples more strongly to S+S decay modes (S+S meaning that the two decay products are mesons both of which are $q\bar{q}$ pairs in S-waves.) Accurate determination of the strengths of the $\rho\pi$ and $\omega\pi\pi$ decay modes would be interesting, as $b_1\pi$ would come exclusively from the quarkonium (because of the singlet selection rule), as would $\omega\rho$. The D/S ratio for the decay to $\rho\pi$ should be very large for the $q\bar{q}$ state, but for the hybrid S-wave is calculated to dominate. Recently, Brookhaven experiment E852 reported a dominantly D-wave $\rho\pi$ decay mode for the $a_1(1700)$ [6], supporting the interpretation of this resonance as the $2\,^3P_1$ $q\bar{q}$ state. The partial wave analysis in Chapter 12 finds evidence for the $\omega\rho$ decay mode, but not for the $b_1\pi$ mode. This is not in perfect agreement with the prediction for the $2\,^3P_1$ $q\bar{q}$ state, but it does provide

evidence against the interpretation of the $a_1(1700)$ as a hybrid meson.

For the $2\,^3P_0$ $a_0(1700)$, $b_1\pi$ is calculated to be the strongest decay mode, with a significant coupling to $\omega\rho$, too. These modes are predicted to be strong for the $2\,^3P_2$ $a_2(1700)$ as well.

For the $\pi_2(1670)$, presumably the $^1D_2$ state, the calculated width to $\omega\rho$ is $41 MeV$. The total width is calculated to be $250 MeV$ in good agreement with PDG value of $258 \pm 18 MeV$. The PDG, however, does not report any information on possible $\omega\pi\pi$ decay modes for this resonance.

Some experiments indicate a possible π_2 signal at $1800 MeV$. BCPS compare a $1\,^1D_2$ $q\bar{q}$ state to a hybrid $\pi_2(1800)$. The calculated widths for the $\omega\rho$ decay mode are $69 MeV$ and zero for the $q\bar{q}$ and hybrid states respectively; for $b_1\pi$ decays, widths are 0 and $15 MeV$. These two $\omega\pi\pi$ modes can distinguish the nature of such a resonance. Total widths are computed as 372 and $80 MeV$.

2.2.2.3 Summary

The $\omega\pi\pi$ decay modes can help distinguish among the interpretations of observed resonances. The analysis in this dissertation is able to provide some information on the $\omega(1600)$ and $a_1(1700)$ resonances. Most of the other resonances in question were not observed in $\omega\pi\pi$ modes. This is not to say that these modes do not exist; it may be that they are not produced in quantities sufficient enough to allow their observation. Additional information from other final states (where these resonances decay in other modes) is needed in order to draw conclusions.

2.3 $\bar{p}p$ Annihilation

There are many theoretical models which strive to explain the dynamics of $\bar{p}p$ annihilation. The treatments of the problem range from very detailed models of the microscopic processes involved, to the completely phenomenological. Tests of these models can be made by comparing their predictions for the rates of production of various two-meson final states to the rates measured in experiments.

In Table 2.5, a comparison is made between the measured rates of several two-body final states, and the predictions of four models. The four models represent four different approaches to the problem. In model A [12], the calculations are based on baryon exchange, as shown in Figure 2.4A. The calculations in model B [13] are based on the quark line rule model, as shown in Figure 2.4B, where both the rearrangement and annihilation diagrams are shown. The authors conclude that the rearrangement contributions are more important than the annihilation contributions. Model C [14] uses a diquark model for the $\bar{p}p$ annihilation, as shown in Figure 2.4C. The proton and antiproton are described as quark-diquark (qD) clusters, and two meson production occurs through the effective interaction $\bar{D}D \to \bar{q}q$. Model D [15] is purely phenomenological; it makes no attempt to model the processes involved, but rather

characterizes the observations and extends the characterization to make predictions. It is based on the observation that in $\bar{p}p$ annihilation, production of mass is preferred over release of kinetic energy (i.e. there is a preference for production heavy particles.) None of the models shows complete agreement with the measurements. Of

Reaction $\bar{p}p \rightarrow$	Rates (%) Measured		Model A	Model B	Model C	Model D
$\pi^\circ\pi^\circ$	0.0693±0.0043	[38]	0.096	-	-	-
$\pi^+\pi^-$	0.307 ±0.013	[38]	0.39	0.36	0.34	0.54
K^+K^-	0.099 ±0.005	[38]	0.21	0.08	-	0.11
$\pi^\circ\eta$	0.0212±0.0012	[38]	0.014	-	-	-
$\pi^\circ\omega$	0.573 ±0.047	[38]	2.18	1.40	0.45	-
$\pi^\circ\eta'$	0.0123±0.0013	[38]	0.014	-	-	-
$\eta\eta$	0.0164±0.0010	[38]	0.015	-	-	-
$\eta\omega$	1.51 ±0.12	[38]	0.13	0.93	1.45	-
$\eta\eta'$	0.0216±0.0025	[38]	0.042	-	-	-
$\omega\omega$	3.23 ±0.25	[This work]	1.66	1.08	0.46	4.4
$\omega\eta'$	0.78 ±0.08	[38]	0.11	-	0.75	-
$\rho^\circ\rho^\circ$	0.12 ±0.12	[19]	1.07	1.1	0.001	-
$b_1^\circ\pi^\circ$	0.92 ±0.11	[58]	-	-	-	0.7
$f_2\omega$	0.67 ±0.09	[58]	0.25	-	-	-
$\omega\rho^\circ$	0.07 ±0.03	[20]	2.77	1.91	2.2	8.6

Table 2.5: Comparison of the calculated rates for production of various 2-meson final states in $\bar{p}p$ annihilation at rest, and the measured rates. The models are described in the text.

particular interest is the large measured rate for $\omega\omega$; all of the models except Model D predict a rate much smaller than what is measured.

In addition to comparing measured to predicted rates, something can be learned from the comparison of rates to one another. In a study of the quark line rule model, Genz *et al* conclude that production rates for $\omega\omega$ and $\rho^\circ\rho^\circ$ would be equal if the annihilation diagram dominates over the rearrangement diagram (in Figure 2.4B.) The measured rates are clearly not equal, implying that the annihilation diagram does not dominate.

2.3.1 Production of ω's

Table 2.5 shows a trend concerning the production of ω's in $\bar{p}p$ annihilation at rest: the rate for $\bar{p}p \rightarrow \omega X$ is always greater than the rates for $\pi^\circ X$, ηX and $\eta' X$ for all of the two-body final states; there seems to be a preference for ω production. Table 2.6

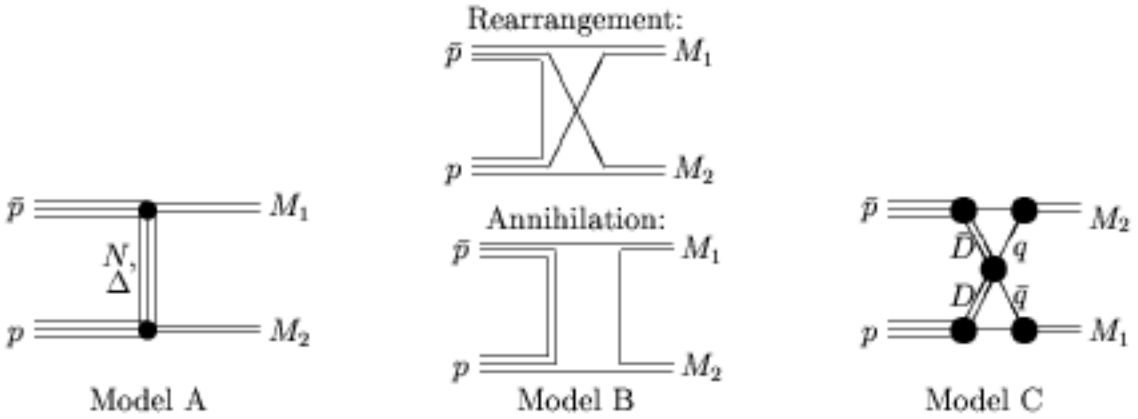

Figure 2.4: These diagrams show the interactions which are used in the calculations of rates for $\bar{p}p \to M_1 M_2$ where M_1 and M_2 are mesons. Model A is based on baryon exchanges. Model B is based on the quark line rule model (both rearrangement and annihilation diagrams are shown.) Model C is based on the diquark (D) model of the proton and antiproton.

lists production rates for several final states which involve ω's. About than 30% of $\bar{p}p$ annihilations at rest produce at least one ω. The $\pi^+\pi^-\pi^\circ\omega$ final state, analyzed

Channel	Rate (%)	Reference
$\pi^+\pi^-\pi^\circ\omega$	16.1 $\pm$1.0	[This work]
$\omega\pi^\circ\pi^\circ$	2.57 $\pm$0.17	[17]
$\omega\pi^+\pi^-$	6.6 $\pm$0.6	[4]
$\omega 2\pi^+ 2\pi^-$	1.3$\pm$0.3	[18]
$\omega\eta\pi^\circ$	0.68 $\pm$0.05	[48]
$\omega\omega$	3.23 $\pm$0.25	[This work]
$\omega\pi^\circ$	0.573$\pm$0.047	[38]
$\omega\eta$	1.51 $\pm$0.12	[38]
$\omega\eta'$	0.78 $\pm$0.08	[38]

Table 2.6: Measured production rates of various final states from $\bar{p}p$ annihilation at rest.

in this dissertation, comprises about half of this total. It will be interesting to see if this trend is observed in the analysis of other final states, especially those involving high pion multiplicities, as these have high rates of production, and 89% of ω's decay to $\pi^+\pi^-\pi^\circ$ so they are most easily observed in such final states.

Chapter 3

The Crystal Barrel Detector

The Crystal Barrel detector is designed to measure the trajectories of charged particles and photons resulting from the annihilations of antiprotons with protons and

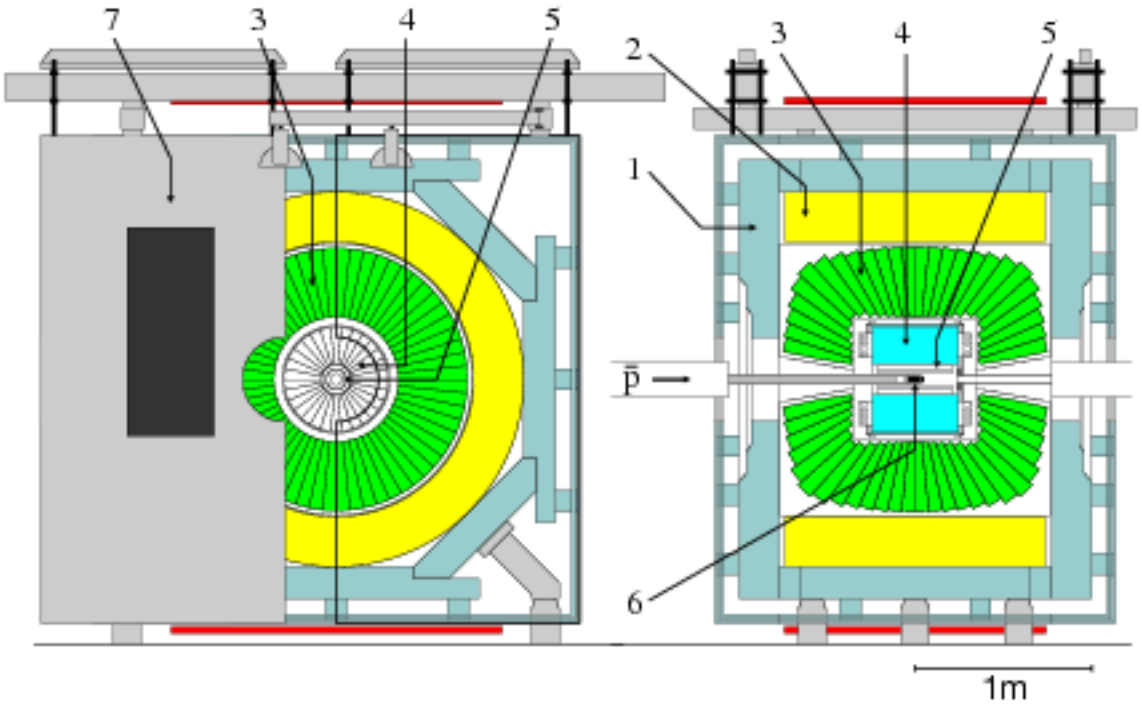

Figure 3.1: The Crystal Barrel detector system: 1) Magnet yoke. 2) Magnet coils. 3) Barrel calorimeter. 4) Jet drift chamber. 5) Proportional wire chamber. 6) Liquid hydrogen target. 7) One half of the movable magnet yoke end-plate.

neutrons. Experiments can be performed under different conditions (annihilations at rest or in flight, in liquid or gaseous targets, etc.) and with different configurations of some of the minor sub-detectors. The following discussion will focus on those aspects of the experiment which apply to the particular data set which is the subject of this

dissertation. A more general and more detailed description of the apparatus can be found in reference [21].

3.1 Antiproton Beam, Target and Beam Defining Detectors

The source of antiprotons is the Low Energy Antiproton Ring (LEAR) at CERN; it delivers a beam of pure antiprotons with a momentum of $200 MeV/c$ at an intensity of about $10^4 \bar{p}/s$. The antiprotons exit the LEAR vacuum through a $100\mu m$ thick beryllium window and pass through the first beam defining detector, a fast compact multi-wire proportional chamber (KC.) The antiprotons then enter the target vacuum via a $50\mu m$ thick mylar window. Air at atmospheric conditions is between the two vacuum volumes. Two silicon diode detectors are located $33mm$ and $28mm$ upstream of the target. They are each $200\mu m$ thick. The downstream one is segmented into quadrants to aid in beam steering. These silicon detectors operate a about $-100°C$, resulting in less noise than operation at room temperature. Their signals are used to start the JDC drift time measurement; the uncertainty in trigger time, due to noise and rise-time, is less than $0.5ns$.

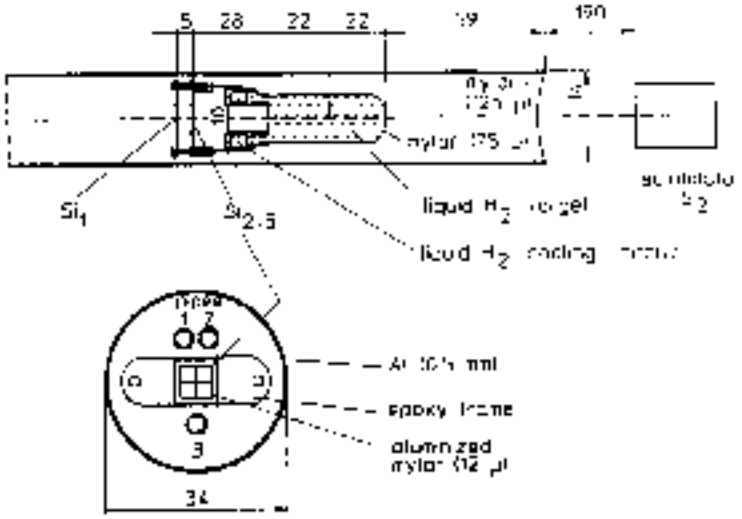

Figure 3.2: The liquid hydrogen target and beam defining detectors. Dimensions are in mm.

The liquid hydrogen target is $17mm$ in diameter and $44mm$ long, with a $10mm$ diameter entrance window. It is made of mylar wrapped in Kevlar. The $\bar{p}$'s stop near the center of the target with a longitudinal spread (σ) of $0.6mm$. They then eject and replace an electron from a hydrogen atom, initially with principal (radial)

quantum number of about 30, and orbital angular momentum of about 20. Due to strong Stark mixing in the liquid hydrogen, the atom quickly cascades to lower angular momentum states, and annihilates (usually) from the $L = 0$ state due to the overlap of the proton and antiproton wave functions in this state. This process takes place in less than $1ns$ [23].

3.2 PWC's

Two concentric cylindrical multi-wire proportional chambers, with their axes along the beam direction, surround the target. They are used in determining the multiplicities of charged particles for triggering, and also give (r, ϕ) coordinates near the target for charged tracks. There are 90 anode wires in the inner PWC (PWC1), at a radius of $25.5mm$. The outer PWC (PWC2), has 150 wires at a radius of $43.0mm$. The wires in both PWC's are 35cm long, amply covering the solid angle subtended by the JDC and BC.. The cathodes are $22\mu m$ thick aluminum foils. The thickness of material in the PWC's traversed by a particle traveling perpendicular to the beam axis is 0.022 radiation lengths (L_R.) The PWC's have intrinsic efficiencies of greater than 99%. A charged particle passing through the PWC's produces a detected signal on an average of 1.6 wires. The signals from the PWC's are collected and processed by the LeCroy PCOS III system.

3.3 JDC

The main apparatus for tracking of charged particles is the Jet Drift Chamber (JDC). Like the PWC, the JDC's sense wires are oriented along the magnetic field axis. The 23 layers of sense wires are spaced $8mm$ apart, at radii of $63mm$ to $239mm$, and are $399mm$ long. The inner 5 layers are divided into 15 azimuthal sectors, and layers 7 to 23 are divided into 30 azimuthal sectors. Layer 6 is not used. The sense wires are staggered by $\pm 200\mu m$ azimuthally to allow resolution of the left/right ambiguity. Field wires along the sector boundaries and between the sense wires provide a drift field of 1000V/cm. The gas used is a 90:10 mixture of CO_2 and isobutane. Under normal operating conditions, the electron drift velocity is $8.4\mu m/ns$ and the Lorentz angle is 7.2°. The temperature, pressure and composition of the JDC gas are precisely maintained and continuously monitored.

The charge collected on the sense wires is measured at both ends of the wire, allowing one to infer where along the wire the ionization occurred. These signals are digitized at 100MHz, giving a time profile of the charge collected, allowing detection of multiple charged particles passing near the same wire. The flash ADC's are operated in a nonlinear mode, to enhance the dynamic range and to improve resolution above the pedestal.

As the JDC is situated between the target and the photon detection apparatus,

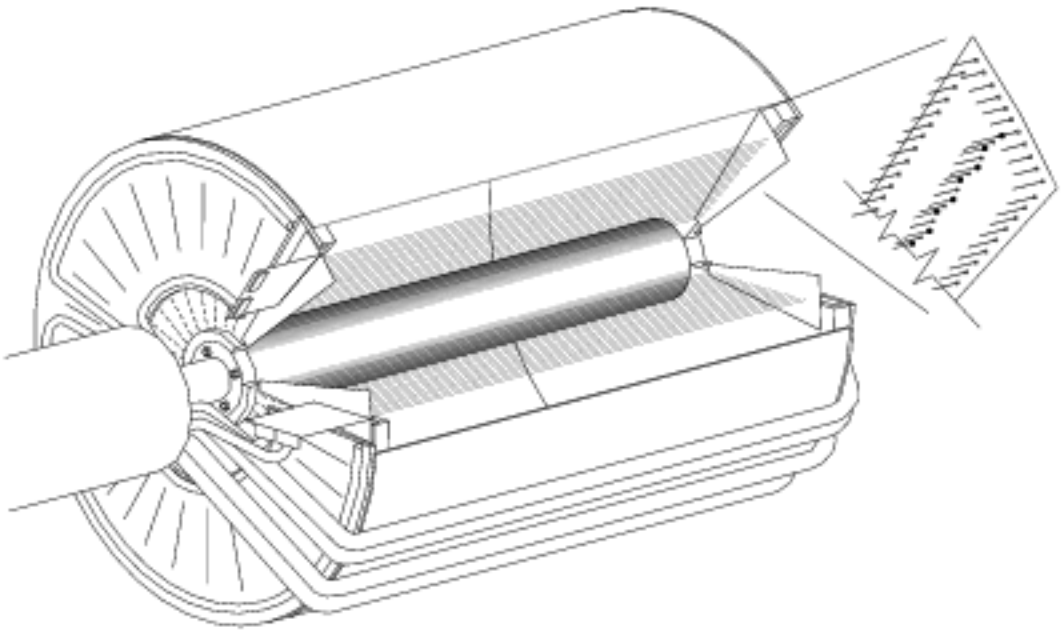

Figure 3.3: The JDC. The staggering of the sense wires, shown in the expanded drawing, is exaggerated for clarity.

it is designed to be small and of low mass. The inner cylinder, wires, gas and outer shell have a combined thickness of $0.0405L_R$ for radial trajectories. The end-plates, including the electronics mounted there, each correspond to $0.20L_R$.

3.4 Electromagnetic Calorimeter

The Barrel Calorimeter (BC) provides high efficiency and good energy and spatial resolution for detection of photons with energies from 10 to $2000MeV$. It consists of 1380 modules in a vertex pointing geometry, covering the range of polar angles from 12° to 168°. The BC completely surrounds the target azimuthally. Each module subtends 6° in both polar and azimuthal angles, except near the beam pipe ($\theta < 30°$ and $\theta > 150°$), where each covers 12° in azimuth. 13 different module shapes are required, one for each pair of polar angles at which the modules are placed. The scintillating material is thallium doped cesium iodide. Each CsI(Tl) crystal is $300mm$ long ($16.1L_R$), which keeps fluctuations in the energy leakage out the rear of the crystals to less than 1%. The crystals and associated electronics are enclosed in $0.1mm$ ($0.056L_R$) thick titanium cans, for isolation and structural purposes. The support structure also requires a $10mm$ ($0.11L_R$) thick aluminum inner wall. Collection of the scintillation light by photomultiplier tubes is precluded because the BC is situated in a strong magnetic field; thus photodiodes were chosen for this purpose. In order to match the light emitting area of the crystal to the sensitive area of the photodiode,

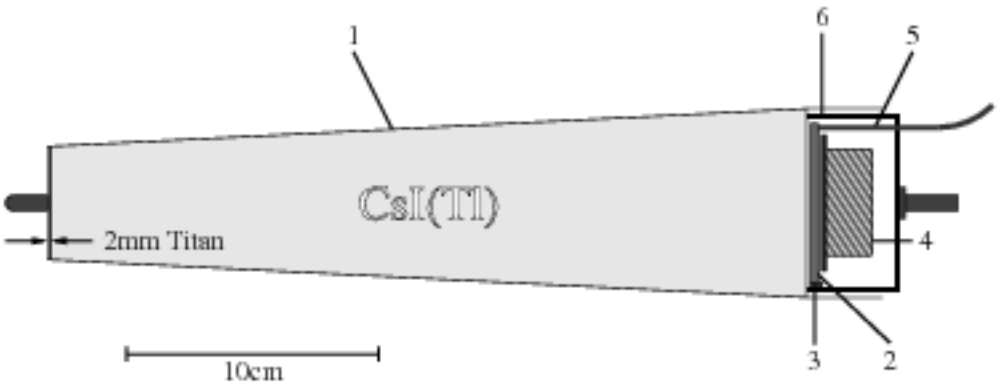

Figure 3.4: A BC module. 1) Titanium can. 2) Wavelength shifter. 3) Photodiode (on the edge of the wavelength shifter.) 4) Preamplifier electronics. 5) Optic fiber from the light-pulser. 6) Brass cover.

wavelength shifters (WLS) are used to collect and re-emit the light. These are $3mm$ thick plastic tiles which absorb the scintillation light and emit it at a longer wavelength. This longer wavelength is better matched to the sensitivity of the photodiode, which is affixed to one of the lateral faces of the WLS. The other lateral faces are painted white to enhance the light collection efficiency. A light fiber is connected to the WLS to allow the light-pulser to test and calibrate the response of the entire BC electronics chain. A charge sensitive preamplifier is also contained in each module of the BC. These preamplifiers have an integration time of $1\mu s$, to match the fast component of the CsI(Tl) scintillation light. The preamplified signals are further processed by pulse shapers, discriminators for triggering purposes, and two ADC systems. The LeCroy 4300-B FERA ADC system gives fast readout (for software triggers requiring measurement of PED energies) and a wide dynamic range (photons up to $2000MeV$), but with limited precision of about $1MeV$. The LeCroy 2282 system provides better precision (about $0.1MeV$) over a limited range of photon energies (0 to $400MeV$) for use in off-line analysis.

3.5 Magnet

The magnet is a conventional solenoid producing a magnetic field of 1.5T in the volume in which the wire chambers BC are situated. The variation of the z-component of the field is less than $\pm 1.5\%$ in the volume containing the JDC. The radial component is less than 0.014T.

3.6 Trigger

The electronics should, of course, only be read out after a $\bar{p}p$ annihilation occurs, or, equivalently, when an antiproton enters the target. This condition is indicated by a

coincidence of signals from KC, Si_1, and Si_{2-5}. That is, all three of the detectors in front of the target, through which an antiproton must pass before entering the target, must fire. This is the only requirement for a *minimum bias* trigger. For a *2-prong* trigger, data from the PWC's and JDC are required. Fast methods for determining the number of charged particles in an event are needed from both the JDC and PWC. A single charged track may fire several PWC wires, so a way of counting these clusters is required. The PCOS III system (which reads the PWC) is designed for such use; its data are fed into *majority logic units* (MALU's), which produce an analog signal proportional to the number of of clusters in the PWC's. This analog signal is digitized by a fast ADC, the output of which represents the number of charged tracks in the PWC's. For the JDC, analog signals from both ends of the wires in layers 2, 3, 4, 5, 19 and 20 are fed into discriminators, whose outputs are fed into MALU's. As with the PWC's, the digitized output of the MALU's represents the number of charged tracks in the JDC. Exactly 2 clusters in the PWC, and exactly 2 hits in each trigger layer of the JDC are required for the *2-prong* trigger.

Other triggering schemes available to the experiment can be based on the number of clusters in the BC or on software triggers which can be based on invariant masses of combinations of clusters in the BC. These features were not used in collecting the data to be analyzed in this work.

3.7 Data Acquisition and Recording

The data from the JDC and BC are read into small VME-based computers called *local event builders* (LEVB's), where simple operations such as pedestal subtraction, zero suppression, and data compression are performed. Data from the LEVB's, PWC's, beam counters, and from the slow control system are assembled in another VME-based computer known as the *global event builder*, which writes the data onto magnetic tapes. It also sends a fraction of the data to other computers which are used for online monitoring of the data.

3.8 Calibration

3.8.1 JDC

The z-coordinate of a hit on a JDC wire is determined by

$$z = z_0 + z_L \frac{A_+ - \alpha A_-}{A_+ + \alpha A_-}$$

where z_0 is the location of the center of the wire, z_L is the wire length, α is the relative gain of the electronics on the two ends of the wire, and A_+ and A_- are the amplitudes of the (charge) signals on the two ends. Each wire has its own set of parameters, z_0,

z_L and α. For determination of these calibration constants, several thousand events with at least four charged tracks each are recorded with the magnetic field off. Using a reasonable guess for the constants, each event's tracks are fit to straight lines pointing to a single vertex. The fitted z-coordinates are used to derive an improved set of calibration constants, and the procedure is iterated to find a stable set of calibration constants. This procedure yields a z resolution of $6mm$ per wire.

The (r, ϕ) coordinates corresponding to a hit on a JDC wire are determined from the drift time. For calibration, several hundred *collinear* events, of the type $\bar{p}p \rightarrow \pi^+\pi^-$ and $\bar{p}p \rightarrow K^+K^-$, are used; the pions have a momentum of $927.8MeV/c$, and the kaons $797.9MeV/c$, and the two charged tracks form a single helix which spans the diameter of the JDC. Using these reactions provides an absolute reference for calibration. An electrostatic computer simulation program, GARFIELD [22], is used to create drift time to coordinate translation tables for several different drift velocities, since drift velocity can vary with gas temperature and pressure. The collinear events are analyzed using a drift time table obtained by interpolating between the Garfield tables, and varying the interpolation factor. The optimum drift time table is that which minimizes the widths of the peaks in the momentum spectra of the charged particles. The momentum resolution is 6% at $p = 927.8MeV/c$. The atmospheric pressure is monitored by the slow control system, and the interpolation factor is corrected run-by-run in the off-line analysis. A 4-prong calibration, using $\bar{p}p \rightarrow \pi^+\pi^-\pi^+\pi^-$, is used to check the resolution for momenta as low as $100MeV/c$.

3.8.2 BC

The location of the π° peak in $\gamma\gamma$ invariant mass spectra provides an absolute reference for calibration of the BC data. About 1 million events are collected using an *all neutral* trigger, requiring no charged tracks. Histograms of $\gamma\gamma$ invariant masses are made for each crystal, where one of the photons hits the given crystal, and is paired with each other photon in the event. Often one of the pairs is from a π°, and hence contributes to the peak, and the others form a combinatoric background. A new set of calibration constants can then be computed, which will shift the peak closer to the π° mass. This procedure is iterated till the π° peak is at the correct mass for all crystals. The original set of constants was derived from the position of the minimum ionizing peak from charged pions traversing the crystals; for subsequent calibrations, the constants from the previous calibration are used. This procedure is usually done once per run period (the run periods last a few weeks.)

The response of the FERA and 2282 ADC systems overlap for energy deposits up to about $400MeV$, allowing the FERA's to be calibrated in terms of the 2282's. A straight line is fitted to a plot of FERA vs 2282 values for each crystal, yielding the FERA *gain ratio*. Corrections for the FERA nonlinearity for small signals are also made.

Linearity of response and changes in gain during the experimental runs are moni-

tored using the light-pulser system. This is a xenon flash lamp whose light is delivered to each crystal's WLS via optic fibers. The light is passed through filter systems to give many different intensities over a wide range. This calibration can be performed in about 10 minutes and is typically done every several hours.

ADC pedestals are also measured every few hours by reading out the BC electronics with no beam incident on the target.

Typical photon energy resolution is $2.5\%/E^{1/4}$, where E is the photon energy in GeV. Deviations from the expected $E^{-1/2}$ dependence of the resolution is typical for calorimeters using homogeneous crystals such as NaI and CsI [1, 24, 25], and occur because of fluctuations in energy leakage and nonuniformity in light collection efficiency. Angular resolution for photons is about 1.5°.

Chapter 4

Event Reconstruction

4.1 Crystal Data Reconstruction

The first step in the analysis of data from the Barrel Calorimeter is to convert the ADC values (FERA and 2282) to energy deposited for each crystal. The pedestals are subtracted from the recorded ADC values, then the corresponding energy deposit is computed: $E_{crystal}$ = ADC value × slope(energy/ADC count) × (LP gain correction). The coefficients for the conversion are taken from a database containing such quantities for each run. Corrections for nonlinearities in detector response are made by adjusting the pedestal subtracted ADC values in such a way that the linear energy conversion formula is valid. A minimum amount of energy is required to have been deposited in order for the crystal to be further considered in the analysis of the event. In the computer program for the analysis, this minimum is determined by the value of the variable EMINBC; for this analysis, its value was set to $1.0 MeV$. The 2282 data is used if it is within the allowed range (some minimum above pedestal, and less than its overflow value). The FERA data is used if the 2282 data isn't used (not available or out of range), and if it is greater than some minimum above the pedestal. Recall that the 2282's have greater resolution, but with a more limited energy range, than the FERA's.

Next, adjacent crystals in which energy was deposited are grouped into *clusters*. All crystals in a cluster share at least one corner with another crystal in the cluster. To be considered part of a cluster, each crystal must have deposited in it a minimum of $1 MeV$, set by the variable EXTLBC. At least one crystal in the cluster must contain ECLSBC=$4.0 MeV$, and the entire cluster must contain at least ECLUBC=$4.0 MeV$ of energy.

A cluster may contain the signals for multiple photons or charged particles. Each cluster is searched for local maxima in its energy distribution. These maxima are assumed at this point to correspond to the detected particles and are called PEDs (Particle Energy Deposits.) Other mechanisms for producing local maxima are discussed in Section 4.1.1. Any secondary PEDs in a cluster are required to contain a minimum of EPEDBC=$10.0 MeV$. The crystal containing a local maximum of energy

is referred to as the *central crystal*. The energy in crystals where PEDs overlap is shared among the PEDs; the splitting of the energy from a crystal among the N PEDs in a cluster is determined by how much energy is in the central crystal plus that in its eight neighboring crystals:

$$E_{\mathrm{PED}i} = E_{\mathrm{cluster}} \times \frac{E_{9i}}{\sum_{j=1}^{N} E_{9j}}.$$

E_{cluster} is the total energy in the cluster. E_9 is the sum of the energies in the central crystal and its 8 neighbors; if a given crystal is a neighbor of more than one central crystal, it contributes to the E_9's of the n PEDs according to the energies in the central crystals:

$$E_{9i} = E_{1i} + \sum_{\mathrm{neighbors},j} E_j \times \frac{E_{1i}}{\sum_{k=1}^{n} E_{1k}}.$$

E_{1j} is the energy in the central crystal of PED j. Given the energy deposited in the crystals, an estimate of the energy of its photon can be made. Some of the photon's energy can leak out of the detector or be absorbed by the titanium cans containing the crystals, so correction factors are applied to the PED energy [26]. The correction factor depends on the PED's energy and polar angle (the detector is symmetric in the azimuthal angle). The position of the PED taken to be that of the centroid of the energy distribution. From this, the direction of flight of the particle from the event vertex is determined. This direction and the PED energy are then stored for later use.

4.1.1 Splitoffs

The lateral distribution of the energy deposited by a photon in the Barrel Calorimeter, being a stochastic process, is not always a monotonically decreasing function of the distance from the point of impact. There may be local maxima; these are known as *electromagnetic splitoffs*. In the analysis described above, these will be interpreted as individual PEDs, and therefore as photons.

Hadronic splitoffs are produced by secondary particles from the interactions of hadrons with the detector, usually from a charged pion hitting the Barrel Calorimeter. The PEDs produced may be well separated from the parent PED if the secondary particle leaves the crystals and hits another part of the barrel.

4.1.1.1 Dolby-C

Dolby-C [27] is an analysis tool for recognition of electromagnetic splitoffs. It relies on two of their characteristics for identification: They are usually 1) very near their parents PED, and 2) of much lower energy than their parents. These are determined qualitatively by the apparent angle, ψ between the lines of flight of two PEDs, and their energy asymmetry, A, defined as

$$A = \frac{E_1 - E_2}{E_1 + E_2}.$$

The region of the space spanned by these two quantities corresponding to small angles and large asymmetry defines splitoffs in this method.

The results of the Dolby-C analysis are ignored in the analysis of the data set used in this dissertation.

4.1.1.2 CBDROP

CBDROP [28] is a set of algorithms for removal of hadronic splitoffs from events. It is used *after* any PEDs corresponding to tracked charged particles have been removed. It makes further cuts on PED energies and topologies to eliminate some PEDs. The central crystal of each PED is required to contain at least ECENUS=$13MeV$. A cut on the minimum photon energy, EGAMUS, is set to $5MeV$, so it is superseded by the central crystal energy cut. A cut on the fraction of the photon energy in the central crystal, E_1/E_9, is made at E1E9US=0.96; hadronic splitoffs are found to frequently produce a signal with most of the energy in one crystal [29].

Next, CBDROP attempts an energy-momentum balance (4 constraint kinematic fit) with various PEDs left out. Hadronic splitoffs will produce PEDs which will appear to be photons which destroy the energy momentum balance. In this analysis, up to 2 PEDs are allowed to be *dropped*, allowing for one splitoff from each of the two charged pions desired in the final state. The result which is used is that which produced the best confidence level in the 4C kinematic fit, whether it had zero, one, or two PEDs dropped. Any PEDs which were required to be dropped are not included in further analysis.

4.2 Charged Particle Tracking

The set of computer code which performs the charged tracking is known as LOCATER [30] [31].

The PCOS data from the PWC consist of lists of wires on which a signal was present. Using information on the orientation of the PWC, these are converted to x and y coordinates. As each track may produce signals on more than one wire (a *cluster*), the coordinates are determined from the centers of the clusters.

The raw JDC data are the flash ADC values from the two ends of each JDC sense wire. These represent the charge collected at the end of the wire during successive 200ps time windows of the allowed drift time. These data trains are searched for *pulses*, identified by local maxima in the time profile of the collected charge. The pulses on the two ends of a given wire are matched with each other to identify *hits* on the wire, indicating the passage of a charged particle through the drift cell. Integrating the pulses gives the amount of charge collected on each end of the wire; by comparing the charge on the two ends of the wire for a given pulse, the position along the wire at which the hit occurred can be inferred. Thus x, y, and z coordinates for each hit can be determined. The detector cannot determine on which side of the wire the charged

particle passed (*left-right ambiguity*); thus two space points are generated for each hit.

To find tracks through the JDC, use is made of the *Fuzzy Radon transform*. The Radon transform is essentially a line integral over a density function, i. e. the sum of hits along the proposed track. The Fuzzy Radon transform makes us of the resolution information from the non-ideal detector system. The initial guesses for track parameters are determined from circle fits to data within a JDC sector. Though it is quite effective for pattern recognition, nonlinearities resulting from the helix parameterization make the Fuzzy Radon transform unsuitable for the actual fitting of helixes to the hits. The fitting is done using a parameterization specifically designed for this purpose, using a χ^2 minimization scheme.

After the pattern recognition phase, the tracks found in the JDC are connected to the hits in the PWC. The tracks are then fitted in three dimensions to helixes. The event vertex, the point from which the tracks originate, is then determined from the point at which the helixes pass most closely.

After all fitting of tracks is done, cuts on the track qualities are imposed. Tracks' first hits must be on layer 3 or less, and the last hits must occur at or beyond layer 21. The tracks must have at least 15 hits on them, and the χ^2 per degree of freedom for the track fit must not be greater than 1.2. These conditions ensure that all tracks are long and well measured.

4.3 Matching PEDs to Charged Tracks

Charged particles which are tracked through the JDC often produce a PED in the Barrel Calorimeter (BC). These PEDs should be recognized a such, and should not be mistaken as photons. To accomplish this, a simple matching algorithm is employed. The track is projected to the the face of the BC and a vector from the event vertex to the point of intersection is formed. The angles between this vector and the vectors for the various PEDs are examined. The cosine of the angle must be greater than 0.98 to be considered a matched PED. The PED nearest the expected location is taken as the match.

4.4 Determination of Cuts and Corrections

Table 4.1 shows a summary of cuts imposed during the event reconstruction.

Parameter	Value	Description
EMINBC	$1 MeV$	Minimum energy in a crystal
EXTLBC	$1 MeV$	Minimum energy in a crystal to be considered part of a cluster
ECLSBC	$4 MeV$	Minimum energy in at least one crystal in a cluster
ECLUBC	$4 MeV$	Minimum energy of a cluster
EPEDBC	$10 MeV$	Minimum energy of a secondary PED in a cluster
ECENUS	$13 MeV$	Minimum energy in the central crystal of a PED
EGAMUS	$5 MeV$	Minimum energy of a PED
E1E9US	0.96	Maximum E_1/E_9 for a PED
LYR1US	3	Maximum JDC layer for start of a track
LYRNUS	21	Minimum JDC layer for end of a track
LONGUS	15	Minimum number of JDC hits on a track
CHCTUS	1.2	Maximum χ^2/n_{DOF} for the helix fit to a track

Table 4.1: Summary of cuts used in the event reconstruction.

4.4.1 Versions of Software Used

Software	Version	Description
CBOFF	1.29/02	Off-line analysis
LOCATER	2.00/05	Charged tracking
BCTRAK	2.04/00	Crystal data reconstruction
GTRACK	1.35/01	Global tracking
CCDBCB	2.05/00	Calibration database
CBDROP	1.11/00	Splitoff dropping
CBKFIT	3.09/00	Kinematic fitting

Chapter 5

The June 1994 Run

The data which were analyzed for this work were collected in June of 1994. One of the primary goals of this run was to collect about 7 million *2-prong* triggered events with a liquid hydrogen target. The experiment and beam were configured for $\bar{p}p$ annihilations at rest. A summary of the numbers of events collected is shown in Table 5.1.

Trigger	Purpose	Events
2-prong	2 long tracks	13.7×10^6
0-prong	BC calibration	1.1×10^6
4-prong	z-calibration	0.05×10^6
	Magnet off.	
Collinear	$r - \phi$ calibration	0.01×10^6
Minimum Bias	Normalizations	1.6×10^6

Table 5.1: Summary of events taken during the June 1994 liquid hydrogen run.

The minimum bias data were collected for about one hour during each day of running. The *4-prong* and *0-prong* data were collected near the beginning of the run period. Runs with the collinear trigger were made throughout the run period at several different atmospheric pressures.

The *2-prong* data were collected during the 9 day period from June 4 to June 12. The beam rate was kept at about $15000\bar{p}/sec$ in the beam wire chamber KC. Approximately 60% of the $\bar{p}$ hitting KC also hit one of the silicon counters Si_{2-5}. During *2-prong* runs, the events were written to tapes at a rate of 50 to 75 Hz.

Two types of problems required rejection of certain runs. All runs on DST tapes on which the problems are present are rejected.

1. An unplugged control cable resulted in the LP flashing during physics data taking. In many events during particular runs, all the crystals in an entire half of the BC would fire. Because of the long component of the decay time of the CsI crystal, even events without an obvious LP flash probably have some extra

energy in their real PEDs. This required rejection of DST's GE1819 through GE1831, and GE1842 through GE1844.

2. Several crystals exhibited unstable pedestals and FERA/2282 ratios during some runs. This required rejection of DST's GE1834, GE1836, GE1842 through GE1845, GE1851, GE1853 through GE1855, GE1886, GE1888 through GE1894.

From the DST's not rejected, 8.0 million *2-prong* triggered events remain.

Chapter 6

Detector Simulation and Efficiency Studies

As in any modern particle physics experiment, detailed Monte Carlo (MC) simulations of the Crystal Barrel experiment are necessary. These studies are used in evaluation of detector and analysis efficiencies, as well as in determination of acceptance corrected normalizations in the partial wave analysis (PWA).

The computer program which performs the simulation is known as CBGEANT, and is based on the GEANT 3.16 package developed at CERN. The sub-package FLUKA was used for simulation of hadronic processes, as it was determined to simulate those processes of concern in the Crystal Barrel detector more accurately than the other available sub-package, GHEISHA [32]. CBGEANT generates events of the desired type, propagates the particles through the detector apparatus, simulates detector response, applies experimental distortions, and records the data in a format compatible with that for actual events. As particles are propagated, they undergo decays, energy loss and straggling, scattering, and other electromagnetic and hadronic interactions. Experimental distortions include efficiencies of detector components and electronic noise. The output data are passed through the same analysis procedure as are the actual events. The detector apparatus is reasonably well represented in the program, including not only the active detector elements, but mechanical supports, cooling equipment, electronics and cables as well.

For background studies and branching fraction measurements, values for absolute efficiencies are desired. These are defined as the number of MC events which are successfully reconstructed and pass all of the cuts imposed on the actual events, divided by the number of events generated.

The versions of the software packages used in analysis of the MC are shown in Table 6.1.

CBGEANT	5.05/00
CBKFIT	3.09/00
CCDBCB	2.05/01
CBDROP	1.11/02
LOCATER	2.01/09
CBOFF	1.30/04
BCTRAK	2.04/03
GTRAK	1.37/01

Table 6.1: Versions of the Crystal Barrel analysis software packages used in analysis of the Monte Carlo data.

6.1 Events for PWA

For use in partial wave analysis, events of the type $\bar{p}p \to \pi^+\pi^-\pi^\circ\omega$ are needed. These events are distributed according to 4-body phase space. The BIGBANG event generator produces $\pi^+\pi^-\pi^\circ\omega$ with a total energy of $2m_p$; the ω is forced to decay to $\pi^\circ\gamma$. The masses of the ω's are randomly selected according to a Breit-Wigner distribution with width of $8.43 MeV/c^2$ between m_{π° and $1564 MeV/c^2$. The two π°'s decay to $\gamma\gamma$ with a branching fraction of 98.8020%; this factor must be accounted for in the efficiency calculations.

Since the actual experimental data for PWA were collected with a *2-prong* trigger, the analysis program accepted only those events which satisfied the *2-prong* trigger conditions: hits on exactly two wires on each of the two trigger layers of the JDC, and exactly 2 clusters in the PWC.

Because of data storage limitations, the MC data were generated in nine separate runs of 100,000 to 150,000 events apiece, with a different initial random number seed for each run.

Table 6.2 summarizes the results of the analysis of these data.

6.2 Events for Branching Fraction Calculations

For computations of branching fractions, one must know the efficiency for reconstructing and counting events of the desired type. For this purpose, an MC data set was constructed which consisted of about 75% $\bar{p}p \to \pi^+\pi^-\pi^\circ\omega$ and 25% $\bar{p}p \to \omega_1\omega_2$ (with $\omega_1 \to \pi^+\pi^-\pi^\circ$ and $\omega_2 \to \pi^\circ\gamma$.) This was intended to mimic the actual data set, in which about 25% of the events were $\bar{p}p \to \omega\omega$ (see Figure 9.3.) This allowed determination of the efficiency for detecting $\omega\omega$ events in a data sample which contained a large fraction of non-$\omega\omega$ events.

The actual experimental data used in the branching fraction measurements were collected with the minimum bias trigger, so the *2-prong* triggering part of the analysis program was disabled while processing the corresponding MC data. Table 6.3 shows

Events generated	1057614
2-prong triggers	270679
$CL(\pi^+\pi^-5\gamma) > 1\%$	109057 (40.3%)
$CL(\pi^+\pi^-\pi^\circ\pi^\circ\gamma) > 1\%$	92785 (34.3%)
$CL(\pi^+\pi^-\pi^\circ\omega) > 1\%$	81578 (30.1%)
$CL(\pi^+\pi^-\pi^\circ\omega) > 25\%$ and $R_{\gamma 4\pi} = 1$ and $N_{\text{drop}} = 0$ and $N_{\pi^+\pi^-\pi^\circ\omega} = 1$	22167 (8.2%)

Table 6.2: Summary of the analysis of the CBGEANT data which were used in the partial wave analysis. The numbers of events generated, events resulting in *2-prong* triggers, and events passing confidence level cuts on kinematic fits are shown. The number of events generated is actually the number of events read into the analysis program from the data tape; corruption of the data recording medium resulted in the loss of many events on some tapes. Statistics for intermediate kinematic fits are shown (as a percent of triggers) for comparison with those for background channels in Table 6.4. ($CL(X)$ refers to the confidence level of a kinematic fit to the hypothesis $\bar{p}p \to X$. The $R_{\gamma 4\pi} = 1$ cut requires consistency between the fits to $\bar{p}p \to \pi^+\pi^-\pi^\circ\omega$ and $\bar{p}p \to \pi^+\pi^-\pi^\circ\pi^\circ\gamma$ in the way that photons are paired into π°'s. The $N_{\pi^+\pi^-\pi^\circ\omega} = 1$ cut requires that there was only one way per event of combining photons to get a successful kinematic fit to $\bar{p}p \to \pi^+\pi^-\pi^\circ\omega$. See Section 8.1.3 for a complete description of the cuts.)

Data set	$\pi^+\pi^-\pi^\circ\omega$	$\omega\omega$
Events generated	149936	49873
$CL(\pi^+\pi^-5\gamma) > 1\%$	22378	7053
$CL(\pi^+\pi^-\pi^\circ\pi^\circ\gamma) > 1\%$	18955	6010
$CL(\pi^+\pi^-\pi^\circ\omega) > 1\%$	16673	5291

Table 6.3: Summary of the analysis (without trigger simulation) of the MC data sets which were used in determining efficiencies for the branching fraction measurements.

Data set	$\pi^+\pi^-\pi^\circ\pi^\circ\pi^\circ$	$\omega\pi^\circ\pi^\circ$
Events generated	100000	99805
2-prong triggers	25643	23706
$CL(\pi^+\pi^-5\gamma) > 1\%$	5444 (21.2%)	4483 (18.9%)
$CL(\pi^+\pi^-\pi^\circ\pi^\circ\gamma) > 1\%$	4399 (17.2%)	3711 (15.6%)
$CL(\pi^+\pi^-\pi^\circ\omega) > 1\%$	418 (1.6%)	471 (2.0%)
$CL(\pi^+\pi^-\pi^\circ\omega) > 25\%$ and $R_{\gamma 4\pi} = 1$ and $N_{\rm drop} = 0$ and $N_{\pi^+\pi^-\pi^\circ\omega} = 1$	28 (0.11%)	37 (0.16%)

Table 6.4: Summary of the analysis of the five pion background Monte Carlo data sets. The numbers of events passing the kinematic fits are shown as a percent of triggered events. See Table 6.2 for a description of the cuts.

a summary of the analysis of the data sets comprising this MC sample.

6.3 Events for Data Tuning and Background Studies

For data tuning (see Chapter 7), events of the type $\bar{p}p \to \pi^+\pi^-\pi^\circ\pi^\circ\pi^\circ$ were used. For tuning of the MC data, a set of about 100,000 such events were generated. These events were analyzed by a program developed for analysis of such events.

This channel was recognized as a possible source of background for $\pi^+\pi^-\pi^\circ\omega$; it has six photons in the final state, but if a low energy photon were to escape detection, it could mimic the five photon final state. This channel also has a large branching fraction from $\bar{p}p$ at rest. For this reason, the $\pi^+\pi^-\pi^\circ\pi^\circ\pi^\circ$ events were submitted for analysis to the $\pi^+\pi^-\pi^\circ\omega$ analysis program. Also, because 24% of actual $\bar{p}p \to \pi^+\pi^-\pi^\circ\pi^\circ\pi^\circ$ events proceed via $\bar{p}p \to \omega\pi^\circ\pi^\circ$, about 50,000 events of this type were also generated for background acceptance studies. Table 6.4 show a summary of the processing of these background MC events. In the data sample selected by a given set of cuts, the numbers of each of the four type of events will be:

$$\begin{aligned} N(\pi^+\pi^-\pi^\circ\omega) &= N_a BR(\bar{p}p \to \pi^+\pi^-\pi^\circ\omega) BR(\omega \to \pi^\circ\gamma) A_{\pi^+\pi^-\pi^\circ\omega} \\ N(\omega\omega) &= N_a BR(\bar{p}p \to \omega\omega) 2BR(\omega \to \pi^\circ\gamma) BR(\omega \to \pi^+\pi^-\pi^\circ) A_{\omega\omega} \end{aligned}$$

Cuts				Acceptances (%)				Bkg.
CL	$R_{\gamma 4\pi}$	N_{drop}	$N_{\pi^+\pi^-\pi^\circ\omega}$	$\pi^+\pi^-\pi^\circ\omega$	$\omega\omega$	$\pi^+\pi^-\pi^\circ\pi^\circ\pi^\circ$	$\omega\pi^\circ\pi^\circ$	(%)
		# Generated:		757710	99733	100000	99805	
1%	-	2	-	7.75	6.89	0.418	0.472	24.8±1.9
15%	1	2	-	5.41	4.92	0.154	0.188	15.0±1.4
25%	1	2	-	4.60	4.18	0.102	0.134	12.3±1.3
40%	1	2	-	3.57	3.28	0.057	0.091	9.7±1.2
60%	1	2	-	2.35	2.18	0.028	0.043	7.3±1.1
1%	-	0	-	3.92	3.65	0.110	0.112	14.2±1.5
15%	1	0	-	2.78	2.66	0.043	0.058	8.9±1.2
25%	1	0	-	2.38	2.27	0.029	0.041	7.2±1.1
40%	1	0	-	1.85	1.81	0.018	0.029	6.0±1.1
60%	1	0	-	1.24	1.20	0.010	0.017	5.2±1.2
15%	1	0	1	2.46	2.36	0.042	0.053	9.5±1.3
25%	1	0	1	2.10	2.00	0.028	0.037	7.7±1.2
40%	1	0	1	1.63	1.59	0.018	0.025	6.5±1.2
60%	1	0	1	1.08	1.05	0.010	0.014	5.5±1.3

Table 6.5: Summary of the acceptance and feed-through rates as functions of the cuts applied, as computed by processing of CBGEANT data. The four cut types are 1) the confidence level of the kinematic fit to $\bar{p}p \to \pi^+\pi^-\pi^\circ\omega$, 2) the rank ($R_{\gamma 4\pi}$) of the fit, 3) the number of photons allowed to be dropped by CBDROP, and 4) the number of successful kinematic fits to the hypothesis $\pi^+\pi^-\pi^\circ\omega$. (These cuts are explained in detail in Section 8.1.3.) For each of the four types of events, the numbers of events which survive the cuts are shown as percentages of the original samples (the sizes of which are shown in the first row.) The last column shows the fraction of the final data sample which would consist of background from the $\pi^+\pi^-\pi^\circ\pi^\circ\pi^\circ$ and $\omega\pi^\circ\pi^\circ$ channels.

$$\begin{aligned} N(\pi^+\pi^+\pi^\circ\pi^\circ\pi^\circ) &= N_a BR(\bar{p}p \to \pi^+\pi^+\pi^\circ\pi^\circ\pi^\circ) A_{\pi^+\pi^+\pi^\circ\pi^\circ\pi^\circ} \\ N(\omega\pi^\circ\pi^\circ) &= N_a BR(\bar{p}p \to \omega\pi^\circ\pi^\circ) BR(\omega \to \pi^+\pi^-\pi^\circ) A_{\omega\pi^\circ\pi^\circ} \end{aligned}$$

where N_a is the number of $\bar{p}p$ annihilations. The following formula was used to determine the fraction of background in the data sample:

$$F_{\text{bkg}} = \frac{N(\pi^+\pi^+\pi^\circ\pi^\circ\pi^\circ) + N(\omega\pi^\circ\pi^\circ)}{N(\pi^+\pi^-\pi^\circ\omega) + N(\omega\omega) + N(\pi^+\pi^+\pi^\circ\pi^\circ\pi^\circ) + N(\omega\pi^\circ\pi^\circ)}$$

The branching fractions for the ω decays are taken from the PDG [1]: $BR(\omega \to \pi^+\pi^-\pi^\circ) = 88.8 \pm 0.7\%$ and $BR(\omega \to \pi^\circ\gamma) = 8.5 \pm 0.5\%$. An analysis of Crystal Barrel data by Curtis Meyer yielded the following branching fractions: $BR(\bar{p}p \to \omega\pi^\circ\pi^\circ) = 2.398 \pm 0.075\%$ and $BR(\bar{p}p \to \pi^+\pi^-\pi^\circ\pi^\circ\pi^\circ) = 9.1 \pm 0.4\%$. The branching fractions measured in Chapter 10.2 were used: $BR(\bar{p}p \to \pi^+\pi^-\pi^\circ\omega) = 15.7 \pm 1.0\%$ and $BR(\bar{p}p \to \omega\omega) = 3.15 \pm 0.25\%$. In computing $N_{\pi^+\pi^-\pi^\circ\omega}$, $BR(\bar{p}p \to \omega\omega)$ was subtracted from $BR(\bar{p}p \to \pi^+\pi^-\pi^\circ\omega)$ since the former includes the latter, and would otherwise double count $\omega\omega$ events. Similarly, $BR(\bar{p}p \to \omega\pi^\circ\pi^\circ)$ was subtracted from $BR(\bar{p}p \to \pi^+\pi^-\pi^\circ\pi^\circ\pi^\circ)$ in computing $N_{\pi^+\pi^+\pi^\circ\pi^\circ\pi^\circ}$. The acceptances for the four channels (A_{channel}) are shown in Table 6.5, and were determined by applying the various cuts to CBGEANT data samples of the four types of events. Values for F_{bkg} are also shown in Table 6.5. The cuts are described in detail in Section 8.1.3.

Chapter 7

Data Tuning

Several of the data selection criteria consist of requiring a minimum confidence level for kinematic fits. (Confidence level cuts are equivalent to cuts on the reduced χ^2.) The confidence level of a fit depends on the uncertainties of the individual measurements. In order to treat each event fairly, these uncertainties must be accurate. Estimated uncertainties are assigned to each measurement during the reconstruction stage of analysis, but these typically need to be refined. The techniques used in doing so are described in this chapter.

7.1 Tuning Method

In order to judge the quality of data used in kinematic fits, the distributions of two quantities are useful:

- *Pulls of the fit quantities,* which should be normally distributed, that is, Gaussian, centered at $\mu_P = 0$, with a standard deviation $\sigma_P = 1$ [34]. (This assumes a normal parent distribution.) The pull of each measurement is computed after an event has undergone a kinematic fit. It is defined as:

$$\frac{x_f - x_m}{\sqrt{\sigma_m^2 - \sigma_f^2}},$$

  where x_f and x_m are the fitted and measured values of the quantity. The estimated uncertainty on the measurement is σ_m, and σ_f is the improved error on the measurement (which is smaller than σ_m because of the constraints imposed in the fit.) The σ_f is derived from the covariance matrix from the fit.

- *Confidence levels of the fits,* which should have a flat distribution, possibly with a sharp rise near zero for background events. The confidence level is a transformation of the reduced χ^2; a true χ^2 distribution produces a flat confidence level distribution.

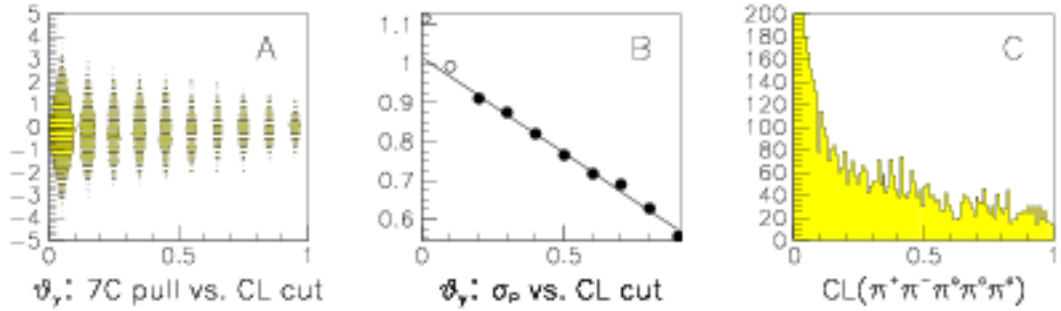

Figure 7.1: A: 2-d histogram of pull versus confidence level for a typical kinematically fit quantity (θ_γ). The distribution is obviously narrower for larger CL cuts. From this, one can fit pull distributions for events satisfying various confidence level cuts. B: A plot of the width (σ_P) of the pull distribution versus the confidence level cut applied to it. Note that the point for the 1% cut is quite far above the fitted line. The hollow circles indicate points which were not included in the line fit. C: The distributions of confidence levels from the kinematic fits.

A systematic offset in a measured quantity will move the center of its pull distribution away from zero. The accuracy of the estimated errors, σ_i, influences the widths of the pull distributions. The process of *tuning* the data typically consists of modifying the measurements and their errors in such a way that the confidence levels and pulls are distributed as described above.

One difficulty in using the procedure outlined above arises from the fact that background events (events whose topologies do not match that which is being fitted) tend to broaden the pull distributions. In order to avoid this complication, one could look at the pulls from only those events which yield a confidence level of at least some minimum value. The problem with that technique is that excluding the *real* events of low confidence levels tends to make the pull distributions artificially narrow (see Figure 7.1). These considerations and the figure suggest a method of determining the width of the desired distribution: Plot the width of the pull distribution versus the confidence level cut applied to it, fit a line to the plot, and project the line to a confidence level cut of zero to determine the *nominal* pull width σ_o. This method was suggested by Crystal Barrel collaborator Curtis Meyer [33]. Such a procedure was carried out in the tuning of both experimental and CBGEANT data; the results follow.

7.2 Tuning the June 1994 2-prong Data

The channel of interest in this analysis is $\bar{p}p \to \pi^+\pi^-\pi^o\omega$, $\omega \to \pi^o\gamma$, but concerns about the possibility of including a large background in the data set selected for tuning

prompted the use in the tuning procedure of a channel which had previously been analyzed, and was known to be cleanly extractable. The reaction $\bar{p}p \to \pi^+\pi^-\pi^\circ\pi^\circ\pi^\circ$, which has only one additional photon, was chosen, for the reasons already mentioned, as well as for the fact that this channel might constitute a great deal of the background in $\pi^+\pi^-\pi^\circ\omega$.

The data used for tuning were obtained from tape DST GD1870. The events were retracked and kinematically fit with each set of tuning parameters. Pulls from nine quantities, listed in Table 7.1, were histogramed for fits to $\pi^+\pi^-\pi^\circ\pi^\circ\pi^\circ$. The distributions of the pulls for the photon measurements (θ, ϕ and $\sqrt{E}$) are the combined distributions for all of the photons in any given event. Figures 7.2 and 7.3 show the

Quantity	Description
α_+, α_-	Curvature of the π^+ and π^- tracks ($\alpha \propto \frac{1}{p}$)
$\tan\lambda_+$, $\tan\lambda_+$	Tangent of the dip angle of the π^+ and π^- trajectories
ψ_+, ψ_-	Initial azimuthal angle of the π^+ and π^- trajectories
θ_γ	Polar angle of a γ trajectory
ϕ_γ	Azimuthal angle of a γ trajectory
$\sqrt{E_\gamma}$	Square root of the energy of a γ

Table 7.1: Quantities used by CBKFIT in fitting events.

pulls and σ_P vs. CL plots for fits with no modification of the data nor errors. Note that the pulls for $1/p_\pi$ are not centered at zero and that the $\sigma_\circ$'s are not near 1.0. The pull for $\sqrt{E_\gamma}$ is not Gaussian, but this is expected since the parent distribution for this quantity also is not Gaussian (the response of a crystal to a photon of a given energy is approximately Gaussian with a long tail extending to low energies). Figure 7.4 shows a comparison of the confidence level distributions before and after the tuning was applied. Before the tuning, the confidence levels are far from flat.

First, the z-vertex position, $z_\circ$, was varied until the width of the pull distribution for θ_γ was minimized, at z=3.3mm.

The shift of μ_P for $1/p_\pi$ indicates that the measured values are systematically offset. Recent investigations [35] have shown that a modification of the form:

$$\frac{1}{p_T} \longrightarrow \frac{1}{p_T} - \frac{1}{D}$$

to the measured curvatures of charged tracks is effective in this regard. This type of correction to the measured curvatures was first used in bubble chamber experiments; $1/D$ corresponds to a "minimum measurable curvature." Such a modification was applied in this tuning process. Additionally, the errors on the nine relevant measurements were each scaled:

$$\sigma_i \longrightarrow R_i\sigma_i.$$

For the errors on the measurements of the charged tracks, the scaling factors for the positive and negative tracks were equal.

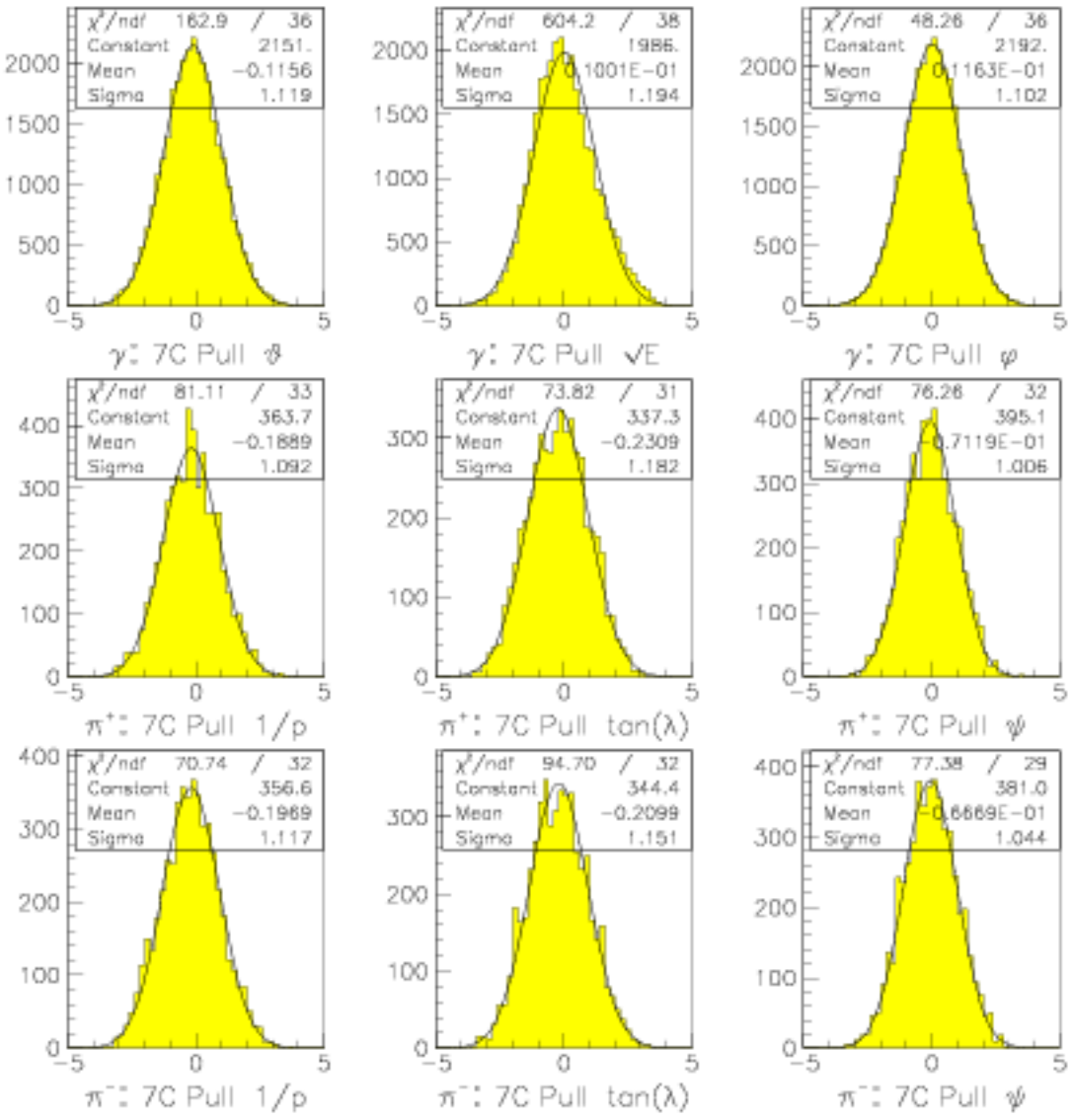

Figure 7.2: Pull distributions from fits of the experimental data to the $\pi^+\pi^-\pi^\circ\pi^\circ\pi^\circ$ channel with no tuning applied. A 1% confidence level cut has been applied. The distributions for the photon measurements (θ_γ, ϕ_γ and $\sqrt{E_\gamma}$) are combined distributions for all of the photons in each event.

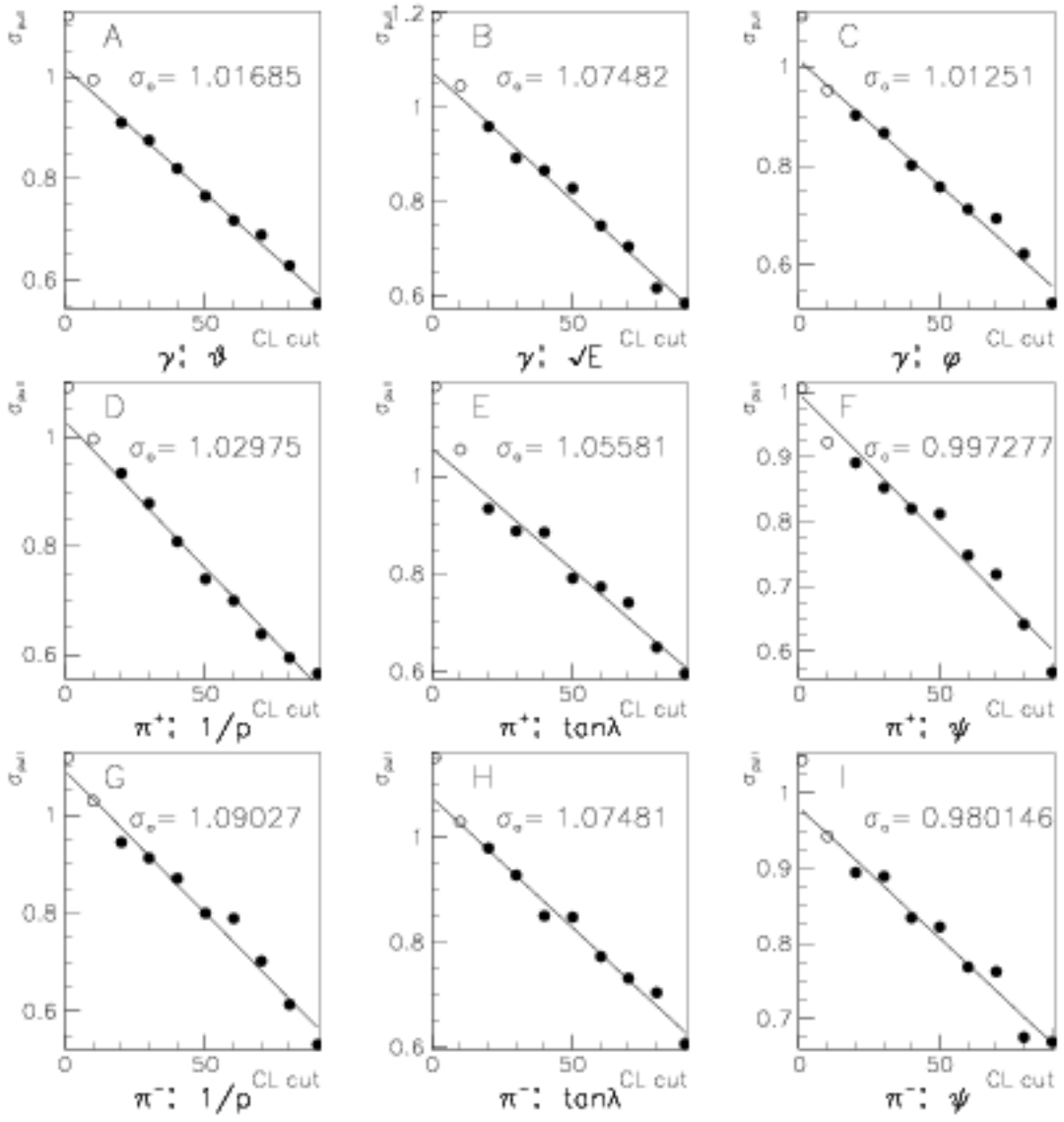

Figure 7.3: Width (σ_P) of the pull distributions versus the confidence level cut applied to it, from fits of the experimental data to the $\pi^+\pi^-\pi^\circ\pi^\circ\pi^\circ$ channel with no tuning applied. The distributions for the photon measurements (θ_γ, ϕ_γ and $\sqrt{E_\gamma}$) are combined distributions for all of the photons in each event.

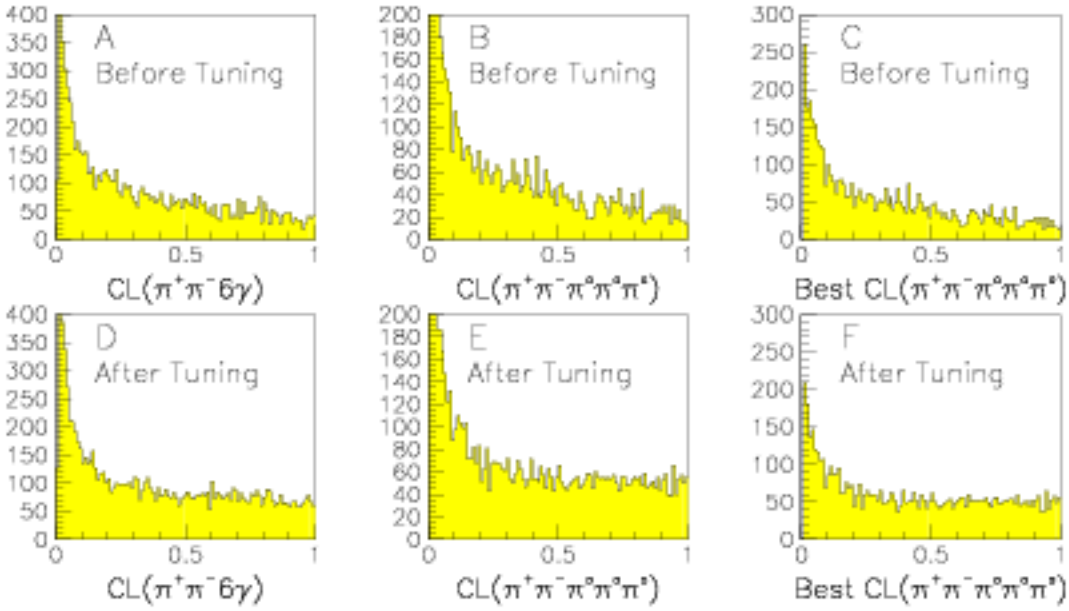

Figure 7.4: A,B,C: Confidence level (CL) distributions from kinematic fits of the experimental $\pi^+\pi^-\pi^o\pi^o\pi^o$ data, *before the tuning was applied.* A confidence level cut of 1% on the fit to $\pi^+\pi^-\pi^o\pi^o\pi^o$ has been applied. A: The CL distribution from the fits to $\pi^+\pi^-6\gamma$. The steady downward slope indicates the presence of backgrounds (combinatoric or from contamination by other channels,) and an inadequate estimation of the errors on the measurements. B: The CL distribution from *all* fits to the hypothesis $\pi^+\pi^-\pi^o\pi^o\pi^o$ (including multiple fits to single events.) C: The CL distribution from the em best fit for each event to the hypothesis $\pi^+\pi^-\pi^o\pi^o\pi^o$. D,E,F: The same CL distributions *after* the tuning was applied.

Many values of the various tuning parameters, R_i and D, were tried until a suitable set was found. The values of the parameters which were used in subsequent analysis of this data set are shown in Table 7.2, and Table 7.3 shows a comparison of the widths and means of the pull distributions before and after the tuning was applied. Note that in Figure 7.3 the σ_P for the 1% confidence level cut is always greater than $\sigma_\circ$. Tuning in such a way that $\sigma_{P1\%}$ is near 1.0 would quite possibly yield a different set of tuning parameters, probably resulting in "overtuning."

Tuning Parameter	Value
R_α	1.08
$R_{tan\lambda}$	1.23
R_ψ	0.89
R_{θ_γ}	1.18
R_{ϕ_γ}	1.25
$R_{\sqrt{E_\gamma}}$	1.08
$z_\circ$	0.33 cm
$1/D$	$2.875 \times 10^{-5} (MeV/c)^{-1}$

Table 7.2: Tuning parameters for the June 1994 2-prong data.

7.3 Tuning CBGEANT Data

For use in the partial wave analysis of $\pi^+\pi^-\pi^\circ\omega$, a set of CBGEANT events must be produced. As with the real data, these data must also be tuned. Again, to reduce the risk of bias, the $\pi^+\pi^-\pi^\circ\pi^\circ\pi^\circ$ channel was used in the tuning process.

Data were generated using CBGEANT version 5.05. Figure 7.5 compares the confidence level distributions from fits of the MC data, before and after the tuning was applied, and Table 7.4 compares the means and widths of the pull distributions. Before the tuning, the deviations from ideal behavior are not nearly as strong as in the real data, but some improvement is realized with the tuning applied. The z-vertex was not shifted, as the data were generated with the vertex at proper location. The tuning parameters which were found to be suitable are shown in Table 7.5.

A further check of the validity of these tuning parameters was to look at the confidence level distribution for fits to $\pi^+\pi^-\pi^\circ\omega$ in CBGEANT events of that type. This is shown in Figure 7.6. The shape is quite good compared to the distributions obtained with no tuning. This inspires confidence in this procedure and in the selected values.

Measurement	Before Tuning		After Tuning	
	μ_{pull}	σ_{pull}	μ_{pull}	σ_{pull}
α_+	-0.189	1.030	0.044	1.028
α_-	-0.197	1.090	0.003	1.011
$\tan\lambda_+$	-0.231	1.056	0.075	1.033
$\tan\lambda_-$	-0.210	1.075	0.068	1.035
ψ_+	-0.071	0.997	-0.132	0.984
ψ_-	-0.067	0.980	0.022	0.964
$\sqrt{E_\gamma}$	0.010	1.075	0.031	1.001
θ_γ	-0.116	1.017	0.057	0.974
ϕ_γ	0.012	1.013	0.012	0.963

Table 7.3: Comparisons of the means and widths of the pull distributions before and after the tuning was applied, for the experimental data.

Measurement	Before Tuning		After Tuning	
	μ_{pull}	σ_{pull}	μ_{pull}	σ_{pull}
α_+	-0.146	0.946	-0.061	0.959
α_-	-0.092	0.959	-0.012	0.961
$\tan\lambda_+$	-0.007	0.959	-0.014	0.950
$\tan\lambda_-$	-0.017	0.963	-0.024	0.965
ψ_+	0.032	0.917	-0.007	0.934
ψ_-	0.015	0.917	-0.042	0.934
$\sqrt{E_\gamma}$	-0.014	1.049	-0.007	1.029
θ_γ	-0.012	1.000	-0.013	1.006
ϕ_γ	-0.011	0.988	-0.009	0.989

Table 7.4: Comparisons of the means and widths of the pull distributions before and after the tuning was applied, for the MC data.

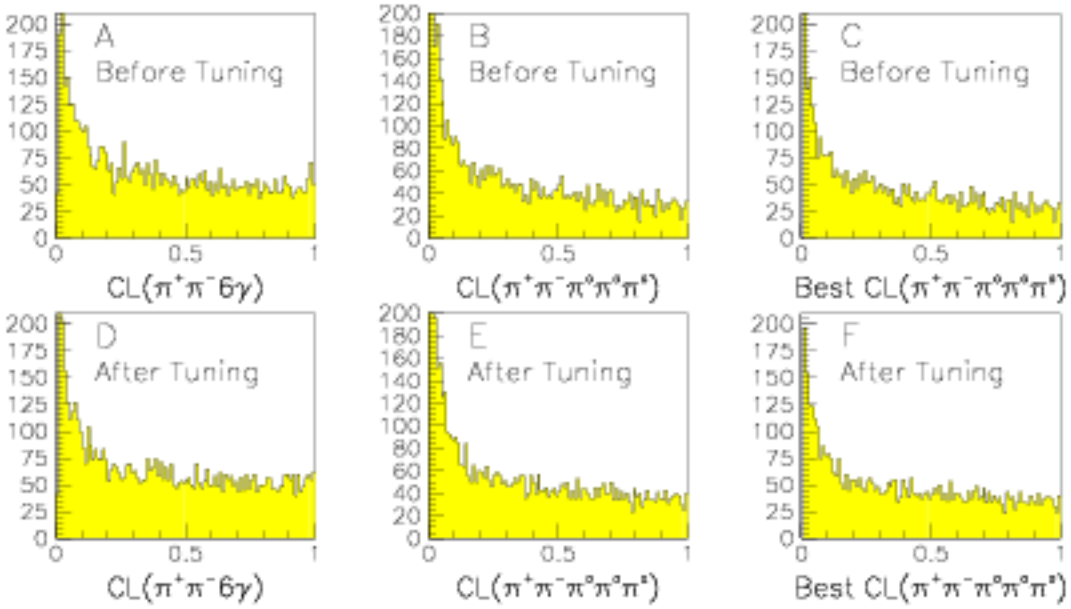

Figure 7.5: A,B,C: Confidence level (CL) distributions from fits of the MC data to the $\pi^+\pi^-\pi^0\pi^0\pi^0$ channel *before the tuning was applied.* A confidence level cut of 1% on the fit to $\pi^+\pi^-\pi^0\pi^0\pi^0$ has been applied. D,E,F: The distributions of the same confidence levels *after* the tuning was applied.

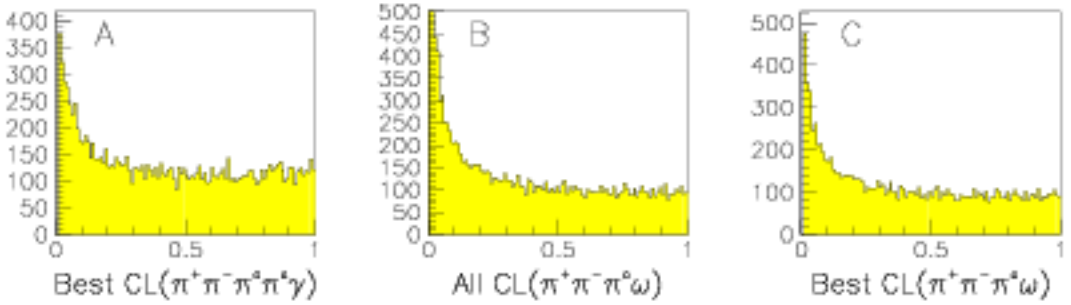

Figure 7.6: Confidence level distributions from fits of the $\pi^+\pi^-\pi^0\omega$ MC data to the $\pi^+\pi^-\pi^0\pi^0\gamma$ and $\pi^+\pi^-\pi^0\omega$ hypotheses with the tuning parameters determined from $\pi^+\pi^-\pi^0\pi^0\pi^0$ applied. A: The $CL(\pi^+\pi^-\pi^0\pi^0\gamma)$ distribution for the best such fit for each event. B: The distribution of $CL(\pi^+\pi^-\pi^0\omega)$ of *all* fits (including multiple fits for some events.) C: The best $CL(\pi^+\pi^-\pi^0\omega)$'s for each event. Confidence level cuts of 1% on the fits have been applied.

Tuning Parameter	Value
R_α	0.97
$R_{tan\lambda}$	1.00
R_ψ	0.97
R_{θ_γ}	1.00
R_{ϕ_γ}	1.00
$R_{\sqrt{E_\gamma}}$	1.10
z_0	0.00 (no correction)
$1/D$	$1.0 \times 10^{-5} (MeV/c)^{-1}$

Table 7.5: Tuning parameters for CBGEANT data.

Chapter 8

Backgrounds and Cuts

8.1 Introduction

Before using the data to perform measurements, it is important to understand what backgrounds are present and to find cuts that can be applied in order to remove the backgrounds. First, some terms will be defined, and the motivations for the various cuts will be explained. Next, the possibility of background events will be discussed for each level of the analysis. The background events can be 1) events of the desired type which were reconstructed incorrectly, or 2) events of the wrong type which pass the selection criteria. Most of the backgrounds are eliminated by applying cuts. The backgrounds which remain are measured and discussed.

8.1.1 Photon Numbering Scheme

It will be useful to have a numbering scheme for the various photons under discussion:

$$\begin{aligned} \bar{p}p &\longrightarrow \pi^+\pi^-\pi^\circ_1\omega \\ \omega &\longrightarrow \pi^\circ_2\gamma_5 \\ \pi^\circ_1 &\longrightarrow \gamma_1\gamma_2 \\ \pi^\circ_2 &\longrightarrow \gamma_3\gamma_4 \end{aligned}$$

8.1.2 Definitions of Terms

Kinematic fits of the data are made to several hypothesis, $\pi^+\pi^-\pi^\circ\pi^\circ\gamma$ and $\pi^+\pi^-\pi^\circ\omega$ among them. For the $\pi^+\pi^-\pi^\circ\omega$ hypothesis, CBKFIT combines four of the five photons into π°'s. A useful quantity is the *rank* of the $\pi^+\pi^-\pi^\circ\pi^\circ\gamma$ fit for that particular combination. If the photon combination yielding the best $\pi^+\pi^-\pi^\circ\omega$ fit also yielded the best $\pi^+\pi^-\pi^\circ\pi^\circ\gamma$ fit, then the rank, $R_{\gamma 4\pi}$, is 1; if it yielded the second best fit, then $R_{\gamma 4\pi} = 2$, and so forth. For cases where that combination's fit to $\pi^+\pi^-\pi^\circ\pi^\circ\gamma$ did not converge, $R_{\gamma 4\pi}$ is defined as zero.

8.1.3 Motivation for the Cuts

The effort to remove events which are not actually of the type $\bar{p}p \to \pi^+\pi^-\pi^\circ\omega$ has been driven by removal of $\bar{p}p \to \pi^+\pi^-\pi^\circ\pi^\circ\pi^\circ$ events. This channel is produced copiously, with a branching fraction of about 9%, and can easily mimic $\bar{p}p \to \pi^+\pi^-\pi^\circ\omega$ when one of the six photons is of low energy. Accepting events of this type requires the loss of one photon, so accepting events in which CBDROP has removed a photon (see Section 4.1.1.2) seems likely to include many background events. Therefore, for use in the PWA fits, events with dropped photons are excluded:

$$N_{\text{drop}} = 0.$$

Background events are also likely to have a lower confidence level from the kinematic fit to $\bar{p}p \to \pi^+\pi^-\pi^\circ\omega$, so a cut on $CL(\pi^+\pi^-\pi^\circ\omega)$ seems prudent. A reasonable compromise between accepting as large number of real events and eliminating background events was found to be:

$$CL(\pi^+\pi^-\pi^\circ\omega) > 25\%.$$

(See Table 6.5.)

Combinatoric backgrounds arise when two or more particles must be combined as the decay products of an intermediate state, such as pairing photons into π°'s for fitting hypotheses involving the decay $\pi^\circ \to \gamma\gamma$. For the two-step decay $\omega \to \pi^\circ\gamma,\ \pi^\circ \to \gamma\gamma$, the best combination of three photons into the ω might not correspond to the best combination of two photons into π°'s; selecting events where these best combinations *do* correspond is desirable, so requiring

$$R_{\gamma 4\pi} = 1$$

eliminates wrong $\gamma\gamma = \pi^\circ$ pairings.

For some events, there will be more than one way to combine the photons to make an ω and a π° which will satisfy the 1% CL cut imposed on the kinematic fit (at an intermediate stage of analysis) to this channel. The ω carries spin, so the direction of the photon from its decay provides valuable information on the polarization of the ω in the PWA fits. It is therefore necessary to ensure that the correct photon is used in this determination. Requiring that only one combination of photons yielded a successful fit to $\bar{p}p \to \pi^+\pi^-\pi^\circ\omega$ eliminates events where some doubt exists as to which photon is the one from the ω decay:

$$N_{\pi^+\pi^-\pi^\circ\omega} = 1.$$

8.1.4 Data Sample

The data used in the following discussions of backgrounds and cuts are a subset of the complete data set which have passed a 1% confidence level cut on the 4-C fit, and on a 6-C fit to *either* $\pi^+\pi^-\pi^\circ\pi^\circ\gamma$ or $\pi^+\pi^-\pi^\circ\eta\gamma$. The data were processed by a

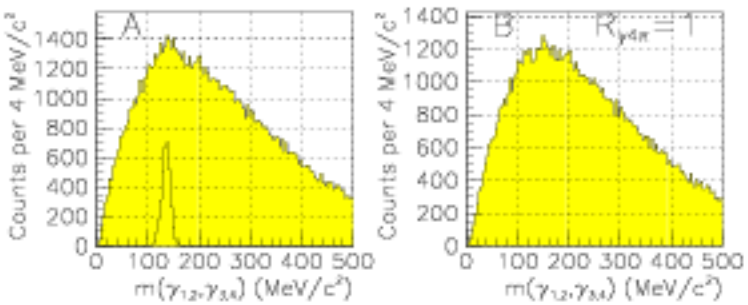

Figure 8.1: A: Invariant mass distributions of photon pairs, with one photon coming from π_1° and the other from π_2°. The plot has superimposed on it the distribution $m(\gamma_1\gamma_2)$ to show the expected location and width of a π° peak. B: The spectrum with $R_{\gamma 4\pi} = 1$.

program which selected for analysis here events for which at least one fit converged for the channel $\pi^+\pi^-\pi^\circ\omega$, with $CL > 1\%$. This set contained 29106 events. The number of events which pass the cuts requiring $CL(\pi^+\pi^-\pi^\circ\omega) > 25\%$ and $R_{\gamma 4\pi} = 1$ and $N_{\rm drop} = 0$ is 8525. Requiring, in addition, that there be only one successful kinematic fit to $\bar{p}p \to \pi^+\pi^-\pi^\circ\omega$ further reduces the number of events to 7291.

8.2 Reconstructing $\pi^+\pi^-\gamma\gamma\gamma\gamma\gamma$ Events

8.2.1 Mis-matched Photons

In the 6-C fit to $\pi^+\pi^-\pi^\circ\pi^\circ\gamma$, two pairs of photons are combined to form π°'s. It is possible that the combination which yields the highest confidence level is not the correct combination. This could arise as a result of statistical fluctuations in the measurements. One way to detect the occurrence of such effects is to look at invariant mass distributions of pairs of photons which were not combined into π°'s. Consider first a γ from π_1° paired with a γ from π_2°. (Recall the distinction between π_1° and π_2°: π_2° is the one which the kinematic fit preferred as resulting from the ω decay, $\omega \to \pi_2^\circ\gamma_5$. Hence, the two π°'s have different energy spectra, and therefore so do their decay products.) The invariant mass distribution for all such pairs is shown in Figure 8.1 A. Note that a π° peak would lie directly at the maximum of this spectrum. Such a signal is weakly indicated by the pointed, as opposed to rounded, structure at the maximum. This feature is eliminated by requiring $R_{\gamma 4\pi} = 1$, as shown in Figure 8.1 B.

Next, consider pairs consisting of γ_5 and a γ from π_1°. This spectrum is shown in Figure 8.2 A. A mis-match signal is clearly present. Fitting the spectrum with a Gaussian peak on a quadratic background, and then integrating the peak, leads to a count of 4.6% of events having such a mis-match. Figure 8.2 B shows the effect of

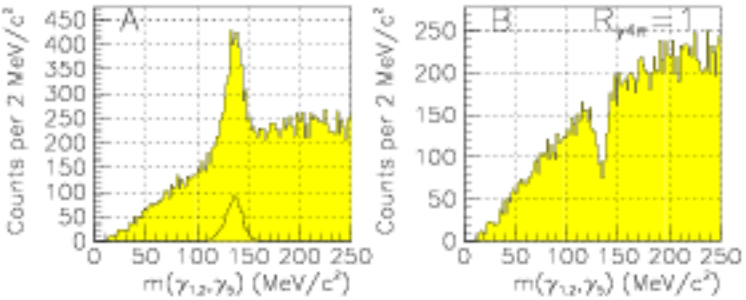

Figure 8.2: A: Invariant mass distribution of photon pairs, where γ_5 is paired with the photons from π_1°. The plot has superimposed on it the distribution $m(\gamma_1\gamma_2)$ to show the expected location and width of a π° peak. B: The spectrum with $R_{\gamma 4\pi} = 1$.

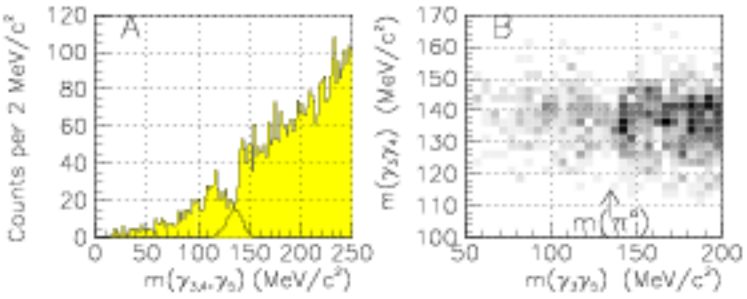

Figure 8.3: A: Invariant mass distribution of photon pairs, where γ_5 is paired with the photons from π_2°. The plot has superimposed on it the distribution $m(\gamma_1\gamma_2)$ to show the expected location and width of a π° peak. B: $m(\gamma_3\gamma_4)$ vs. $m(\gamma_3\gamma_5)$.

requiring $R_{\gamma 4\pi} = 1$. This cut removes the background, leaving a hole in the spectrum in its place, demonstrating that this cut eliminates events with incorrect $\gamma\gamma$ pairings.

The last photon pairing to consider is the combination of γ_5 and a γ from π_2°. This spectrum is shown in Figure 8.3 A. There is a distinct *depletion* at the π° mass. Figure 8.3 B shows $m(\gamma_3\gamma_4)$ vs. $m(\gamma_3\gamma_5)$. Notice that as $m(\gamma_3\gamma_5)$ nears the π° mass, the width of the $m(\gamma_3\gamma_4)$ distribution becomes narrower, producing the "waist" shape. That is, when $m(\gamma_3\gamma_5)$ is near $m(\pi^\circ)$, $m(\gamma_3\gamma_4)$ must have been *even nearer* in order to have been chosen as the pair which constitutes the π° (otherwise, γ_5 would have been called "γ_4").

8.2.2 Other Channels Which Produce $\pi^+\pi^-\gamma\gamma\gamma\gamma\gamma\gamma$

Table 8.1 lists channels which would result in a $\pi^+\pi^-\gamma\gamma\gamma\gamma\gamma\gamma$ final state, and could therefore contaminate the data sample. Many of these channels involve an η'. Fig-

$\bar{p}p \to \eta' 4\gamma$	$\eta' \longrightarrow \pi^+\pi^-\gamma$	(28%)	Fig. 8.6
$\bar{p}p \to \eta' 4\gamma$	$\eta' \longrightarrow \omega\gamma$	(3%)	Fig. 8.6
	$\omega \longrightarrow \pi^+\pi^-$	(2%)	
$\bar{p}p \to \eta' 3\gamma$	$\eta' \longrightarrow \pi^+\pi^-\eta$	(44%)	Fig. 8.7
	$\eta \longrightarrow \gamma\gamma$	(39%)	
$\bar{p}p \to \eta'\pi^+\pi^- 3\gamma$	$\eta' \longrightarrow \gamma\gamma$	(2%)	Fig. 8.4
$\bar{p}p \to \eta' 2\gamma$	$\eta' \longrightarrow \omega\gamma$	(3%)	Fig. 8.8
	$\omega \longrightarrow \pi^+\pi^-\pi^\circ$	(89%)	
	$\pi^\circ \longrightarrow \gamma\gamma$	(99%)	
$\bar{p}p \to \eta'\pi^+\pi^-\gamma$	$\eta' \longrightarrow \omega\gamma$	(3%)	Fig. 8.5
	$\omega \longrightarrow \pi^\circ\gamma$	(8%)	
	$\pi^\circ \longrightarrow \gamma\gamma$	(99%)	
$\bar{p}p \to \eta\pi^+\pi^-3\gamma$	$\eta \longrightarrow \gamma\gamma$	(39%)	Fig. 8.9
$\bar{p}p \to \eta 4\gamma$	$\eta \longrightarrow \pi^+\pi^-\gamma$	(4.9%)	Fig. 8.10
$\bar{p}p \to \eta\pi^+\pi^-\gamma$	$\eta \longrightarrow \pi^\circ\gamma\gamma$	(0.07%)	Fig. 8.11
	$\pi^\circ \longrightarrow \gamma\gamma$	(99%)	
$\bar{p}p \to \rho^\circ 4\gamma$	$\rho^\circ \longrightarrow \pi^+\pi^-\gamma$	(1%)	Fig. 8.12
$\bar{p}p \to \omega 4\gamma$	$\omega \longrightarrow \pi^+\pi^-\gamma$	(<.036%)	Fig. 8.12

Table 8.1: $\bar{p}p$ annihilation channels which would result in $\pi^+\pi^-5\gamma$ final states. Branching fractions for decays of the mesons are also shown.

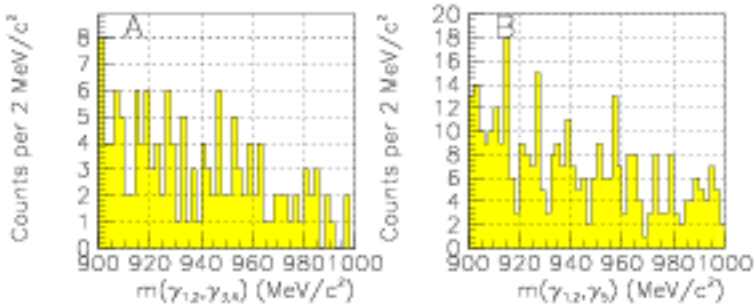

Figure 8.4: Invariant mass distributions of various photon pairs, in the mass range near $m(\eta') = 958 MeV/c^2$. A: Combinations of one photon from π_1° and one photon from π_2°. B: Combinations of γ_5 with one photon from π_1°. The mass spectra $m(\gamma_3\gamma_5)$ and $m(\gamma_4\gamma_5)$ extend only to about $800 MeV$, well below $m(\eta')$, and are therefore not shown.

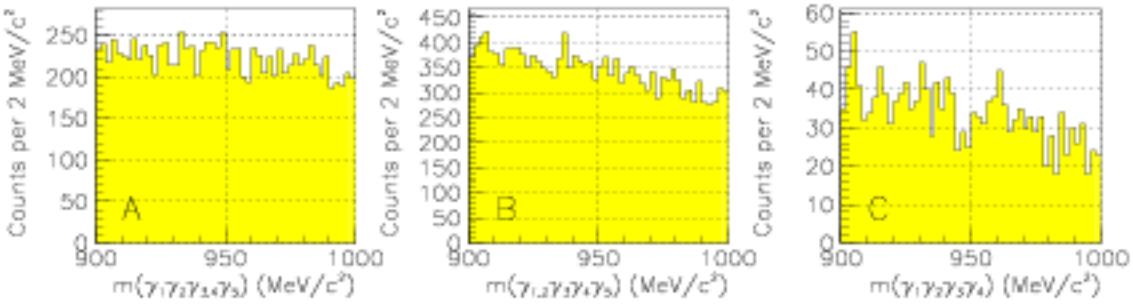

Figure 8.5: The 4γ invariant mass distributions, in the mass range near $m(\eta') = 958 MeV/c^2$. A: All photons except one from π_2°. B: All photons except one from π_1°. C: All photons except γ_5.

ures 8.4, 8.5, 8.6, 8.7, and 8.8 show the various invariant mass spectra in which an η' signal would be found if these background channels were present. None shows evidence of this type of contamination.

Figures 8.9, 8.10 and 8.11 show $\gamma\gamma$ and $\pi^+\pi^-\gamma$ and $\gamma\gamma\gamma\gamma$ mass spectra for masses near that of the η. No significant η signal is evident. Figure 8.12 shows $\pi^+\pi^-\gamma$ mass spectra near the ω and ρ masses. No signal is evident for either, though a small ρ contaimination would be difficult to see because of its width ($\Gamma_\rho \simeq 150 MeV/c^2$.) The broad peak in Figure 8.12 A is due to $\bar{p}p \to \omega_1\omega_2$, with $\omega_1 \to \pi^+\pi^-\pi_1^\circ$, as shown in Figure 8.12 B.

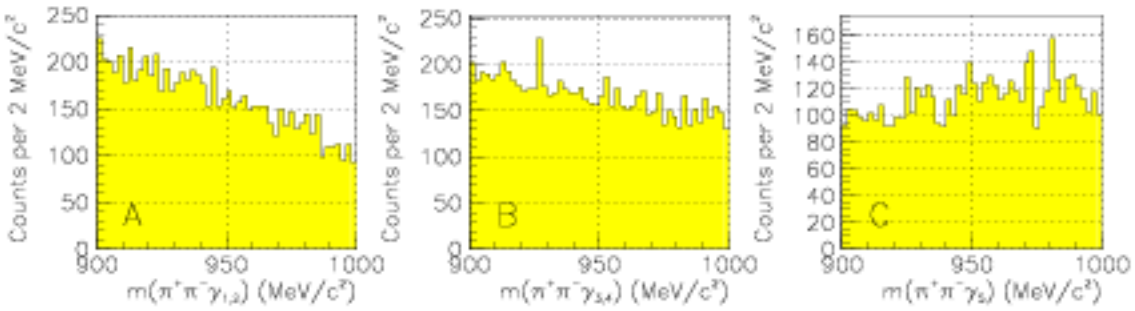

Figure 8.6: Invariant mass distributions of $\pi^+\pi^-\gamma$ combinations, in the mass range near $m(\eta') = 958 MeV/c^2$. A: Combinations of $\pi^+\pi^-$ with one photon from π_1°. B: Combinations of $\pi^+\pi^-$ with one photon from π_2°. C: Combinations of $\pi^+\pi^-$ with γ_5.

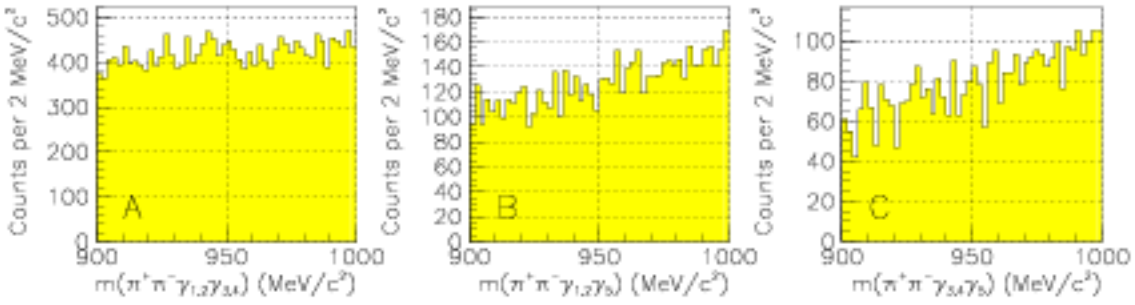

Figure 8.7: Invariant mass distributions of $\pi^+\pi^-\gamma\gamma$, in the mass range near $m(\eta') = 958 MeV/c^2$. A: Combinations of $\pi^+\pi^-$ with one photon from π_1° and one photon from π_2°. B: Combinations of $\pi^+\pi^-$ with one photon from π_1° and γ_5. C: Combinations of $\pi^+\pi^-$ with one photon from π_2° and γ_5.

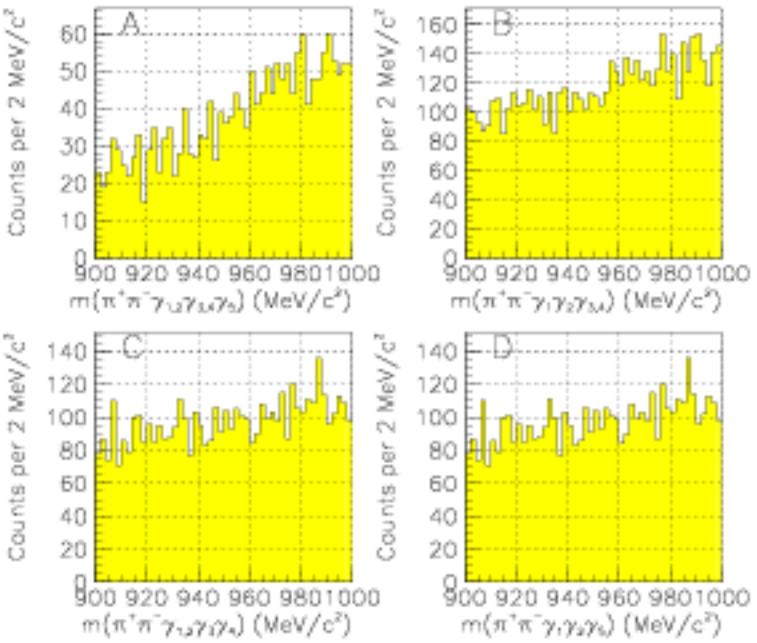

Figure 8.8: Invariant mass distributions of $\pi^+\pi^-\gamma\gamma\gamma$, in the mass range near $m(\eta') = 958 MeV/c^2$. The mass spectrum for $\pi^+\pi^-\gamma_3\gamma_4\gamma_5 \equiv \pi^+\pi^-\omega$, has no entries for masses less than $1000 MeV/c^2$, and is therefore not shown. A: Combinations of $\pi^+\pi^-$ with one photon from π_1°, one photon from π_2° and γ_5. B: Combinations of $\pi^+\pi^-$ with both photons from π_1° and one photon from π_2°. C: Combinations of $\pi^+\pi^-$ with both photons from π_2° and one photon from π_1°. D: Combinations of $\pi^+\pi^-$ with both photons from π_1° and γ_5.

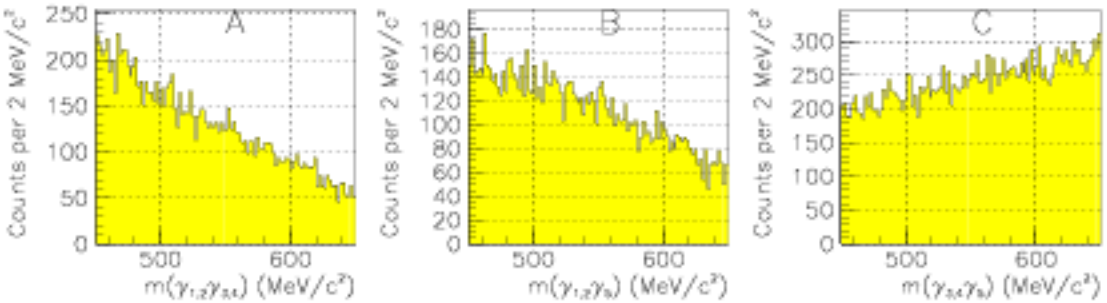

Figure 8.9: Invariant mass distributions of various photon pairs, in the mass range near $m(\eta) = 548 MeV/c^2$. A: Combinations of one photon from π_1° and one photon from π_2°. B: Combinations of one photon from π_1° and γ_5. C: Combinations of one photon from π_2° and γ_5.

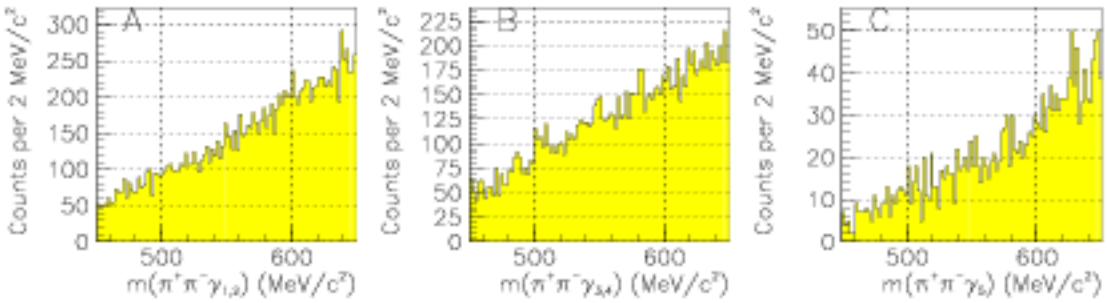

Figure 8.10: Invariant mass distributions of $\pi^+\pi^-\gamma$ combinations, in the mass range near $m(\eta) = 548 MeV/c^2$. A: Combinations of $\pi^+\pi^-$ with one photon from π_1°. B: Combinations of $\pi^+\pi^-$ with one photon from π_2°. C: Combinations of $\pi^+\pi^-$ with γ_5.

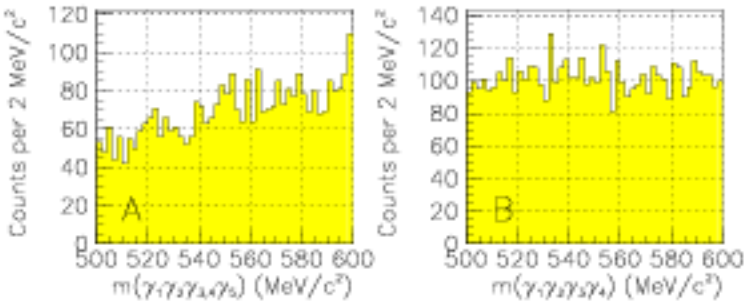

Figure 8.11: Invariant mass distributions of $\gamma\gamma\gamma\gamma$ combinations, in the mass range near $m(\eta) = 548 MeV/c^2$. A: One photon from π_2° is left out. B: γ_5 is left out.

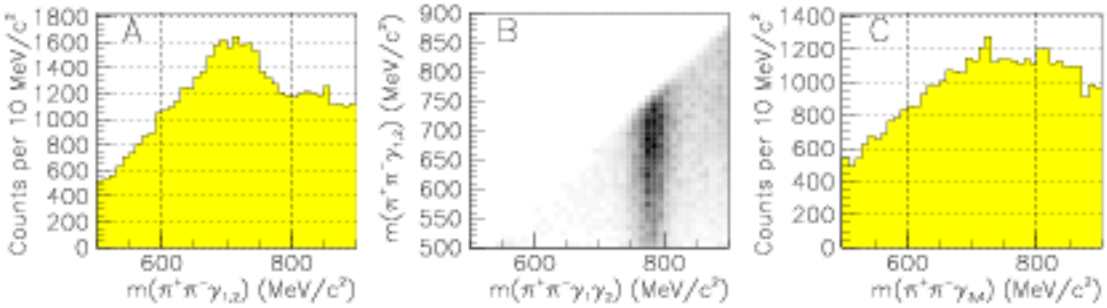

Figure 8.12: A,C: Invariant mass distributions of $\pi^+\pi^-\gamma$ combinations, in the mass range near $m(\omega)$. B: $m(\pi^+\pi^-\gamma_{1,2})$ vs. $m(\pi^+\pi^-\gamma_{1,2})$, demonstrating that the peak in A is produced by $\omega \to \pi^+\pi^-\pi^\circ \to \pi^+\pi^-\gamma_1\gamma_2$ (i.e. by legitimate events.)

8.3 Reconstructing $\pi^+\pi^-\pi^\circ\pi^\circ\gamma$ Events

It is possible that some of the $\pi^+\pi^-\pi^\circ\pi^\circ\gamma$ events did not proceed via the $\pi^+\pi^-\pi^\circ\omega$ channel. Listed in Table 8.2 are some channels which could result in a $\pi^+\pi^-\pi^\circ\pi^\circ\gamma$ topology. Figure 8.13 shows $m(\pi^+\pi^-\pi_2^\circ)$; there are no signs of η's contaminating this

$\bar{p}p \to \eta'\pi^\circ\pi^\circ$	$\eta' \longrightarrow \pi^+\pi^-\gamma$	(28%)	Fig.8.6
$\bar{p}p \to \eta'\pi^\circ\pi^\circ$	$\eta' \longrightarrow \omega\gamma$	(3%)	Fig.8.6
	$\omega \longrightarrow \pi^+\pi^-$	(2%)	
$\bar{p}p \to \eta'\pi^\circ$	$\eta' \longrightarrow \omega\gamma$	(3%)	Fig.8.8
	$\omega \longrightarrow \pi^+\pi^-\pi^\circ$	(89%)	
$\bar{p}p \to \eta\pi^\circ\pi^\circ$	$\eta \longrightarrow \pi^+\pi^-\gamma$	(5%)	Fig.8.10
$\bar{p}p \to \eta\pi_1^\circ\gamma$	$\eta \longrightarrow \pi^+\pi^-\pi_2^\circ$	(24%)	Fig.8.13
$\bar{p}p \to \omega\pi_1^\circ\gamma$	$\omega \longrightarrow \pi^+\pi^-\pi_2^\circ$	(24%)	Fig.8.12

Table 8.2: $\bar{p}p$ annihilation channels which would result in a $\pi^+\pi^-\pi^\circ\pi^\circ\gamma$ final state. Branching fractions for the meson decays are shown.

spectrum, but an ω signal is clearly present. Even when the final cuts are applied, this background is present at a level of $3.0 \pm 0.2\%$ of the data sample. There are two possible sources for this peak: 1) incorrect pairing of $\pi^\circ\gamma$ to form ω's in the kinematic fitting, and 2) $\bar{p}p \to \omega\pi^\circ\pi^\circ$, with $\omega \to \pi^+\pi^-\pi_2^\circ$ and one missing γ from the decay of one of the π°'s (see section 8.4.) There is no way to determine the relative amounts from these two sources.

The other channels in Table 8.2 have been addressed in the searches for backgrounds in the $\pi^+\pi^-\gamma\gamma\gamma\gamma\gamma$ channel.

8.4 Missing Photons

Of great concern is the possibility of contamination of the data sample by events of the type $\bar{p}p \longrightarrow \pi^+\pi^-\pi^\circ\pi^\circ\pi^\circ \longrightarrow \pi^+\pi^-(\gamma\gamma)(\gamma\gamma)(\gamma\gamma_{\rm missing})$, where $\gamma_{\rm missing}$ indicates a photon which goes undetected or is of low energy and is therefore either cut by the minimum photon energy cut or is dropped by CBDROP. For some events of this type, the photon combinations into π°'s for the $\pi^+\pi^-\pi^\circ\pi^\circ\gamma$ fit will be incorrect; these events would result in unexpected π° peaks in $\gamma\gamma$ mass spectra. The removal of such peaks by rank and confidence level cuts was demonstrated above. Some $\gamma_{\rm missing}$ events, however, will have their photons matched correctly in the $\pi^+\pi^-\pi^\circ\pi^\circ\gamma$ fit. For these,

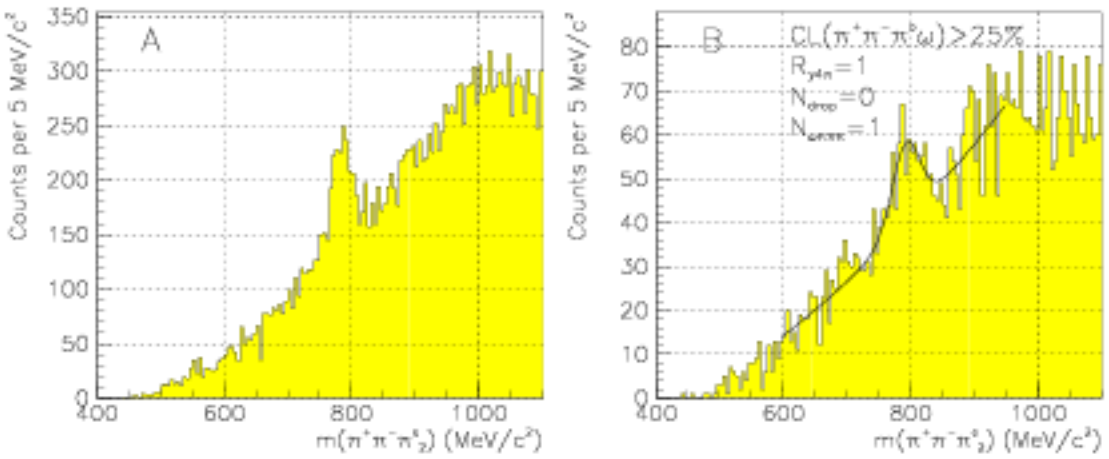

Figure 8.13: A: The $\pi^+\pi^-\pi_2^\circ$ invariant mass distribution. B: The spectrum with the $R_{\gamma 4\pi} = 1$, $CL(\pi^+\pi^-\pi^\circ\omega) > 25\%$, $N_{\rm drop} = 0$ and $N_{\pi+\pi-\pi^\circ\omega} = 1$ cuts applied. 217 events are in the peak (fitted with a Voigtian + background function. The Voigtian is a Gaussian convoluted with a Breit-Wigner function. [See Section 11.3.2.])

the $\gamma_{\rm missing}$ would combine with γ_5 to form a π° mass. One way to detect the presence of such events is to use the fact that $24.0 \pm 0.6\%$ of all $\pi^+\pi^-\pi^\circ\pi^\circ\pi^\circ$ events proceed via $\omega\pi^\circ\pi^\circ$, with $\omega \longrightarrow \pi^+\pi^-\pi^\circ$ [36]. Monte Carlo studies of this process show that in about 20% of such events, one of the photons from the $\omega \to \pi^+\pi^-\pi^\circ \to \pi^+\pi^-\gamma\gamma$ is lost, and a peak is present which corresponds to $\omega \to \pi^+\pi^-\gamma_{\rm missing}$. (In the other 80%, the π°'s from the ω decay are correctly reconstructed, and are evenly distributed among π_1° and π_2°.) Figure 8.14 A shows the distribution $m(\pi^+\pi^-\gamma_5)$; there is a peak just below the ω mass, at about $750 MeV/c^2$. Figure 8.14 B shows the spectrum for events where $CL(\pi^+\pi^-\pi^\circ\pi^\circ\pi^\circ) > 15\%$ (to favor background events); the ω peak is somewhat enhanced. In Figure 8.14 C, the spectrum with the final cuts applied is shown; perhaps small peak remains. An estimation of the background contribution in the peak is difficult for two reasons: 1) the spectrum is not smooth enough to allow a reliable fit, and 2) signal events of the type $\bar{p}p \to \omega\omega$ also produce an enhancement in the same region of this spectrum (as shown in Figure 8.14 D.)

8.5 Summary

The only measurable background is present at a level of $3.0 \pm 0.2\%$ of the selected data set. (This background is a combination of $\bar{p}p \to \omega\pi^\circ\pi^\circ$ events with one missing photon, and $\bar{p}p \to \pi^+\pi^-\pi^\circ\omega$ events with the wrong photon paired with a π° to form the ω.) Monte Carlo studies indicate that $\bar{p}p \to \pi^+\pi^-\pi^\circ\pi^\circ\pi^\circ$ contaminates the data at a level of $7.2 \pm 1.1\%$ (see Section 6.3.) The former includes some of the latter, so

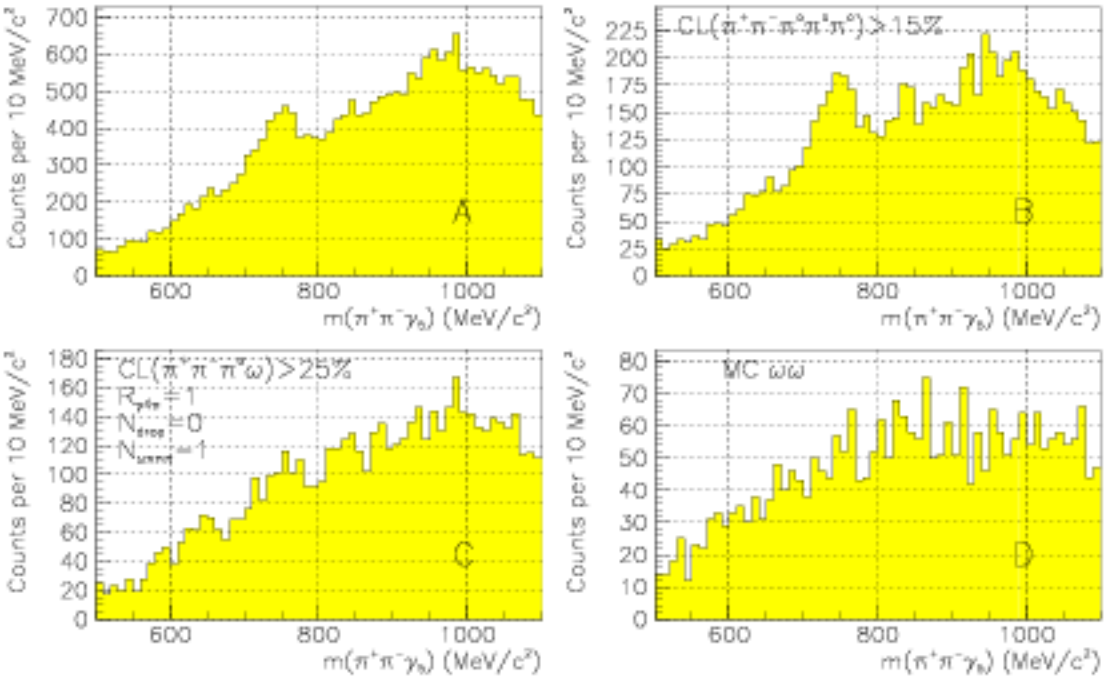

Figure 8.14: A: The $\pi^+\pi^-\gamma_5$ invariant mass distribution. B: The spectrum with a $CL(\pi^+\pi^-\pi^\circ\pi^\circ\pi^\circ) > 15\%$, to increase the level of this background. C: The spectrum with the final cuts applied. D: The spectrum from a sample of *Monte Carlo* events of the type $\bar{p}p \to \omega\omega$, showing that legitimate events may produce some structure in this region.

one cannot simply add these two values to determine the total contamination level, but it is certainly less than 10%.

Chapter 9

Data Overview

9.1 Summary of Data Selection

Table 9.1 shows a summary of the data selection criteria and the numbers of events passing each. Figure 9.1 shows the confidence level distribution of the events used in the PWA.

9.2 Invariant Mass Spectra

Figure 9.2 shows the 2γ versus 3γ invariant masses for events passing the $4-C$ kinematic fits to the hypothesis $\pi^+\pi^-\gamma\gamma\gamma\gamma$. A strong signal for $\pi^+\pi^-\pi^\circ\omega$ is clearly visible.

Figure 9.3 shows comparisons of the invariant mass spectra of the experimental and Monte Carlo (MC) data. The most striking features are the peaks in the $m(\pi^+\pi^-\pi^\circ)$ spectrum at the ω and η masses, corresponding to $\bar{p}p \to \omega\omega$ and $\bar{p}p \to \omega\eta$. The published value of $BR(\bar{p}p \to \omega\omega)$ is $3.32 \pm 0.34\%$ [38], and this represents about 25% of the events in this data sample. Assuming detection efficiencies are similar for detection of $\omega\omega$ and other $\pi^+\pi^-\pi^\circ\omega$ events, this gives a rough estimate of the branching fraction for $\bar{p}p$ annihilation into $\pi^+\pi^-\pi^\circ\omega$ of greater than 13%.

Criteria	# Events
Events read from good tapes	7993782
$CL(\pi^+\pi^-5\gamma) > 1\%$	780456
$CL(\pi^+\pi^-\pi^\circ\pi^\circ\gamma) > 1\%$	612038
$CL(\pi^+\pi^-\pi^\circ\omega) > 1\%$	132311
$CL(\pi^+\pi^-\pi^\circ\omega) > 25\%$ and rank=1 and $N_{\text{drop}} = 0$ and $N_{\pi^+\pi^-\pi^\circ\omega} = 1$	32231

Table 9.1: Summary of the cuts made and the numbers of experimental data events passing each, in selecting data for partial wave analysis.

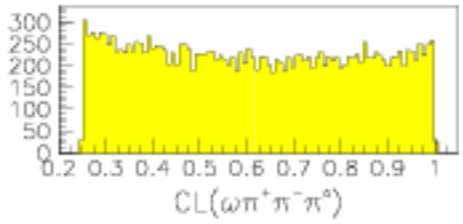

Figure 9.1: Distributions of the confidence levels from fits to $\bar{p}p \to \pi^+\pi^-\pi^0\omega$ for experimental data which are used in the PWA fits.

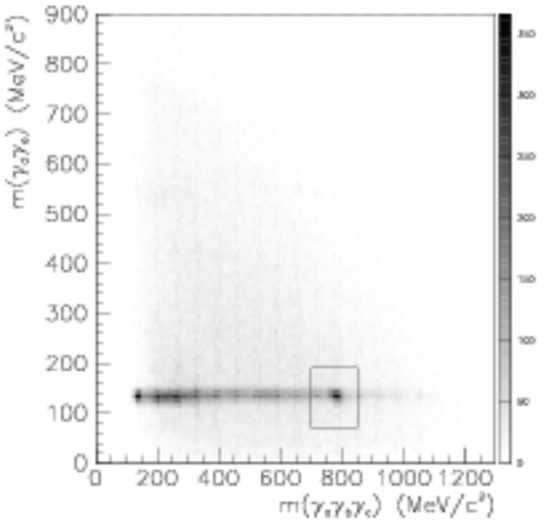

Figure 9.2: 2γ invariant mass versus 3γ invariant mass for events satisfying the kinematic fit to $\pi^+\pi^-\gamma\gamma\gamma\gamma\gamma\gamma$. There are 10 entries per event, corresponding to all possible γ pairs and triplets. The accumulation of events at $m(\gamma\gamma) \simeq 135 MeV/c^2$, $m(\gamma\gamma\gamma) \simeq 780 MeV/c^2$ corresponds to events of the type $\bar{p}p \to \pi^+\pi^-\pi^0\omega$. The momenta of the γ's have not been adjusted by the kinematic fit.

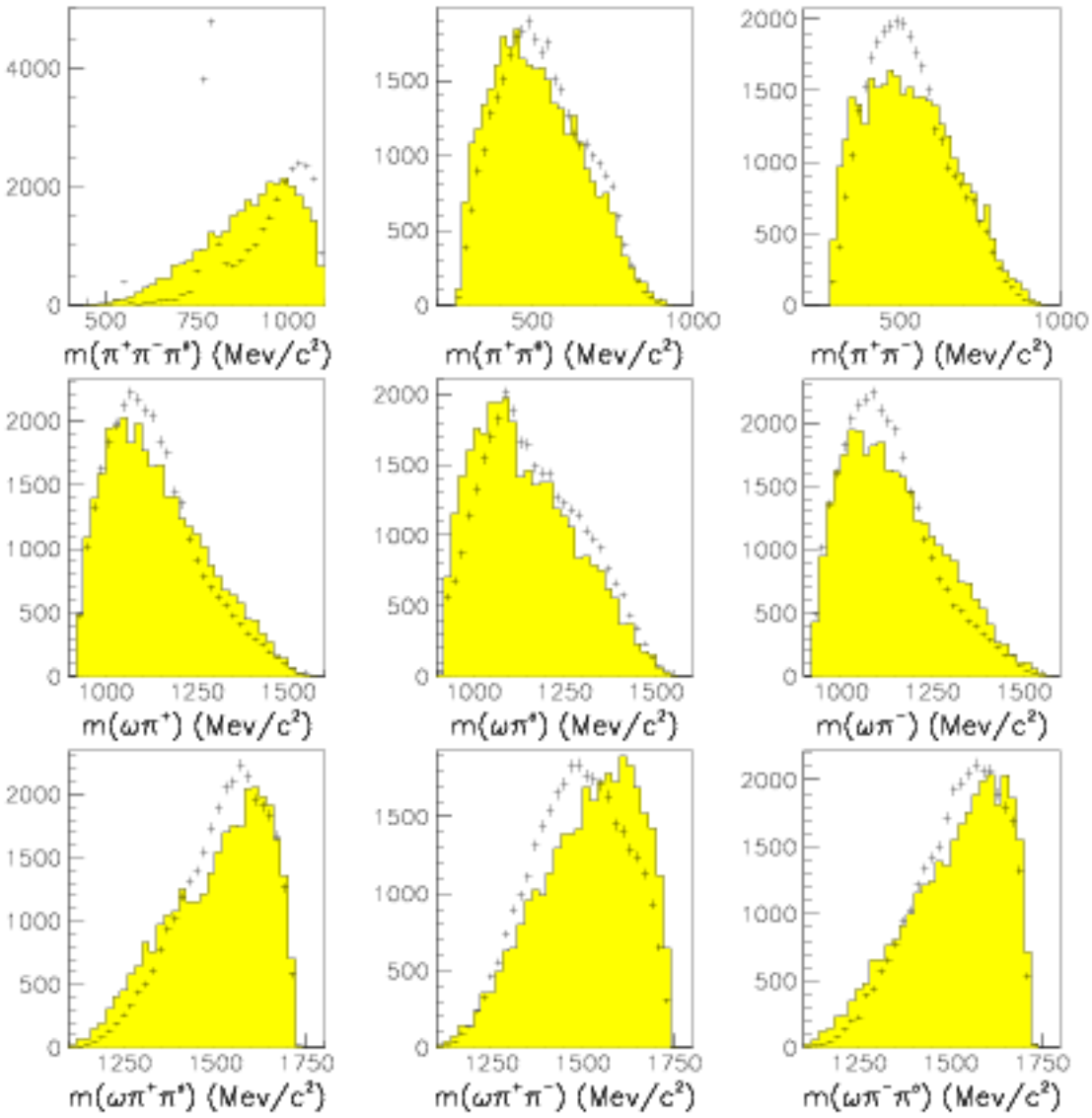

Figure 9.3: Invariant mass spectra from the experimental data (crosses) and MC data (shaded) which were used in the PWA fits. The plot for $m(\pi^-\pi^\circ)$ is not shown; it is very similar to that for $m(\pi^+\pi^\circ)$. The MC histograms have been scaled up to have the same numbers of events as those for the experimental data. All of the histograms have bin sizes of $20 MeV/c^2$.

Many of the features in the other mass spectra in Figure 9.3 are due to the $\omega\omega$ events, so it is useful to remove them in order to see what other resonances are likely to be present. Figure 9.4 shows the mass spectra for events with $m(\pi^+\pi^-\pi^\circ) > 830 MeV/c^2$. The experimental data show an excess of events with large $\pi^+\pi^-\pi^\circ$ masses relative to the MC data. This is possibly indicative of production, along with an ω, of a resonance decaying to $\pi^+\pi^-\pi^\circ$, with a mass greater than $1000 MeV/c^2$.

The charged $\pi\pi$ masses show an excess at high masses, probably indicating the production of ρ mesons, either directly or in the decays of other resonances.

The $\omega\pi$ masses are peaked near $1100 MeV/c^2$, with a depletion at high masses for the charged combinations, and at low masses for the neutral combination. There is no known $\omega\pi$ resonance at this mass. Such a peak could be an artifact of production and decay of resonances in other decay modes which result in correlations among the ω's and π's (known as a *reflection*.) The only resonance expected in $\omega\pi$ is the $b_1(1235)$; a peak at that mass is conspicuously absent.

The $\omega\pi\pi$ spectra show peaks near $1500 MeV/c^2$, a bit higher for $\omega\pi^+\pi^-$. The depletions for the charged combinations are at low masses, while the neutral combination's depletion is at high masses. Again, these could be reflections. At least one isoscalar vector meson is known to decay to $\omega\pi\pi$ [37]; the peak in the neutral spectrum could be a result of its production. Other possibilities include $a_0(1450) \to \omega\pi\pi$ and $\hat{\rho} \to \omega\pi\pi$.

Many of the angular distributions also show discrepancies. Figure 9.5 shows nine angular distributions which are representative of these discrepancies. In Figure 9.5C the experimental and MC data are closely matched, but this distribution will be discussed in Sections 12.4 and 12.5.1.

Figure 9.6 shows a 3π Dalitz plot for events with $m(\pi^+\pi^-\pi^\circ) > 1000 MeV/c^2$. Bands in the $\pi^\pm\pi^\circ$ spectra are evident (though at masses just below that of the ρ), but such a band in the $\pi^+\pi^-$ spectrum is weak or absent. This may indicate that these events had a stronger contribution from $\rho^\pm$ than from ρ°. This behavior is expected for $I = 1$ $\rho\pi$ resonances, since they cannot decay to $\rho^\circ\pi^\circ$. A preponderance of charged ρ's could also result from decays of $\omega\rho$ resonances: many such resonances are produced only from the $^3S_1$ initial state, which must have $I = 1$, and thus cannot produce a neutral $\omega\rho$ resonance along with a π°.

9.3 Data and Simulation for $\bar{p}p \to \omega\omega$

The $\pi^+\pi^-\pi^\circ$ mass spectrum near the ω mass is shown in Figure 9.7. The $\omega \to \pi^+\pi^-\pi^\circ$ peak is fit with a Gaussian function with variance σ, which is used in defining a peak region ($m_\omega - 2\sigma \le m \le m_\omega + 2\sigma$) and two sidebands ($m_\omega - 8\sigma \le m \le m_\omega - 4\sigma$ and $m_\omega + 4\sigma \le m \le m_\omega + 8\sigma$). The tails of the ω peak seem to extend quite far from the mean. This is due not only to its natural width of $8.43 MeV/c^2$, but also to the fact that, during the kinematic fitting, the ω decaying to $\pi^\circ\gamma$ has its mass fixed to the nominal ω mass. The momenta of the three pions are then adjusted to fit

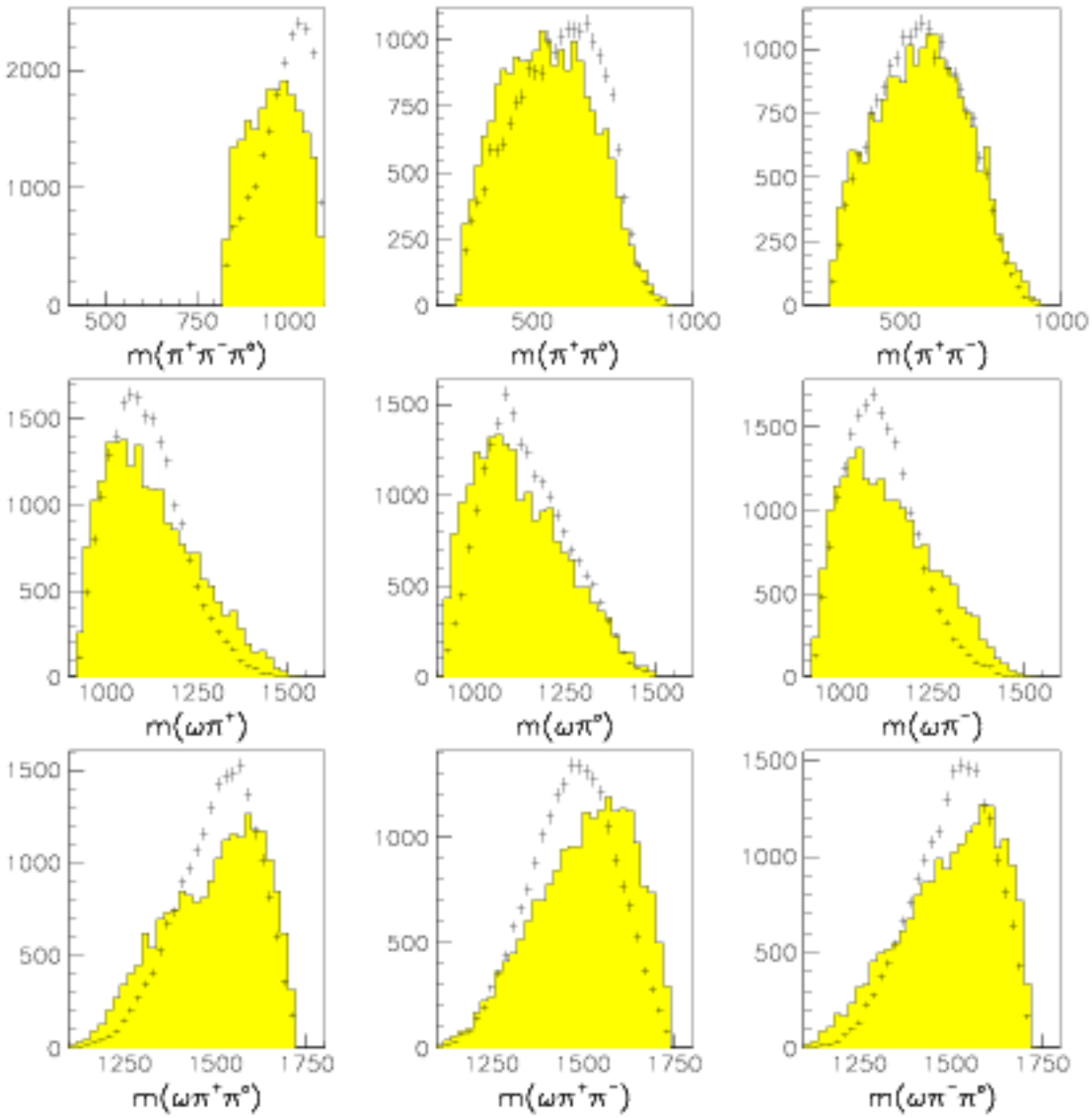

Figure 9.4: Invariant mass spectra, as in Figure 9.3, except that most of the $\bar{p}p \to \omega\omega$ events have been eliminated by requiring that $m(\pi^+\pi^-\pi^\circ) > 830 MeV/c^2$. The MC histograms have been scaled up to have the same numbers of events as those for the experimental data. All of the histograms have bin sizes of $20 MeV/c^2$.

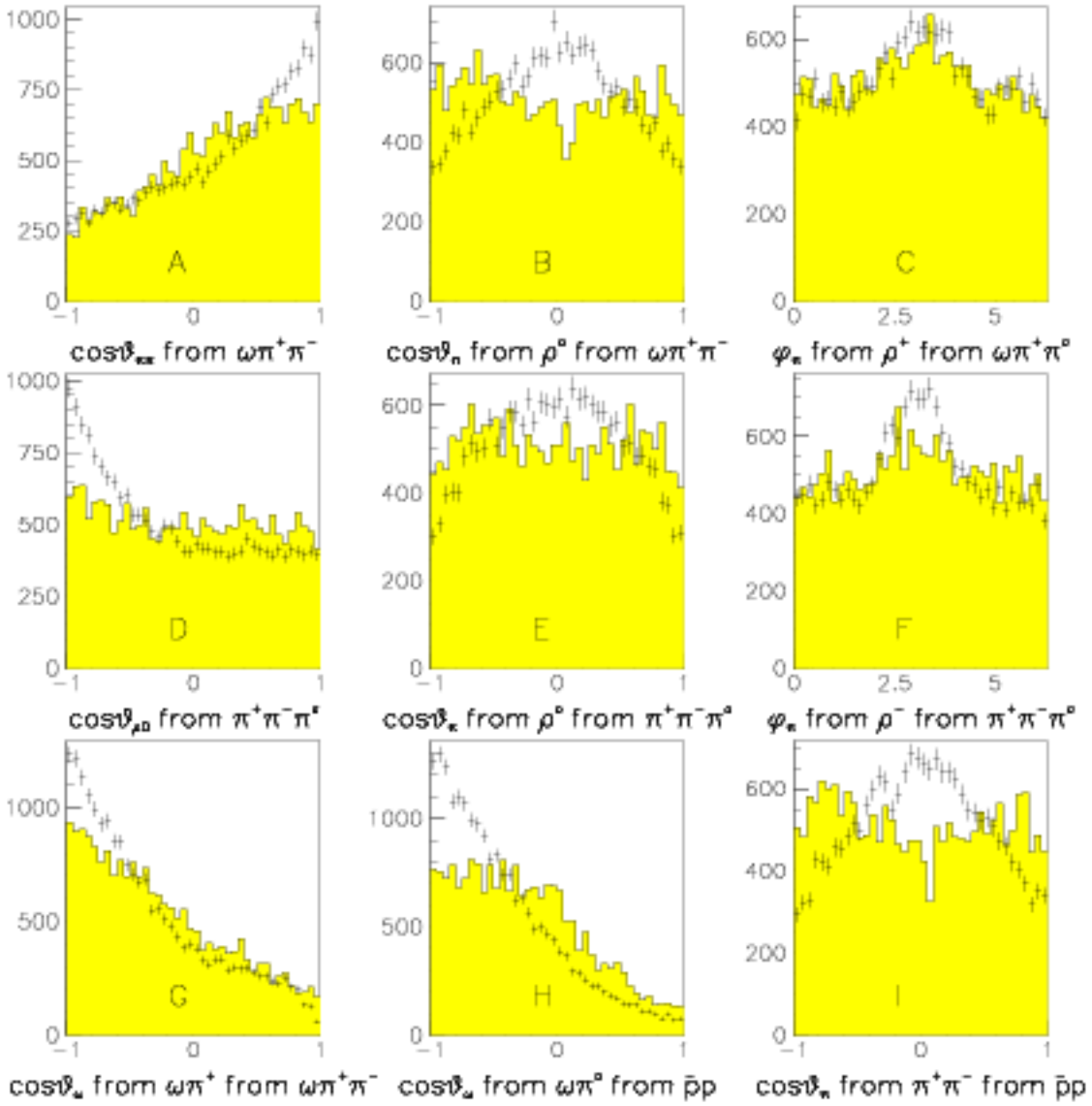

Figure 9.5: Nine angular distributions are shown, with the experimental data shown as crosses and the Monte Carlo data shown as the shaded histograms. The $\bar{p}p \rightarrow \omega\omega$ events have been eliminated by requiring that $m(\pi^+\pi^-\pi^\circ) > 830 MeV/c^2$. The MC histograms have been scaled up to have the same numbers of events as those for the experimental data.

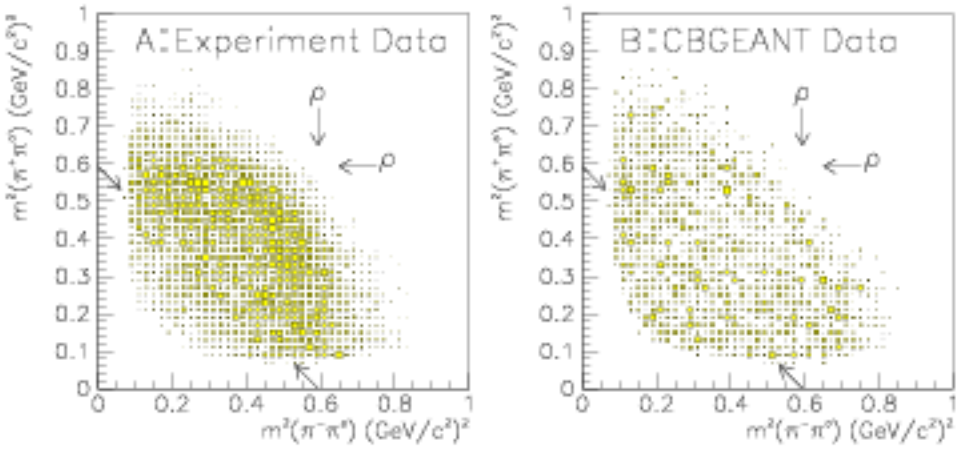

Figure 9.6: Dalitz plot of $\pi^+\pi^-\pi^\circ$ for events with $m(\pi^+\pi^-\pi^\circ) > 1000 MeV/c^2$. That is, for each event with $m(\pi^+\pi^-\pi^\circ) > 1000 MeV/c^2$ the square of the invariant mass of the $\pi^+\pi^\circ$ pair is plotted vs. the square of the invariant mass of the $\pi^-\pi^\circ$ pair. Arrows indicate where ρ bands should appear; they correspond to $\pi\pi$ masses of $770 MeV/c^2$. The diagonal arrows are for $\pi^+\pi^-$ masses of $770 MeV/c^2$.

this constraint, thereby artificially broadening the $\omega \to \pi^+\pi^-\pi^\circ$ peak. Dalitz plots for events in each of these regions are also shown. The Dalitz plot for the ω peak region shows the expected behavior for a $J^P = 1^-$ meson: the density of events is greatest near the center of the plot, and approaches zero near the boundary. From the sidebands, this behavior is much less pronounced.

One way to see the dependence of the density of events as a function of distance from the center of the Dalitz plot is to histogram the quantity

$$\lambda = \frac{|\vec{p_+} \times \vec{p_-} + \vec{p_-} \times \vec{p_\circ} + \vec{p_\circ} \times \vec{p_+}|^2}{\frac{27}{4}(\frac{1}{9}m^2_{\pi\pi\pi} - m^2_\pi)^2},$$

where $\vec{p_+}$, $\vec{p_\circ}$ and $\vec{p_-}$ refer to the momenta of the three pions. The denominator is the maximum value of the expression in the numerator and forces λ to be between 0 and 1; $m_{\pi\pi\pi}$ is the invariant mass of the three pion system, and m_π is the average of the three pions' rest masses. Figure 9.8 shows histograms of λ for the ω peak and the sidebands. The steep, linearly rising distribution for events from the peak is a sign that these are truly $\omega \to \pi^+\pi^-\pi^\circ$ events. (This distribution of λ for a $J^P = 1^-$ resonance is predicted by considerations of symmetries and transformation laws. This distribution is how the spin and parity of the ω were first determined [39].) The distributions of λ from the sidebands have much smaller slopes, indicating a smaller fraction of ω events.

The Dalitz plot and λ are shown in Figure 9.9 for the same omega peak region in

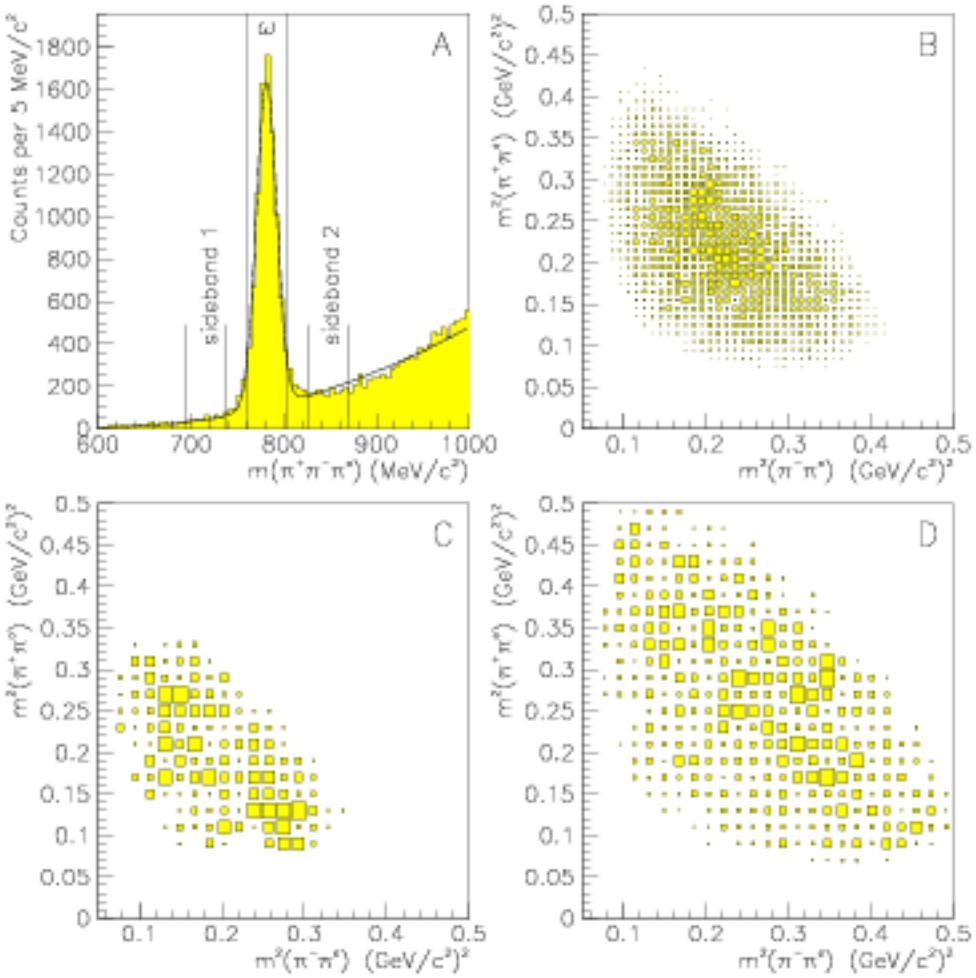

Figure 9.7: A: The $m(\pi^+\pi^-\pi^\circ)$ spectrum for experimental data. The cuts defining the peak and sidebands are shown. B, C, D: The $\pi^+\pi^-\pi^\circ$ Dalitz plot for events from the ω peak, sideband 1 and sideband 2, respectively.

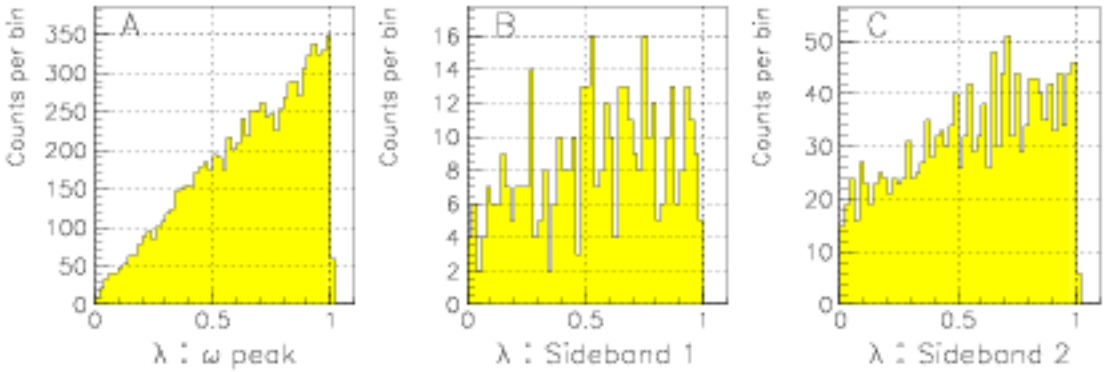

Figure 9.8: The distribution of λ from the ω peak, and sidebands 1 and 2.

$\pi^+\pi^-\pi^\circ\omega$ Monte Carlo data (without the $\omega \to \pi^+\pi^-\pi^\circ$ resonance). The λ distribution is nearly flat, resembling those from the sideband regions above.

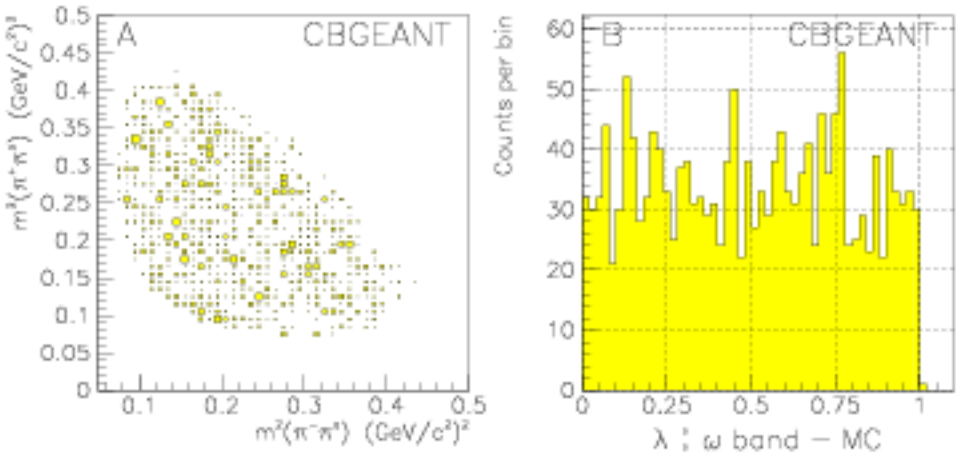

Figure 9.9: CBGEANT $\pi^+\pi^-\pi^\circ\omega$ data. A: The $\pi^+\pi^-\pi^\circ$ Dalitz plot for events from the ω band as defined for the peak in the experimental data. B: Distribution of λ from the ω band.

Chapter 10

Branching Fractions for $\bar{p}p \to \pi^+\pi^-\pi^\circ\omega$ and $\bar{p}p \to \omega\omega$

Accurate determination of the rate of production of $\omega\omega$ is important to the study of $\bar{p}p$ annihilation dynamics. This rate, when compared to the rate for $\rho^\circ\rho^\circ$ ($0.12 \pm 0.12\%$,) can provide strong constraints on the relative contributions of quark rearrangement and quark annihilation processes in the annihilations. (See Section 2.3.)

In a 1993 publication by the Crystal Barrel collaboration, the rate ($3.32 \pm 0.34\%$ [19]) was found to be about twice as strong as had been previously measured (in bubble chamber experiments,) and was much stronger than theorists had calculated using a wide variety of models. This measurement was made with both ω's decaying to $\pi^\circ\gamma$, and was performed by examining invariant mass spectra, and the lineshape used in fitting the peak was an incomplete description (Gaussian.) The measurement needed to be redone. In this chapter, the measurement will be made with the two ω's in two different decay modes, and will be performed such a manner as to be far less susceptible to background contributions. The value obtained is consistent with the previous measurement.

Also presented is a measurement of the rate of production of $\pi^+\pi^-\pi^\circ\omega$. This will guide expectations of what will be seen in the PWA and the unexpectedly large result may also be of interest in the study of $\bar{p}p$ annihilation dynamics.

10.1 Data Samples

The branching fractions $BR(\bar{p}p \to \pi^+\pi^-\pi^\circ\omega)$ and $BR(\bar{p}p \to \omega\omega)$ are determined from the fractions of such events in the minimum bias data sample (see Section 3.6.) In this way, one does not rely on trigger simulation in the determination of the detection efficiency from Monte Carlo data, as one would when using triggered data. Table 10.1 shows a summary of the selection of the experimental minimum bias data for use in the following calculations of branching fractions. Because the branching fractions will be determined by counting contents of peaks atop smooth backgrounds, the selection

Criterion	Number of events
Events read from MB tapes	1652518
$CL(\pi^+\pi^-5\gamma) > 1\%$	23922
$CL(\pi^+\pi^-\pi^\circ\pi^\circ\gamma) > 1\%$	18529

Table 10.1: Summary of the cuts made and the numbers of events passing each, in selecting Minimum Bias data for measurements of branching fractions.

criteria need not be as stringent as those for selection of events for partial wave analysis. Specifically:

- Events for which CBDROP dropped PEDs were retained.
- Events for which there were more than one successful kinematic fit to $\bar{p}p \to \pi^+\pi^-\pi^\circ\omega$ were retained.

The less stringent cuts allow greater numbers of events to be used, thereby reducing the statistical errors on the measurements. These cuts were imposed to exclude certain types of events in the PWA; relaxing them does not contribute background to the branching fraction measurements.

The efficiencies for event detection are determined by passing a known number of Monte Carlo events through the same analysis procedure as the experimental data. The fraction of events which are detected is defined as the detection efficiency for the given analysis method. The Monte Carlo data sample used in the efficiency calculations consists of two sets which were combined after detector simulation and kinematic fitting were done. The first set had 18955 events resulting from the analysis of 149936 events of the type $\bar{p}p \to \pi^+\pi^-\pi^\circ\omega,\ \omega \to \pi^\circ\gamma$. The second set was 6010 events from 49873 events of the type $\bar{p}p \to \omega_1\omega_2,\ \omega_1 \to \pi^+\pi^-\pi^\circ,\ \omega_2 \to \pi^\circ\gamma$. The generated events allowed the π°'s to decay to $\gamma\gamma$ with a branching fraction of 98.802%, so the number of generated events should be multiplied by $(0.98802)^2$ to get the number of generated events in the desired final state: 146365 ± 59 for $\pi^+\pi^-\pi^\circ\omega$, and 48685 ± 34 for $\omega\omega$. These data sets were combined to mimic the experimental data, which had about 25% $\omega\omega$ events.

The masses of the ω's in the Monte Carlo simulation are Breit-Wigner distributed between 0 and $2m_\omega$; they were not restricted to $m_\omega \pm 3\Gamma$ as in older versions of CBGEANT.

10.2 $BR(\bar{p}p \to \pi^+\pi^-\pi^\circ\omega)$

The number of $\pi^+\pi^-\pi^\circ\omega$ events detected in the data sample is

$$N_{\pi^+\pi^-\pi^\circ\omega} = N_{mb} \cdot f_{ann} \cdot BR(\bar{p}p \to \pi^+\pi^-\pi^\circ\omega) \cdot BR(\omega \to \pi^\circ\gamma) \cdot (BR(\pi^\circ \to \gamma\gamma))^2 \cdot \epsilon_{\pi^+\pi^-\pi^\circ\omega},$$

so

$$BR(\bar{p}p \to \pi^+\pi^-\pi^\circ\omega) = \frac{N_{\pi^+\pi^-\pi^\circ\omega}}{N_{mb} \cdot f_{ann} \cdot BR(\omega \to \pi^\circ\gamma) \cdot (BR(\pi^\circ \to \gamma\gamma))^2 \cdot \epsilon_{\pi^+\pi^-\pi^\circ\omega}}.$$

$N_{mb} = 1652518$ is the number of minimum bias triggers which resulted in events being recorded. Some of these events, however, occur with the antiproton still in flight. Studies [40] indicate that $f_{ann} = 96 \pm 1\%$ of the minimum bias triggers result in $\bar{p}p$ annihilation at rest. For $BR(\omega \to \pi^\circ\gamma)$ and $BR(\pi^\circ \to \gamma\gamma)$, the PDG [1] values of $8.5 \pm 0.5\%$ and $98.798 \pm 0.032\%$ are used. $\epsilon_{\pi^+\pi^-\pi^\circ\omega}$ is the efficiency for detection of the events.

The number of events of the type $\bar{p}p \to \pi^+\pi^-\pi^\circ\omega$ is determined by examining the $\pi^\circ\gamma$ mass spectrum of events which satisfy a kinematic fit to the hypothesis $\bar{p}p \to \pi^+\pi^-\pi^\circ\pi^\circ\gamma$. The cut on the confidence level of this fit is varied to check for its effect on the result. This cut should ensure that the events to be analyzed are from the flat region of the confidence level (CL) distributions in order to eliminate background events, which possibly have different effects in the Monte Carlo data than in the experimental data, and thus effect the calculated efficiency. Figure 10.1 shows the CL distributions of the events under analysis. A cut of $CL > 0.20$ satisfies the stated requirement. A histogram of the invariant masses of *both* $\pi^\circ\gamma$ pairs from each event is shown in Figure 10.2. The peaks in the histograms are fit, and the numbers of events in the peaks are determined from the integral of the function describing the peak. Because the measurement resolution is expected to be of similar magnitude to the natural width of the distribution, the peaks in the experimental and Monte Carlo data are fitted with a Voigtian function (see Section 11.3.2.) The Voigtian is a Breit-Wigner function (the natural shape) convoluted with a Gaussian (representing the resolution). In the fit, Γ, the natural width of the ω, is fixed to $8.43 MeV/c^2$, the PDG value [1]. The Gaussian width, σ is fit; the values obtained are $11.82 \pm 0.56 MeV/c^2$ for experimental data and $11.14 \pm 0.14 MeV/c^2$ for Monte Carlo data.

Table 10.2 shows the results of the branching ratio calculation with various CL cuts. The result does not depend strongly on the cut. With a cut of $CL > 0.20$, the result is:

$$BR(\bar{p}p \to \pi^+\pi^-\pi^\circ\omega) = 16.1 \pm 1.0 \pm 0.4\% \quad (\pm\sigma_{systematic} \pm \sigma_{statistical}).$$

The statistical uncertainty is based on the number of events in the peak and on the uncertainty in the efficiency (because it was computed by counting the number of events in the peak for Monte Carlo data.) The systematic uncertainty includes contributions from the uncertainty on f_{ann}, and the uncertainties on the branching fractions for $\omega \to \pi^\circ\gamma$ and $\pi^\circ \to \gamma\gamma$. Any background in this signal would consist of events where the $\pi^\circ\gamma$ constitutes an ω, but the other particles in the event were not $\pi^+\pi^-\pi^\circ$. The background studies presented in Chapter 8 shows this to be of negligible magnitude. In particular, events of the type $\bar{p}p \to \omega\pi^\circ\pi^\circ \to \pi^+\pi^-\pi^\circ\pi^\circ\pi^\circ$ won't contribute, nor will $\bar{p}p \to \pi^+\pi^-\pi^\circ\pi^\circ\pi^\circ$ events; these are the only channels which were shown to contaminate the $\pi^+\pi^-\pi^\circ\omega$ data set.

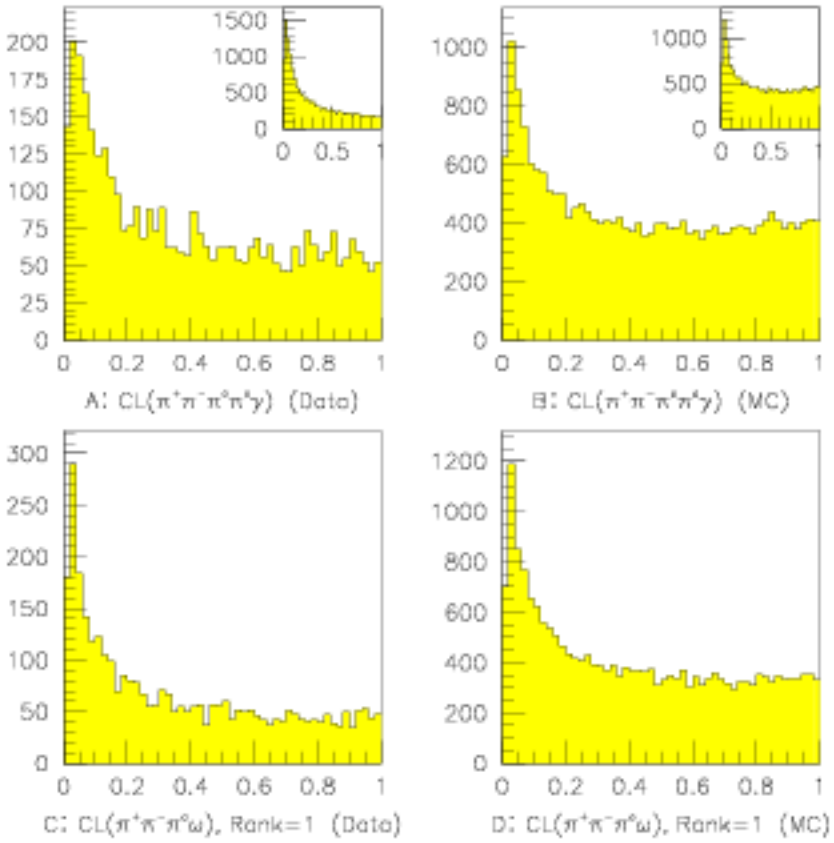

Figure 10.1: A,B: The Confidence Level (CL) distributions for fits to $\bar{p}p \rightarrow \pi^+\pi^-\pi^0\pi^0\gamma$, for Experimental and Monte Carlo data respectively. The mass of one $\pi^0\gamma$ combination is required to lie within $50MeV/c^2$ of the ω mass. The CL distributions without this cut on the $\pi^0\gamma$ mass are shown inset. C,D: The CL distributions for fits to $\bar{p}p \rightarrow \pi^+\pi^-\pi^0\omega$, requiring the rank of the fit to be 1, for Experimental and Monte Carlo data respectively.

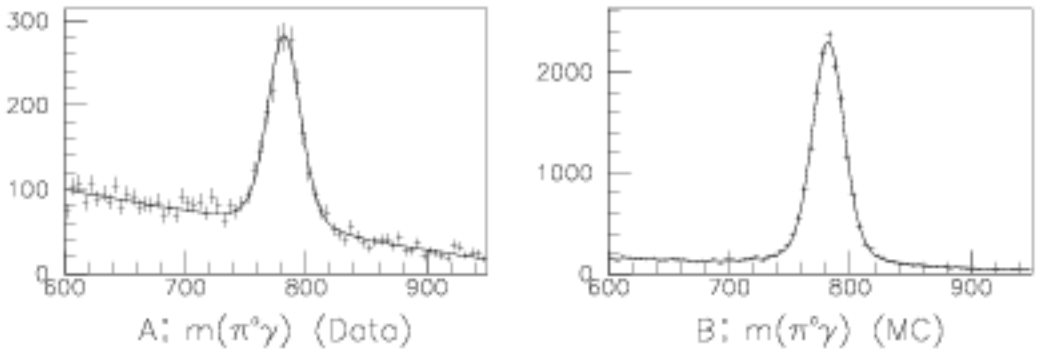

Figure 10.2: A: The $\pi^\circ\gamma$ mass distribution (2 entries per event) in the region of the ω mass, for experimental data, with a 20% CL cut. B: The same histogram for the Monte Carlo data.

CL cut	$N_{MC\,\pi^+\pi^-\pi^\circ\omega}$	$\epsilon_{\pi^+\pi^-\pi^\circ\omega}$	$N_{\pi^+\pi^-\pi^\circ\omega}$	$BR(\bar{p}p \to \pi^+\pi^-\pi^\circ\omega)$
1%	22983	.11783± .00078	2366	.1526 ± .0097
5%	20902	.10716± .00074	2229	.1580 ± .0099
10%	19084	.09784± .00071	2098	.1629 ± .0103
15%	17659	.09054± .00068	1872	.1571 ± .0100
20%	16347	.08381± .00066	1779	.1612 ± .0103
25%	15173	.07779± .00063	1666	.1627 ± .0104
30%	14101	.07229± .00061	1545	.1624 ± .0105
35%	13064	.06698± .00059	1465	.1662 ± .0108

Table 10.2: Results of analysis of the $\pi^\circ\gamma$ mass spectra with various cuts on $CL(\pi^+\pi^-\pi^\circ\pi^\circ\gamma)$. The measured number of events in the MC data set, and the efficiency determined from it are shown in the second and third columns. The measured number of *real* events and the resulting branching fraction are shown in the last two columns.

10.3 $BR(\bar{p}p \rightarrow \omega\omega)$ from the $\omega\omega$ Momentum Spectrum

The $BR(\bar{p}p \rightarrow \omega\omega)$ can be determined by examining the momentum spectrum of the decay products of the ω's. For $\bar{p}p$ annihilation at rest, the ω's will each have a momentum of $518.5 MeV/c$, if both ω's have masses of $781.96 MeV/c^2$. Measurement of the contents of such a signal allows one to count the number of $\bar{p}p \rightarrow \omega\omega$ events.

In order to investigate the effects of the Breit-Wigner shape of the ω mass spectra on the momentum spectrum, a simple computer program was used to generate ω's with masses independently distributed according to a Breit-Wigner function with width $\Gamma = 8.43 MeV/c^2$. The momentum, $q_{\omega\omega}$, that each pair would have (from $\bar{p}p$ annihilation) is then calculated. This program simulates kinematics only; no detector response nor resolution effects are included. The $q_{\omega\omega}$ spectrum is also described well by a Breit-Wigner function (see Figure 10.3 A.)

Table 10.3 lists momenta for other 2-body channels which could appear in the $\pi^+\pi^-\pi^\circ\pi^\circ\gamma$ data sample; the $\omega\omega$ peak should be well separated from the others.

Channel	Momentum
$\bar{p}p \rightarrow \omega\omega$	518.5 MeV/c
$\bar{p}p \rightarrow \omega\eta$	656.4 MeV/c
$\bar{p}p \rightarrow \omega\eta'$	350.5 MeV/c

Table 10.3: Momenta for $\bar{p}p$ annihilations into two mesons.

Note that only $\omega\omega$ events will contribute to the peak in the momentum spectrum. In contrast, the mass spectra of the decay products will show peaks at the ω mass regardless of whether the other final state particles constituted an ω. This leads to the expectation that this $q_{\omega\omega}$ spectrum method will produce a more pure signal, and will allow easy integration of the signal without requiring a background subtraction.

Because the natural shape of the peak in the momentum spectrum is a Breit-Wigner function whose width is similar to the experimental resolution, the peaks are fit with Voigtian functions.

There are some practical limitations of this measurement scheme, however. If the mass spectrum of one of the ω's is restricted, the shape of the momentum spectrum changes (see Figure 10.3 B.) Making CL cuts changes the mass distributions, but not in a simple way, so determining the correct value for the natural width of the momentum distribution is difficult. Leaving Γ_q as a free parameter in the fits results in large fluctuations in its fitted value. Figure 10.4 shows the distribution of $\omega \rightarrow \pi^\circ\gamma$ masses, for a CL cut of 25%. The distributions span a range of about $50 MeV/c^2$, so in the Voigtian fits to the peaks, Γ_q is fixed to $10.0 MeV/c$ (see Figure 10.1.)

The data used in this analysis were kinematically fit to $\bar{p}p \rightarrow \pi^+\pi^-\pi^\circ\pi^\circ\gamma$ with CL>1%, and also had been successfully fit to $\bar{p}p \rightarrow \pi^+\pi^-\pi^\circ\omega$ (but the kinematic

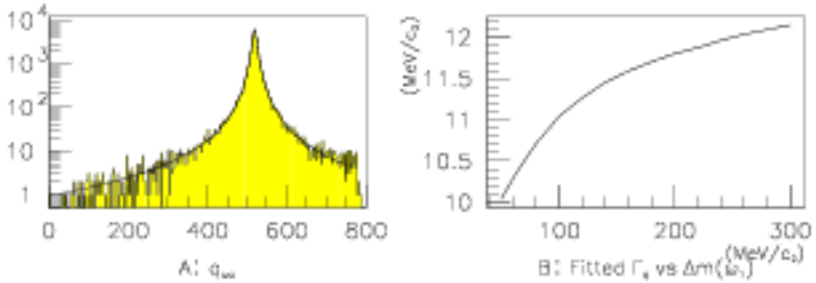

Figure 10.3: A: Simulation of the distribution of momenta, $q_{\omega\omega}$, of ω's from $\bar{p}p \to \omega\omega$, where the ω masses have a non-relativistic Breit-Wigner distribution. The simulation is of kinematics only; no detector response nor resolution effects are included. The fit to the $q_{\omega\omega}$ distribution with a non-relativistic Breit-Wigner function yields a width $\Gamma_q = 12.6 MeV/c^2$. These are displayed on a logarithmic scale in order to show the quality of the fit in the tails of the distribution. B: The fitted width, Γ_q, of the $q_{\omega\omega}$ distribution, where the mass of one of the ω's is required to lie within a mass window $\Delta(m_1)$ centered at the central mass of the ω, as a function of the width of the mass window.

variables were not adjusted to reflect the latter fit; using the fitted values creates an artificially large signal.) The momentum spectra contain the momenta of the $\pi^+\pi^-\pi^\circ_1$ system, where π°_1 is the π° which was not the $\omega \to \pi^\circ\gamma$ decay product. Figure 10.5 shows the $q_{\omega\omega}$ spectra. The Voigtian fits, with fixed $\Gamma_q = 10 MeV/c$, yield Gaussian widths of $6.36 \pm .77 MeV/c$ and $5.65 \pm .26 MeV/c$ for the experimental and Monte Carlo data.

The formula used in the calculation is:

$$BR(\bar{p}p \to \omega\omega) = \frac{N_{\omega\omega}}{N_{mb} \cdot f_{ann} \cdot BR(\omega\omega \to \pi^+\pi^-\pi^\circ\pi^\circ\gamma) \cdot (BR(\pi^\circ \to \gamma\gamma))^2 \cdot \epsilon_{\omega\omega}}.$$

Here $BR(\omega\omega \to \pi^+\pi^-\pi^\circ\pi^\circ\gamma) = 2 \times BR(\omega \to \pi^\circ\gamma) \times BR(\omega \to \pi^+\pi^-\pi^\circ) = 15.0 \pm 0.9\%$. The factor of two accounts for the two combinations of of ω decays which lead to the desired final state ($\omega_1 \to \pi^+\pi^-\pi^\circ, \omega_2 \to \pi^\circ\gamma$, *and* $\omega_2 \to \pi^+\pi^-\pi^\circ, \omega_1 \to \pi^\circ\gamma$.) The values for the individual branching fractions of the ω are taken from the PDG [1]: for $\omega \to \pi^\circ\gamma$, $8.5 \pm 0.5\%$; for $\omega \to \pi^+\pi^-\pi^\circ$, $88.8 \pm 0.7\%$.

Table 10.4 shows the results of this method. The CL cut for event selection was varied to demonstrate that its value does not significantly affect the result. A CL cut of 25% selects events from the flat region of the CL distribution (see Figure 10.1.) With these values, the result for the branching fraction is:

$$BR(\bar{p}p \to \omega\omega) = 3.23 \pm 0.20 \pm 0.15\% \quad (\pm\sigma_{systematic} \pm \sigma_{statistical}).$$

CL cut	$N_{MC\,\omega\omega}$	$\epsilon_{\omega\omega}$	$N_{\omega\omega}$	$BR(\bar{p}p \to \omega\omega)$
5%	4366	.08968 ± .00136	720	.0343 ± .0025
10%	3930	.08072 ± .00129	650	.0344 ± .0024
15%	3582	.07358 ± .00123	586	.0341 ± .0026
20%	3316	.06811 ± .00118	520	.0327 ± .0025
25%	3069	.06304 ± .00114	476	.0323 ± .0025
30%	2818	.05788 ± .00109	454	.0335 ± .0026
35%	2558	.05254 ± .00104	394	.0321 ± .0026
40%	2391	.04911 ± .00100	354	.0308 ± .0026
45%	2168	.04453 ± .00096	327	.0314 ± .0027
50%	1969	.04044 ± .00091	302	.0319 ± .0028

Table 10.4: Results of analysis of the ω decay products' momentum spectra: the numbers of detected events, detection efficiencies, and resulting branching fractions are shown as a function of the CL cut.

This is compatible with the previous measurement by Crystal Barrel: $3.32 \pm 0.34\%$. The statistical uncertainty is based on the number of events in the peak and on the uncertainty in the efficiency (because it was computed by counting the number of events in the peak for Monte Carlo data.) The systematic uncertainty includes contributions from the uncertainty on f_{ann}, and the uncertainties on the branching fractions for $\omega \to \pi^\circ\gamma$, $\omega \to \pi^+\pi^-\pi^\circ$ and $\pi^\circ \to \gamma\gamma$.

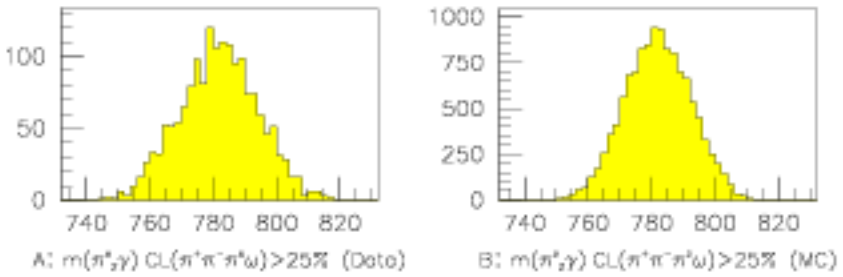

Figure 10.4: A: The distribution of $\pi_2^\circ\gamma$ masses for events where the fit to $\bar{p}p \to \pi^+\pi^-\pi^\circ\omega$, $\omega \to \pi_2^\circ\gamma$ had $CL \geq 25\%$ and a rank of 1, for experimental data. B: The same histogram for Monte Carlo data.

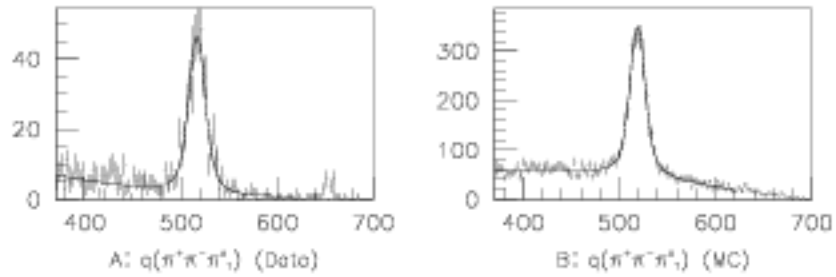

Figure 10.5: A: The distribution of momenta, $q_{\pi\pi\pi}$, of the $\pi^+\pi^-\pi_1^\circ$ system, for events satisfying the fit to $\bar{p}p \to \pi^+\pi^-\pi^\circ\omega$,$\omega \to \pi_2^\circ\gamma$ with $CL \geq 25\%$ and a rank of 1, for experimental data. The small peak near $650 MeV/c$ is due to $\bar{p}p \to \omega\eta$. B: The same histogram for Monte Carlo data.

10.4 Comparison with Previous CB Measurements

The $BR(\bar{p}p \to \omega\omega)$ has previously been measured and published as $3.32 \pm 0.34\%$ [38]. The method for this previous measurement differed from that presented here in three significant ways:

1. Mass peaks, as opposed to momentum peaks, were fitted.
2. The peaks were fitted with Gaussian, instead of Voigtian, functions.
3. The version of CBGEANT used to generate the Monte Carlo events for the efficiency calculation generated ω's whose masses were within 3Γ of the central mass of the ω.

Both ω's were seen in the $\pi^\circ\gamma$ decay mode. The reason for fitting mass peaks instead of the momentum peaks was that the background under the momentum peak was poorly defined. In the analysis presented here, the data which had been kinematically fit to $\bar{p}p \to \pi^+\pi^-\pi^\circ\pi^\circ\gamma$ also had a poorly defined background, probably because of a large contribution from events which were not of the desired type. Requiring a successful kinematic fit to $\bar{p}p \to \pi^+\pi^-\pi^\circ\omega$ was the crucial step in cleaning up the spectrum. The data for the previous measurement had been fit to $\bar{p}p \to \pi^\circ\pi^\circ\gamma\gamma$, and probably had a large level of contamination.

Measuring the contents of the $\omega \to \pi^\circ\gamma$ mass peak will include events where the other set of final state particles were not from ω decays; that is, events of the type $\bar{p}p \to X\omega$, where X is not necessarily and ω. This would overestimate the number of $\bar{p}p \to \omega\omega$ events, causing the measured value of $BR(\bar{p}p \to \omega\omega)$ to be too large.

Use of a Gaussian function underestimates the number of events in the peak, because the tails fall of rapidly and thus do not include events in the much larger tails

of the Breit-Wigner distribution. This would cause the measured value of $BR(\bar{p}p \rightarrow \omega\omega)$ to be too small.

The truncated mass distribution of the CBGEANT ω's make those ω's more easily identifiable than in the real data, since they lie close to the central mass (particularly since the distribution is fitted with a Gaussian function.) This would make the efficiency for detection seem higher, and therefore make the measured branching fraction smaller than its true value.

These effects appear to offset each other in such a way as to not significantly effect the final result for $BR(\bar{p}p \rightarrow \omega\omega)$.

This rate is much larger than the rate measured for $\rho^\circ\rho^\circ$, $0.12\pm0.12\%$. Recall that in the quark line rule model of Genz *et al*, the rates for $\omega\omega$ and $\rho^\circ\rho^\circ$ would be equal if the annihilation diagram dominates over the rearrangement diagram (in Figure 2.4B.) These measurements offer evidence against dominance of the annihilation diagram.

Chapter 11

Partial Wave Analysis Technique

The experimental data for the reaction $\bar{p}p \to \pi^+\pi^-\pi^\circ\omega$ indicate that the four final state particles are not distributed according to four body phase space (see Figures 9.4 and 9.5. The purpose of the partial wave analysis (PWA) is to determine what processes occurred to yield the final state distribution.

In χ^2 fitting, one proposes a distribution (the fitting function) and examines the quantity

$$\chi^2 = \sum_{j=1}^{n} \frac{(f(\{x_j\}) - y(\{x_j\}))^2}{\sigma_j(f)^2},$$

which is the weighted sum of squares of deviations of the data from the proposed distribution. Here, $\{x\}$ is the set of measurements which describe an event, $y(\{x\})$ is the value of the fitting function for $\{x\}$, $f(\{x_j\})$ is the number of events measured at $\{x_j\}$, and $\sigma_j(f)$ is the uncertainty in $f(\{x_j\})$. Usually, the data are binned: the space spanned by $\{x\}$ is divided into bins and $f(\{x_j\})$ is the number of events falling into the bin centered at $\{x_j\}$. The sum is over all bins. The optimum fitting function is that which yields the minimum χ^2. This technique works well for 3-particle final states, where $\{x\}$ is two-dimensional, i.e. a Dalitz plot. For a 4-particle final state, though, the measurement space is five dimensional, so even with only 10 bins per dimension and fewer than 10^5 events, the number of events per bin would be small, making statistical analysis difficult. The 4-particle final state is better handled by unbinned fits, where one optimizes by maximizing the probability that the given data set would result from the proposed distribution. This method is referred to as unbinned likelihood fitting.

The fitting function is a probability density function (PDF.) In order to allow for interferences among the various processes in the fit, amplitude densities are computed, added, and squared to get probability densities. An outline of the computation, in the form of an example, follows.

One assumption made in the analysis model is that the $\bar{p}p$ annihilation occurs when the $\bar{p}p$ atom is in its $^1S_0$ or $^3S_1$ state. The isobar model provides the framework for the sequence of decays leading to the four particle final state; that is, all processes proceed via two-body modes: Two mesons (resonances or final state particles) are produced in

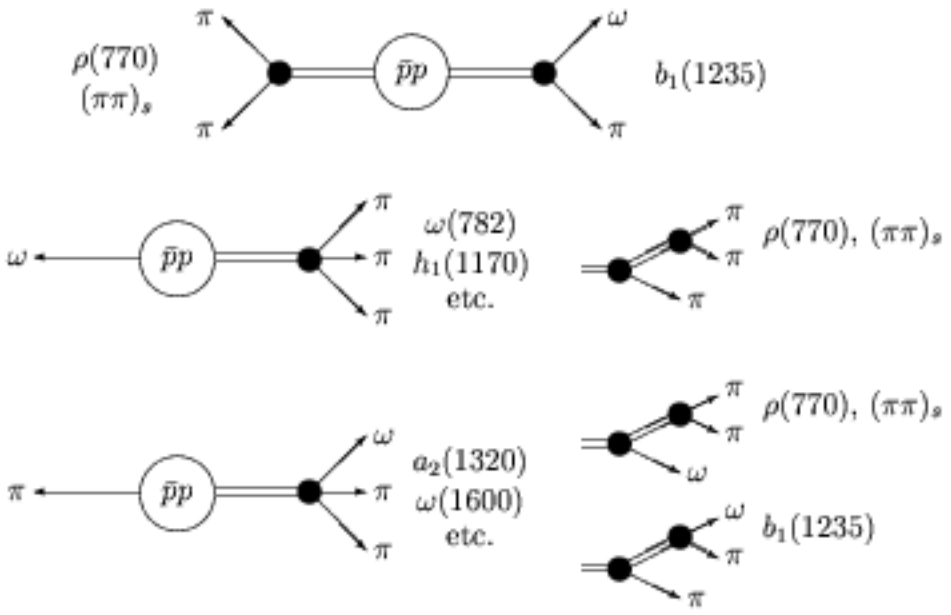

Figure 11.1: The three modes of annihilation into two mesons which are modeled in this analysis. The two body decay modes of the resonances are also shown.

the annihilation; resonances further decay into 2 mesons, and so forth, until the final state $\pi^+\pi^-\pi^\circ\omega$ is reached. Figure 11.1 shows the ways that the $\pi^+\pi^-\pi^\circ\omega$ final state can be produced via two-body modes. A particular sequence of resonance productions and decays is called a *decay chain*.

As an example, consider the following decay chain:

$$\bar{p}p(\,^1S_0) \to b_1^\circ(1235)\rho^\circ, \quad b_1 \to \omega\pi^\circ, \quad \rho \to \pi^+\pi^-, \quad \omega \to \pi^\circ\gamma.$$

The amplitude is:

$$\begin{aligned} A(b_1^\circ\rho^\circ) &= \mathcal{H}_a(\theta_\rho, \phi_\rho, \theta_\omega, \phi_\omega, \theta_{\pi^+}, \phi_{\pi^+}, \theta_\gamma, \phi_\gamma,) \\ &\times \cdot\mathcal{K}(\bar{p}p \to b_1^\circ\rho^\circ) \cdot \mathcal{K}(\rho \to \pi^+\pi^-) \cdot \mathcal{K}(b_1 \to \omega\pi^\circ), \end{aligned}$$

where $\mathcal{H}$ is the helicity amplitude for the decay chain; it depends on the angles in which the particles are emitted in the annihilation and in each decay, and on the spins of all of the intermediate and final state mesons. Note that the angles describing the direction of the photon from the ω decay are included in the analysis. This is computed using the helicity formalism, which is discussed in Section 11.2. The $\mathcal{K}()$ functions are kinematic amplitudes; for resonance decays, these are computed using Breit-Wigner functions, which depend on the mass of the decaying resonance and the invariant mass of the decay products. For example, the probability that a $\pi^+\pi^-$ pair came from a ρ is described by a Breit-Wigner function with a mass of $770 MeV$ and

a width of $150 MeV$. For the annihilation, the $\mathcal{K}(\bar{p}p \to b_1^\circ \rho^\circ)$ function is a centrifugal barrier function, which depends on the masses of the b_1 and ρ, and on the orbital angular momentum between them. Section 11.3 describes the kinematic amplitudes in detail. (No kinematic amplitude is necessary for the ω decay, since the $\pi^\circ\gamma$ mass is fixed at the central mass of the ω in the kinematic fit stage of analysis.)

Because there are pions of all three charges in this final state, all three charge combinations of $b_1\rho$ can be produced: $b_1^+\rho^-$, $b_1^\circ\rho^\circ$, and $b_1^-\rho^+$. Amplitudes for each of these processes are computed, and added to get the total amplitude:

$$A(^1S_0 \to b_1\rho) = +\sqrt{\frac{1}{3}}A(^1S_0 \to b_1^+\rho^-) - \sqrt{\frac{1}{3}}A(^1S_0 \to b_1^\circ\rho^\circ) + \sqrt{\frac{1}{3}}A(^1S_0 \to b_1^-\rho^+).$$

The three amplitudes are added with fixed strengths and phases determined by the Clebsch-Gordan coefficients coupling the isospin in the initial state ($I = 0$) to the isovector b_1 and ρ resonances.

All processes originating from the $^1S_0$ initial state are allowed to interfere with one another by adding all of the amplitudes for such processes:

$$A(^1S_0) = b_1 A(^1S_0 \to b_1(1235)\rho)e^{i\phi_1} + b_2 A(^1S_0 \to h_1(1170)\omega)e^{i\phi_2} + \cdots$$

The b's and ϕ's are fitted parameters describing the strengths and phases of the processes. The $^1S_0$ and $^3S_1$ amplitudes are added incoherently:

$$\text{PDF} = c_1|a(^1S_0)|^2 + c_2|a(^3S_1)|^2,$$

where c_1 and c_2 are fitted parameters describing the relative amounts of the two initial states.

The values of the PDF for all of the events can be multiplied together to get the joint probability density that the proposed set of processes would produce the data set. The proposed strengths and phases are varied to maximize the joint probability density.

In the following sections, details on each aspect of the PWA are given.

11.1 Likelihood Fitting

The basis of *likelihood fitting* is calculating the probability that a hypothesized probability distribution function (PDF) would produce the data set under consideration. If the probability density for the parent distribution to produce event i, characterized by the measurements $\{x_i\}$, is $P(\{x_1\})$, then the joint probability density for observing the N events in the data sample is

$$\mathcal{L} = \prod_{i=1}^{N} P(\{x_i\}).$$

It is this function, with careful attention to the normalization, which is to be maximized by varying the parameters of the of the PDF. Since the value of the PDF is less than one for each event, the product above becomes a very small number quite rapidly for large numbers of events, so the negative logarithm of $\mathcal{L}$ is minimized in the fitting procedure:

$$-2\ln\mathcal{L} = -2\sum_{i=1}^{N}\ln P(\{x_i\}).$$

Minimization is chosen because of the availability of computer programs for this purpose.

The normalization condition for $P(\{x_i\})$ is that its integral over its domain must not depend on the values of the fit parameters. Suppose μ_i is the unnormalized PDF for producing event i. Then

$$P(\{x_i\}) = \frac{\mu_i}{\int \mu d\Omega}$$

where the integration is over the domain of μ.

For the purpose of normalizing the PDF used in fitting the experimental $\omega\pi^+\pi^-\pi^\circ$ data set, several thousand Monte Carlo (MC) events were generated. These events had the four final state particles distributed according to four body phase space. The events undergo a complete detector simulation and are passed through the same analysis procedure as are the experimental data, and thus the distribution of the MC events passing into the final stage of analysis contains the acceptance information. The normalization integral is then computed as:

$$\int \mu d\Omega \rightarrow \sum_{j=1}^{N_{MC}} \mu_j.$$

The sum of μ_i over the MC events approximates the weighted integral over the domain of μ_i; the weighting is that of the density of states and of detection efficiency. The density of states weighting is achieved by generating the MC events with such a distribution. Since the MC events are treated in the same way as are the experimental events, detection efficiency is unity for those events which survive the analysis cuts and zero for those which do not.

11.1.1 The Fitting Algorithm

The main elements of the PDF are the dynamical weight functions, $W(\{\theta,\phi\})$, described in Section 11.2. They are the complex amplitude matrices for a proposed decay chain to produce a given event, and are the products of the helicity and the kinematic amplitudes. For a given set of proposed masses and widths of the resonances involved in the decay chain, the dynamical weight function for a given event is fixed. For this reason, the fitting algorithm consists of choosing a set of masses and widths and allowing the computer program to find a set of weights and phases

for the decay chains. The masses and widths can then be scanned "by hand" to find appropriate values.

11.1.1.1 Computed Once for a Given Set of Masses and Widths

First, a specified number, N_D, of experimental data events are read from a file, and $A^D_{a,i}$ is computed for each event and each decay chain. It is the amplitude matrix for event i in decay chain a. Similarly, $A^M_{a,i}$ is computed for each of the N_M Monte Carlo events which are also read. The phase space weights, ϕ^D_i and ϕ^M_i, for the events are also read and stored. These always have a value of one in the analysis scheme used on the data set considered here. The sums of these weights are Φ^D and Φ^M. After all of the events have been read, the first normalization is prepared. For each decay chain a, the sum of the weighted squared amplitudes is computed:

$$\alpha_a = \frac{\sum_{i=1}^{N_M} \phi^M_i}{\sum_{i=1}^{N_M} \phi^M_i |A^M_{a,i}|^2} \equiv \frac{\Phi^M}{\mathcal{N}_a}.$$

Note that α_a, Φ^D, Φ^M and $\mathcal{N}_a$ will not depend on the values of the fit parameters.

11.1.1.2 Each Iteration

On each iteration of the fit, the fit parameters change, and a normalization for that particular set of parameters is needed. The parameters to be fit consist of a strength b_a and phase ϕ_a for each decay chain a:

$$\xi_a = b_a e^{i\phi_a},$$

which are then normalized by the sum over phase space for that channel:

$$\xi_a \to \xi_a \cdot \sqrt{\alpha_a} = b_a e^{i\phi_a} \cdot \sqrt{\frac{\sum_{i=1}^{N_M} \phi^M_i}{\sum_{i=1}^{N_M} \phi^M_i |A^M_{a,i}|^2}}.$$

This makes for a more stable fit when using MINUIT, the minimization program. The decay chains in the fit proceed from given initial states I (states of the $\bar{p}p$ atom which annihilates.) All decay chains from any one initial state interfere with one another. A coherent sum over phase space of the N_I amplitudes which are allowed to interfere can then be computed for each initial state I:

$$\mathcal{W}^M_{I,i} = \left| \sum_{a=1}^{N_I} \sqrt{\alpha_a} b_a e^{i\phi_a} A^M_{a,i} \right|^2.$$

The sums of these weights over Monte Carlo events are computed and are used in normalization:

$$\mathcal{S}_I = \frac{\Phi^M}{\sum_{i=1}^{N_M} \mathcal{W}^M_{I,i}}.$$

The value of $\mathcal{S}_I$ depends on the fit parameters b_a and ϕ_a, and must therefore be recomputed each time they are changed. Now the normalized probability density function, for each initial state, can be computed for the experimental data events:

$$\mathcal{W}^D_{I,i} = \left| \sum_{a=1}^{N_I} \sqrt{\alpha_a} \sqrt{\mathcal{S}_I} b_a e^{i\phi_a} A^D_{a,i} \right|^2 .$$

Additional fitting parameters, d_I, specify the relative abundances of the initial states. The full probability density function includes all of the N_k initial states under consideration:

$$w_i = \sum_{I=1}^{N_k} \mathcal{W}^D_{I,i} d_I \quad (\sum d_I = 1),$$

but to simplify the discussion, suppose only one initial state I is to be considered. Then $w_i = \mathcal{W}^D_{I,i}$. The quantity to be minimized is:

$$\begin{aligned} -2\ln\mathcal{L} &= -2\sum_{i=1}^{N_D} \ln\left(w_i\right) \\ &= -2\sum_{i=1}^{N_D} \ln\left(\left| \sum_{a=1}^{N_I} \frac{b_a e^{i\phi_a}}{\sqrt{N_a}} A^D_{a,i} \right|^2 \cdot \frac{\Phi^M}{\sum_{j=1}^{N_M} \left| \sum_{c=1}^{N_I} \frac{b_c e^{i\phi_c}}{\sqrt{N_c}} A^M_{c,j} \right|^2} \right) \\ &\sim -2\sum_{i=1}^{N_D} \ln\left(\frac{\Phi^M \mu_{I,i}}{\int \mu_I d\Omega} \right) \qquad \text{where} \qquad \mu_{I,i} = \left| \sum_{a=1}^{N_I} \frac{b_a e^{i\phi_a}}{\sqrt{N_a}} A_{a,i} \right|^2 \end{aligned}$$

This is the sum over data points of the negative logarithm of the normalized PDF. The integral of the PDF over phase space is Φ^M, which is independent of the fit parameters as required.

Now suppose that more than one initial state is allowed. For each initial state I there is an unnormalized PDF $\mu_{I,i}$, and

$$-2\ln\mathcal{L} = -2\sum_{i=1}^{N_D} \ln\left(P(\{x_i\})\right) = -2\sum_{i=1}^{N_D} \ln\left(\sum_I d_I \frac{\Phi^M \mu_{I,i}}{\int \mu_I d\Omega} \right)$$

and

$$P(\{x_i\}) = \sum_I d_I \frac{\Phi^M \mu_{I,i}}{\int \mu_I d\Omega}, \quad \Rightarrow \quad \int P(\{x_i\}) = \Phi^M \sum_I d_I = \Phi^M.$$

The normalization condition is satisfied. The parameters b_a, ϕ_a, and d_I are varied until a set is found which minimizes the value of $-2\ln\mathcal{L}$.

11.2 Helicity Amplitudes

The *helicity formalism* [41, 42] is used in calculating amplitudes concerning the angular distributions of the final state particles. It is convenient because the helicity operator $\lambda = \vec{s} \cdot \vec{p}$ is invariant under both rotations and Lorentz boosts along $\vec{p}$.

Consider the decay of system α, with angular momentum J and projection M onto the z-axis, into particles a and b with spins s_a and s_b, helicities λ_a and λ_b, and relative orbital angular momentum L. In the center of mass the state vector of α is $|J, M\rangle$, and a and b have momenta $\vec{p_f}$ and $-\vec{p_f}$. The amplitude for the decay is

$$\mathcal{H}_{(\lambda_a,\lambda_b),M}(\vec{p_f}) \;=\; \langle \vec{p_a} = \vec{p_f},\, \lambda_a,\, \vec{p_b} = -\vec{p_f},\, \lambda_b | U | J, M \rangle,$$

where U is the time evolution operator which propagates the initial state through the decay. The final state wave function is written as a *two particle plane wave helicity state*, which is the direct product of the one particle helicity states for a and b. Since the decay products are back-to-back with momentum $|\vec{p_f}|$, the final state can be written in terms of the direction, $\hat{n}(\theta_a, \phi_a)$ of particle a:

$$\mathcal{H}_{(\lambda_a,\lambda_b),M}(\theta_a, \phi_a) = \langle \theta_a, \phi_a, \lambda_a, \lambda_b | U | J, M \rangle,$$

where $|\vec{p_f}|$ is suppressed since it is fixed.

Now define a set of two-particle states $|j, m, \lambda_a, \lambda_b\rangle$ which have total angular momentum j with projection m along the decay axis $\hat{n}(\theta_a, \phi_a)$. A complete set of states can be inserted into the expression for the amplitude:

$$\begin{aligned}
\mathcal{H}_{(\lambda_a,\lambda_b),M}(\theta_a, \phi_a) &= \sum_{j,m} \langle \theta_a, \phi_a, \lambda_a, \lambda_b | j, m, \lambda_a, \lambda_b \rangle \langle j, m, \lambda_a, \lambda_b | U | J, M \rangle \\
&= \sum_{j,m} \langle \theta_a, \phi_a, \lambda_a, \lambda_b | j, m, \lambda_a, \lambda_b \rangle \delta_{j,J} \delta_{m,M} \langle \lambda_a, \lambda_b | M \rangle \\
&= \langle \theta_a, \phi_a, \lambda_a, \lambda_b | J, M, \lambda_a, \lambda_b \rangle T_{\lambda_a,\lambda_b}. \qquad (11.1)
\end{aligned}$$

$T_{\lambda_a,\lambda_b} = \langle \lambda_a, \lambda_b | M \rangle$ is written without M dependence since it must be rotationally invariant. Now let $\lambda = \lambda_a - \lambda_b$; it is the projection of the final state spin onto the decay axis. The first factor in equation 11.1, $\langle \theta_a, \phi_a, \lambda_a, \lambda_b | J, M, \lambda_a, \lambda_b \rangle$, is the amplitude for α to have spin projection λ along the decay axis. To determine this, consider the state $|j, m\rangle$ written in terms of a set of basis vectors with quantization along the z'-axis, in a coordinate system which is rotated with respect the the original one by Euler angles (α, β, γ):

$$|j, m\rangle = \sqrt{\frac{2j+1}{4\pi}} \sum_{m'=-j}^{j} \mathcal{D}^{*j}_{m,m'}(\alpha, \beta, \gamma), \text{ where } \mathcal{D}^{j}_{m,m'}(\alpha, \beta, \gamma) = e^{-i\alpha m} d^{j}_{m,m'}(\beta) e^{-i\gamma m'},$$

and the d-function is given by the Wigner formula:

$$\begin{aligned}
d^{j}_{m,m'}(\beta) \;=\; & \sum_{n} \left\{ \frac{(-1)^n \sqrt{(j+m')!(j-m')!(j+m)!(j-m)!}}{(j-m-n)!(j+m'-n)!(n+m-m')!n!} \right. \\
& \left. \times \left(\cos\frac{\beta}{2}\right)^{2j+m'-m-2n} \left(-\sin\frac{\beta}{2}\right)^{m-m'+2n} \right\}.
\end{aligned}$$

The amplitude for α to have spin projection λ along the decay axis $\hat{n}(\theta_a, \phi_a)$ is

$$\langle \theta_a, \phi_a, \lambda_a, \lambda_b | J, M, \lambda_a, \lambda_b \rangle = \sqrt{\frac{2J+1}{4\pi}} \frac{1}{\sqrt{2L+1}} \mathcal{D}^{*J}_{M,\lambda}(\phi_a, \theta_a, 0).$$

The choice of zero for the third argument of the $\mathcal{D}$-function is a matter of convention, and has no physical meaning; it will be dropped from the notation. The amplitude for the decay is then

$$\mathcal{H}_{\{\lambda_a,\lambda_b\},M}(\theta_a, \phi_a) = \sqrt{\frac{2J+1}{4\pi}} \frac{1}{\sqrt{2L+1}} \mathcal{D}^{*J}_{M,\lambda}(\phi_a, \theta_a) T_{\lambda_a,\lambda_b}.$$

T_{λ_a,λ_b} is the coupling of the angular momentum in the final state to $|J, \lambda\rangle$; this includes the spins $\vec{s}_a$ and $\vec{s}_b$, and $\vec{L}_{ab}$, the relative orbital angular momentum between a and b. Since $\vec{L} = \vec{r} \times \vec{p}$ is perpendicular to $\vec{p}$, its projection onto the decay axis is zero. T_{λ_a,λ_b} is expressed as the Clebsch-Gordan coefficients coupling $\vec{s}_a$ and $\vec{s}_b$ to total spin $\vec{s}_{(ab)}$, and the coupling of $\vec{s}_{(ab)}$ and $\vec{L}_{ab}$ to $\vec{J}$:

$$T_{\lambda_a,\lambda_b} = \langle s_a \lambda_a; s_b \lambda_b | s, \lambda \rangle \langle L_{ab}, 0; s_{ab}, \lambda | J, \lambda \rangle.$$

The angular probability distribution function for the decay axis, for the decay from magnetic substate M, is the amplitude squared summed over the final state helicities, since they are not observed:

$$W_M(\theta_a, \phi_a) = \sum_{\lambda_a,\lambda_b} \mathcal{H}_{\{\lambda_a,\lambda_b\},M}(\theta_a, \phi_a) \mathcal{H}^*_{\{\lambda_a,\lambda_b\},M}(\theta_a, \phi_a).$$

If the population of the initial magnetic substates is described by the spin density matrix ρ, then

$$W(\theta_a, \phi_a) = \sum_{M,\mu} \sum_{\lambda_a,\lambda_b} \mathcal{H}_{\{\lambda_a,\lambda_b\},M}(\theta_a, \phi_a)\ \rho_{M,\mu}\ \mathcal{H}^*_{\{\lambda_a,\lambda_b\},\mu}(\theta_a, \phi_a).$$

Now suppose that one of the decay products of α subsequently decays, $a \to bc$, with decay axis along $\hat{n}(\theta_c, \phi_c)$ in the rest frame of a. Then the full amplitude is the product of the amplitudes for the individual decays, summed over the unobservable helicity of a:

$$\mathcal{H}_{\{\lambda_b,\lambda_c,\lambda_d\},M}(\theta_a, \phi_a, \theta_c, \phi_c) = \sum_{\lambda_a} \mathcal{H}_{\{\lambda_c,\lambda_d\},\lambda_a}(\theta_c, \phi_c) \mathcal{H}_{\{\lambda_a,\lambda_b\},M}(\theta_a, \phi_a).$$

Here, the z-axis in the rest frame of a is taken to be the line of flight of a, so that its spin projection s_z is its helicity λ_a. Subsequent decays of b, c or d are handled similarly.

The initial state $\bar{p}p$ atom is assumed to decay from either ${}^1S_0$ or ${}^3S_1$, but its magnetic substate is not measured, and the atom is taken to be unpolarized. For ${}^1S_0$,

only $M = 0$ is allowed; for ${}^3S_1$ the three states $M = -1, 0, 1$ are equally populated and the initial spin density matrix is $1/3$ times the identity matrix:

$$\rho({}^3S_1) = \begin{pmatrix} \frac{1}{3} & 0 & 0 \\ 0 & \frac{1}{3} & 0 \\ 0 & 0 & \frac{1}{3} \end{pmatrix}.$$

The only spin in the final state is that of the photon from the ω decay, with spin $s = 1$, and only $\lambda = \pm 1$ are allowed so the total amplitude for a decay chain is specified by $\mathcal{H}_{\lambda_\gamma, M}(\{\theta, \phi\})$. The angular probability distribution function is

$$W(\{\theta, \phi\}) = \sum_{\lambda_\gamma} \sum_{M,\mu} \mathcal{H}_{\lambda_\gamma, M}(\{\theta, \phi\})\ \rho_{M,\mu}\ \mathcal{H}^*_{\lambda_\gamma, \mu}(\{\theta, \phi\}) = \frac{1}{3} \sum_{\lambda_\gamma, M} \left| \mathcal{H}_{\lambda_\gamma, M} \right|^2.$$

The computation of the directions of decay products in the rest frame of a decaying resonance α, with its momentum in the direction $\hat{n}(\theta, \phi)$, is as follows: the 4-momentum of the resonance is determined from the sum of the 4-momenta of the decay products: $p_\alpha = p_a + p_b$. A vector $\vec{\beta}$ can be formed: $\vec{\beta} = \vec{p}_\alpha / E_\alpha$, and the familiar relativistic quantities are calculated: $\beta = |\vec{\beta}|$ and $\gamma = (1 - \beta^2)^{-1/2}$. The 4-momenta of the decay products are then rotated and boosted into the rest frame of α:

$$\begin{pmatrix} p'_x \\ p'_y \\ p'_z \\ E' \end{pmatrix} = \begin{pmatrix} 1 & 0 & 0 & 0 \\ 0 & 1 & 0 & 0 \\ 0 & 0 & \gamma & -\beta\gamma \\ 0 & 0 & -\beta\gamma & \gamma \end{pmatrix} \begin{pmatrix} \cos\theta\cos\phi & \cos\theta\sin\phi & \cos\theta\sin\theta & 0 \\ -\sin\phi & \cos\phi & 0 & 0 \\ \sin\theta\cos\phi & \sin\theta\sin\phi & \sin\theta\cos\theta & 0 \\ 0 & 0 & 0 & 1 \end{pmatrix} \begin{pmatrix} p_x \\ p_y \\ p_z \\ E \end{pmatrix}$$

11.3 Kinematic Amplitudes

11.3.1 Breit-Wigners

The kinematic amplitudes $\mathcal{K}$ for resonances are described by a relativistic Breit-Wigner function:

$$\mathrm{BW}_r = \frac{m_0 \Gamma_0}{m_0^2 - m^2 - i m_0 \Gamma(m)} \frac{F_L(z)}{F_L(z_0)} \quad \text{where} \quad \Gamma(m) = \Gamma_0 \frac{\rho(m)}{\rho(m_0)} \frac{F_L^2(z)}{F_L^2(z_0)}.$$

Γ_0 and m_0 are the width and central mass of the resonance, and m is the invariant mass of the decay products. $\Gamma(m)$ is the *mass dependent width*, and models the variation in the coupling to the decay channel with the kinematic density of states, $\rho(m)$, and the centrifugal barrier, $F_L(z)$ (see below.) The quantity z is proportional to the square of the momentum, q, of the decay products in the COM:

$$z = \frac{q^2}{p_R^2}\ ;\ q^2(m) = \frac{(m^2 - (m_b + m_c)^2)\,(m^2 - (m_b - m_c)^2)}{4m^2},$$

where m_b and m_c are the masses of the decay products. The value of p_R is $197.3 MeV/c$, corresponding to a size of $1fm$ for the decaying resonance.

For resonances which decay into other resonances, the sum of the masses of the decay products can be greater than the central mass of the resonance. In this case, $q^2(m_0)$ is negative, which causes a problem for calculating $\rho(m_0)$ and $F_L(z_0)$. For example, in the decay $a_0(1450) \rightarrow \omega\rho$, if the mass of the $\pi\pi$ pair comprising the ρ is greater than $670 MeV/c^2$, this issue arises. For such resonances, where $a \rightarrow bc$, $c \rightarrow de$, the value for m_c in the above equation for $q^2(m)$ is replaced by $m_d + m_e$. Figure 11.2 shows comparisons of the relativistic and non-relativistic Breit-Wigner

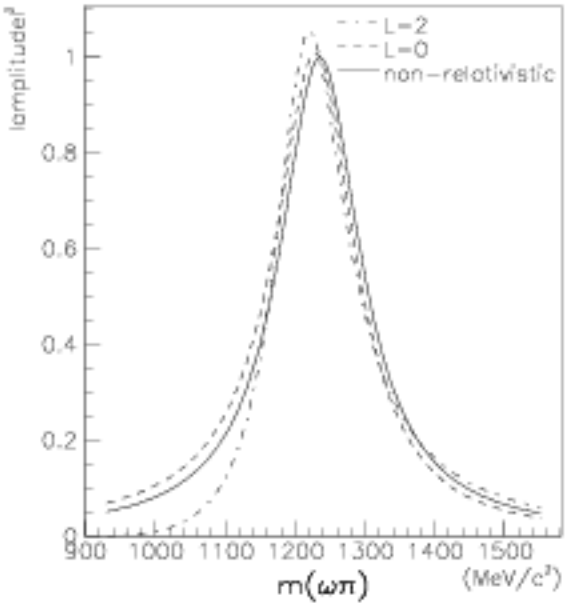

Figure 11.2: The squares of the non-relativistic and relativistic Breit-Wigner functions for $b_1(1235) \rightarrow \omega\pi$. The relativistic version is shown for $L = 0$ and $L = 2$ (L is the orbital angular momentum of the ω and π.) The asymmetry of the relativistic functions is due to the phase space and centrifugal barrier factors.

functions. The non-relativistic function is:

$$|\mathrm{BW}_{nr}|^2 = \left| \frac{\Gamma_0/2}{m_0 - m - i\Gamma_0/2} \right|^2 ,$$

The asymmetry in the relativistic function reflects the variation in $\Gamma(m)$.

11.3.1.1 Centrifugal Barriers

The functions $F_L(z)$ account for the centrifugal barrier present which depends on the orbital angular momentum between the decay products and on their relative linear

momentum. The dependence is correlated in a simple way with the semi-classical *impact parameter:*

$$b = \sqrt{L(L+1)}/q.$$

The functions are those specified by von Hippel and Quigg in reference [43]. The model assumes that phase space and centrifugal effects dominate the reaction for particle separation r greater than a constant *interaction radius*, R. The dynamics of the decay occur for $r < R$. Defining $\rho = kr$, the radial probability density for the outgoing wave is

$$[T_L(q)]^{-1} \equiv \rho^2 \left| h_L^{(1)}(\rho) \right|^2$$

times that at infinity. As such, $T_L(q)$ can be regarded as the transmission coefficient through the centrifugal barrier outside of R. Here, $h_L^{(1)}(\rho)$ is the spherical Hankel function of the first kind. This transmission coefficient is multiplied by the nominal decay width to correct for the centrifugal barrier. For this purpose, $F_L^2(z) = T_L(q)$, and the function is divided by its value at $q(m_0)$ in order to avoid scaling the value of Γ_0, thereby approximately maintaining its meaning as the full width at half maximum. The formulas for the functions $F_L(z)$ are:

$$\begin{aligned}
F_0(z) &= 1 \\
F_1(z) &= \sqrt{\frac{2z}{z+1}} \\
F_2(z) &= \sqrt{\frac{13z^2}{(z-3)^2+9z}} \\
F_3(z) &= \sqrt{\frac{277z^3}{z(z-15)^2+9(2z-5)^2}}
\end{aligned}$$

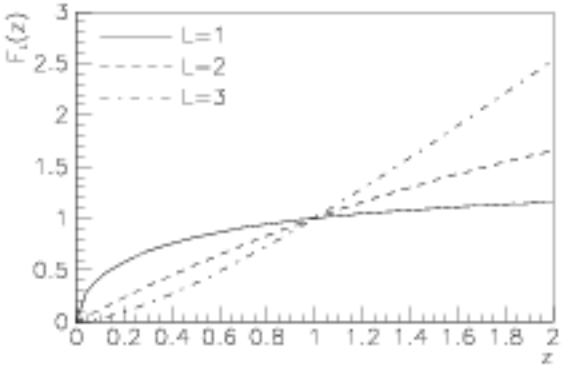

Figure 11.3 shows the behavior of the centrifugal barrier functions for selected decay channels.

11.3.1.2 Phase Space Factors

The phase space factor, $\rho(m) = q/2m$, is proportional to the kinematic density of states, and is derived from the Lorentz invariant phase space integral for two-body decay. This factor allows for a coupling to the decay channel which varies with the density of states available. It is normalized by $\rho(m_0)$ so that the value at the central mass is unity. Figure 11.4 shows $\rho(m)$ for selected decay channels.

11.3.2 Voigtian

The ω peak in the $\pi^+\pi^-\pi^\circ$ mass spectrum requires special care when fitting; the Breit-Wigner width of $8.43 MeV/c^2$ is similar in magnitude to the resolution of the

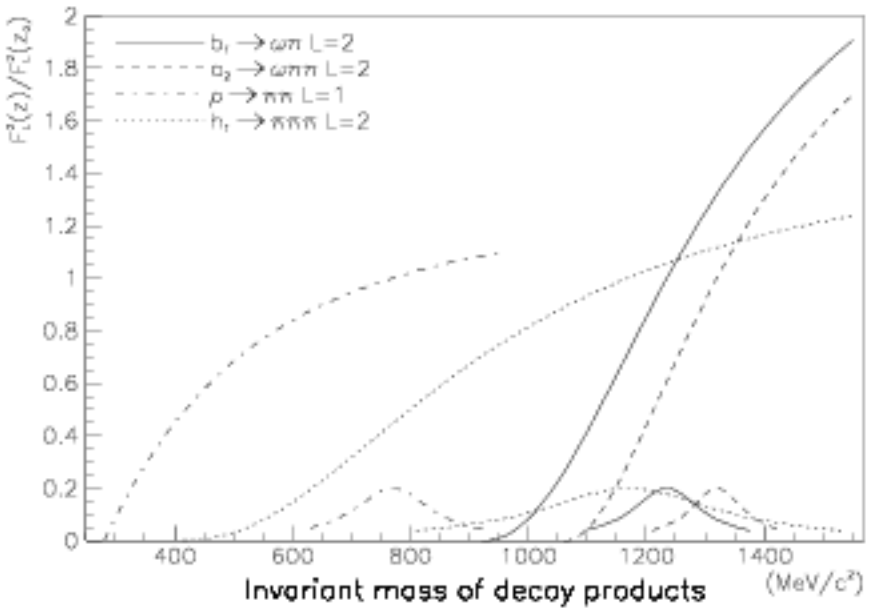

Figure 11.3: The centrifugal barrier factor, $F_L^2(q)/F_L^2(q_0)$, for several specific resonance decays. The Breit-Wigner functions for the decays are shown (scaled down) to illustrate the variation of the centrifugal barrier functions over the width of the resonance.

detector system ($\sigma \sim 10 MeV/c^2$). The peak is fitted with a *Voigtian* function, which is a non-relativistic Breit-Wigner convoluted with a Gaussian resolution function:

$$V(m) = C \int_{-\infty}^{+\infty} \frac{1}{\sqrt{2\pi}\sigma} e^{-\frac{x^2}{2\sigma}} \frac{\Gamma^2/4}{(m - m_0 - x)^2) + \Gamma^2/4} dx. \tag{11.2}$$

C is a scaling parameter and σ is the variance of the Gaussian. This integral can be evaluated analytically [46]:

$$V(m) = C \frac{\sqrt{2\pi}}{4} \frac{\Gamma}{\sigma} \mathrm{Re}[\omega(v + ia)] \quad \text{where} \quad v = \frac{m - m_0}{\sqrt{2}\sigma} \quad \text{and} \quad a = \frac{\Gamma}{2\sqrt{2}\sigma}.$$

$\omega(z)$ is the complex error function, for which a computer algorithm is readily available [44, 45].

In the partial wave analysis, the kinematic amplitude $\mathcal{K}(\omega \rightarrow \pi^+\pi^-\pi^\circ)$ for the decay of the ω into three pions is the square root of the Voigtian function.

To count the number of events in the peak, Equation 11.2 can be integrated over m:

$$\int_{-\infty}^{+\infty} V(m) dm = C \frac{\pi}{2} \Gamma$$

Figure 11.5 shows $V(m)$ for a fit to the $\omega \rightarrow \pi^+\pi^-\pi^\circ$ peak. Also shown are Gaussian

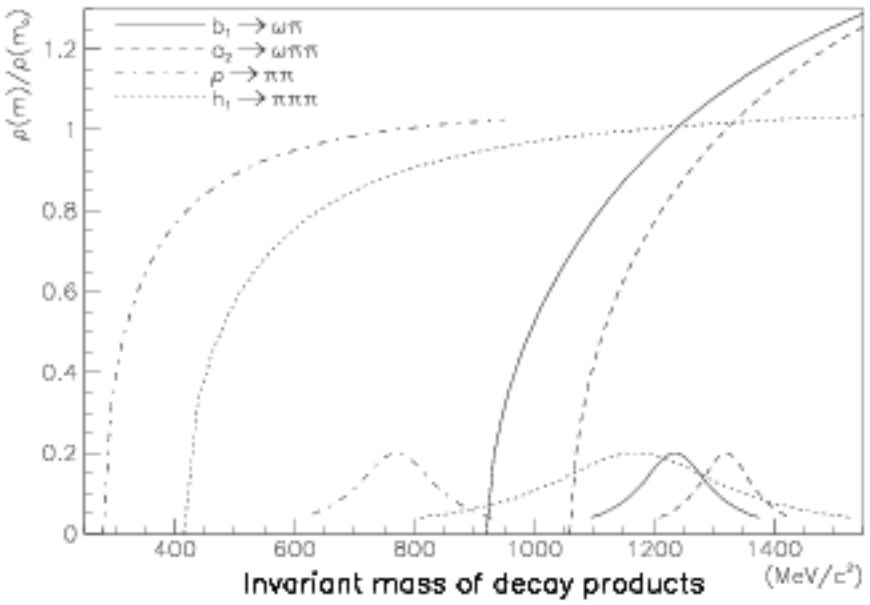

Figure 11.4: The normalized phase space factors for several specific resonance decays. The Breit-Wigner functions for the decays are shown (scaled down) to illustrate the variation of the phase space factors over the width of the resonance.

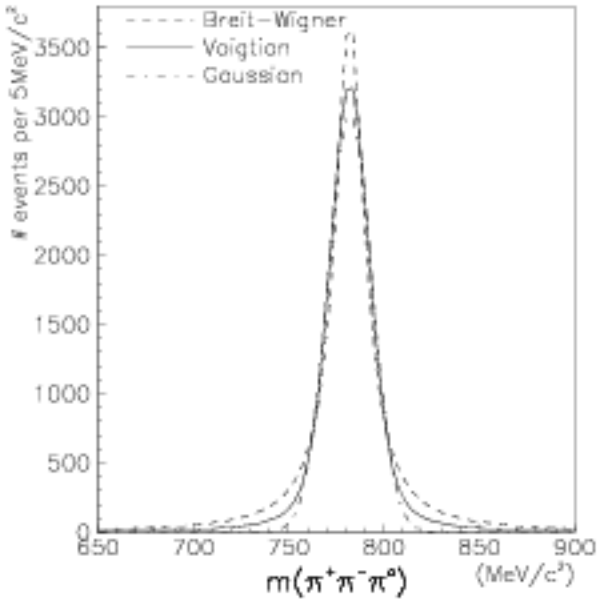

Figure 11.5: Comparison of the Voigtian function to a Gaussian and a Breit-Wigner function. Each was fitted to the ω peak in the $\pi^+\pi^-\pi^0$ mass spectrum in the $\bar{p}p \rightarrow \pi^+\pi^-\pi^0\omega$ data set.

and Breit-Wigner functions which were also fit to the peak. The Voigtian includes the long Breit-Wigner tails which are not well represented by the Gaussian. The fit using only a Breit-Wigner required a large value for Γ_0 in order to account for the broadening due to resolution.

11.3.3 $\pi\pi$ $S-wave$ Amplitudes

When two pions are produced in an $I = 0$ *S-wave*, as in $\omega(1600) \to \omega(\pi\pi)_s$ for example, the amplitude describing the breakup of the $\pi\pi$ system is an empirical parameterization derived from an analysis of $\pi\pi$ and $K\bar{K}$ data. This amplitude depends only on the invariant mass of the $\pi\pi$ pair. The parameterization is valid for

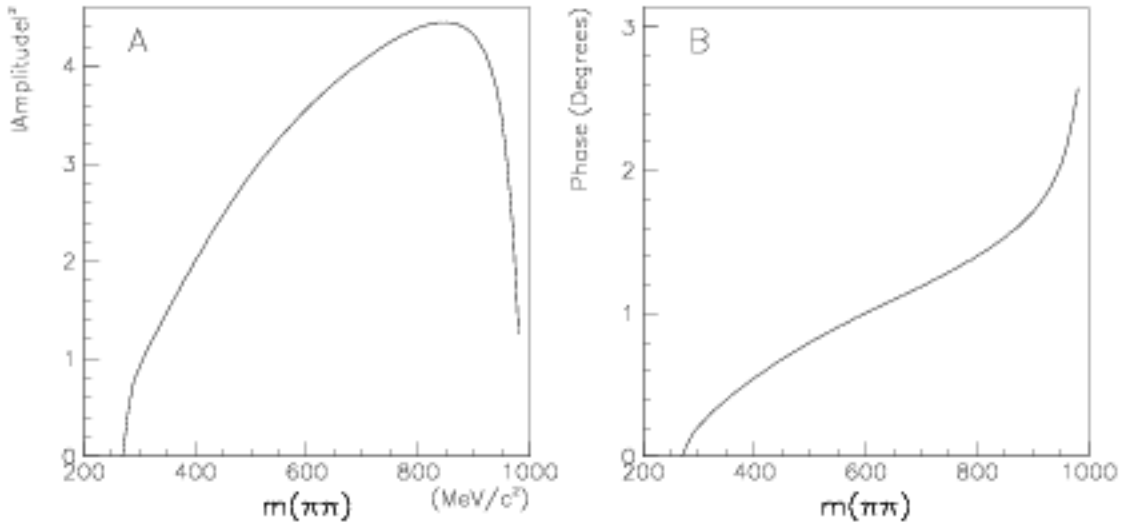

Figure 11.6: The $(\pi\pi)_s$ parameterization which is used in the PWA fits. Plot A shows the square of the $(\pi\pi)_s$ amplitude versus the invariant mass of the $\pi\pi$ pair. Plot B shows the phase of the amplitude.

$\pi\pi$ masses in the range $270 MeV/c^2$ to $1800 MeV/c^2$, though the maximum $\pi\pi$ mass in $\bar{p}p \to \pi^+\pi^-\pi^\circ\omega$ is about $960 MeV/c^2$. Figure 11.6 shows the behavior of the $(\pi\pi)_s$ amplitude.

11.4 Isospin Combinations

Many of the decay chains to be considered can proceed via several isospin combinations; for example, $\bar{p}p$ annihilation into $a_2\pi$ can proceed via $a_2^+\pi^-$, $a_2^\circ\pi^\circ$ and $a_2^-\pi^+$. When this reaction occurs from the $^1S_0$ state of antiprotonium, the system is in an isospin $I = 0$ state (see Section 11.5); the a_2 and π both have $I = 1$, so their coupling

to the initial $I = 0$ state is

$$\begin{aligned} |0,0\rangle &= +\sqrt{\tfrac{1}{3}}\,|1,+1;1,-1\rangle - \sqrt{\tfrac{1}{3}}\,|1,0;1,0\rangle + \sqrt{\tfrac{1}{3}}\,|1,-1;1,+1\rangle \\ &= +\sqrt{\tfrac{1}{3}}\,|a_2^+\pi^-\rangle - \sqrt{\tfrac{1}{3}}\,|a_2^\circ\pi^\circ\rangle + \sqrt{\tfrac{1}{3}}\,|a_2^-\pi^+\rangle. \end{aligned}$$

In the fitting procedure, an amplitude for each of these processes is computed, and they are allowed to interfere with fixed relative strengths and phases by adding their amplitudes weighted by the isospin coupling Clebsch-Gordan coefficients. To ensure proper phases when computing $\langle I^{(\text{total})}, I_z^{(\text{total})} | I^{(1)}, I_z^{(1)}; I^{(2)}, I_z^{(2)} \rangle$, particle 1 must the particle whose angles are used in the $\mathcal{D}$ functions for the helicity amplitudes (see Section 11.2.)

For subsequent decays, the isospin vector coupling coefficients are multiplied by those from the parent reactions. If the a_2 decays to $b_1\pi$ (both of which are isospin 1),

$$\begin{aligned} |a_2^+\rangle &= +\sqrt{\tfrac{1}{2}}\,|b_1^+\pi^\circ\rangle - \sqrt{\tfrac{1}{2}}\,|b_1^\circ\pi^+\rangle \\ |a_2^\circ\rangle &= +\sqrt{\tfrac{1}{2}}\,|b_1^+\pi^-\rangle - \sqrt{\tfrac{1}{2}}\,|b_1^-\pi^+\rangle \\ |a_2^-\rangle &= +\sqrt{\tfrac{1}{2}}\,|b_1^\circ\pi^-\rangle - \sqrt{\tfrac{1}{2}}\,|b_1^-\pi^\circ\rangle. \end{aligned}$$

So the six decay chains and their coefficients are:

$$\begin{aligned} \bar{p}p(\,^1S_0) \to a_2^+\pi^-,\quad a_2^+ \to b_1^+\pi^\circ &: +\sqrt{\tfrac{1}{3}} \times +\sqrt{\tfrac{1}{2}} = +\sqrt{\tfrac{1}{6}} \\ \bar{p}p(\,^1S_0) \to a_2^+\pi^-,\quad a_2^+ \to b_1^\circ\pi^+ &: +\sqrt{\tfrac{1}{3}} \times -\sqrt{\tfrac{1}{2}} = -\sqrt{\tfrac{1}{6}} \\ \bar{p}p(\,^1S_0) \to a_2^\circ\pi^\circ,\quad a_2^\circ \to b_1^+\pi^- &: -\sqrt{\tfrac{1}{3}} \times +\sqrt{\tfrac{1}{2}} = -\sqrt{\tfrac{1}{6}} \\ \bar{p}p(\,^1S_0) \to a_2^\circ\pi^\circ,\quad a_2^\circ \to b_1^-\pi^+ &: -\sqrt{\tfrac{1}{3}} \times -\sqrt{\tfrac{1}{2}} = +\sqrt{\tfrac{1}{6}} \\ \bar{p}p(\,^1S_0) \to a_2^-\pi^+,\quad a_2^- \to b_1^\circ\pi^- &: +\sqrt{\tfrac{1}{3}} \times +\sqrt{\tfrac{1}{2}} = +\sqrt{\tfrac{1}{6}} \\ \bar{p}p(\,^1S_0) \to a_2^-\pi^+,\quad a_2^- \to b_1^-\pi^\circ &: +\sqrt{\tfrac{1}{3}} \times -\sqrt{\tfrac{1}{2}} = -\sqrt{\tfrac{1}{6}} \end{aligned}$$

11.5 Allowed States and Decays

As stated before, in the model for PWA fitting, the quantum numbers I, G, J, P and C are conserved in all resonance decays and in the $\bar{p}p$ annihilation; this restricts the set of reactions which are allowed to occur. Tables 11.1 and 11.2 list the quantum numbers of antiprotonium and of the mesons which are germane to this analysis.

G-parity is a multiplicative quantum number. for the $\pi^+\pi^-\pi^\circ\omega$ final state, $G = G_{\pi^+}G_{\pi^-}G_{\pi^\circ}G_\omega = (-1)\cdot(-1)\cdot(-1)\cdot(-1) = +1$. To have positive G-parity in the initial state,the isospin for $^1S_0$ must be $I = 0$, and for $^3S_1$, $I = 1$ (see Table 11.1.)

$^{2s+1}L_J$	J^{PC}	I^G
$^1S_0$	0^{-+}	$\mathbf{0^+}, 1^-$
$^3S_1$	1^{--}	$0^-, \mathbf{1^+}$
$^1P_1$	1^{+-}	$0^-, \mathbf{1^+}$
$^3P_0$	0^{++}	$\mathbf{0^+}, 1^-$
$^3P_1$	1^{++}	$\mathbf{0^+}, 1^-$
$^3P_2$	2^{++}	$\mathbf{0^+}, 1^-$

Table 11.1: Quantum numbers of the S and P states of antiprotonium. The $I = \frac{1}{2}$, $I_z = +\frac{1}{2}$ proton and the $I = \frac{1}{2}$, $I_z = -\frac{1}{2}$ antiproton can couple to total isospin of 0 or 1; the G-parity is $(-1)^{L+s+I}$. Both combinations of I^G are shown for each state of antiprotonium. The $\pi^+\pi^-\pi^\circ\omega$ final state has $G = +1$ (see text).

Name	$I^G J^{PC}$
π	1^-0^{-+}
η	0^+0^{-+}
ρ	1^+1^{--}
$(\pi\pi)_s$	0^+0^{++}
ω	0^-1^{--}
ω_3	0^-3^{--}
h_1	0^-1^{+-}
b_1	1^+1^{+-}
a_0	1^-0^{++}
a_1	1^-1^{++}
a_2	1^-2^{++}

Table 11.2: Quantum numbers of resonances germane to this analysis.

The requirement is that $G_a = G_b \cdot G_c$. So, for the reaction $\bar{p}p(^3S_1) \to a_2(1320)\pi$, the G-parity of the final state is $(-1) \cdot (-1) = +1$, so the antiprotonium must be in the $I^G = 1^+$ state.

Consider the reaction $a \to bc$. For isospin (I) conservation, the triangular condition must be met: $I_a \leq I_b + I_c$. For example $\omega(1420) \not\to \omega\rho$ because $I = 0$ in the initial state and $I = 1$ in the final state. Additionally, the vector coupling (Clebsch-Gordan) coefficients between the initial and final states govern the relative strengths and phases among the decays to the various charge states of b and c, as demonstrated in Section 11.4. For example, $a_1(1260) \not\to \rho^\circ\pi^\circ$ because the Clebsch-Gordan coefficient coupling two $I = 1$, $I_z = 0$ mesons to an $I = 1$, $I_z = 0$ state is zero.

Total angular momentum J is composed of the spin of a in the initial state, and, in the final state, the spins of b and c and their relative orbital angular momentum L. The triangular condition is then $s_a \leq s_b + s_c + L$. The strengths and phases among the various polarization states are determined by the Clebsch-Gordan coefficients and are implemented in the $T_{\lambda_b\lambda_c}$ coefficients described in Section 11.2.

The parity (P) in the initial state is the intrinsic parity of state a. In the final state, it is the product of the intrinsic parities of b and c and the parity of their spatial wave function, $(-1)^L$. For the decay $b_1(1235) \to \omega\pi$, the parities are $(+1) \to (-1) \cdot (-1) \cdot (-1)^L$, so orbital angular momenta of $L = 0, 2$ are permitted.

C-parity is a good quantum number only for neutral states, and therefore imposes restrictions on all-neutral reactions. C is a multiplicative quantum number. For example, $\bar{p}p(^3S_1) \not\to a_2^0\pi^\circ$ because the C-parity of the initial state is -1, but in the final state C is $(+1) \cdot (+1) = +1$.

11.6 Histogram Filling

After finding an optimum set of parameters (b_a's, ϕ_a's and d_I's) for a proposed set of decay chains, histograms of mass spectra and angular distributions are filled to allow a visual comparison of the fit to the experimental data. For the MC data, each event is entered into the histograms with a weighting factor corresponding to the value of the PDF for that event.

$$\text{weighting factor for MC event } i = \frac{\Phi^D}{\Phi^M} \cdot \phi_i^M \cdot \sum_{i=1}^{N_k} d_I \left| \sum_{a=1}^{N_I} \sqrt{\alpha_a} \sqrt{\mathcal{S}_I} b_a e^{i\phi_a} A_{a,i}^M \right|^2 .$$

The first factor is to make the total contents of the MC histogram equal to that of the corresponding histogram for the experimental data. The MC histograms will then show the distributions of events which would result from the proposed set of decay chains.

11.7 Calculating Branching Fractions

The branching fraction, $\mathcal{B}_a$ of decay chain a in the data sample is the integral over phase space (i.e. the sum over the MC events) of the PDF for that decay chain:

$$\mathcal{A}_a = \sum_{i=1}^{N_M} \left| \sqrt{\alpha_a} \sqrt{\mathcal{S}_I} b_a e^{i\phi_a} A_{a,i}^M \right|^2 \cdot \phi_i^M .$$

This is normalized by the integral of the total PDF over phase space:

$$\omega^M = \sum_{i=1}^{N_M} \left(\sum_{I=1}^{N_k} d_I \left| \sqrt{\alpha_a} \sqrt{\mathcal{S}_I} b_a e^{i\phi_a} A_{a,i}^M \right|^2 \right) ,$$

and scaled by the strength, d_I, of the initial state from which the decay chain originates:

$$\mathcal{B}_a = \mathcal{A}_a \cdot d_I / \omega^M .$$

This computation ignores the interferences among the decay chains, so the sum of the $\mathcal{B}_a$'s will not be 100% (the interferences among the isospin combinations within a decay are retained, though.) An additional normalization is performed in order to make $\sum_a \mathcal{B}_a = 100\%$:

$$F_I = d_I / \sum_a \mathcal{B}_a, \ \mathcal{B}_a \to \mathcal{B}_a \cdot F_I,$$

where I is the initial state from which decay chain a originates.

11.8 How many events to use in the fits

Ultimately, one would like to use as many as possible of the experimental data and Monte Carlo events. Limitations on computer time and memory, however, make it advantageous to use smaller samples. Figure 11.7 shows the variation in the result

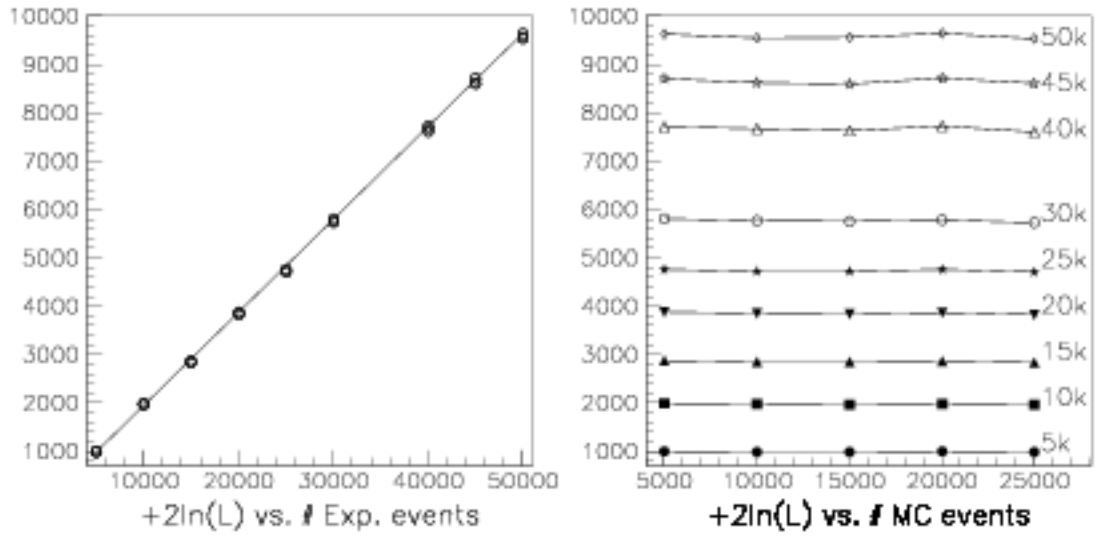

Figure 11.7: The effect on the fit result of the numbers of events used in a fit. A: The value of $2\ln(\mathcal{L})$ versus the number of experimental events. The expected linearity is observed. B: $2\ln(\mathcal{L})$ versus the number of MC events. The different symbols indicate fits using different numbers of experimental events. (The numbers of experimental data events are indicated to the right of each line.) There is no strong variation in the result with the number of events.

of running the fitting program with various numbers of events. The fit included only the decay chain $\bar{p}p \to \omega(1420)\pi$, with $\omega(1420) \to \omega(\pi\pi)_s\,(L = 0, 2)$, which at the time appeared to be the most significant contribution to the data set. The Monte Carlo events are used in computing normalizations only, so the value of $\ln(\mathcal{L})$ should not depend on the number of MC events used. Even with as few as 5000 MC events, the result of the fit remains very stable. The value of $\ln(\mathcal{L})$ is computed as a sum over the experimental events, so it should vary linearly with the number of events. This is the behavior which is exhibited in the figure. For most fits presented in the following chapter, 20000 MC and 20000 experimental events were used. This allowed fits to be done in a timely manner, making efficient use of computing resources, with confidence that statistical fluctuations would not significantly effect the results of the fits.

Chapter 12

The PWA Fits

In this chapter, the results of the partial wave analysis are presented. First, though, some information on what processes to expect to be present will be given, including what is known from previous measurements.

The process $\bar{p}p \to \omega\omega$ required special care in the PWA fits; the particulars of this channel are discussed in Section 12.2.

The PWA then begins with those processes which are most likely to contribute: known resonances in known decay modes. Additional processes are then added to the fits in order to improve the fits.

The $\pi^+\pi^-\pi^\circ\omega$ final state is produced in $16.1 \pm 1.0\%$ of $\bar{p}p$ annihilations at rest, so one should expect that many intermediate states will be needed in the fits. The complexity of the fitting procedure (and limited computing resources,) limit the number of processes which can be included in the fits, however, so only the large contributions will be detected.

12.1 The Most Likely Contributions

As modeled, three types of resonance production can occur: 1) a $\pi^+\pi^-\pi^\circ$ resonance produced along with an ω; 2) a $\omega\pi\pi$ resonance produced along with a π; 3) an $\omega\pi$ resonance produced along with a $\pi\pi$ system. The resonances expected in each of these three scenarios are discussed in the following sections.

12.1.1 $\bar{p}p \to \omega M,\ M \to \pi^+\pi^-\pi^\circ$.

The energy available to meson M is $m_{\bar{p}p} - m_\omega \simeq 1094 MeV$. Events with $M = \eta$ and $M = \omega$, requiring $782 MeV$ and $547 MeV$, are obvious in the data. The $\phi(1020)$ is known to decay to $\pi^+\pi^-\pi^\circ$ with a branching fraction of about 15% [1]. A measurement of $\bar{p}p \to \phi(1020)\omega$ was made in a bubble chamber experiment with the ϕ decaying to $K\bar{K}$ [47]. These data ($R(\bar{p}p \to \omega\phi) = (0.63 \pm 0.23) \times 10^{-3}$) indicate that $\phi(1020)\omega$ would be present in the $\pi^+\pi^-\pi^\circ\omega$ data set at the level of $< 0.1\%$, a very small

contribution. This, combined with the lack of a narrow peak in the $\pi^+\pi^-\pi^\circ$ mass spectrum at $1020 MeV$ led to the exclusion of this channel in the PWA fits.

The next lightest known 3π resonance is the $h_1(1170)$, whose central mass is greater than the available energy. It could be produced, however, due to its large width ($\Gamma \simeq 360 MeV/c^2$). Other possibilities for M are shown in Table 12.1. Of

Resonance M	$\Gamma\ (MeV)$	$I^G J^{PC}$	$\bar{p}p$ state
$h_1(1170)$	360	0^-1^{+-}	${}^1S_0\ (L=0)$
$a_1(1260)$	~ 400	1^-1^{++}	${}^3S_1\ (L=0,2)$
$\pi(1300)$	200 to 600	1^-0^{-+}	${}^3S_1\ (L=1)$
$a_2(1320)$	107	1^-2^{++}	${}^3S_1\ (L=0,2)$
$\omega(1420)$	174	0^-1^{--}	${}^1S_0\ (L=1)$

Table 12.1: Possible resonances in the $\pi^+\pi^-\pi^\circ$ channel. Shown for each resonance are its width, quantum numbers, and the $\bar{p}p$ S states from which it can be produced along with an ω. L is the orbital angular momentum between the resonance and the ω.

these channels, only $\bar{p}p \to \omega a_2(1320)$ has been observed, with a branching fraction of $BR(\bar{p}p \to a_2\omega) = (1.88 \pm 0.08 \pm 0.21)\%$ [48]. In $\pi^+\pi^-\pi^\circ\omega$ the a_2 will be seen in its $\rho\pi$ decay mode, which has a branching fraction of $BR(a_2(1320) \to \rho\pi) = 70.1 \pm 2.7\%$ [1]. Using the measured $BR(\bar{p}p \to \omega\pi^+\pi^-\pi^\circ) = 16.1 \pm 1.0\%$ (see Section 10.2), $a_2\omega$ should constitute $8.2 \pm 1.1\%$ of the $\omega\pi^+\pi^-\pi^\circ$ data set.

In keeping with the isobar model, these resonances decay to $\rho\pi$ or $\pi(\pi\pi)_s$. Isospin conservation determines whether or not these resonances can decay into $\rho^\circ\pi^\circ$: an $I = 1$ resonance cannot, because the Clebsch-Gordan coefficient for coupling two $|I, I_z\rangle = |1, 0\rangle$ states to a $|1, 0\rangle$ state is zero. Hence, $I = 1$ resonances, such as the $a_1(1260)$, can decay only via the charged mode, but $I = 0$ resonances such as the $h_1(1170)$ can decay into $\rho^\circ\pi^\circ$. Figure 12.1 shows a 3π Dalitz plot for events with $m(\pi^+\pi^-\pi^\circ) > 1000 MeV/c^2$. Bands in the $\pi^\pm\pi^\circ$ spectra are evident (though at masses less than that of the ρ), but such a band in the $\pi^+\pi^-$ spectrum is weak or absent. This may indicate that $I = 1$ resonances are the stronger contribution to the $\pi^+\pi^-\pi^\circ$ spectrum.

12.1.2 $\bar{p}p \to (\omega\pi)(\pi\pi)$

The strongest candidates for this type of process are $b_1\rho$ and $b_1(\pi\pi)_s$. The latter requires at least one unit of orbital angular momentum, and is therefore suppressed by the centrifugal barrier. Regarding the former, the central masses of the $b_1(1235)$ and ρ add up to more than the total energy available in $\bar{p}p$ annihilation at rest, but with both resonances having widths of $\Gamma \sim 150 MeV/c^2$, this process is possible, but would be suppressed by the restricted phase space available. It is no surprise therefore that no peak near the $b_1(1235)$ mass is observed in the data.

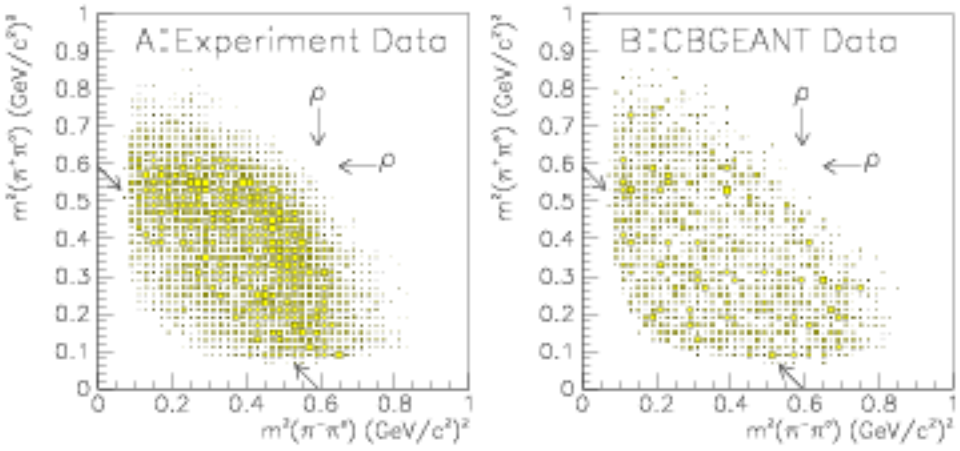

Figure 12.1: Dalitz plot of $\pi^+\pi^-\pi^\circ$ for events with $m(\pi^+\pi^-\pi^\circ) > 1000 MeV/c^2$. That is, for each event with $m(\pi^+\pi^-\pi^\circ) > 1000 MeV/c^2$ the square of the invariant mass of the $\pi^+\pi^\circ$ pair is plotted vs. the square of the invariant mass of the $\pi^-\pi^\circ$ pair. Arrows indicate where ρ bands should appear; they correspond to $\pi\pi$ masses of $770 MeV/c^2$. The diagonal arrows are for $\pi^+\pi^-$ masses of $770 MeV/c^2$.

12.1.3 $\bar{p}p \to M\pi,\ M \to \omega\pi\pi$

The $\omega\pi\pi$ decay of M can be modeled in three ways: $\omega\rho$, $\omega(\pi\pi)_s$, and $b_1\pi$. The $\omega\rho$ system has $I = 1$, $\omega(\pi\pi)_s$ has $I = 0$, but $b_1\pi$ couples to $I = 0, 1$ or 2. Table 12.2 lists the quantum numbers available to these $\omega\pi\pi$ systems, and possible resonances and their allowed decay modes.

L	$\omega\sigma$		$\omega\rho$		$b_1\pi$	
0	1^{--}	ω	$(0,1,2)^{++}$	a_0,a_1,a_2	1^{--}	ω
1	$(0,1,2)^{+-}$	h_1	$(0\cdots3)^{-+}$	π,$\hat{\rho}$,π_2	$(0,1,2)^{+-}$	a_0,a_1,a_2,h_1
2	$(1,2,3)^{--}$	ω,ω_3	$(0\cdots4)^{++}$	a_0,a_1,a_2	$(1,2,3)^{--}$	ω,ω_3,$\hat{\rho}$,π_2
3	$(2,3,4)^{+-}$		$(1\cdots5)^{-+}$	$\hat{\rho}$,π_2	$(2,3,4)^{+-}$	a_2
4	$(3,4,5)^{--}$	ω_3	$(2\cdots6)^{++}$	a_2	$(3,4,5)^{--}$	ω_3

Table 12.2: The J^{PC} quantum numbers available to three types of two-body $\omega\pi\pi$ systems and the corresponding resonances, for several values of orbital angular momenta between the two decay products.

Two measurements provide some information on the possibility of the reaction $\bar{p}p \to a_0(1450)\pi,\ a_0 \to \omega\pi\pi$:

- $BR(\bar{p}p \to a_0\pi^\circ,\ a_0 \to \eta'\pi^\circ) = (.117 \pm .022) \times 10^{-3}$ [50]
- $BR(\bar{p}p \to a_0\pi^\circ,\ a_0 \to \eta\pi^\circ) = (.29 \pm .11) \times 10^{-3}$ [52]

Measurement	$BR(a_2)$[1]	Fraction of $\pi^+\pi^-\pi^\circ\omega$
$BR(\bar{p}p \to a_2^\circ(1320)\pi^\circ;\ a_2 \to \eta\pi^\circ)$ $= (1.97 \pm 0.09) \times 10^{-3}$[53]	$BR(a_2 \to \eta\pi)$ $= 14.5 \pm 1.2\%$	$2.7 \pm 0.9\%$
$BR(\bar{p}p \to \pi a_2(1320))$ $= 1.55 \pm 0.31\%$[51]		$1.0 \pm 0.4\%$
$BR(\bar{p}p \to a_2^\circ(1320)\pi^\circ,\ a_2 \to \pi^\circ\eta')$ $= (0.064 \pm 0.013) \times 10^{-3}$ [50]	$BR(a_2 \to \eta'\pi)$ $= 0.57 \pm 0.11\%$	$2.3 \pm 0.9\%$
$BR(\bar{p}p(^1S_0) \to a_2(1320)\pi;\ a_2 \to \bar{K}K)$ $= (12.00\ ^{+0.93}_{-2.53} \times 10^{-4}$ [54]	$BR(a_2 \to \bar{K}K)$ $4.9 \pm 0.8\%$	$1.6\ ^{+0.6}_{-0.7}\ \%\ (^1S_0)$
$BR(\bar{p}p(^3S_1) \to a_2(1320)\pi;\ a_2 \to \bar{K}K)$ $= (2.85 \pm 0.88) \times 10^{-4}$ [54]		$0.4 \pm 0.2\%\ (^3S_1)$

Table 12.3: Crystal Barrel measurements of the rate of $a_2(1320)\pi$ production, and the amount of $a_2(1320)\pi$ in the $\pi^+\pi^-\pi^\circ\omega$ final state implied by the measurements. The middle column shows the branching fraction of the $a_2(1320)$ in the decay mode of the measurement. The branching fraction for $a_2(1320) \to \omega\pi\pi$ is $10.6 \pm 3.2\%$. The a_2 branching fractions are taken from the PDG [1].

Note that both of these measurements were made in the all neutral mode. In $\pi^+\pi^-\pi^\circ\omega$, all three charge states could be seen, so a factor of three is introduced into the formula for the fraction of $a_0\pi$ in $\pi^+\pi^-\pi^\circ\omega$:

$$\begin{aligned} F_{a_0} &= \frac{3 \times BR(\bar{p}p \to a_0\pi^\circ)BR(a_0 \to \eta\pi^\circ)}{BR(\bar{p}p \to \pi^+\pi^-\pi^\circ\omega)} \frac{BR(a_0 \to \omega\pi\pi)}{BR(a_0 \to \eta\pi^\circ)} \\ &\simeq .0036 \cdot \frac{BR(a_0 \to \omega\pi\pi)}{BR(a_0 \to \eta\pi^\circ)}. \end{aligned}$$

So the branching fraction of $a_0(1450)$ into $\omega\pi\pi$ will need to be 3 times larger than into $\eta\pi$ in order for $a_0\pi$ to be present at the 1% level in this analysis (~ 4 times larger than $\eta'\pi$.)

The $a_1(1700)$ was reported, decaying into $\rho\pi$ in reference [6]. Its mass and width were measured as $m = 1728 \pm 9 MeV/c^2$ and $\Gamma = 253 \pm 22 MeV/c^2$. It was produced in $\pi^- p^+$ collisions, so no prediction as to its production in $\bar{p}p$ annihilation is possible.

Several measurements of the rate of production of $a_2(1320)\pi$ in $\bar{p}p$ annihilation are shown in Table 12.3, along with the predicted amount of this channel in the $\pi^+\pi^-\pi^\circ\omega$ data set. Again, the measurements made in all neutral final states give information only on production from the $^1S_0$ initial state. Using the branching fractions for the $a_2(1320)$ from the PDG, and the production rate of the $\pi^+\pi^-\pi^\circ\omega$ final state (16.1±1.0%), these lead to the expectation that $a_2(1320)\pi$ will constitute of couple of percent of the $\pi^+\pi^-\pi^\circ\omega$ final state.

The $a_1(1260)$ resonance has not been observed in $\omega\pi\pi$ decay modes. It is quite broad ($\Gamma \simeq 400 MeV/c^2$), though, and would not produce a clear peak in invariant

mass spectra. Its mass is nominally below both the $\omega\rho$ and $b_1\pi$ thresholds, but $\omega\pi\pi$ decays may still occur (as for the $a_2(1320)$.)

Production of $\omega(1600)\pi$ has never been observed in $\bar{p}p$ annihilation. This is a well established resonance, and has been observed in $\omega\pi\pi$ decay modes [61]. $\omega(1600)\pi$ production can proceed with $L = 0$ and 2 from $\bar{p}p$ S-states.

Production of $\omega_3(1670)\pi$ must occur with $L = 4$, and would be suppressed by the centrifugal barrier; as only $70MeV$ of excess energy is available for $\omega_3(1670)\pi$ production, it is not likely to be present in great quantity in this data set.

The $h_1(1170)$ has been observed only in its $\rho\pi$ decay mode; no effort to find it in $\omega\pi\pi$ has been reported, however. Recently, an $h_1(1540)$ resonance has been reported ($m = 1542 \pm 13MeV/c^2$, $\Gamma = 285 \pm 30MeV/c^2$), decaying to $\omega\eta$. Observation of h_1's in the $\omega\pi\pi$ decay mode would be of great value.

An $I^G J^{PC} = 1^-1^{-+}$ resonance, called π_1 or $\hat{\rho}$, has been reported decaying to $\eta\pi$ [55, 56], with a mass near $1400MeV/c^2$ and width of 300 to $400MeV/c^2$. The possibility exists of seeing such a state decaying to $\omega\pi\pi$.

The $\pi(1300)$, $\pi_2(1670)$ have not been observed in $\omega\pi\pi$ decay modes [1].

Given the above considerations, the decay chains which seem most likely to contribute to the final state under study are:

- $\bar{p}p \to \omega\omega$
- $\bar{p}p \to h_1(1170)\omega$, $h_1 \to \rho\pi$
- $\bar{p}p \to a_1(1260)\omega$, $a_1 \to \rho\pi$
- $\bar{p}p \to a_2(1320)\omega$, $a_2 \to \rho\pi$
- $\bar{p}p \to b_1(1235)\rho$
- $\bar{p}p \to b_1(1235)(\pi\pi)_s$
- $\bar{p}p \to a_2(1320)\pi$, $a_2 \to \omega\pi\pi$
- $\bar{p}p \to \omega(1600)\pi$, $\omega(1600) \to \omega\pi\pi$

These are known resonances decaying into known decay modes.

12.2 Fitting $\bar{p}p \to \omega\omega$

Evidence for the process $\bar{p}p \to \omega\omega$ is clearly visible in the $\pi^+\pi^-\pi^\circ\omega$ data set as a large peak in the $\pi^+\pi^-\pi^\circ$ mass spectrum. This process is included in the fits, but is modeled as a combination of two processes in order to adequately describe the data. (Some preliminary investigations indicated that a description of the decay $\omega \to \pi^+\pi^-\pi^\circ$ in terms of a two-body mode ($\omega \to \rho\pi$) was inadequate.) The two processes which are modeled differ in the description of the process $\omega \to \pi^+\pi^-\pi^\circ$. One way is to compute

amplitudes for the two step process $\omega \to \rho\pi,\ \rho \to \pi\pi$. The other way is to compute an amplitude for a direct three-body decay.

In both cases, the ω lineshape (i.e. the kinematic amplitude) is described by a Voigtian. The Voigtian does not have a phase variation across the ω peak, but since the σ of the Voigtian is $8.5MeV$, a $\pi^+\pi^-\pi^\circ$ system whose mass was measured to have been less than the central mass could actually have had a mass greater than the central mass. Using a Breit-Wigner, the phase of which would vary rapidly over a range of about $10MeV$, may end up assigning the wrong phase to a great number of the $\pi^+\pi^-\pi^\circ$ combinations which are likely to have comprised the ω's.

The two ways of computing amplitudes for this process are described in the following two sections.

12.2.0.1 Amplitudes for $\omega \to \rho\pi$

The decay $\omega \to \pi^+\pi^-\pi^\circ$ can be modeled in the 2-body helicity formalism (see Section 11.2) as a two step process: $\omega \to \rho\pi,\quad \rho \to \pi\pi$. A relativistic Breit-Wigner weighting for the ρ is included, though it varies by only a small amount over the range of $m(\pi\pi)$ produced by ω's. Amplitudes for the decay proceeding via all three ρ charge states are computed and added coherently with the appropriate isospin weighting (see Section 11.4.)

12.2.0.2 Direct 3-Body decays

In order to model a direct 3-body decay of the ω, a helicity amplitude involving two factors was used: $\mathcal{H}_{0,\lambda_\omega}(\theta_\hat{n}, \phi_\hat{n}, \lambda) = \mathcal{P}_{Dalitz}(\lambda) \cdot \mathcal{P}_n(\theta_\hat{n}, \phi_\hat{n})$. The probability associated with the position of the event on the Dalitz plot is $\mathcal{P}_{Dalitz}(\lambda)$. It is proportional to the λ parameter described in Section 9.3, and describes the probability that the 3π system has quantum numbers $J^P = 1^-$. $\mathcal{P}_n(\theta_\hat{n}, \phi_\hat{n})$ accounts for the probability of producing the decay plane with a given orientation; this is a manifestation of angular momentum conservation, and is computed using the 3-body helicity formalism [59]. This factor describes the probability that the 3π system resulted from the decay of an ω in a particular polarization state.

The function $\mathcal{H}_{0,\lambda_\omega}(\theta_\hat{n}, \phi_\hat{n}, \lambda)$, which is the amplitude for the process $\omega \to 3\pi$, is multiplied by the amplitude for the combined process $\bar{p}p \to \omega_1\omega_2,\ \omega_2 \to \pi^\circ\gamma$ to form the amplitude for the entire decay chain. (See Section 11.2.)

12.2.1 Fit Results

Figure 12.2 and Table 12.4 are comparisons of fitting with the two models of the ω decay described above, separately and together. Also included in these fits were the channels: $b_1\rho$, $b_1(\pi\pi)_s$, $a_2(1320)\pi$, $\omega(1600)\pi$, $h_1\omega$, $a_1\omega$, $a_2\omega$ and $\omega(1420)\omega$. The parameters of the Voigtian lineshape for the ω were determined by scanning their

$\omega\omega, \omega \to \rho\pi$	$\omega\omega, \omega \to \pi\pi\pi$	Total $\omega\omega$	$2\ln(\mathcal{L})$
33.0	-	33.0	17669
-	29.8	29.7	16162
25.6	9.8	26.8	17957

Table 12.4: Comparison of results of fits including the Base fit, and $\bar{p}p \to \omega\omega$ modeled as either $\omega \to \rho\pi$ ($\omega(2)$), $\omega \to \pi\pi\pi$ ($\omega(3)$), and both. Shown are the fitted branching fractions for each of the two channels, the branching fraction of the coherent sum of the two channels, and the fit quality parameter, $2\ln(\mathcal{L})$.

values for the fit with both types ω decays included. The values used were $m_\omega = 780.4 MeV/c^2$ and $\sigma_\omega = 8.5 MeV/c^2$. Γ_ω was fixed at $8.43 MeV/c^2$, the PDG value.

In the table, the total $\omega\omega$ contribution to the $\pi^+\pi^-\pi^\circ\omega$ final state is determined as a *coherent* sum of the two $\omega\omega$ channels. The $\omega\omega$ contributions are high compared to the abundance as determined by the branching fraction calculations because of different acceptances for $\omega\omega$ events compared to other $\pi^+\pi^-\pi^\circ\omega$ events, and because of the interferences with other channels in the fits. (From the measured branching fractions, one would expect $\omega\omega$ to be 20 to 25% of the final state.) The sum of the branching ratios indicates that there are destructive interferences among the two amplitudes describing the $\omega\omega$ production and decays. The $\rho\pi$ mode is 2.6 times stronger than the direct $\pi\pi\pi$ mode. The fit with $\omega \to \rho\pi$ is 1507 better, in the parameter $2\ln(\mathcal{L})$, than that with $\omega \to \pi\pi\pi$. With both ω decay models included, $2\ln(\mathcal{L})$ improves by 288 over the fit with $\omega \to \rho\pi$ only. The λ distribution appears to be better fit by the combined fit, as the fit is poor at the low end for the $\omega \to \pi\pi\pi$ model and at the high end for the $\omega \to \rho\pi$ model.

The relative strengths of these two decay modes will be discussed further, in the context of the final fit, in Section 12.7.

12.3 The D/S ratio for $b_1 \to \omega\pi$

The $b_1(1235)$ resonance can decay to $\omega\pi$ with orbital angular momentum $L = 0$ and $L = 2$ between the ω and π. The relative strengths of these two decays has been measured in other experiments, and the average of these results, as reckoned by the Particle Data Group, is $D/S = 0.29 \pm 0.04$ [1]. The D/S ratio is defined as:

$$D/S = \frac{amplitude(L = 2)}{amplitude(L = 0)}$$

Because a factor of $1/\sqrt{2L+1}$ was left out of the overall normalizations of the amplitudes, the ratio of the fitted coefficients must be divided by $\sqrt{5}$ to determine the

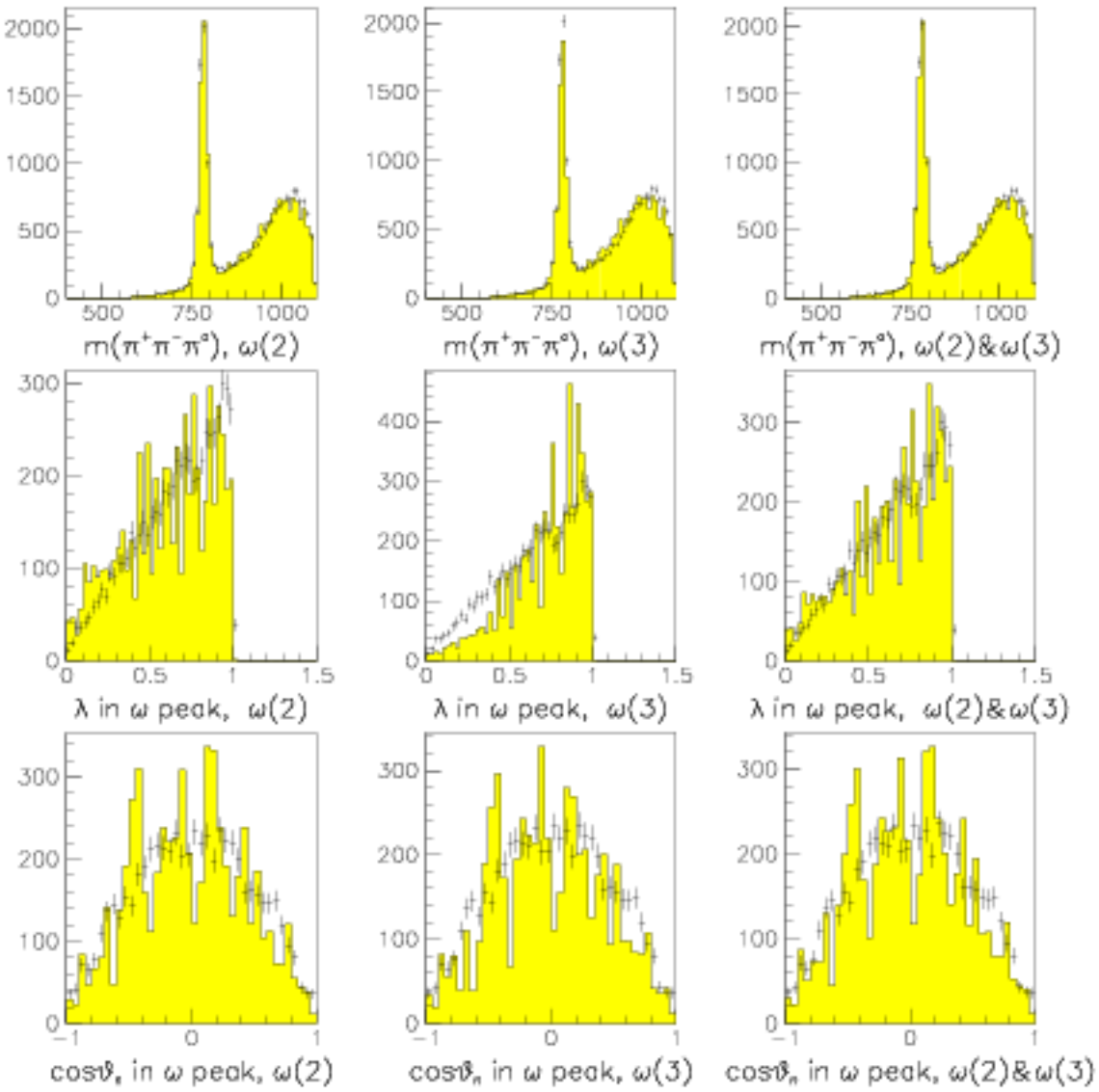

Figure 12.2: Comparisons of fits including $\bar{p}p \to \omega\omega$ modeled as either $\omega \to \rho\pi$ ($\omega(2)$), $\omega \to \pi\pi\pi$ ($\omega(3)$), and both. The $\pi^+\pi^-\pi^0$ mass spectrum, λ distribution, and distribution of the normal to the decay plane are shown for each of the three fits. Experimental data are shown as crosses, and the fitted Monte Carlo data are in the shaded histograms.

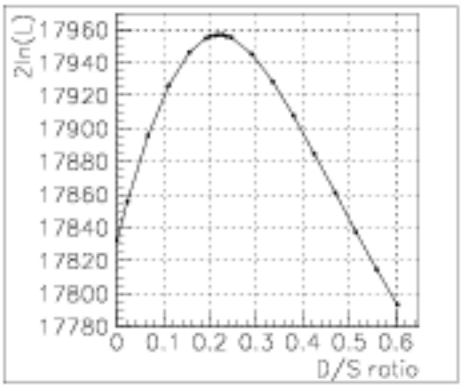

Figure 12.3: Results of fits where the D/S ratio for the decay $b_1(1235) \to \omega\pi$ was varied. All other parameters were optimized by the minimization program. The fits included all channels in the *Base* fit.

D/S ratio:

$$D/S = \frac{1}{\sqrt{5}} \frac{b_{L=2}}{b_{L=0}}$$

In order see the variation in $2\ln\mathcal{L}$ with the D/S ratio, some PWA fits were performed with the ratio set to several values. The results are shown in Figure 12.3. The fit optimizes for a D/S ratio of about 0.22, somewhat less than the PDG value, but the value of $2\ln\mathcal{L}$ changes by less than 20 with the D/S ratio set to 0.29. The fits for the scan included those decay chains in the *Base* case (see the following section,) which is probably an incomplete description of the data. The D/S ratio might optimize at a low value as a result of the inadequate fitting function. Another possible reason for the low value is that much of the $b_1(1235)$ signal results from $\bar{p}p \to b_1\rho$, where the b_1's are biased toward low masses; it is possible that lower mass b_1's decay with a lower D/S ratio as a result of having less energy available to penetrate the centrifugal barrier for $L = 2$ decays. The value of the D/S ratio will be discussed in the context of more complete fits in the following sections.

12.4 Fitting the Most Likely Contributions

The fits presented in this section were performed under the following conditions:

- 20000 Monte Carlo events and 20000 experimental events have been used
- $\bar{p}p \to \omega\eta$ events have been eliminated by requiring all events to have $m(\pi^+\pi^-\pi^\circ) > 580 MeV/c^2$
- The $\omega\omega$ contribution is fitted with the $\omega \to \rho\pi$ and $\omega \to \pi^+\pi^-\pi^\circ$ methods, as described above, with $m_\omega = 780.4 MeV/c^2$, $\Gamma_\omega = 8.43 MeV/c^2$, and $\sigma_\omega = 8.5 MeV/c^2$.

Production $\bar{p}p \to$	Included in Base fit	Not Included in Base fit
$b_1\rho$	${}^1S_0 \to b_1\rho$ L=0;s=0 ${}^3S_1 \to b_1\rho$ L=0;s=1 $b_1 \to \omega\pi$ L=0,2	${}^1S_0 \to b_1\rho$ L=2;s=2 ${}^3S_1 \to b_1\rho$ L=2;s=1,2
$b_1(\pi\pi)_s$	${}^3S_1 \to b_1(\pi\pi)_s$ L=1	
$a_2(1320)\pi$	${}^1S_0 \to a_2\pi$ L=2 ${}^3S_1 \to a_2\pi$ L=2 $a_2 \to \omega\rho$ L=0;s=2 $a_2 \to b_1\pi$ L=1	 $a_2 \to \omega\rho$ L=2;s=0,1,2 $a_2 \to b_1\pi$ L=3
$\omega(1600)\pi$	${}^3S_1 \to \omega()\pi$ L=1 $\omega() \to \omega(\pi\pi)_s$ L=0 $\omega() \to b_1\pi$ L=0	 $\omega() \to \omega(\pi\pi)_s$ L=2 $\omega() \to b_1\pi$ L=2
$h_1(1170)\omega$	${}^3S_1 \to h_1\omega$ L=0 $h_1 \to \rho\pi$ L=0	${}^3S_1 \to h_1\omega$ L=2 $h_1 \to \rho\pi$ L=2
$a_1(1260)\omega$	${}^3S_1 \to a_1\omega$ L=0;s=1 $a_1 \to \rho\pi$ L=0	${}^3S_1 \to a_1\omega$ L=0;s=1,2 $a_1 \to \rho\pi$ L=2
$a_2(1320)\omega$	${}^3S_1 \to a_2\omega$ L=0;s=1 $a_2 \to \rho\pi$ L=2	${}^3S_1 \to a_2\omega$ L=3;s=2,3
$\omega(1420)\omega$	${}^1S_0 \to \omega()\omega$ L=1 $\omega() \to \rho\pi$ L=1	

State	m MeV	Γ MeV
ρ	770	150
b_1	1230	140
$a_2(1320)$	1318	107
$\omega(1600)$	1649	220
$h_1(1170)$	1170	360
$a_1(1260)$	1230	400
$\omega(1420)$	1419	174

Table 12.5: Reactions and resonances used in the Base fits ("A" of Table 12.6.) Both $L = 0$ and $L = 2$ are included for all b_1 decays, whether they originate in production or from resonance decays. The decay chains listed under "Not Included" are those which are allowed by the conservation of the I, G, J, P and C quantum numbers, but which are suppressed by the centrifugal barrier effect. For decays of the $h_1(1170)$, $a_1(1260)$ and $\omega(1600)$ (those in boxes,) the $L = 2$ decays *are* allowed in fit "B" of Table 12.6.

- The D/S ratio for b_1 decays was forced to be the same for all channels, but its value was left to vary as a fit parameter.

For a Base fit, a set of decay chains was chosen which includes known resonances in known decay modes; the elements of the Base case are shown in Table 12.5. Except for $b_1 \to \omega\pi$, only the lowest orbital angular momenta were allowed in production and decays. This keeps the number of fitting parameters reasonable, allowing fits to be performed in a timely manner with the available computing resources. Table 12.6(A) shows a summary of the Base fit. The contributions don't total to 100% because the $\omega\omega$ contribution is quoted as the *coherent* sum of the $\rho\pi$ and direct 3π decay modes (see Table 12.4 and Section 11.7.) The contribution from $a_2(1320)\pi$ is smaller than expected (see Table 12.3.) The $\omega(1600)\pi$ channel is fit as a 17% contribution,

$\omega\omega$	$b_1\rho$	$b_1(\pi\pi)_s$	$a_2()\pi$		$\omega()\pi$		$h_1()\omega$	$a_1()\omega$	$a_2()\omega$	$\omega()\omega$	bkg	$2\ln\mathcal{L}$	$\Delta 2\ln\mathcal{L}$ Base	ref
			$\omega\rho$	$b_1\pi$	$\omega\rho$	$b_1\pi$								
26.8	15.2	2.1	0.4	0.6	5.4	11.2	2.9	12.2	10.9	3.7	-	17957	0	A
25.3	10.7	2.1	0.2	0.5	3.4	9.3	6.9	18.1	17.2	6.7	-	18302	345	B
26.6	14.6	2.0	0.3	0.6	5.0	10.8	2.7	12.0	11.0	3.8	2.4	17964	-7	C
26.2	13.6	1.7	0.1	0.5	4.1	9.9	2.4	11.1	11.3	4.0	7.5	17934	-23	D
24.2	-	1.4	4.3	0.4	8.2	9.0	2.6	10.5	14.3	10.6	8.0	17635	-322	E
26.7	15.4	-	0.3	0.2	5.1	11.6	2.9	7.4	12.6	4.9	4.8	17844	-113	F
26.9	15.5	1.9	-	-	4.9	11.2	2.8	11.3	11.3	3.4	2.4	17909	-48	G
27.1	10.8	2.2	1.2	1.5	-	-	2.2	16.4	15.1	3.8	11.1	17448	-509	H
25.2	18.1	1.4	1.9	1.4	4.8	10.5	-	12.3	12.0	1.4	4.5	17800	-157	I
26.4	16.2	.02	0.1	0.4	8.3	10.8	2.9	-	16.1	5.6	5.1	17692	-65	J
26.0	13.2	2.1	0.3	0.9	4.8	10.8	3.5	22.4	-	5.2	3.0	17437	-520	K
25.6	20.1	2.2	0.5	0.6	5.7	9.6	2.0	12.8	12.0	-	1.7	17857	-100	L
26.1	18.9	2.9	0.6	0.9	5.4	9.4	2.7	24.2	-	-	2.0	17335	-622	M

Table 12.6: A summary of results from fits which included decay chains in the the *Base* fit. For each decay chain, the percent contribution to the total $\pi^+\pi^-\pi^\circ\omega$ final state is shown. Also shown are the percentage contribution from the background term, the value of $2\ln\mathcal{L}$ for the fit, and the change in $2\ln\mathcal{L}$ relative to the Base fit. A: Base fit. B: Base, with with higher $L = 2$ included for decays of the $h_1(1170)$, $a_1(1260)$ and $\omega(1600)$. C: With a background term, the contribution of which was determined by the optimization program. D: With background term at fixed 7.5% contribution level. E-M: Excluding channels, and allowing a background term.

with the $b_1\pi$ decay mode of the $\omega(1600)$ about twice as strong as the $\omega(\pi\pi)_s$ mode, consistent with previous observations. The channels which are nominally above phase space ($b_1\rho$, $h_1\omega$, $a_1\omega$, $a_2\omega$ and $\omega(1420)\omega$) comprise nearly 50% of the fit contributions. This type of behavior has been observed in other channels, particularly where there is production of a heavy resonance in conjunction with a ρ or ω vector meson [48, 58].

The fit shown in Table 12.6(B) allowed for higher orbital angular momenta among the decay products of the $h_1(1170)$, $a_1(1260)$ and $\omega(1600)$ resonances. The value of $2\ln\mathcal{L}$ improves by 345 as a result, a significant change. The total contribution from $h_1\omega$ increases twofold, with $L = 2$ decays about five times stronger than $L = 0$ decays. (This is quite inconsistent with previous measurements [60].) The $a_1\omega$ contribution increases by a factor of 1.5, with a D/S ratio of 0.16, compared to the PDG value of 0.09 ± 0.03, for the decay $a_1(1260) \to \rho\pi$. The contribution from $\omega(1600)\pi$ actually falls to about 3/4 of its value in the Base fit, with $L = 0$ decays dominant by more than a factor of 8, which seems quite reasonable. These $L = 2$ decays will be excluded from the fits which follow (in order to keep the number of fit parameters reasonable), but the results warrant further investigation when a final set of channels is decided

upon.

A 4-body ($\pi^+\pi^-\pi^\circ\omega$) phase space background term was included in the fits shown in Table 12.6(C,D). This might not be a good description of the backgrounds which are present, but no better method was obvious. In Table 12.6(C), the level of the background was a fit parameter which optimized at 2.4%. The value of $2\ln\mathcal{L}$ increased by only 8, a very small amount. In Table 12.6(D), the amount of background was fixed at 7.5%, approximately the level expected from feed-through studies of the $\pi^+\pi^-\pi^\circ\pi^\circ\pi^\circ$ channel. The fit was worse than the Base fit by $\Delta 2\ln\mathcal{L} = 23$. This background channel seems to make a quite small difference in the fit quality and in the contributions from the other channels; it will be excluded as the fits are expanded to include additional channels. It is included, however, in the fits shown in Table 12.6(E-M), where various channels are left out of the fit. In these fits, as one might expect, large changes in $2\ln\mathcal{L}$ result when the channels which had been fit as large contributions are excluded. This indicates that the Base fit is not finding a shallow local minimum, with the contributions easily rearranged to yield a result which is nearly as good.

Figure 12.4 show mass spectra which result from the Base fit. Some of the MC histograms appear ragged; this is primarily due to the fact that the relatively small number of events in the $\omega \to \pi^+\pi^-\pi^\circ$ peak receive a large weighting. Otherwise, the gross features of the mass spectra are well described by this fit.

Nine angular distributions resulting from the Base fit are shown in Figure 12.5; these are to be compared to Figure 9.5. (This is a small sample of the complete set of angular distributions.) Several of these are well fit, but the Base fit has caused a discrepancy in the angular distribution C. These fits to these distributions will be improved as additional channels are added to the fit.

The masses and widths of the resonances in the Base fit are scanned in Figures 12.6, 12.7, 12.8 and 12.9. Discussions of these scans follow.

12.4.1 Scan of $b_1 \to \omega\pi$

Figure 12.6 shows the results of scanning the mass and width of the $b_1 \to \omega\pi$ resonance. All b_1's are affected, both those in $b_1\rho$ production and those from decays of the $a_2(1320)$ and $\omega(1600)$ resonances. The scan shows the expected behavior: a peak in $2\ln\mathcal{L}$ for masses and widths near those which are widely accepted for the $b_1(1235)$. The optimum is at $m = 1250$, $\Gamma = 200$, with the value of $2\ln\mathcal{L}$ 38 greater than at the PDG values. The value of $2\ln\mathcal{L}$ falls by several hundred away from the peak. While it doesn't allow an accurate measurement of the mass and width of the $b_1(1235)$, this result does indicate the presence of b_1's in this data.

12.4.2 Scans of the $\rho\pi$ Resonances

Scans of the masses and widths of the $\rho\pi$ resonances are shown in Figure 12.7. These resonances all have masses which are greater than the maximum energy available to

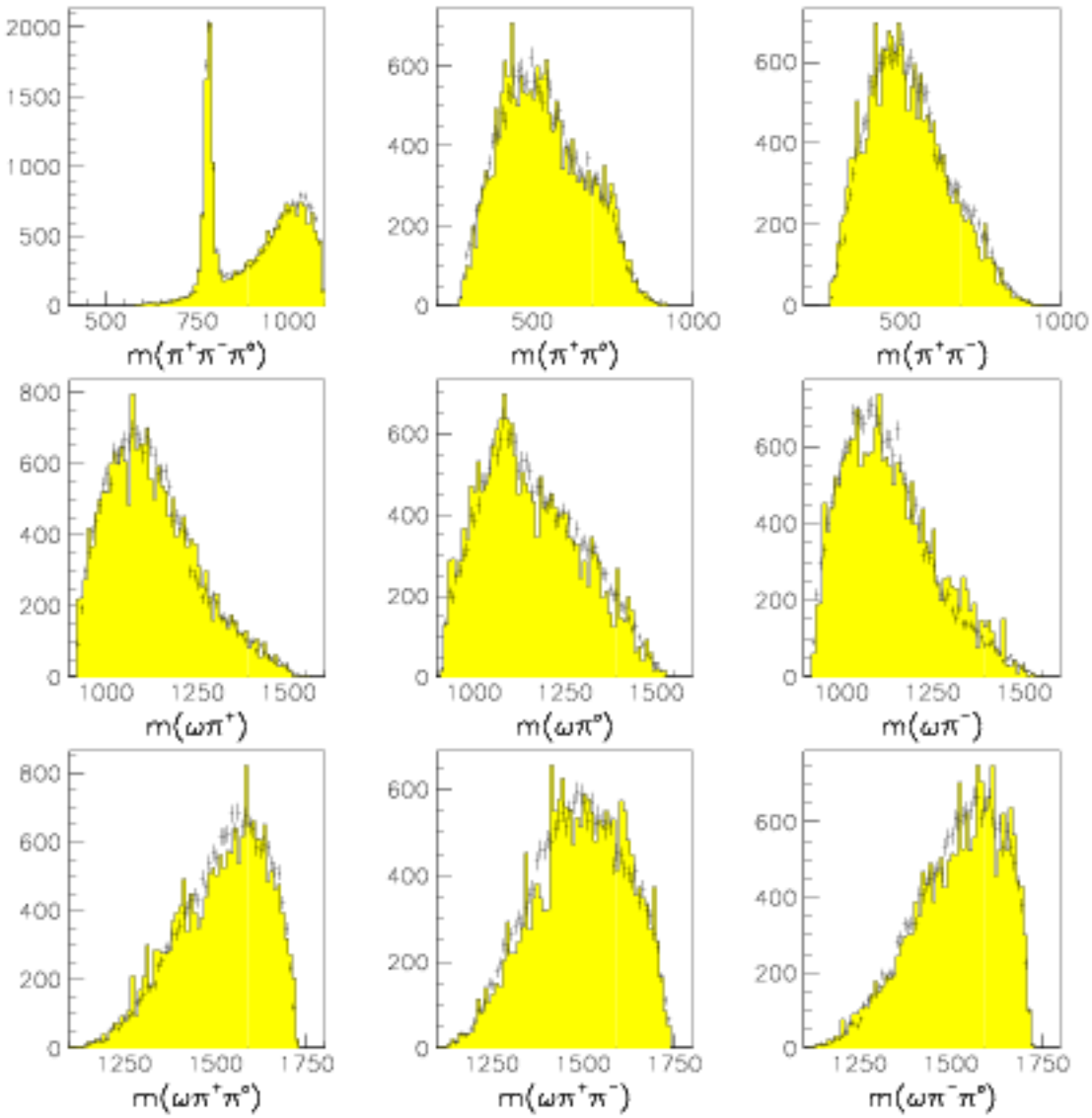

Figure 12.4: Mass spectra from the Base fit, with the experimental data shown as crosses and the Monte Carlo data shown as the shaded histograms. The Monte Carlo histograms have been weighted according to the fit, and have been scaled up to have the same numbers of events as those for the experimental data. All of the histograms have bin sizes of $20 MeV/c^2$.

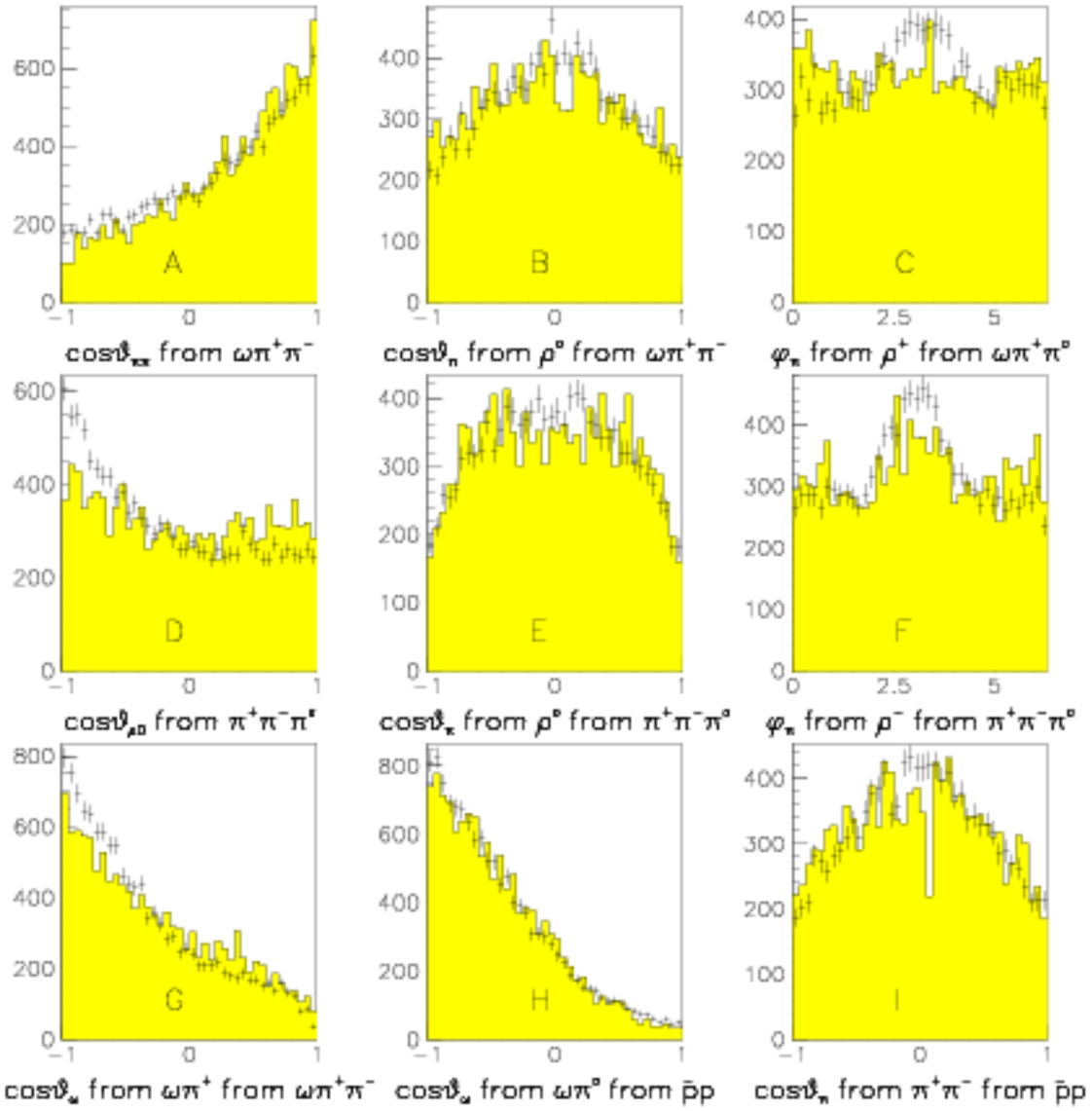

Figure 12.5: Nine angular distributions from the Base fit are shown, with the experimental data shown as crosses and the Monte Carlo data shown as the shaded histograms. The $\bar{p}p \to \omega\omega$ events have been eliminated by requiring that $m(\pi^+\pi^-\pi^\circ) > 830 MeV/c^2$. The MC histograms have been weighted according to the Base fit, and have been scaled up to have the same numbers of events as those for the experimental data.

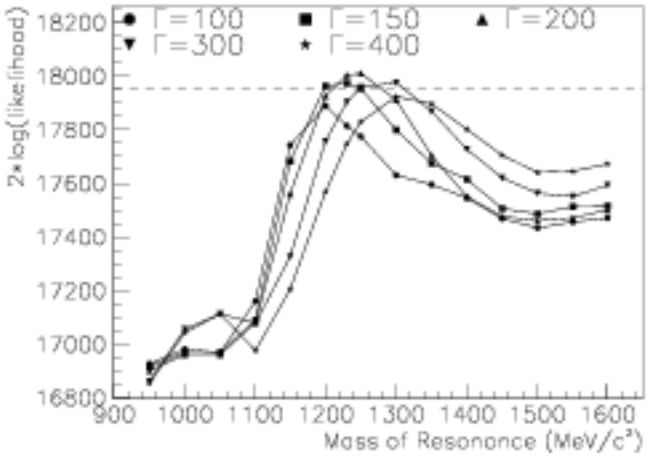

Figure 12.6: Scan of the mass and width of $b_1() \to \omega\pi$ in the Base fit.

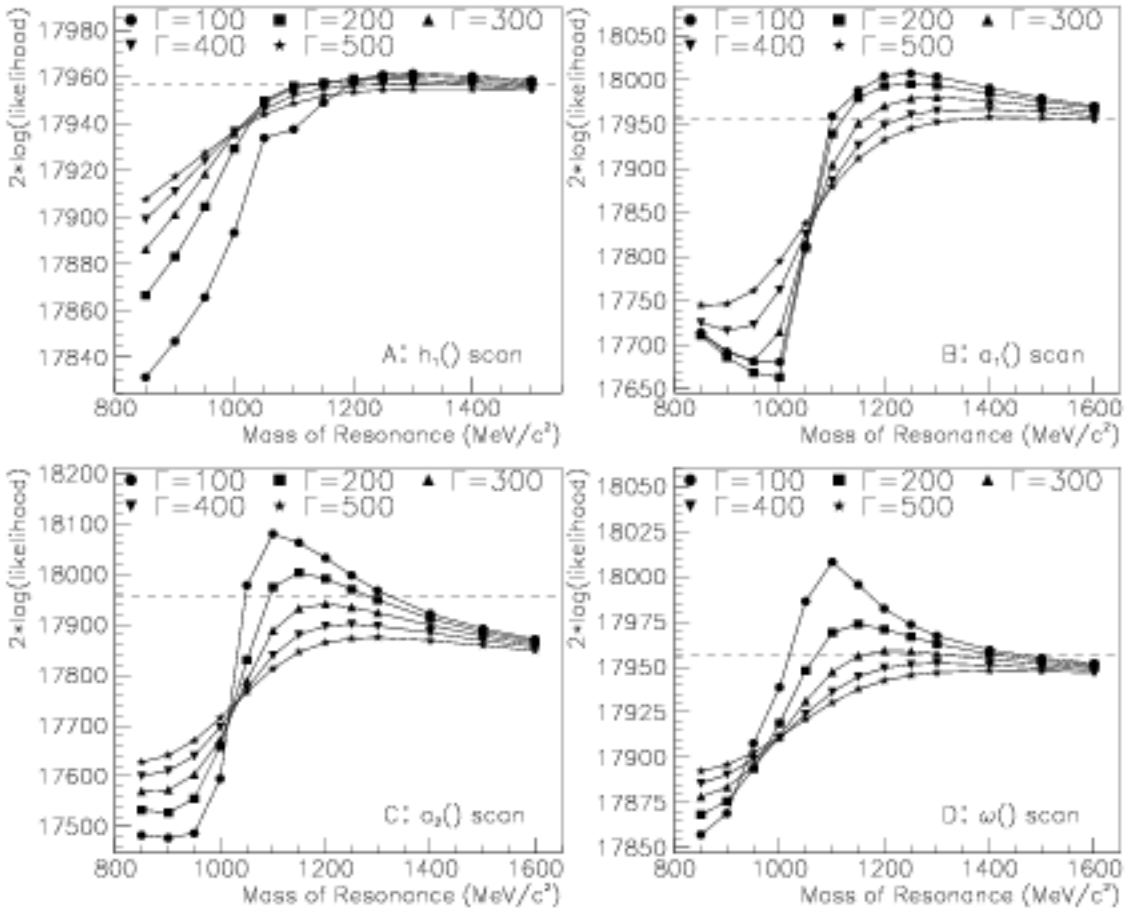

Figure 12.7: Scans of masses and widths of the $\rho\pi$ resonances in the Base fit. A) $h_1(1170) \to \rho\pi$, B) $a_1(1260) \to \rho\pi$, C) $a_2(1320) \to \rho\pi$, D) $\omega(1420) \to \rho\pi$.

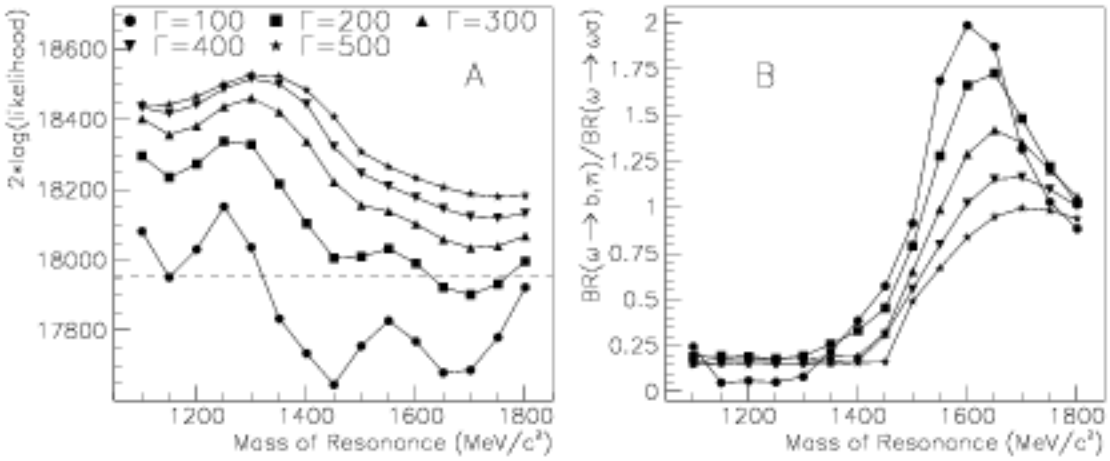

Figure 12.8: A: $2\ln\mathcal{L}$ vs. $\omega(1600)$ mass for a scan of $\omega(1600) \to \omega\pi\pi$ in the Base fit. B: The ratio of the branching fractions of the scanned $\omega(1600)$ into the $b_1\pi$ and $\omega(\pi\pi)_s$ decay modes.

the $\rho\pi$ combinations in the data; one would not expect a peak in $2\ln\mathcal{L}$ at the true mass of the resonances, but rather a plateau at high masses, and a drop in $2\ln\mathcal{L}$ for masses less than $1100MeV$. This behavior is exhibited quite well in the scans, particularly for the h_1 and a_1 resonances. The $\omega(1420) \to \rho\pi$ scan shows a weak peak ($\Delta 2\ln\mathcal{L} \sim 30$) at $1100MeV$ for small widths. A rise at $1100MeV$ is also present in the $a_2 \to \rho\pi$ scan, but is stronger, with $\Delta 2\ln\mathcal{L} \sim 90$ over the Base fit. These peaks indicate a preference for having a rapidly changing phase near the end of the $\rho\pi$ phase space. This preference is difficult to interpret, either as an interference or a background effect; this effect will warrant some attention in fits which include a more complete set of channels.

Recall that the $\phi(1020)$ meson has the same quantum numbers as an ω meson. It is the primarily $s\bar{s}$ counterpart of the $\omega(782)$, and is known to decay to $\rho\pi$ with a branching fraction of $12.9 \pm 0.7\%$ [1]. The $\omega \to \rho\pi$ scan was run with a rather small width of $\Gamma = 20MeV$ in order to see a signal for $\phi(1020) \to \rho\pi$, if it is present. There is no evidence for the ϕ in this scan.

12.4.3 Scan of the $\omega(1600) \to \omega\pi\pi$ Resonance

The scan of the mass and width of the $\omega(1600)$ is shown in Figure 12.8A. The most prominent feature in the plot is the peak at 1250-1300MeV, with the fits improving with larger widths up to $\Gamma = 500MeV$. At this peak, the value of $2\ln\mathcal{L}$ is about 500 greater than in the Base fit, and the contribution of the $\omega()\pi$ channel is greater than 30%. This mass seems too low for the $\omega(1420)$, and large width is clearly preferred. This feature may be indicative of the $h_1(1170)$ which has the opposite parity, but a lower mass and is broader than the $\omega(1420)$. There is also a small bump in $2\ln\mathcal{L}$

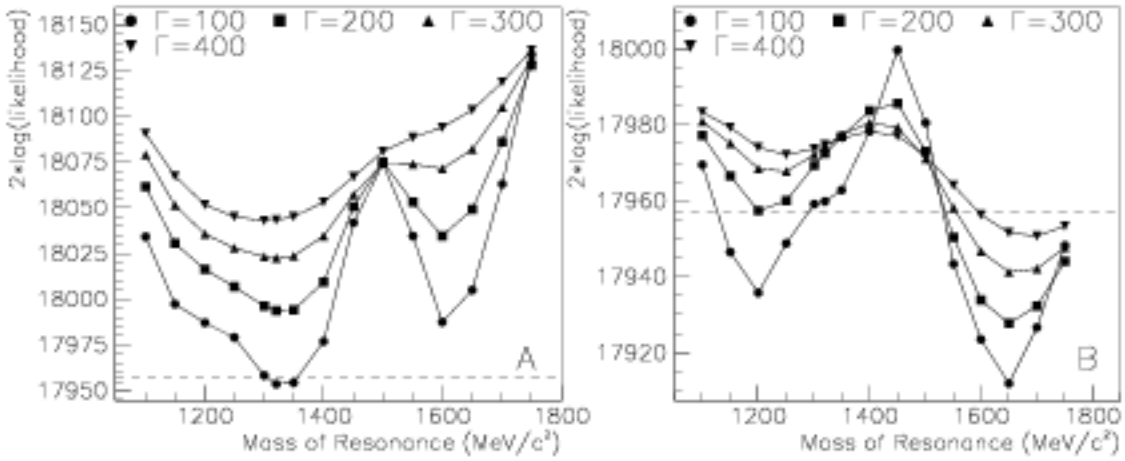

Figure 12.9: A: Scan of the mass and width of the $a_2() \to \omega\pi\pi$ in the Base fit. B: The same scan, but no Breit-Wigner term included for the ρ and b_1 decay products of the a_2.

for smaller widths at masses near $1500MeV$. There is no rise near $1649MeV$ (the accepted mass of the $\omega(1600)$ resonance.) In Figure 12.8B, the ratio of the fitted strengths of the $b_1\pi$ and $\omega(\pi\pi)_s$ decay modes of the scanned resonance is shown; it has a consistently small value ($\sim .25$) for $m < 1400MeV$, but rises sharply above this mass. For $\Gamma = 200MeV$ (near that of the $\omega(1600)$,) the ratio peaks at $m = 1650MeV$. As the $\omega(1600)$ is known to decay to $b_1\pi$, this is taken as an indication of its presence in this data.

The peak at 1250-1300MeV will be investigated in Section 12.5.1.

12.4.4 Scan of the $a_2(1320) \to \omega\pi\pi$ Resonance

A scan of the mass and width of the $a_2 \to \omega\pi\pi$ resonance is shown in Figure 12.9A. (This is $\bar{p}p \to a_2(1320)\pi$, $a_2 \to \omega\pi\pi$ in the Base fit; the mass and width of the $a_2(1320)$ decaying to $\rho\pi$ were held fixed for this scan.) There is no peak at $m = 1320MeV$, as one might expect, but rather a minimum. Most striking is the peak at 1450-1500MeV, where $2\ln\mathcal{L}$ is about 150 greater than in the Base fit. This mass is conspicuously near the $\omega\rho$ threshold; the computed kinematic amplitudes for $\omega\rho$ decays rise sharply around $1500MeV$ due to the Breit-Wigner describing the $\rho = \pi\pi$ amplitudes. In order to see if this effect causes the peak, a similar scan was done, with the only difference being that in the computed amplitudes for the decays $a_2 \to b_1\pi$ and $a_2 \to \omega\rho$, the Breit-Wigner terms for the b_1 and ρ were set to 1.0 (i.e. they had no dependence on the $\omega\pi$ and $\pi\pi$ masses.) The results are shown in Figure 12.9B. The peak is still near $1450MeV$. The values of $2\ln\mathcal{L}$ are smaller by 30-100. The peak appears not to be an artifact of the computation of the $\pi\pi$ and $\omega\pi$ kinematic amplitudes.

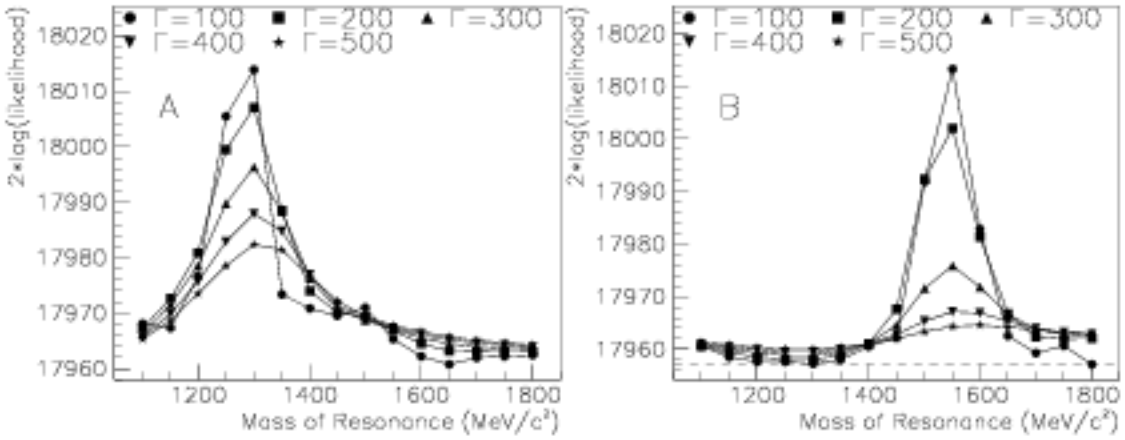

Figure 12.10: Scan of the mass and width of simple $\omega\pi\pi$ Breit-Wigner terms added to the Base fit. A) $X \to \omega\pi^+\pi^-$. B) $X \to \omega\pi^\pm\pi^\circ$.

Further investigation of this peak at 1450-1500MeV is discussed in Section 12.5.2

12.5 Adding $\omega\pi\pi$ Resonances to the Base Fit

Of the three types of production schemes possible in the analysis model, two have been exhausted in the Base fit: $(\omega\pi)+(\pi\pi)$ by including $b_1\rho$ and $b_1(\pi\pi)_s$, and $\omega+(\pi\pi\pi)$ by including $\omega h_1(1170)$, $\omega a_1(1260)$, $\omega a_2(1320)$ and $\omega\omega(1420)$ in the Base fit. This leaves production of π plus $\omega\pi\pi$ resonances as explanations for deficiencies in the Base fit.

First, two anomalous results of the Base fit scans will be addressed: the peak near 1300MeV for $I = 0$ $\omega\pi\pi$ resonances, and the peak near 1500MeV for $I = 1$ $\omega\pi\pi$ resonances. Next, resonances which are known or predicted and could decay in $\omega\pi\pi$ modes are explored. A satisfactory fit is found which includes three previously observed resonances in new $\omega\pi\pi$ decay modes.

12.5.1 $I = 0$ $\omega\pi\pi$ Resonances Near 1300MeV

To determine if the peak at $m = 1300MeV$ in the $\omega(1600) \to \omega\pi^+\pi^-$ scan is due to the kinematic amplitude or the helicity amplitude in the fitting function, a scan was performed over the mass and width of a pure Breit-Wigner (i.e. kinematic only) term. The amplitude depended only on the $\omega\pi^+\pi^-$ invariant mass, and the scanned term was added coherently to the other $^3S_1$ amplitudes. That is, this term was similar to the $\bar{p}p \to \omega(1600)\pi^\circ$, $\omega(1600) \to \omega\pi^+\pi^-$ term, except that there was no dependence on the angular distributions of the decay products; it corresponds to a generic $I = 0$ $\omega\pi\pi$ resonance. The results are shown in Figure 12.10A. A clear peak arises at 1300MeV, as in the $\omega() \to \omega\pi^+\pi^-$ scan, but here, small widths are

Add	Γ	contr		$\omega\omega$	$b_1\rho$	$b_1\sigma$	$a_2()\pi$		$\omega()\pi$		$h_1()\omega$	$a_1()\omega$	$a_2()\omega$	$\omega()\omega$	$2\ln\mathcal{L}$	$\Delta 2\ln\mathcal{L}$
	MeV	$\omega\sigma$	$b_1\pi$				$\omega\rho$	$b_1\pi$	$\omega\sigma$	$b_1\pi$						Base
ω	200	15.7	4.1	26.9	11.4	1.0	1.5	0.1	0.9	11.9	3.8	6.2	7.1	3.0	18539	582
h_1	200	5.5	0.4	27.0	15.6	0.7	0.5	0.3	4.6	10.4	2.6	12.7	9.9	3.4	18645	688
ω	400	21.2	4.7	26.9	9.7	1.0	1.7	0.1	.02	9.4	3.8	5.5	6.5	2.8	18578	621
h_1	400	6.2	0.7	26.7	15.4	0.7	0.6	0.3	4.1	10.2	2.3	13.2	10.0	3.2	18663	706
h_1	200	4.1	0.3	26.7	14.3	0.9	1.0	0.2	1.9	12.1	2.9	13.1	8.9	3.2	18725	768
ω		2.9	1.3													
h_1	400	3.8	1.1	26.4	11.2	1.1	1.9	0.2	0.2	12.5	2.6	12.3	9.1	2.5	18744	787
ω		6.4	2.1													

Table 12.7: A summary of results of fits in which $I = 0$ $\omega\pi\pi$ resonances were added to the Base fit. Each resonance was given a mass of $1300MeV$, and a width of 200 and $400MeV$. Each of these two channels adds 4 parameters to the fit. The first three columns show the type of added resonance (h_1 or ω), its width, and its contribution as a percentage of the $\pi^+\pi^-\pi^\circ\omega$ final state in both of the allowed decay modes. Also shown are the value of $2\ln\mathcal{L}$ for the fit, and the change in $2\ln\mathcal{L}$ relative to the Base fit.

preferred. The value of $2\ln\mathcal{L}$ at the peak is only 30-70 better than in the Base fit. This peak probably indicates the presence of events at this mass which are not correctly accounted for by the channels in the Base fit. This effect is quite possibly due to the opening of the $\omega(\pi\pi)_s$ phase space near this mass.

To further investigate the peak in the $\omega() \to \omega\pi^+\pi^-$ scan at $m = 1300MeV$, some fits were run which included, in addition to the Base case, additional h_1 or ω resonances, or both. (Recall that the quantum numbers for the h_1 and ω are $I^G J^{PC} = 0^-1^{+-}$ and 0^-1^{--} respectively; they differ only in parity.) For these fits, the masses of the added resonances were set to $1300MeV$, and widths of $\Gamma = 200$ and $400MeV$ were used. Results are summarized in Table 12.7. When added individually, the h_1 consistently improves $2\ln\mathcal{L}$ more than the ω does, though both improve it by several hundred. The ω resonance is fit as a large contribution (20-25%), and draws away contributions from $b_1\rho$, $a_1\omega$, $a_2\omega$ and from the $\omega(\pi\pi)_s$ decay mode of the $\omega(1600)$. The h_1 is fit as a 6-7% contribution and leaves the other channels relatively undisturbed. When both h_1 and ω resonances are added, $2\ln\mathcal{L}$ further improves, by ~ 200 as a result of adding the h_1 and by ~ 100 by addition of the ω. The fitted contribution of the ω falls to 4-8%; that of the h_1 falls to about 4%. For both types of resonances, the $\omega(\pi\pi)_s$ decay mode is stronger than the $b_1\pi$ mode.

Two reasonable possibilities for an $\omega\pi^+\pi^-$ resonance in this mass region are the $h_1(1170)$ and the $\omega(1420)$. Despite efforts to observe it, the $\omega(1420)$ has not been seen in the $\omega\pi\pi$ decay mode [37]; theoretical models also predict this decay mode to be very weak. For the $h_1(1170)$, however, the $\omega\pi\pi$ mode has not been ruled out. Figure 12.11 shows scans of the masses and widths of h_1 and ω resonances (produced with a π° and decaying to $\omega\pi^+\pi^-$) which were added to the Base fit. Both show

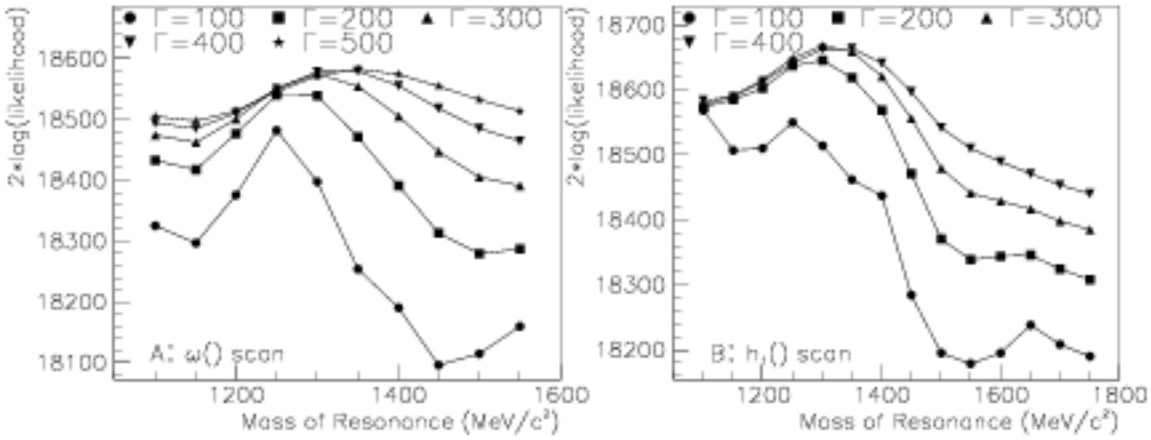

Figure 12.11: Scans of $\omega() \to \omega\pi\pi$ (A), $h_1() \to \omega\pi\pi$ (B), which were added to the Base fit, in production along with a π°.

similar behavior, with the value of $-2\ln\mathcal{L}$ about 100 greater for the h_1 than for the ω. (Note that $\omega(1600) \to \omega\pi\pi$ is included in these fits.) The peaking of $2\ln\mathcal{L}$ at $m = 1300MeV$ rather than at $1170MeV$ is possibly due to 1) the absence of some interfering channel in the Base fit, or 2) the opening of the $\omega(\pi\pi)_s$ phase space, which is inadequately modeled in the fits.

Another indication of the necessity of including an $I = 0$ $\omega\pi\pi$ is shown in Figure 12.12, where four angular distributions are plotted. These angular distributions result from a fit which included the Base fit plus $\bar{p}p \to h_1(1170)\pi$, $h_1 \to \omega\pi\pi$ (for the $h_1(1170)$, the PDG values of mass and width were used.) These are the four angular distributions from Figure 12.5 which were not well described by the Base fit. The agreement between the fit and data is excellent. These distributions are nearly as well fit when an ω-type resonance is included instead of the $h_1(1170)$.

After discussion of the $I = 1$ $\omega\pi\pi$ channels, $\bar{p}p \to h_1(1170)\pi^\circ$, $h_1 \to \omega\pi\pi$ will be included in fits.

12.5.2 $I = 1$ $\omega\pi\pi$ Resonances Near $1500MeV$

The fits and scans in this section are motivated by a desire to explain the result of the scan of the $a_2(1320) \to \omega\pi\pi$ shown in Figure 12.9, in which the mass optimized near $1500MeV$. It will be demonstrated that all $I = 1$ $\omega\pi\pi$ resonances optimize near this mass (not just the a_2) and that the peak is probably not due to a resonance near $1500MeV$.

Figure 12.10B shows the results of scanning the mass and width of an $\omega\pi\pi$ Breit-Wigner term *without any angular dependencies*. That is, it corresponds to no particular resonance type. This term was based only on the $\omega\pi^+\pi^\circ$ and $\omega\pi^-\pi^\circ$ masses, with a Breit-Wigner computed for each of the two combinations and added coherently.

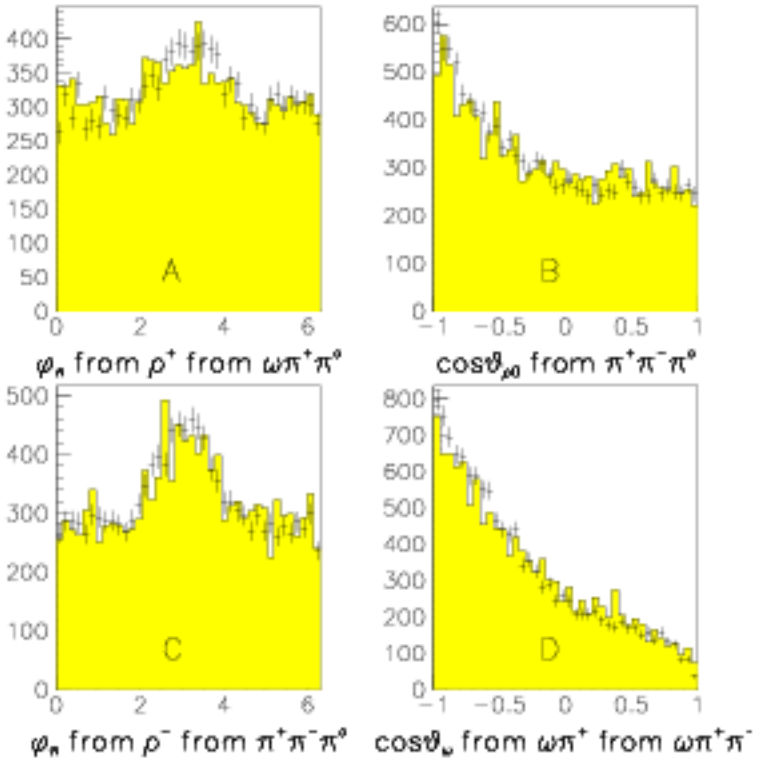

Figure 12.12: Four angular distributions are shown; these are the result of a fit which included the Base fit plus $\bar{p}p \to h_1(1170)\pi$, $h_1 \to \omega\pi\pi$. These are to be compared to Figure 12.5C, D, F and G. The experimental data are shown as crosses and the Monte Carlo data are shown as the shaded histograms. The $\bar{p}p \to \omega\omega$ events have been eliminated by requiring that $m(\pi^+\pi^-\pi^\circ) > 830 MeV/c^2$. The MC histograms have been weighted according to the fit, and have been scaled up to have the same numbers of events as those for the experimental data.

Add	P	contr $\omega\rho$	contr $b_1\pi$	$\omega\omega$	$b_1\rho$	$b_1\sigma$	$a_2\pi$ $\omega\rho$	$a_2\pi$ $b_1\pi$	$\omega()\pi$ $\omega\sigma$	$\omega()\pi$ $b_1\pi$	$h_1()\omega$	$a_1()\omega$	$a_2()\omega$	$\omega()\omega$	$2\ln\mathcal{L}$	$\Delta 2\ln\mathcal{L}$ Base
a_0	4	0.4	1.5	26.5	11.7	1.8	0.7	0.7	4.6	10.6	4.8	13.5	10.7	4.0	18055	98
a_1	4	20.7	0.8	27.4	14.7	1.5	0.3	0.3	2.1	1.1	2.9	5.4	11.5	2.2	18273	316
a_2	6	10.2	4.3	25.1	7.5	2.3	0.7	1.2	4.2	6.6	2.8	10.6	10.5	5.5	18142	185
π	2	8.0	-	25.6	12.1	2.5	0.3	1.1	5.2	9.4	3.6	11.8	7.4	4.7	18204	247
π_2	6	4.7	0.1	26.7	10.6	1.9	0.7	1.1	3.6	8.0	2.8	17.6	9.9	3.9	18235	278
$\hat{\rho}$	10	5.9	6.0	24.5	5.0	3.9	1.3	0.8	5.4	5.9	2.6	11.7	12.0	6.4	18094	137

Table 12.8: Results of fits in which various $I = 1$ $\omega\pi\pi$ resonances were added to the Base fit. Each added resonance was given a mass of $1500MeV$ and a width of $200MeV$. The first three columns show the type of resonance which was added, the number of parameters (P) which were added to the fit, and the contribution of the added channel as a percentage of the total $\pi^+\pi^-\pi^\circ\omega$ final state. Also shown are the value of $2\ln\mathcal{L}$ for the fit, and the change in $2\ln\mathcal{L}$ relative to the Base fit.

The amplitudes for $\lambda_\gamma = \pm 1$ and $m = -1, 0, +1$ were all equal. These combined amplitudes were then added coherently to the other $^3S_1$ amplitudes. The peak is at $m = 1550MeV$, with small widths preferred, and an improvement to $2\ln\mathcal{L}$ of 10-60. This indicates that the peak in the $a_2 \to \omega\pi\pi$ scan is driven in part by kinematics.

The only known $I = 1$ resonance in the 1450-1500MeV mass range which could decay to $\omega\pi\pi$ is the $a_0(1470)$. Preliminary scans showed that an a_0 resonance will show a peak near $1470MeV$, but since the a_2 resonance also does, other resonances should be included in the investigation of this mass region. Table 12.8 shows the results of fits which included the Base case, plus each of six types of $I = 1$ $\omega\pi\pi$ resonances. The added resonances all had their masses set to $1500MeV$ and widths of $200MeV$, to allow comparison of the *type* of resonance independent of the kinematic parameters. All except the π-type resonance had both $\omega\rho$ and $b_1\pi$ decay modes allowed. ($\pi() \to b_1\pi$ is forbidden by angular momentum and parity conservation.) The a_1 type resonance was fit as a rather large ($\sim$25%) contribution, and improved $2\ln\mathcal{L}$ more than the others. The a_0 resonance fared worst, improving $2\ln\mathcal{L}$ by only 99, and being fit as a very weak contribution. These results do not indicate that the $a_0(1470)$ is absent, but the peak in the $a_2 \to \omega\pi\pi$ scan is probably not due to its presence.

Figure 12.13 shows the results of scanning the masses and widths of these six types of resonances. For each scan, the fits included the Base case, along with $\bar{p}p \to R\pi$, $R \to \omega\pi\pi$, where R is the scanned resonance. None shows a maximum which corresponds to a known resonance.

All six scans show a rise in $2\ln\mathcal{L}$ for masses of 1400-1550MeV. This raises the suspicion that the opening of the $\omega\rho$ and $b_1\pi$ phase space is having an effect, and that it is inadequately modeled in the amplitude calculation. Recall that the phase space factor in the Breit-Wigner functions for $\omega\pi\pi$ resonances is Based on $m_\omega + m_\pi$

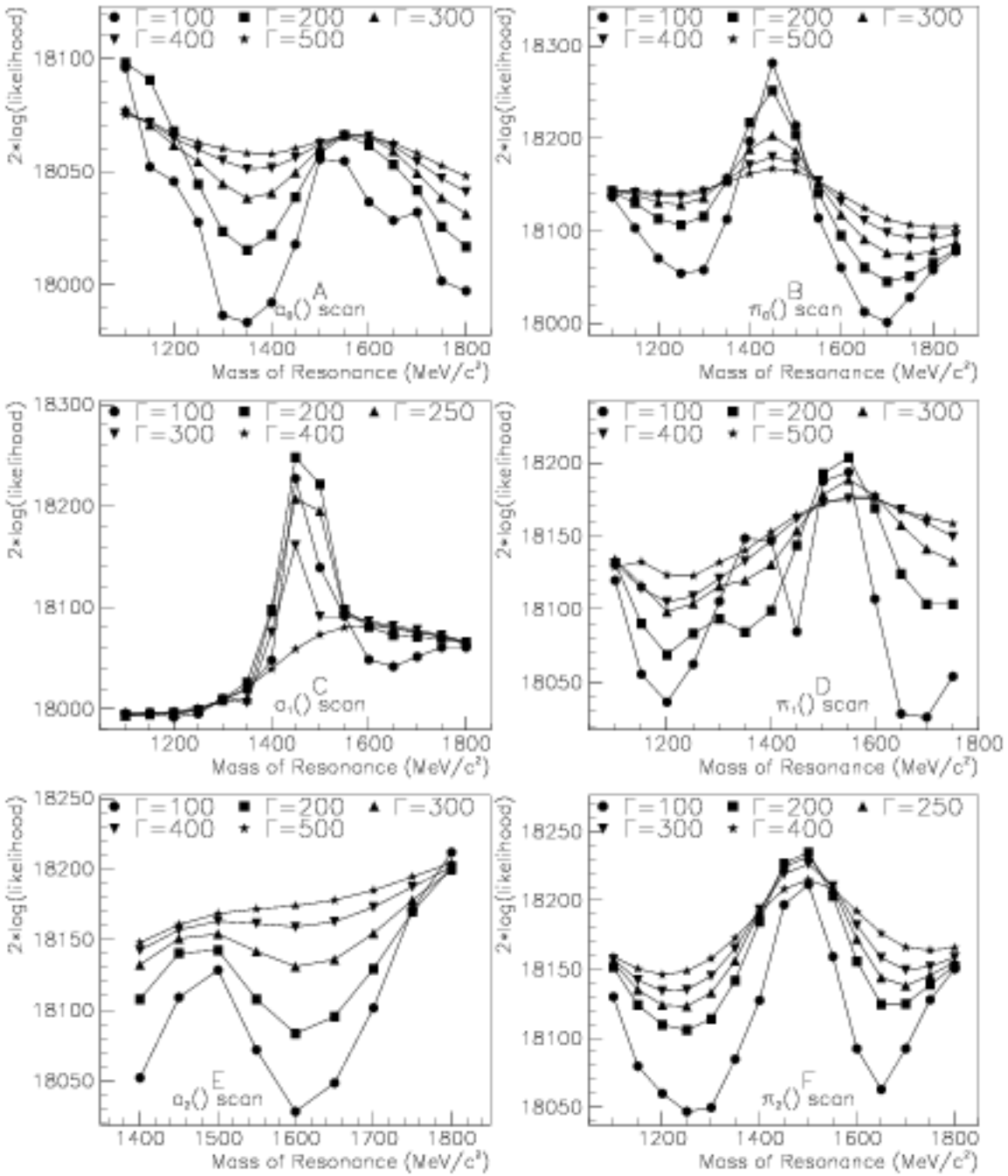

Figure 12.13: Scans of possible isospin 1 $\omega\pi\pi$ resonances' masses and widths: A: $a_0() \to \omega\pi\pi$, B: $\pi() \to \omega\pi\pi$, C: $a_1() \to \omega\pi\pi$, D: $\hat{\rho}() \to \omega\pi\pi$, E: $a_2() \to \omega\pi\pi$, F: $\pi_2() \to \omega\pi\pi$. In these fits, the scanned resonances were added to the Base fit, in production along with a pion.

and m_π (for $b_1\pi$ decays) or $m_\pi + m_\pi$ and m_ω (for $\omega\rho$ and $\omega(\pi\pi)_s$ decays.) (See Section 11.3.1.) This puts the rapidly rising part of the phase space factor at masses near $1000 MeV$. In the physical data, however, the resonances are decaying to objects which are heavier than the sum of the rest masses of the final state particles, and the relativistic corrections to the Breit-Wigner width ($\Gamma(m)$) are almost certainly quite important in the 1400-1550MeV mass region (and at lower masses for $\omega(\pi\pi)_s$ resonances.) A few suggestions have been made as to how to model this effect. Some seemed physically unintuitive, others yielded results which were difficult to interpret and justify. In the end, it seemed better to have a known weakness in the model than to have an elaborate, unfamiliar description which would produce questionable results.

12.5.3 Known and Expected $\omega\pi\pi$ Resonances

Table 12.10 shows the results of fits which included the Base case plus known or expected $\omega\pi\pi$ resonances. (Table 12.9 shows the decay modes which were included and the masses and widths of the resonances which were added.) In the first block, single $\omega\pi\pi$ resonances were added. The addition of the $h_1(1170)\pi$ channel gives by far the greatest improvement to $2\ln\mathcal{L}$. This, plus the issues discussed in Section 12.5.1, indicate that this process may be at work here, so it will be included in subsequent fits. The second block shows fits which included the $h_1(1170)\pi$ channel, along with the Base fit, plus additional $\omega\pi\pi$ resonances. Only the addition of $h_1(1700)$ and $\hat{\rho}(1400)$ cause further improvement of more than 100.

Next, both $a_1(1260)\pi$ and $a_1(1700)\pi$ (with a_1's $\rightarrow \omega\pi\pi$) were added, with and without the $h_1(1170)\pi$ channel, as preliminary fits had shown an interesting effect when *both* a_1's were included: whereas individually they were fit as weak ($< 5\%$) channels, together each is fit as an 8-9% contribution. The value of $2\ln\mathcal{L}$ also improves by 286 over the fit without the two a_1's. This effect will be investigated in Section 12.5.5, but first some observations from Table 12.10 should be pointed out:

- The b_1 D/S ratio usually optimizes at a value near the PDG value of 0.29 ± 0.04. This is a strong indication of the presence of b_1's in the data, probably from $b_1\rho$ production and from decays of the $\omega(1600)$.

- $b_1\rho$ is always strong (7-16% except when $\hat{\rho}(1400)\pi$ is included.) This is no surprise, as $\bar{p}p$ annihilation seems to produce vector mesons (like the ρ) quite copiously. The contribution of this channel is somewhat unstable, though, which may be due to the fact that it is "above phase space," i.e. the central masses of the $b_1(1235)$ and $\rho(770)$ add up to more than the mass of the $\bar{p}p$ system. Only the low-mass tails of the b_1 and ρ are fitted in this channel; this may be causing some ambiguity.

- $b_1(\pi\pi)_s$ falls to less than 1% when $h_1(1170)\pi$, $a_1(1260)\pi$ and $a_1(1700)\pi$ are included. The more channels that are added, the weaker this one becomes.

Resonance	Mass	Width	Included	Not Included
$a_0(1470)$	1470	270	${}^1S_0 \to a_0\pi\ L=0$ $a_0 \to \omega\rho\ L=0; s=0$ $a_0 \to b_1\pi\ L=1$	 $a_0 \to \omega\rho\ L=2, s=2$
$a_1(1260)$	1230	400	${}^3S_1 \to a_1\pi\ L=0$ $a_1 \to \omega\rho\ L=0; s=1$ $a_1 \to b_1\pi\ L=1$	$\boxed{{}^3S_1 \to a_1\pi\ L=2}$ $a_1 \to \omega\rho\ L=2, s=1,2$
$a_1(1700)$	1700	250	${}^3S_1 \to a_1\pi\ L=0$ $a_1 \to \omega\rho\ L=0; s=1$ $a_1 \to b_1\pi\ L=1$	${}^3S_1 \to a_1\pi\ L=2$ $\boxed{a_1 \to \omega\rho\ L=2, s=1,2}$
$a_2(1650)$	1650	250	${}^1S_0 \to a_2\pi\ L=2$ ${}^3S_1 \to a_2\pi\ L=2$ $a_2 \to \omega\rho\ L=0; s=2$ $a_2 \to b_1\pi\ L=1$	 $a_2 \to \omega\rho\ L=2, s=0,1,2$ $a_2 \to \omega\rho\ L=4, s=2$ $a_2 \to b_1\pi\ L=3$
$\pi(1300)$ $\pi(1800)$	1300 1800	400 210	${}^3S_1 \to \pi()\pi\ L=1$ $\pi() \to \omega\rho\ L=1; s=1$	
$\pi_2(1670)$	1670	258	${}^3S_1 \to \pi_2\pi\ L=1$ $\pi_2 \to \omega\rho\ L=1; s=1,2$ $\pi_2 \to b_1\pi\ L=2$	${}^3S_1 \to \pi_2\pi\ L=3$ $\pi_2 \to \omega\rho\ L=3; s=1,2$
$\hat{\rho}(1400)$	1400	300	${}^1S_0 \to \hat{\rho}\pi\ L=1$ ${}^3S_1 \to \hat{\rho}\pi\ L=1$ $\hat{\rho} \to \omega\rho\ L=1; s=0,1,2$ $\hat{\rho} \to b_1\pi\ L=0$	 $\hat{\rho} \to \omega\rho\ L=3; s=2$ $\hat{\rho} \to b_1\pi\ L=2$
$h_1(1170)$	1170	360	${}^3S_1 \to h_1\pi\ L=0$ $h_1 \to \omega(\pi\pi)_s\ L=1$ $h_1 \to b_1\pi\ L=1$	$\boxed{{}^3S_1 \to h_1\pi\ L=2}$
$h_1(1700)$ $h_1(1540)$	1700 1540	250 285	${}^3S_1 \to h_1\pi\ L=0$ $h_1 \to \omega(\pi\pi)_s\ L=1$ $h_1 \to b_1\pi\ L=1$	${}^3S_1 \to h_1\pi\ L=2$
$\omega(1420)$	1419	174	${}^3S_1 \to \omega()\pi\ L=1$ $\omega() \to \omega(\pi\pi)_s\ L=0$ $\omega() \to b_1\pi\ L=0$	 $\omega() \to \omega(\pi\pi)_s\ L=2$ $\omega() \to b_1\pi\ L=2$

Table 12.9: For the $\omega\pi\pi$ resonances which were added to the Base fit, this table shows the allowed angular momenta in production and decays, and the masses and widths of the resonances. The decay chains listed under "Not Included" are those which are allowed by the conservation of the I, G, J, P and C quantum numbers, but which were not included in the fits shown in Table 12.10. Those in the boxes *are* allowed in some of the fits discussed in Section 12.5.5.

$\omega\omega$	$b_1\rho$	$b_1\sigma$	$h_1\omega$	$a_1\omega$	$a_2\omega$	$\omega^*\omega$	$a_2(1320)\pi$		$\omega(1600)\pi$		$h_1(1170)\pi$		$a_1(1260)\pi$		$a_1(1700)\pi$		Added	Contr			$-2\ln\mathcal{L}$	$\Delta 2\ln\mathcal{L}$	D/S
							$\omega\rho$	$b_1\pi$	$\omega\sigma$	$b_1\pi$	$\omega\sigma$	$b_1\pi$	$\omega\rho$	$b_1\pi$	$\omega\rho$	$b_1\pi$		$\omega\rho$	$\omega\sigma$	$b_1\pi$		Base	
26.7	11.0	1.8	5.4	13.5	10.6	4.1	0.7	0.6	4.7	10.7	-	-	-	-	-	-	$a_0(1470)$	0.5	-	1.4	18052	95	.21
25.2	12.3	2.0	5.1	13.2	10.9	4.1	0.9	0.9	4.8	10.5	-	-	-	-	-	-	$a_0(1700)$	0.9	-	1.3	18045	88	.22
26.5	13.4	3.6	3.2	10.9	10.4	4.2	0.2	0.4	5.1	11.8	-	-	-	-	-	-	$a_1(1260)$	0.2	-	1.4	17999	42	.24
26.7	11.1	6.8	3.8	12.0	9.9	3.8	0.5	0.3	5.5	7.4	-	-	-	-	-	-	$a_1(1700)$	1.6		1.4	18069	112	.24
25.0	10.0	2.2	2.6	12.7	11.8	5.3	0.4	0.4	4.6	8.5	-	-	-	-	-	-	$a_2(1650)$	5.6	-	3.0	18117	160	.21
26.2	15.7	2.3	3.2	11.6	8.3	3.7	0.2	0.6	5.6	11.3	-	-	-	-	-	-	$\pi(1300)$	3.0	-	-	18142	185	.25
26.8	15.9	2.2	3.1	10.9	8.9	3.8	0.2	0.4	6.1	12.1	-	-	-	-	-	-	$\pi(1800)$	1.2	-	-	18067	110	.24
26.8	12.5	1.6	2.7	15.7	11.1	3.5	0.5	0.8	4.5	9.7	-	-	-	-	-	-	$\pi_2(1670)$	2.3	-	0.1	18142	185	.18
23.4	13.2	2.6	1.1	12.1	11.4	7.4	0.5	0.5	5.3	10.4	-	-	-	-	-	-	$\hat{\rho}(1400)$	3.6	-	0.3	18116	159	.24
26.8	16.2	0.7	2.1	11.7	10.2	2.4	0.6	0.3	4.4	11.0	-	-	-	-	-	-	$h_1(1170)$	-	5.1	1.5	18599	642	.24
26.3	15.0	1.1	1.5	13.5	10.8	1.9	1.3	0.4	3.7	9.9	-	-	-	-	-	-	$h_1(1700)$	-	3.2	3.3	18364	407	.22
26.2	9.1	1.3	3.6	6.7	7.8	4.7	2.0	0.1	3.8	12.8	-	-	-	-	-	-	$\omega(1420)$	-	12.8	2.3	18314	357	.19
27.3	14.6	0.6	3.3	11.1	10.6	2.5	0.6	0.1	4.5	10.9	5.2	0.7	-	-	-	-	$a_0(1470)$	1.2	-	0.7	18632	675	.25
25.0	17.1	0.7	2.1	11.9	11.4	2.1	0.4	0.3	4.4	9.2	6.2	0.5	-	-	-	-	$a_0(1700)$	0.7	-	1.3	18643	686	.28
26.7	15.2	0.9	2.2	14.0	9.9	2.0	0.5	0.3	4.5	9.6	5.3	0.6	-	-	-	-	$a_1(1260)$	0.9	-	0.4	18624	667	.26
26.3	12.2	1.5	2.5	15.2	8.1	2.4	0.5	0.6	4.7	8.2	5.9	2.1	-	-	-	-	$a_1(1700)$	2.5	-	0.1	18759	802	.21
26.4	18.2	0.6	1.9	12.2	10.6	2.2	0.4	0.3	5.1	9.7	5.2	0.3	-	-	-	-	$a_2(1650)$	0.6	-	0.3	18616	659	.29
26.7	17.8	0.6	2.2	11.0	10.3	1.8	0.6	0.2	5.2	10.7	5.2	0.5	-	-	-	-	$\pi(1300)$	0.2	-	-	18603	646	.26
26.7	16.7	0.6	2.1	10.9	10.7	2.2	0.6	0.3	5.1	11.0	5.5	0.7	-	-	-	-	$\pi(1800)$	.01	-	-	18594	637	.25
26.5	15.8	0.6	2.1	13.0	11.1	2.6	0.5	0.3	4.4	10.2	4.9	0.4	-	-	-	-	$\pi_2(1670)$	0.9	-	0.0	18647	690	.25
23.7	21.5	1.0	0.4	11.7	9.8	0.4	0.3	0.1	4.4	9.7	5.4	0.7	-	-	-	-	$\hat{\rho}(1400)$	2.6	-	2.0	18731	774	.28
26.1	10.0	1.1	2.3	11.4	9.8	2.9	2.1	0.5	1.7	13.0	4.1	2.9	-	-	-	-	$\omega(1420)$	-	5.1	0.5	18685	728	.16
25.6	15.6	0.4	1.4	9.9	9.4	1.5	1.8	0.2	3.8	10.1	6.0	0.1	-	-	-	-	$h_1(1700)$	-	2.4	6.0	18710	753	.17
26.2	15.2	0.6	2.0	13.1	10.5	3.4	0.6	0.2	4.6	9.1	4.7	1.5	-	-	-	-	$h_1(1540)$	-	1.8	0.6	18656	699	.27
26.5	10.5	4.6	3.9	13.1	9.0	4.1	0.4	0.4	5.3	7.8	-	-	1.9	0.3	2.8	0.4	-	-	-	-	18105	148	.24
26.0	9.3	0.6	2.3	15.3	5.8	2.5	0.4	0.2	2.8	4.8	4.7	1.0	8.9	0.1	8.2	.01	-	-	-	-	18885	928	.26

Table 12.10: Results of fits in which decay chains involving various known and expected $\omega\pi\pi$ resonances were added to the Base fit. Contributions are shown as percentage contributions to the total $\pi^+\pi^-\pi^\circ\omega$ final state. $\Delta 2\ln\mathcal{L}$ is the change in $2\ln\mathcal{L}$ relative to the Base fit.

Production of $b_1(\pi\pi)_s$ appears to be too weak to be reliably detected in this analysis.

- $h_1(1170)\omega$ is consistently fit as a contribution of about 2%. The width of the $h_1(1170)$ ($\Gamma \simeq 360MeV$) makes this channel seem very reasonable (the $h_1(1170)$ is only $100MeV$ above phase space.)

- $a_1(1260)\omega$ is always strong (usually 11-15%). This is not too surprising, as the $a_1(1260)$ is quite broad, and the low mass tail of its mass distribution falls well within the available 3π mass range. This channel's contribution becomes stronger when $a_1(1260)\pi$ and $a_1(1700)\pi$ are both included in the fit.

- $a_2(1320)\omega$ is consistently strong, usually 5-11%. This is surprising, but consistent with the previous measurement in $\omega\eta\pi^\circ$ (which indicated that $a_2(1320)\omega$ would be an $8.2 \pm 1.1\%$ contribution here.)

- $\omega(1420)\omega$ seems an unlikely intermediate state to produce, given the high mass and small width of the $\omega(1420)$, yet the fit consistently attributes 1 to 5% of the final state to this channel.

- $a_2(1320)\pi$ is almost always weaker than predicted by CB measurements and by the PDG values for the $\omega\pi\pi$ branching fraction. (These predict a 1 to 3% contribution; see Table 12.3.) Addition of certain channels ($I = 0$ $\omega\pi\pi$ channels) strengthens its contribution: the strongest contribution comes when $\omega(1420)\pi$ is included; adding h_1's seems to strengthen it, too.

- $\omega(1600)\pi$: The total strength of this channel varies somewhat. It is weaker as more channels are added (this is not true for all elements of the Base fit.) Even in the last fit in the table, though, this intermediate state is fit as a 7.6% contribution. Decay of $\omega(1600)$ to $b_1\pi$ is always 1.5 to 2.0 times as strong as to $\omega(\pi\pi)_s$ in the fits. A contribution by this channel of 7% would imply a total rate of $BR(\bar{p}p \to \omega(1600)\pi^\circ, \omega(1600) \to \omega\pi\pi) \simeq 1.1\%$; compare this to $BR(\bar{p}p \to \omega(782)\pi^\circ) = 0.573 \pm 0.047\%$ [38].

- $a_1(1260)\pi$ and $a_1(1700)\pi$ are weak, except when *both* are included, along with $h_1(1170)\pi$; then they are both at about 9% (mostly in the $\omega\rho$, not the $b_1\pi$, decay mode.) Including both of these channels (with $h_1(1170)\pi$) improves $2\ln\mathcal{L}$ by 286 over the fit with neither, by 261 over the fit without $a_1(1700)\pi$, and by 126 over the fit without $a_1(1260)\pi$. This effect is not duplicated with other resonances at these masses. (This will be demonstrated below.) From the results of this PWA one would conclude that the product branching fractions for production and subsequent $\omega\pi\pi$ decays of these two resonances would be about 1.0 to 1.5% of all annihilations. This is suspicious, particularly for the $a_1(1260)$ since its dominant decay mode is believed to be $\rho\pi$.

- $h_1(1170)\pi$ is consistently about 5%, mostly in $\omega(\pi\pi)_s$ as opposed to $b_1\pi$. Including this channel improves $2\ln\mathcal{L}$ by several hundred, and is a necessary ingredient in the afore mentioned effect involving the interference between the $a_1(1260)$ and $a_1(1700)$.

Comments on the other $\omega\pi\pi$ resonances will be presented below, in the discussion of fits in which they were added to the last fit in Table 12.10.

The first block of Table 12.11 shows fits with the Base case plus $h_1(1170)\pi$, $a_1(1260)\pi$ and $a_1(1700)\pi$ (fit "B16"), along with additional $\omega\pi\pi$ resonances. Only the $\tilde{\rho}(1400)\pi$ channel yields further improvement of more than 100.

Below are comments concerning the resonances which were added in the fits shown in the first block of Table 12.11:

- Neither $\pi(1300)\pi$ nor $\pi(1800)\pi$ gives a strong contribution, nor do they improve $2\ln\mathcal{L}$ much.

- $\pi_2(1670)$: There is no compelling evidence for observation of this resonance in an $\omega\pi\pi$ decay mode.

- Neither $a_0(1470)$ nor $a_0(1700)$ yields much improvement to $2\ln\mathcal{L}$; they are both fit as small (1-2%) contributions. This is consistent with expectations, that $a_0(1470)\pi$ would have a strength similar to that of $a_2(1320)\pi$. There is a great interest in the possible $\omega\pi\pi$ decay mode of the $a_0(1470)$, but with its production being weak in comparison to the very large total rate for $\pi^+\pi^-\pi^\circ\omega$, this analysis is just not sensitive to it.

- $\omega(1420)\pi$ improves $2\ln\mathcal{L}$ when included without $h_1(1170)\pi$, and is fitted as a 15% contribution. In this fit, the D/S ratio for $b_1 \to \omega\pi$ drops to 0.19. The $\omega(\pi\pi)_s$ decay mode is preferred for the $\omega(1420)\pi$ (in contrast to the $\omega(1600)$.) When $h_1(1170)\pi$ is included, it falls to a 7.5% contribution, and falls to a 1% contribution when $a_1(1260)\pi$ and $a_1(1700)\pi$ are also included. As a negative result concerning a search for $\omega(1420) \to \omega\pi\pi$ has been published, and the fit prefers other descriptions, no claim for observation of this channel is made here. The strong effect of this channel in the incomplete fits (when $a_1(1260)\pi$ and $a_1(1700)\pi$ are not included) demonstrates that one channel can mimic another, and that a large change in $2\ln\mathcal{L}$ and a large fitted contribution aren't necessarily signs that a hypothesized description is correct.

- $h_1(1540)$ and $h_1(1700)$ have effects similar to those of the $\omega(1420)$; they are fit as relatively strong contributions with good improvement to $2\ln\mathcal{L}$ in Table 12.10, but in the more complete fits in Table 12.11 they produce small changes.

Including the $\tilde{\rho}(1400)\pi$ channel in the fits has the effect of reducing the contribution of $\omega\omega$ compared to other fits, and also changes the contributions for other decay chains, most notably $b_1\rho$, $h_1\omega$ and $\omega(1420)\omega$. Its contribution is fit as about

$\omega\omega$	$b_1\rho$	$b_1\sigma$	$h_1\omega$	$a_1\omega$	$a_2\omega$	$\omega^*\omega$	$a_2(1320)\pi$		$\omega(1600)\pi$		$h_1(1170)\pi$		$a_1(1260)\pi$		$a_1(1700)\pi$		Added	Contr			$-2\ln\mathcal{L}$	$\Delta 2\ln\mathcal{L}$	$\Delta 2\ln\mathcal{L}$	D/S
							$\omega\rho$	$b_1\pi$	$\omega\sigma$	$b_1\pi$	$\omega\sigma$	$b_1\pi$	$\omega\rho$	$b_1\pi$	$\omega\rho$	$b_1\pi$		$\omega\rho$	$\omega\sigma$	$b_1\pi$		Base	B16	
26.0	9.3	0.6	2.3	15.3	5.8	2.5	0.4	0.2	2.8	4.8	4.7	1.0	8.9	0.1	8.2	.01	-	-	-	-	18885	928	0	.26
26.9	7.8	0.5	2.5	16.0	6.0	2.0	0.7	0.1	2.4	4.2	4.6	0.8	8.8	0.1	8.6	.01	$a_0(1470)$	0.1	-	0.7	18930	973	45	.31
25.6	9.9	0.7	1.5	15.3	6.3	2.0	0.9	0.2	2.5	3.9	4.9	0.9	8.6	0.3	8.3	.04	$a_0(1700)$	0.4	-	0.8	18919	962	34	.33
25.6	9.2	0.5	2.3	14.7	5.5	2.5	0.5	0.3	2.4	5.0	4.1	1.0	9.2	0.1	8.9	.06	$a_2(1650)$	1.1	-	0.1	18955	998	70	.26
25.9	9.0	0.6	2.5	15.6	5.6	2.3	0.4	0.2	2.6	4.4	4.6	0.7	9.5	0.1	8.6	0.0	$\pi(1300)$	0.2	-	-	18893	936	8	.28
26.0	9.0	0.6	2.5	15.5	5.7	2.4	0.4	0.2	2.6	4.5	4.7	0.7	9.1	0.1	8.6	0.0	$\pi(1800)$	0.1	-	-	18889	932	4	.28
25.9	7.6	0.5	2.3	16.6	6.4	2.4	0.7	0.2	2.4	4.2	4.6	1.0	8.7	.04	9.0	.02	$\pi_2(1670)$	0.3	-	.09	18923	966	38	.26
21.3	2.2	0.6	2.1	14.8	4.7	7.2	0.4	.02	2.2	4.1	4.8	1.7	8.9	.04	11.4	0.2	$\tilde{\rho}(1400)$	6.3	-	1.0	19101	1144	216	.10
25.9	8.0	1.0	2.4	14.8	5.1	3.4	0.6	0.3	2.6	6.0	3.8	1.6	8.2	0.1	8.2	.08	$\omega(1420)$	-	0.8	0.4	18918	961	33	.27
26.3	8.9	0.7	2.5	15.2	6.0	1.9	0.4	0.1	2.8	4.3	4.5	2.0	6.8	0.3	7.8	.04	$h_1(1700)$	-	0.8	1.4	18952	995	67	.25
26.3	8.7	0.8	2.6	13.8	5.2	2.5	0.4	0.2	3.2	4.8	3.3	3.4	7.3	0.3	7.7	0.2	$h_1(1540)$	-	0.6	1.6	18959	1002	74	.25
26.8	7.7	0.6	2.9	15.9	5.9	2.0	0.6	0.2	2.5	4.3	4.6	0.8	8.8	0.1	8.5	0.0	$a_0(1400)$	0.2	-	0.5	18924	967	39	.31
25.4	9.3	0.8	2.0	14.2	6.0	3.0	0.3	0.5	3.0	5.2	5.0	1.1	7.7	0.1	8.0	0.0	$a_2(1400)$	0.1	-	1.5	18915	958	30	.25
25.9	9.2	0.6	2.5	15.6	5.6	2.1	0.5	0.2	2.5	4.3	4.6	0.7	9.5	0.1	8.5	0.0	$\pi(1400)$	0.2	-		18893	936	8	.28
26.1	7.8	0.5	2.0	13.2	7.3	2.0	1.6	0.1	2.0	4.3	5.7	1.0	7.9	0.5	8.8	0.0	$\pi_2(1400)$	1.4	-	0.6	18969	1012	84	.31

Table 12.11: First block: Results of fits in which decay chains involving various known and expected $\omega\pi\pi$ resonances were added to the fit B16. Second block: Fits in which other types of resonances were used in place of the $\tilde{\rho}(1400)$. Contributions are shown as percentage contributions to the total $\pi^+\pi^-\pi^\circ\omega$ final state. Also shown are the changes in $2\ln\mathcal{L}$, relative to the Base fit and relative to fit B16.

4-7% to this channel. It always improves $2\ln\mathcal{L}$ more than other resonances do, but it also adds more parameters (10) than other channels do. This channel deserves some consideration.

In the second block of Table 12.11, fits are shown which were performed to investigate the strong improvement to $2\ln\mathcal{L}$ that results by including the $\hat{\rho}(1400)\pi$ channel. These fits were run with a_0, a_2, π and π_2 type resonances with their masses and widths set to those of the $\hat{\rho}(1400)$ ($m = 1400MeV$, $\Gamma = 300MeV$.) None produces an improvement as large as that caused by including the $\hat{\rho}(1400)$. This indicates that it is not just kinematics (i.e. the location and width of the resonance) driving the results; there *is* a dependence on the J^{PC} of the resonance.

The production of $\hat{\rho}\pi$ can occur from both $^1S_0$ and $^3S_1$; for the three fits in Tables 12.10 and 12.11 which involve the $\hat{\rho}(1400)$, the fitted ratios of production rates are:

Fit	$\frac{BR(\,^1S_0\to\hat{\rho}\pi]}{BR(\,^3S_1\to\hat{\rho}\pi]}$
Base + $\hat{\rho}\pi$	41.3
Base + $h_1(1170)\pi$ + $\hat{\rho}\pi$	6.5
B16 + $\hat{\rho}\pi$	5.0

That is, production from $^1S_0$ is fitted as being much stronger that from $^3S_1$. This pattern is in conflict with the other Crystal Barrel analyses in which the $\hat{\rho}(1400)\pi$ is observed (in its $\eta\pi$ decay mode) [56]; production from $^1S_0$ is seen to be very weak compared to production from $^3S_1$ and from P states.

Notice (see Table 12.9) that the $\hat{\rho}$ can decay to $\omega\rho$ with $s_{\omega\rho} = 0, 1, 2$ (which is why 10 parameters are required for its description in the fits.) The interferences among these spin states may allow for the high values of $2\ln\mathcal{L}$ which result when $\hat{\rho}$ is included in the fits. The relative strengths of these three states in the $\hat{\rho}$ decays are not consistent among the three fits in which the $\hat{\rho}(1400)$ is involved:

Fit	$BR(s=0) : BR(s=1) : BR(s=2)$
Base + $\hat{\rho}\pi$	1 : 28.2 : 13.1
Base + $h_1(1170)\pi$ + $\hat{\rho}\pi$	1 : 9.8 : 0.4
B16 + $\hat{\rho}\pi$	1 : 1.8 : 2.8

For a comparison with another resonance, note that when $L = 2$ is allowed for $\omega\rho$ decays of the a_1 resonance, all three spin couplings of the $\omega\rho$ system are allowed. In these fits, even greater improvement is seen in $2\ln\mathcal{L}$ (see Table 12.12.)

The internal instability and inconsistency with previous measurements do not support a claim of the observation of this resonance.

For the fits shown in Table 12.11, there are many parameters, and it is difficult to find true minimum. The minimum found by the minimization program depends on initial values for the parameters, so each fit must be run several times, each with different sets of initial values. The value of $2\ln\mathcal{L}$ varies by 10 to 70 among these fits, with the contributions varying by up to 1 percentage point. To continue to add

decay chains to the fits is not only expensive in terms of computing resources, but the results are unreliable, in that the optimum set of parameters which is found may be due to a local minimum, rather than the true best fit. For this reason, the set of decay chains in fit B16 will be accepted as the major contributions to this final state, but only after some verifications of the reliability of this solution are performed.

12.5.4 Scans of Resonances in the B16 Fit

Fit "B16" includes the Base fit plus $\bar{p}p \to h_1(1170)\pi$, $\bar{p}p \to a_1(1260)\pi$ and $\bar{p}p \to a_1(1700)\pi$. This is the fit shown in the last line of Table 12.10. To determine if the masses and widths of the resonances involved in this fit optimize at the values obtained in other experiments, some scans will again be performed. In order to reduce by 4 the number of parameters in the fit, the $b_1\pi$ decay mode for the $a_1(1260)$ and $a_1(1700)$ is not included, as it was consistently fit as quite weak ($< 1\%$.) Disallowing the $b_1\pi$ decay mode changes the value of $2\ln\mathcal{L}$ by only 2, to 18883. Figure 12.14 shows the results of scanning the masses and widths of the $\omega\pi\pi$ resonances in the B16 fit. The scan of $a_1(1260) \to \omega\pi\pi$ peaks at $m = 1300$ to $1350 MeV$ for small widths, but at $m = 1250$ and $\Gamma = 400$, the value of $2\ln\mathcal{L}$ is lower by only about 10 than at the peak. The value drops rapidly for masses greater than $1400 MeV$. The results seem consistent with the presence of the $a_1(1260)$ in the $\omega\pi\pi$ decay mode.

The scan of the higher-mass $a_1 \to \omega\pi\pi$ shows a rise and plateau at masses greater than $1700 MeV$, where the $\omega\pi\pi$ phase space cuts off. This behavior is consistent with the presence of the $a_1 \to \omega\pi\pi$ near the high mass end of phase space. For $\Gamma = 200$ and $300 MeV$, there is a small dip in $2\ln\mathcal{L}$ centered at $1650 MeV$.

The $h_1 \to \omega\pi\pi$ scan shows a peak at $1300 MeV$, but $2\ln\mathcal{L}$ is only greater by about 50 there than at $1170 MeV$. Given the limitations of the analysis model in regard to the $\omega\pi\pi$ phase space, this seems consistent with observation of $\bar{p}p \to h_1(1170)\pi^\circ$, $h_1 \to \omega\pi\pi$.

The scan of $a_2 \to \omega\pi\pi$ still shows the disturbing trend of peaking at 1450-1500MeV, with a minimum near $1320 MeV$ (as it did in the scans in the Base fit.) The lack of a peak at $1320 MeV$ may indicate that $BR(a2(1320) \to \omega\pi\pi)$ is much smaller than it is currently believed to be. The peak at 1450-1500MeV is probably due to the opening of the $\omega\rho$ phase space, as discussed in Section 12.5.2.

The scan of $\omega(1600) \to \omega\pi\pi$ shows a rise is $2\ln\mathcal{L}$ at $1650 MeV$, with a small preference for large widths. This seems to indicate the presence of the process $\bar{p}p \to \omega(1600)\pi^\circ$, $\omega(1600) \to \omega\pi\pi$ in the data.

Because of the results shown in Figure 12.7C and D, the $a_2(1320) \to \rho\pi$ and $\omega(1420) \to \rho\pi$ resonances were scanned in the B16 fit. The results, shown in Figure 12.15, are similar to the earlier scans. The $\omega \to \rho\pi$ scan optimizes at $1050 MeV$ for small widths. The fit at the optimum is better than at the PDG values by only about 20 in $2\ln\mathcal{L}$; this may not be a great concern. For the a_2 scan, however, the fit at the optimum is better by nearly 100 than at the PDG values. Leaving out the

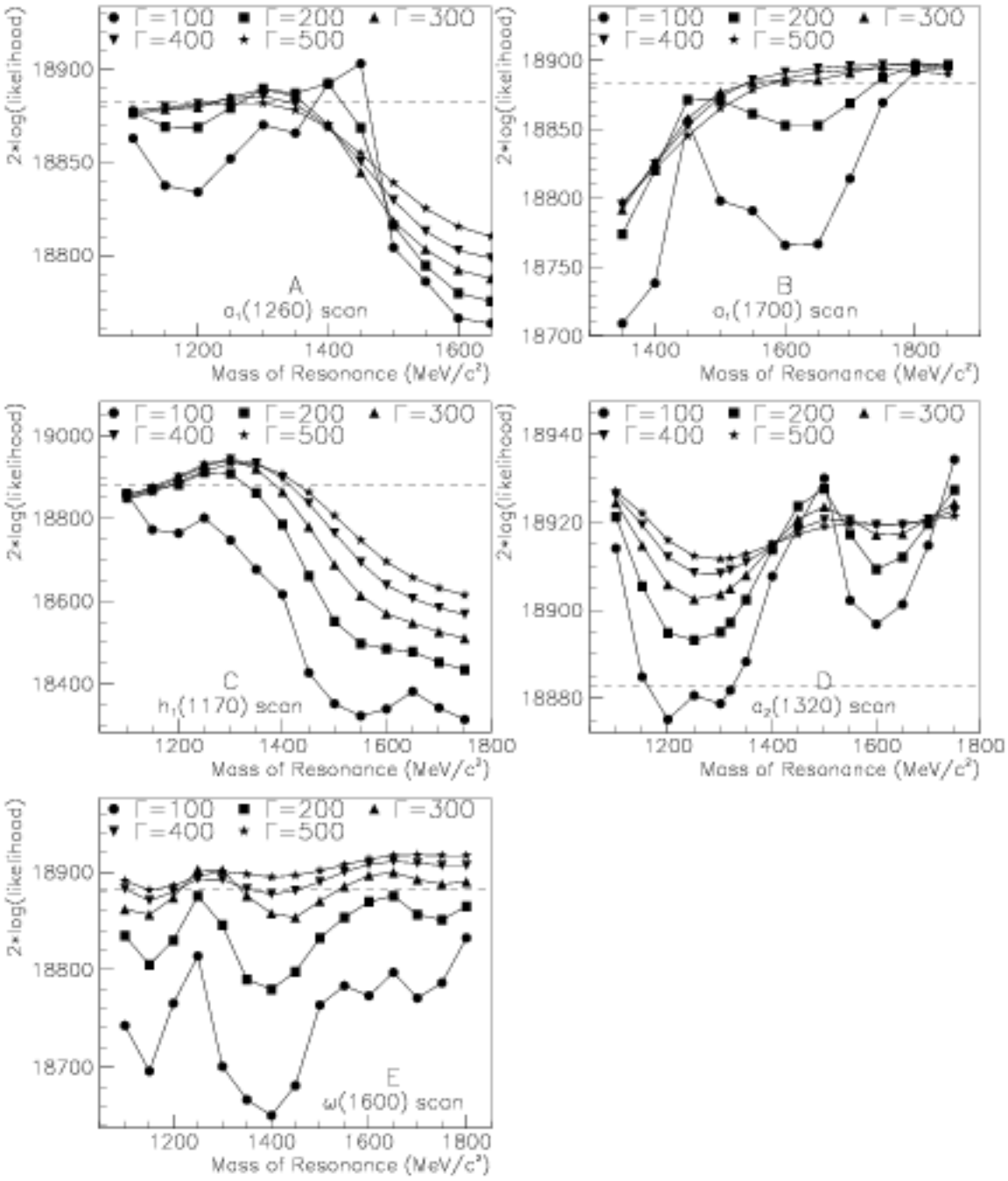

Figure 12.14: Scans of $\omega(1600) \to \omega\pi\pi$ (A), $h_1(1170) \to \omega\pi\pi$ (B), $a_1(1260) \to \omega\rho$ (C), $a_1(1700) \to \omega\rho$ (D) and $a_2 \to \omega\pi\pi$ (E). These are the $\omega\pi\pi$ resonances involved in the B16 fit (see text.)

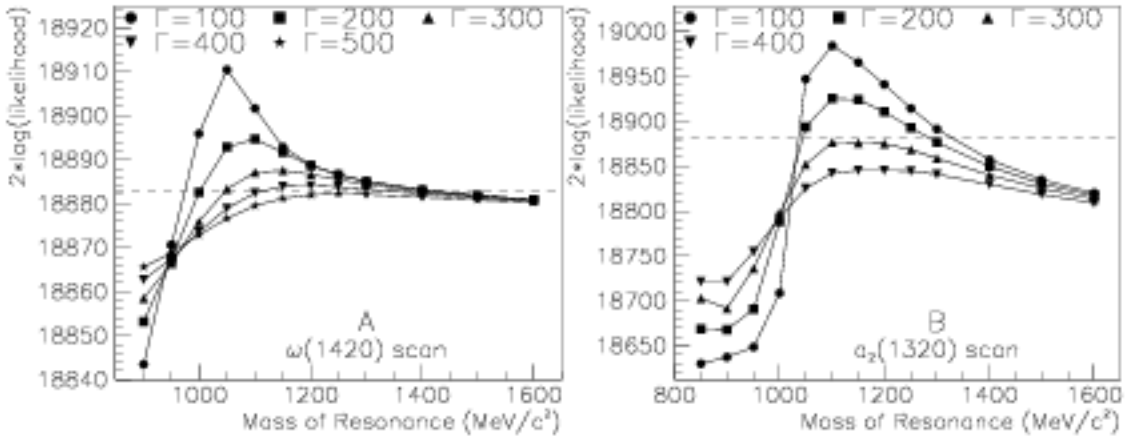

Figure 12.15: Scans of $\omega(1420) \to \rho\pi$ (A) and $a_2(1320) \to \rho\pi$ (B) in fit B16.

$a_2\omega$ channel results in a change of $\Delta 2 \ln \mathcal{L} = 323$, however, indicating that this decay chain plays an important role in the fit. It may be mimicking a background or an $\omega\pi\pi$ resonance that is not included in the fits, but again, the level at which it is fit is consistent with that obtained in the Crystal Barrel analysis of $\bar{p}p \to \omega\eta\pi^\circ$. It is hard to believe that this decay chain is mimicking the same process in the two data sets.

12.5.5 Further Investigations

To investigate some of the interesting features found in the fits in Table 12.10 and in Figures 12.14 and 12.15, additional fits were run and are shown in Table 12.12.

Note that $a_1(1260)\pi$ and $a_1(1700)\pi$ contribute 8-9% each when they are both included along with $h_1(1170)\pi$ in the fit. When any one of these three channels is excluded, the $a_1\pi$ channels each contribute less than 5%. Perhaps *any* two types of resonances at these masses would produce a similar result. In order to determine if this is necessarily due to a_1-type resonances, some fits were run with a_0 and a_2 resonances with their masses and widths set to those of the a_1's ($\{m, \Gamma\} = \{1230, 400\}$ and $\{1700, 250\}$). (In the fits where two a_1-like a_2's were included, the $a_2(1320) \to \omega\pi\pi$ was replaced by the "$a_2(1230)$.") Results are shown in the first block of Table 12.12. Neither a_0 nor a_2 resonances produce the same effect as the a_1's; the $a_{0,1,2}\pi$ decay chains are consistently fit as weak contributions, with small improvements to $2 \ln \mathcal{L}$. Only the inclusion of $a_1(1260)\pi$ and $a_1(1700)\pi$ produces the reinforcing effect. This test supports the claim for observation of the $\omega\pi\pi$ decay mode the these two a_1 resonances.

This is further investigated by including the $a_1(1260)\pi$ channel along with $\pi(1800)\pi$ and $\pi_2(1670)$ and also by including the $a_1(1700)\pi$ along with $\pi(1300)\pi$; see the second block of Table 12.12. Again, none of these combinations produces the effect seen by combining the $a_1(1260)\pi$ and $a_1(1700)\pi$ channels.

$\omega\omega$	$b_1\rho$	$b_1\sigma$	$h_1\omega$	$a_1\omega$	$a_2\omega$	$\omega^*\omega$	$a_2(1320)\pi$		$\omega(1600)\pi$		$h_1(1170)\pi$		$a_1(1260)\pi$		$a_1(1700)\pi$		Note	$-2\ln\mathcal{L}$	$\Delta 2\ln\mathcal{L}$	$\Delta 2\ln\mathcal{L}$
							$\omega\rho$	$b_1\pi$	$\omega\sigma$	$b_1\pi$	$\omega\sigma$	$b_1\pi$	$\omega\rho$	$b_1\pi$	$\omega\rho$	$b_1\pi$			Base	B16
25.4	14.9	0.8	3.2	12.5	10.2	1.9	0.7	0.3	3.8	9.6	5.3	1.3	0.6†	0.1†	1.2‡	1.0‡	†$a_0(1230)$, ‡$a_0(1700)$	18662	705	-223
24.3	12.9	0.7	1.9	11.8	10.5	4.0	-	-	3.8	10.6	5.0	1.9	2.6†	0.9†	1.7‡	0.4‡	†$a_2(1230)$, ‡$a_2(1700)$	18665	708	-220
22.7	10.5	0.7	2.6	10.6	11.1	4.9	0.6	0.7	3.4	10.0	5.7	1.1	3.7†	1.4†	3.2‡	1.5‡	†$a_0(1230)$, ‡$a_2(1700)$	18743	786	-142
25.9	15.4	0.7	2.0	11.6	10.0	3.3	0.9	0.1	4.4	11.1	5.0	1.5	0.6†	0.8†	0.0‡	0.0‡	†$a_2(1230)$, ‡$a_0(1700)$	18636	679	-249
26.7	14.3	0.9	2.3	13.3	9.4	2.4	0.6	0.4	4.0	10.8	5.0	1.5	0.8†	0.4†	0.0‡	0.0‡	†$a_1(1230)$, ‡$a_0(1700)$	18627	670	-258
25.2	11.5	0.7	2.0	13.9	9.8	3.7	1.1	0.3	3.6	10.6	5.0	1.8	1.1†	0.4†	1.6‡	0.7‡	†$a_1(1230)$, ‡$a_2(1700)$	18655	698	-230
26.4	12.4	1.8	2.4	15.5	7.7	2.5	0.7	0.4	4.1	7.9	5.6	2.4	0.0†	0.0†	2.2‡	4.0‡	†$a_0(1230)$, ‡$a_1(1700)$	18761	804	-124
26.1	11.4	1.6	2.3	15.2	7.9	3.3	1.0	0.2	4.0	8.3	5.7	2.4	0.0†	0.7†	2.4‡	0.3‡	†$a_2(1230)$, ‡$a_1(1700)$	18793	836	-92
26.5	12.7	1.2	2.6	13.9	9.8	2.8	0.8	0.4	3.6	10.3	4.3	1.2	1.1	0.8	0.7‡	0.1‡	‡$\pi_2(1670)$	18675	718	-210
26.7	14.2	0.8	2.3	13.4	9.4	2.4	0.6	0.4	4.0	10.8	5.1	1.5	0.8	0.4	0.0‡	-	‡$\pi(1800)$	18627	670	-258
26.0	9.9	0.4	2.1	11.6	8.9	3.5	1.0	0.2	3.2	11.8	5.3	4.2	1.6	1.1	0.2‡	2.2‡	‡$a_2(1650)$	18671	714	-214
26.7	7.2	0.2	2.6	17.5	8.1	2.7	1.1	0.6	2.9	7.1	7.1	3.8	1.1†	-	4.2	0.1	†$\pi(1300)$	18773	816	-112
25.0	7.5	0.9	*5.9	*19.5	2.6	4.4	0.4	0.3	*1.8	*5.2	3.5	1.1	7.7	0.2	6.4	0.3	*Higher L's allowed	19129	1172	244
23.4	9.7	0.5	*5.7	*16.4	2.0	5.0	0.4	0.0	*2.3	*4.6	*4.6	*0.5	*10.0	*0.1	*11.1	*0.1	*Higher L's allowed	19224	1267	339
25.9	9.0	0.3	2.4	*16.4	2.1	1.7	0.3	0.1	*2.5	*4.4	*4.2	*0.4	* 9.8	*0.4	*14.0	*0.0	*Higher L's allowed	19150	1193	265
23.8	4.8	0.6	4.4	22.9	-	4.6	0.5	0.3	2.5	4.0	4.7	1.1	8.4	0.6	9.6	0.1	No $a_2\omega$	18512	555	-373
26.7	9.3	0.4	2.9	15.9	6.4	-	0.9	.03	2.6	2.9	4.9	0.8	9.4	0.1	9.7	0.0	No $\omega(1420)\omega$	18834	877	-51
25.8	6.5	0.8	4.7	23.7	-	-	0.6	0.1	2.6	3.3	4.5	0.9	8.7	0.7	10.3	.01	No $a_2\omega$, $\omega(1420)\omega$	18460	503	-425
25.1	10.1	0.8	2.2	15.6	5.1	1.4	0.8	0.2	2.6	3.5	4.6	0.8	9.6	0.5	8.7	0.0	15% CL cut	18581	624	-304
26.5	9.8	0.5	2.1	14.4	5.2	2.7	0.1	0.3	2.5	4.2	4.1	1.2	10.8	0.4	8.4	0.1	20% CL cut	18759	802	-126
26.0	9.3	0.6	2.3	15.3	5.8	2.5	0.4	0.2	2.8	4.8	4.7	1.0	8.9	0.1	8.2	0.0	25% CL cut	18885	928	0
26.3	10.4	0.8	2.3	15.5	6.0	2.2	0.4	0.2	2.7	5.1	4.8	1.0	6.8	0.1	8.1	0.1	30% CL cut	18957	1000	72
26.7	9.1	0.5	2.4	16.1	6.2	2.5	0.4	0.2	2.4	4.4	5.5	0.8	6.7	0.1	8.8	0.0	35% CL cut	19290	1333	405
26.4	4.5	0.7	2.6	15.9	6.0	3.1	0.6	0.3	2.2	3.1	6.4	1.5	8.5	0.6	12.0	0.1	40% CL cut	19530	1573	645
28.0	7.7	0.6	3.1	17.4	7.2	1.0	0.5	0.4	2.5	2.8	6.2	0.3	7.2	0.1	9.0	0.0	45% CL cut	19428	1471	543
27.1	6.4	1.0	3.0	16.2	6.9	1.0	1.1	0.5	2.5	2.7	6.1	0.9	7.5	0.1	9.6	0.0	50% CL cut	19652	1695	767

Table 12.12: Results of supplemental fits. Contributions are shown as percentage contributions to the total $\pi^+\pi^-\pi^\circ\omega$ final state. Also shown is the change in $2\ln\mathcal{L}$ relative to the Base fit and relative to fit B16. 1st Block: Replacing the $a_1(1260)$ and $a_1(1700)$ $\omega\pi\pi$ resonances with a_0 and a_2 type resonances with similar masses and widths, to verify that a_1's are needed. 2nd Block: $a_1(1700)$ or $a_1(1260)$ with other known resonances. 3rd Block: Include higher L's in production and decays. 4th Block: Excluding $a_2(1320)\omega$ and $\omega(1420)\omega$ production from the fits. 5th Block: Changing the CL cut, and thus the amount of background. 6th Block: Try other types of $I = 1$ $\omega\pi\pi$ resonances in place of the $\hat{\rho}(1400)$ (but with the mass and width of the $\tilde{\rho}(1400)$.)

Recall that when $L = 2$ decays were included in the Base fit a significant improvement resulted (see Table 12.6(B).) The $h_1(1170) \to \rho\pi$, however, showed stronger decays with $L = 2$ than with $L = 0$, which seemed physically unlikely and is inconsistent with previous measurements. This is further investigated by the fits shown in the third block of Table 12.12, where, in addition to the Base case, the $h_1(1170)\pi$, $a_1(1260)\pi$ and $a_1(1700)\pi$ channels are included (as in fit B16.) Below, the D/S ratios are shown for the processes in the three fits discussed here. For the decay $a_1(1700) \to \omega\rho$, both $D(s_{\omega\rho} = 1)/S$ and $D(s_{\omega\rho} = 2)/S$ are shown.

Reaction	D/S ratios		
	B16a	B16b	B16c
$h_1(1170) \to \rho\pi$	.91	.53	-
$a_1(1260) \to \rho\pi$	.13	.13	.08
$\omega(1600) \to \omega(\pi\pi)_s$	.18	.16	.13
$\omega(1600) \to b_1\pi$	.10	.15	.12
$\bar{p}p \to h_1(1170)\pi$	-	.19	.17
$\bar{p}p \to a_1(1260)\pi$	-	.09	.06
$a_1(1700) \to \omega\rho$	-	.17,.06	.17,.05

In the first of these fits (B16a in the table above,) only those resonances in the Base fit had $L = 2$ decays allowed (to see if the previous anomalous result was due to the exclusion of one of the additional channels.) The unphysical result is still found: $L = 2$ decays are about 4 times stronger than $L = 0$ decays for $h_1(1170) \to \rho\pi$. In the 2nd of these fits (B16b,) a very reasonable set of higher angular momenta was allowed: in *production* of the low mass $\omega\pi\pi$ resonances $a_1(1260)$ and $h_1(1170)$, and in *decays* of the higher mass $\omega\pi\pi$ resonances $a_1(1700)$ and $\omega(1600)$, and also in decays of the $\rho\pi$ resonances $h_1(1170)$ and $a_1(1260)$. Still, for $h_1(1170) \to \rho\pi$, $L = 2$ decays are about 40% stronger than $L = 0$ decays. Other process show quite reasonable results. Because of the unlikely result involving $h_1(1170) \to \rho\pi$, its $L = 2$ decay was disallowed for the next fit (B16c.) The value of $2\ln\mathcal{L}$ falls by 74, but the D/S ratios are still reasonable; that for $a_1(1260) \to \rho\pi$ falls to 0.08, which agrees well with the PDG value of 0.09 ± 0.03.

Notice that in the fits where $L = 2$ is allowed for the decay of the $a_1(1700)$, it can decay to $\omega\rho$ with all three spin couplings ($s_{\omega\rho} = 0, 1, 2$.) The interferences among these spin states was put forth above as the reason for the good values of $2\ln\mathcal{L}$ obtained from fits which involved the $\hat{\rho}(1400)$. Allowing the three spin states for the $a_1(1700)$ actually yields a better value for $2\ln\mathcal{L}$, thus supporting the proposition.

The scans of the $\omega(1420) \to \rho\pi$ and $a_2(1320) \to \rho\pi$ resonances showed some inexplicable behavior, perhaps indicating that these decay chains are mimicking some other process (see Figure 12.15.) Leaving these channels out of the Base fit had a strong effect on the fit (see Table 12.6(K-M).) In the fourth block of Table 12.12, fits are shown in which these two decay chains are excluded, separately and together. In these fits, in addition to the Base case, the $h_1(1170)\pi$, $a_1(1260)\pi$ and $a_1(1700)\pi$ channels are included. The strong effects of dropping these two decay chains remain.

In the fifth block of Table 12.12, the effect of background in the data is investigated by varying the cut on the confidence level of the kinematic fit to $\bar{p}p \to \pi^+\pi^-\pi^\circ\omega$, and thus varying the amount of background in the data sample. The values of these eight fits (in addition to others) were used in the derivation of the systematic uncertainties on the measured contributions to the final state. (See Section 12.6.2.)

12.6 Error Analysis

In this section, the methods used in computing the uncertainties on the measured contributions to the $\pi^+\pi^-\pi^\circ\omega$ final state are presented. The systematic uncertainties are based on fluctuations in the measurements resulting from two factors: 1) the effect of backgrounds (events which are not $\pi^+\pi^-\pi^\circ\omega$) in the data sample, and 2) what processes are included in the PWA fits. The statistical uncertainties on the measurements are derived from the uncertainties in the parameters involved in the computer fitting algorithm. These are discussed in the following subsections.

12.6.1 Statistical Errors

Recall that the parameters used in the fitting function are strengths and phases of the various process, relative amounts of the two initial states ($^1S_0$ and $^3S_1$), and others such as those which determine the D/S ratio in the $b_1 \to \omega\pi$ decays. The contribution level of the production and decay processes are derived from the parameters in a complicated way involving numerical integration of the individual amplitudes. Additionally, the error matrix which is generated by MINUIT [62], the minimization package used in the fits, is not positive definite and cannot be used in the conventional way to ascertain the uncertainties. This non-positive definiteness is probably the result of the strong correlations among the parameters and the formulation of the fitting function in terms of strength coefficients and phase angles. These strong correlations are due to the parameterization of the fitting function; for example, the amplitude for $\bar{p}p \to \omega(1600)\pi,\ \omega(1600) \to b_1\pi,\ b_1 \to \omega\pi\ (L=2)$ is multiplied by a function of 5 parameters:

$$b_1 e^{i\phi_1} \cdot b_2 e^{i\phi_2} \cdot (1 - F_{^1S_0}),$$

where b_1 and ϕ_1 are the strength and phase for production of $\omega(1600)\pi$, b_2 and ϕ_2 are the strength and phase for $b_1 \to \omega\pi\ L=2$ (relative to $L=0$), and $F_{^1S_0}$ is the fraction of annihilations occurring from the $^1S_0$ initial state of the $\bar{p}p$ atom. This type of formulation results in large correlation coefficients for the parameters, and makes errors on the individual parameters difficult to interpret. A numerical scheme is used to extract the uncertainties on the contribution levels (branching fractions) which are derived from the fitted parameters.

The procedure for determining the statistical uncertainties on the branching fractions is shown schematically in Figure 12.16. The 1σ errors on the fit parameters are

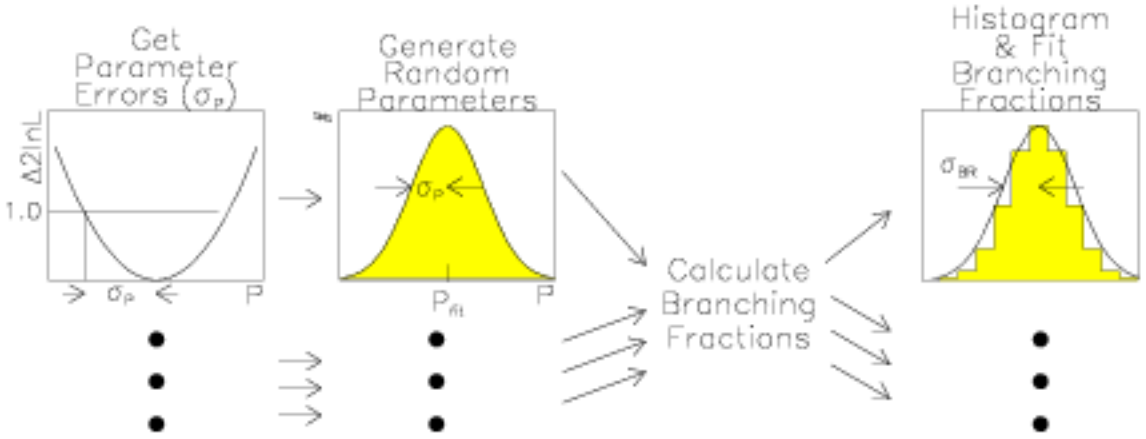

Figure 12.16: The procedure for determining the statistical uncertainties on the branching fractions is shown schematically. The error, σ_P, on fitting parameter P is determined by finding the change in the parameter which changes the value of $-2\ln\mathcal{L}$ by 1.0. Many sets of parameters are then generated, with each parameter distributed as a Gaussian with $\sigma = \sigma_P$. Using these sets of parameters, branching fractions are computed. These branching fractions are then histogramed, and the distributions are fit with Gaussian functions. The width (σ) of the fit function is taken as the statistical error on the branching fraction.

extracted from MINUIT as the change in each parameter which results in an increase of 1.0 in $-2\ln\mathcal{L}$ (see, for example, reference [62].) Next, 1000 sets of fit parameters were generated in which each of the fitting parameters was set to a value determined by a random number generator. These random numbers were distributed as Gaussian functions, centered at the best fit value, with a standard deviation (σ) corresponding to that which changes $-2\ln\mathcal{L}$ by 1.0. The branching fraction for each process was then calculated with each of the 1000 sets of parameters, and these branching fractions were histogramed. A Gaussian function was then fit to each of these histograms; the standard deviations (σ) of these fit Gaussians were then taken to be the statistical uncertainties of the measured branching fractions.

This method almost certainly overestimates the statistical uncertainties. The effects of correlations among the parameters are amplified by changing all of the parameters simultaneously, but this is preferable to the underestimation which would occur by ignoring the correlations. For most of the branching fractions, the systematic uncertainties are much larger than the statistical uncertainties.

The statistical uncertainties on the ratios $\Gamma(\omega(1600)\to b_1\pi)/\Gamma(\omega(1600)\to\omega(\pi\pi)_s)$ and $\Gamma(\omega(782)\to\rho\pi)/\Gamma(\omega(782)\to\pi\pi\pi(\text{direct}))$ were also computed using this method.

12.6.2 Systematic Errors

The systematic uncertainties on the measured branching fractions are dominated by 1) fluctuations which occur as a result of changing what processes are included in the PWA fits and 2) by the effects of background events in the data sample. The results of several fits were used in determining standard deviations of the branching fractions of the various processes. To address issue #1 above, the following fits were considered:

- Fit B16.
- Fits which consisted of fit B16 with additional $\omega\pi\pi$ resonances added (in block 1 of Table 12.11,) except the one with the $\tilde{\rho}(1400)$, as this fit gave a value of the D/S ratio for $b_1\to\omega\pi$ of 0.10, more than 4σ from the PDG value of 0.29 ± 0.04.
- Fit B16 with the addition of higher angular momenta allowed in productions and decays (the last fit in block 3 of Table 12.12.)
- Fit B16 with the $\bar{p}p\to\omega(1420)\omega$ process eliminated (the second fit in block 4 of Table 12.12.) There was some doubt concerning $\omega(1420)\omega$, because of the large mass of this intermediate state relative to the initial state, and the relatively small width of the $\omega(1420)$.

To address issue #2, the effect of backgrounds, the cut on the confidence level of the kinematic fit to $\bar{p}p\to\pi^+\pi^-\pi^\circ\omega$ was varied. This was shown in Table 6.5 to vary the level of the contamination by the $\pi^+\pi^-\pi^\circ\pi^\circ\pi^\circ$ final state. These fits are shown in the last block of Table 12.12.

A total of 19 fits are used in this determination of the systematic uncertainties. The arithmetic mean of each branching fraction among these fits is quoted below as the fraction of the $\pi^+\pi^-\pi^\circ\omega$ final state that it constitutes. The standard deviation of these values is quoted as the systematic uncertainty.

12.7 PWA Results

The complexity of the fitting procedure has limited the number of processes which can be included the PWA fits. Because of the large overall rate of production of the $\pi^+\pi^-\pi^\circ\omega$ final state, some processes have almost certainly been unaccounted for in this analysis, but the largest contributions have been found. In addition to $\bar{p}p \to \omega\omega$, the following intermediate states are found to contribute to the $\pi^+\pi^-\pi^\circ\omega$ final state:

Produced State	Fraction $\pm\sigma_{systematic} \pm \sigma_{statistical}$
$b_1(1235)\rho$	8.6± 2.0± 0.3 %
$b_1(1235)(\pi\pi)_s$	0.66±0.03±0.12 %
$h_1(1170)\omega$	2.4± 0.1± 0.2 %
$a_1(1260)\omega$	15.6± 0.7± 0.6 %
$a_2(1320)\omega$	5.7± 1.1± 0.4 %
$\omega(1420)\omega$	2.1± 0.6± 0.2 %
$a_2(1320)\pi$	0.77±0.09±0.18 %
$\omega(1600)\pi^\circ$	6.8± 0.9± 0.4 %
$h_1(1170)\pi^\circ$	5.9± 0.6± 0.3 %
$a_1(1260)\pi$	8.7± 1.5± 0.5 %
$a_1(1700)\pi$	9.1± 2.3± 0.4 %

The derivation of the statistical and systematic errors is explained above in Section 12.6. The sum of the contributions is not 100% because of the interferences between the two modeled decay modes of the $\omega(782)$ (see Section 12.2.)

The above branching fractions, determined from the PWA combined with the overall rate for production of the $\pi^+\pi^-\pi^\circ\omega$ final state as determined in Section 10.2 ($BR(\bar{p}p \to \pi^+\pi^-\pi^\circ\omega) = 16.1 \pm 1.0\%$,) lead to the product rates for production and decays into particular modes listed in Table 12.13. Here, three uncertainties are listed: $\sigma_{systematic}$ and $\sigma_{statistical}$ correspond to those discussed above for the determination of the fractional contributions to the $\pi^+\pi^-\pi^\circ\omega$ final state. The σ_{BR} is that which results from the uncertainty in the measurement of the total rate for the $\pi^+\pi^-\pi^\circ\omega$ final state.

A rate for $\bar{p}p \to b_1(1235)(\pi\pi)_s$ is not listed in Table 12.13. This process was fit as a very small ($< 1\%$) contribution to the $\pi^+\pi^-\pi^\circ\omega$ final state, and its contribution decreased as more processes were added to the PWA fits, so the evidence for the presence of this process is not convincing. (Production of $a_2(1320)\pi$ is also fit as a $< 1\%$ contribution, but this process has been observed in other final states, so there is more confidence in this measurement.)

Process	Rate $\pm\sigma_{systematic} \pm \sigma_{statistical} \pm \sigma_{BR}$
$BR(\bar{p}p \to b_1(1235)\rho,\ b_1 \to \omega\pi)$	1.4± 0.3± 0.1± 0.1 %
$BR(\bar{p}p \to h_1(1170)\omega,\ h_1 \to \rho\pi)$	0.39±0.02±0.03±0.02 %
$BR(\bar{p}p \to a_1(1260)\omega,\ a_1 \to \rho\pi)$	2.5± 0.1± 0.1± 0.2 %
$BR(\bar{p}p \to a_2(1320)\omega,\ a_2 \to \rho\pi)$	0.92±0.18±0.06±0.06 %
$BR(\bar{p}p \to \omega(1420)\omega,\ \omega(1420) \to \rho\pi)$	0.33±0.10±0.03±0.02 %
$BR(\bar{p}p \to a_2(1320)\pi,\ a_2(1320) \to \omega\pi\pi)$	0.12±0.01±0.03±0.01 %
$BR(\bar{p}p \to \omega(1600)\pi^\circ,\ \omega(1600) \to \omega\pi\pi)$	1.1± 0.1± 0.1± 0.1 %
$BR(\bar{p}p \to h_1(1170)\pi^\circ,\ h_1 \to \omega\pi\pi)$	0.9± 0.1± 0.1± 0.1 %
$BR(\bar{p}p \to a_1(1260)\pi,\ a_1 \to \omega\pi\pi)$	1.4± 0.2± 0.1± 0.1 %
$BR(\bar{p}p \to a_1(1700)\pi,\ a_1 \to \omega\pi\pi)$	1.5± 0.4± 0.1± 0.1 %

Table 12.13: Product branching fractions derived from the PWA fits. Each measurement has three errors associated with it: systematic error, statistical error, and the error associated with the uncertainty in the overall branching fraction of $\bar{p}p \to \pi^+\pi^-\pi^\circ\omega$ (σ_{BR}.)

Mass spectra which result from fit B16 are shown in Figure 12.17. The ragged appearance of some of the MC histograms is primarily due to the large weight applied to the relatively small number of events in the $\omega \to \pi^+\pi^-\pi^\circ$ peak; mass spectra with these events removed are shown in Figure 12.18. Nine representative angular distributions are shown in Figure 12.19. All of these distributions are well fit, as are all of the others which are not shown here.

For the decay $b_1(1235) \to \omega\pi$, both $L = 0$ and $L = 2$ were modeled in the PWA fits. (See Section 12.3.) The D/S ratio is found to be:

$$D/S\ (b_1(1235) \to \omega\pi)\ = 0.28 \pm .01 \pm .04 \quad (\pm\sigma_{systematic} \pm \sigma_{statistical}).$$

This is in agreement with the PDG value for the world average: 0.29 ± 0.04 [1].

The $\omega\pi\pi$ resonances each had two decay modes modeled in the fits: $\omega\rho$ and $b_1\pi$ for $I = 1$ resonances, and $\omega(\pi\pi)_s$ and $b_1\pi$ for $I = 0$ resonances. The contributions for the two decay modes are added in the above table. The $b_1\pi$ decay modes are weak except for the $\omega(1600)$ where it is consistently fit as the stronger mode:

$$\frac{\Gamma(\omega(1600) \to b_1\pi)}{\Gamma(\omega(1600) \to \omega(\pi\pi)_s)} = 1.6 \pm 0.1 \pm 0.2 \quad (\pm\sigma_{systematic} \pm \sigma_{statistical}).$$

The decay $\omega(782) \to \pi^+\pi^-\pi^\circ$ was modeled as a combination of $\omega \to \rho\pi$ (the isobar type model,) and a direct $\omega \to \pi\pi\pi$ term. (See Section 12.2.) The ratio of the strengths of these two modes is found to be:

$$\frac{\Gamma(\omega(782) \to \rho\pi)}{\Gamma(\omega(782) \to \pi\pi\pi(\text{direct}))} = 2.38 \pm 0.02 \pm 0.18 \quad (\pm\sigma_{systematic} \pm \sigma_{statistical}).$$

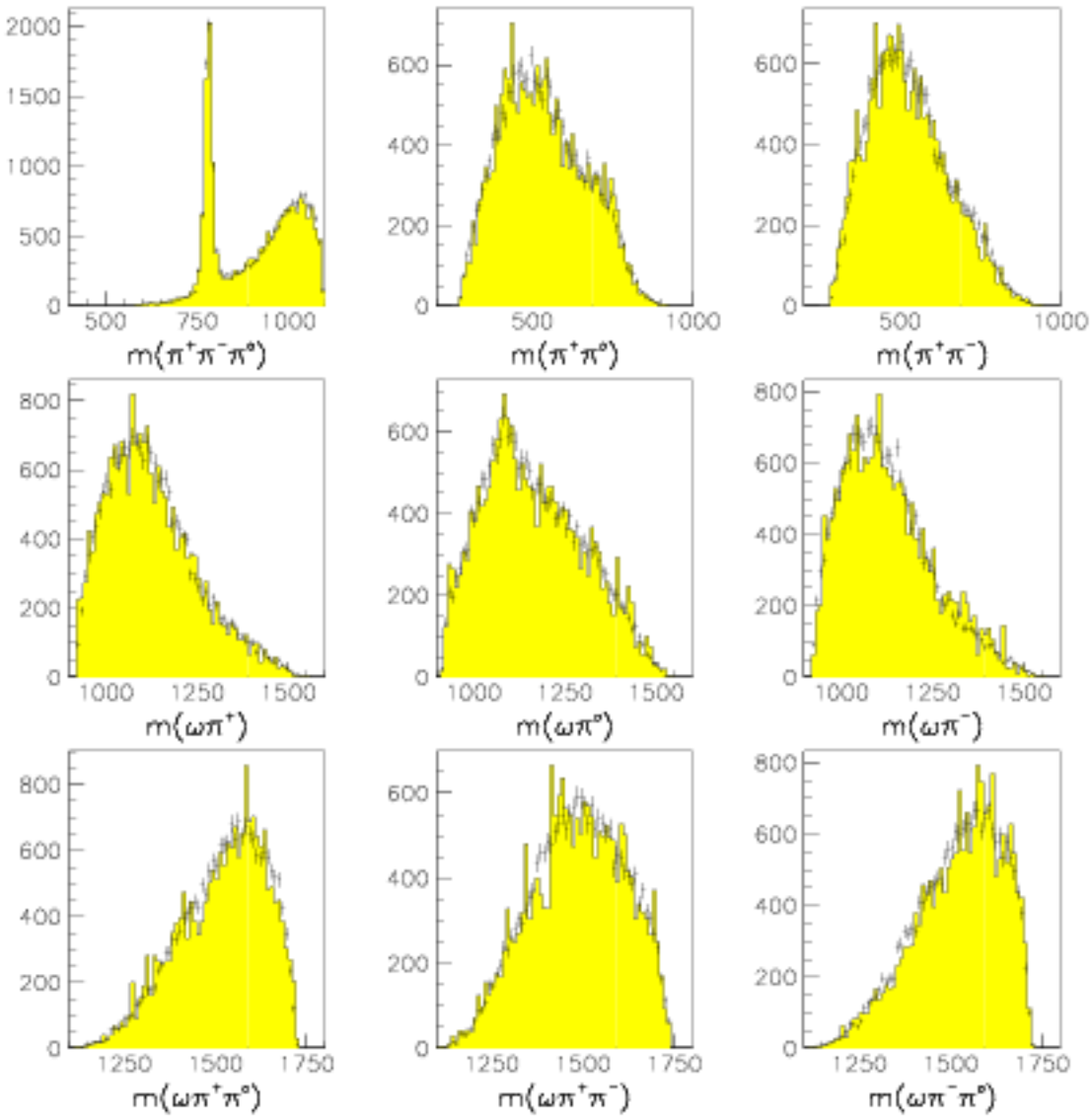

Figure 12.17: Mass spectra from fit B16, with the experimental data shown as crosses and the Monte Carlo data shown as the shaded histograms. The Monte Carlo histograms have been weighted according to the fit, and have been scaled up to have the same numbers of events as those for the experimental data. All of the histograms have bin sizes of $20 MeV/c^2$.

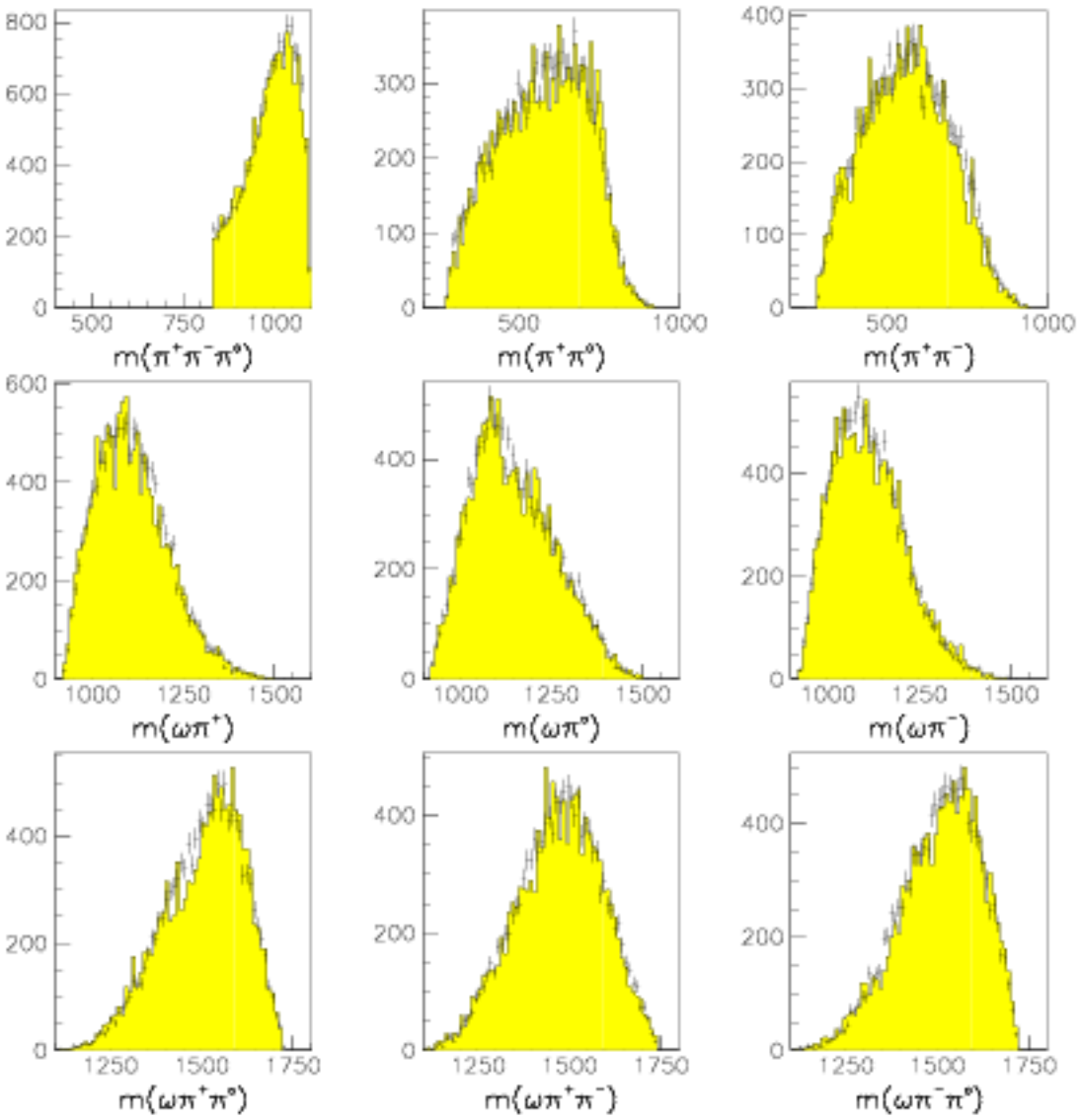

Figure 12.18: Mass spectra from fit B16, with the experimental data shown as crosses and the Monte Carlo data shown as the shaded histograms. The $\bar{p}p \to \omega\omega$ events have been eliminated by requiring that $m(\pi^+\pi^-\pi^0) > 830 MeV/c^2$. The Monte Carlo histograms have been weighted according to the fit, and have been scaled up to have the same numbers of events as those for the experimental data. All of the histograms have bin sizes of $20 MeV/c^2$.

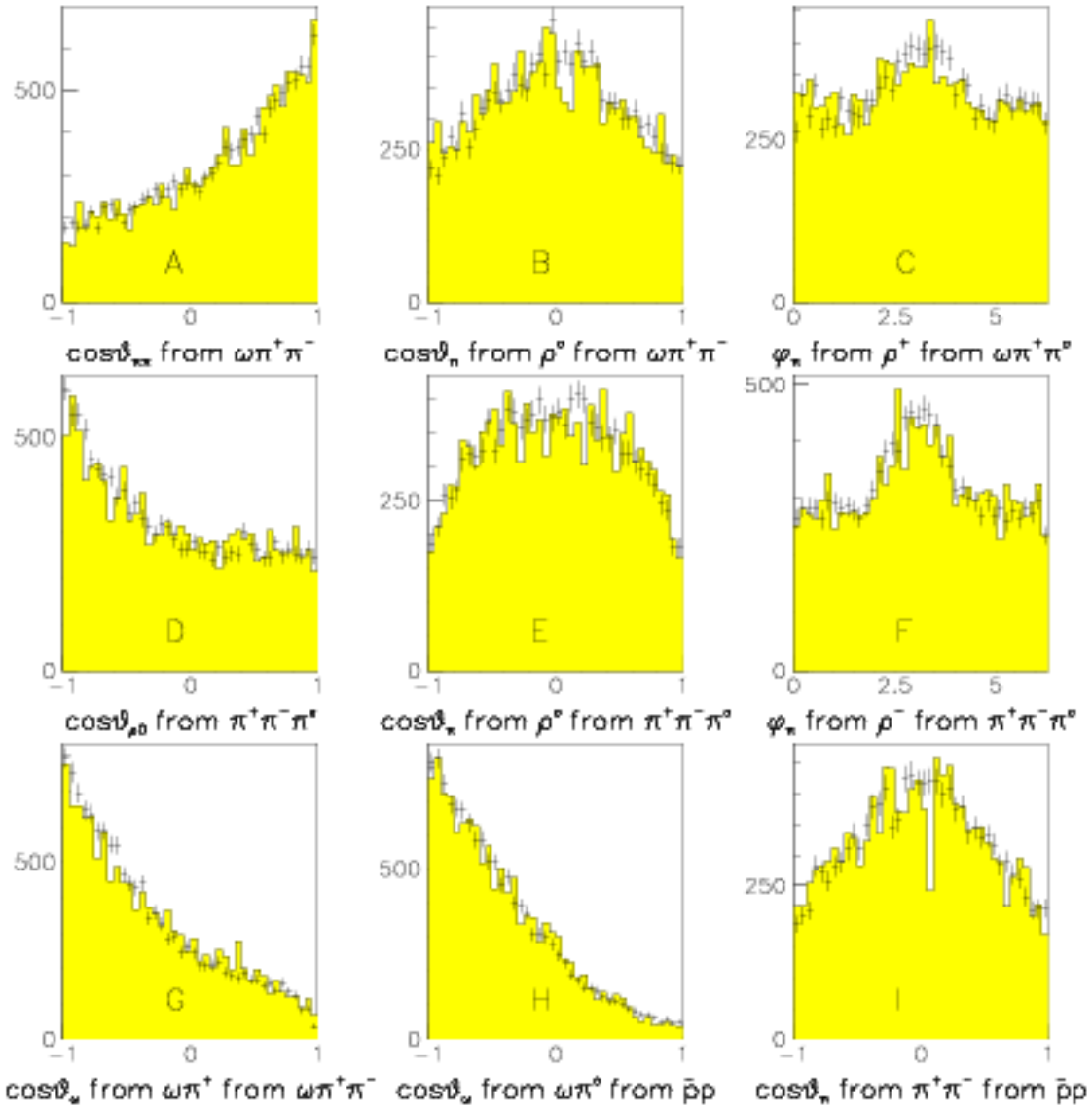

Figure 12.19: Nine angular distributions from the fit B16 are shown, with the experimental data shown as crosses and the Monte Carlo data shown as the shaded histograms. This is merely a representative sample of the complete set of angular distributions; all are fit very well. The $\bar{p}p \to \omega\omega$ events have been eliminated by requiring that $m(\pi^+\pi^-\pi^0) > 830 MeV/c^2$. The MC histograms have been weighted according to the Base fit, and have been scaled up to have the same numbers of events as those for the experimental data.

Chapter 13

Conclusions

An analysis of $\bar{p}p$ annihilation at rest in liquid hydrogen has been carried out. Direct measurements were made of the total rate for this process, and of the $\omega\omega$ intermediate state. A determination of the other intermediate states which play a significant role was made using a partial wave analysis.

Results of this analysis are summarized in the following sections. First, those results which are particular to this analysis are discussed, including ways in which the new results could be verified. Trends suggested by these results and by previous analyses are then discussed. Finally, suggestions for further study are presented.

13.1 Production Rates for $\pi^+\pi^-\pi^\circ\omega$ and $\omega\omega$

The overall rate for production of $\pi^+\pi^-\pi^\circ\omega$ was measured to be:

$$BR(\bar{p}p \to \pi^+\pi^-\pi^\circ\omega) = 16.1 \pm 1.0 \pm 0.4\% \quad (\pm\sigma_{systematic} \pm \sigma_{statistical}).$$

This about one out of every six annihilations.

The rate for production of $\omega\omega$ was measured in a way that is free from backgrounds. The value obtained is

$$BR(\bar{p}p \to \omega\omega) = 3.23 \pm 0.20 \pm 0.15\% \quad (\pm\sigma_{systematic} \pm \sigma_{statistical}).$$

This is in agreement with a result which was previously published by the Crystal Barrel collaboration ($3.32 \pm 0.34\%$ [38]), and was made in a different final state, thus providing confirmation of the measurement. This rate provides valuable information on $\bar{p}p$ annihilation dynamics.

13.2 Results from the Partial Wave Analysis

The partial wave analysis provided the results shown in Table 13.1. With an overall rate of production of the $\pi^+\pi^-\pi^\circ\omega$ final state of $16.1 \pm 1.0\%$, one would expect many

Process	Rate $\pm\sigma_{systematic} \pm \sigma_{statistical} \pm \sigma_{BR}$
$BR(\bar{p}p \to b_1(1235)\rho,\ b_1 \to \omega\pi)$	1.4± 0.3± 0.1± 0.1 %
$BR(\bar{p}p \to h_1(1170)\omega,\ h_1 \to \rho\pi)$	0.39±0.02±0.03±0.02 %
$BR(\bar{p}p \to a_1(1260)\omega,\ a_1 \to \rho\pi)$	2.5± 0.1± 0.1± 0.2 %
$BR(\bar{p}p \to a_2(1320)\omega,\ a_2 \to \rho\pi)$	0.92±0.18±0.06±0.06 %
$BR(\bar{p}p \to \omega(1420)\omega,\ \omega(1420) \to \rho\pi)$	0.33±0.10±0.03±0.02 %
$BR(\bar{p}p \to a_2(1320)\pi,\ a_2(1320) \to \omega\pi\pi)$	0.12±0.01±0.03±0.01 %
$BR(\bar{p}p \to \omega(1600)\pi^\circ,\ \omega(1600) \to \omega\pi\pi)$	1.1± 0.1± 0.1± 0.1 %
$BR(\bar{p}p \to h_1(1170)\pi^\circ,\ h_1 \to \omega\pi\pi)$	0.9± 0.1± 0.1± 0.1 %
$BR(\bar{p}p \to a_1(1260)\pi,\ a_1 \to \omega\pi\pi)$	1.4± 0.2± 0.1± 0.1 %
$BR(\bar{p}p \to a_1(1700)\pi,\ a_1 \to \omega\pi\pi)$	1.5± 0.4± 0.1± 0.1 %

Table 13.1: The results of the partial wave analysis, in the form of product branching fractions for production and decays in the specified modes. Each measurement has three errors associated with it: systematic error, statistical error, and the error associated with the uncertainty in the overall branching fraction of $\bar{p}p \to \pi^+\pi^-\pi^\circ\omega$ (σ_{BR}.)

processes to contribute. The complexity of the fitting procedure, however, limits the number of processes which can be included in the fits. Some small processes have almost certainly been neglected in the PWA. This analysis has determined what the large contributions are.

The only result among these which can be compared to previous measurements is that of $a_2(1320)\pi$ production. Correcting for the $10.6 \pm 3.2\%$ [1] branching fraction for $a_2(1320) \to \omega\pi\pi$, this analysis finds a rate for $\bar{p}p \to a_2(1320)\pi$ of $1.1 \pm 0.4\%$. This can be compared to previous results. Other Crystal Barrel analyses have reported rates for this process; using these and the PDG [1] values for the branching fractions of the $a_2(1320)$ decays, the following rates for $\bar{p}p \to a_2(1320)\pi$ production are found: $4.1 \pm 0.4\%$ [53], $1.55 \pm 0.31\%$ [51], $3.4 \pm 0.9\%$ [50], $3.0 \pm 0.9\%$ [54]. Only the smallest of these is compatible (within 1σ) with the result found here. This may be a result of the PWA fits having difficulty in fitting this very small contribution ($< 1\%$) to the $\pi^+\pi^-\pi^\circ\omega$ final state. Also, some processes which have strong interference effects on $a_2\pi$ may have been neglected in the fits (such as $a_0(1470)\pi$.) Additionally, the PDG values for the a_2 branching fractions may be incorrect; this may also account for the apparent discrepancies among the previous measurements.

For the decay $b_1(1235) \to \omega\pi$, both $L = 0$ and $L = 2$ were modeled in the PWA fits. (See Section 12.3.) The D/S ratio is found to be:

$$D/S\ (b_1(1235) \to \omega\pi)\ = 0.28 \pm .01 \pm .04 \quad (\pm\sigma_{systematic} \pm \sigma_{statistical}).$$

This is in agreement with the PDG value for the world average: 0.29 ± 0.04 [1].

The decay $\omega(782) \to \pi^+\pi^-\pi^\circ$ was modeled as a combination of $\omega \to \rho\pi$ (the isobar type model,) and a direct $\omega \to \pi\pi\pi$ term. (See Section 12.2.) The ratio of the

strengths of these two modes is found to be:

$$\frac{\Gamma(\omega(782) \to \rho\pi)}{\Gamma(\omega(782) \to \pi\pi\pi(\text{direct}))} = 2.38 \pm 0.02 \pm 0.18 \quad (\pm\sigma_{systematic} \pm \sigma_{statistical}).$$

13.3 Production of $b_1\rho$

The results of the PWA indicate that this channel is produced in 1.4±0.3% of all annihilations. Presence of this channel is supported by the fitted value for the D/S ratio in $b_1 \to \omega\pi$, $0.28 \pm .01 \pm .04$, which is in good agreement with the PDG value of 0.29 ± 0.04. It is seen here in the dominant decay modes of both resonances; neither the b_1 nor the ρ has another decay mode with a branching fraction of 1% or more, so observation of $b_1\rho$ in another final state is very unlikely. Perhaps the only way to confirm this result is in $\pi^+\pi^-\pi^\circ\omega$ with the ω in its 3π decay mode (instead of the $\pi^\circ\gamma$ mode as is used here.)

13.4 Production of $\omega(1600)\pi^\circ$

This channel is fit as a $6.8 \pm 1.0\%$ contribution to the $\pi^+\pi^-\pi^\circ\omega$ final state, which corresponds to a rate $BR(\bar{p}p \to \omega(1600)\pi^\circ) = 1.1 \pm 0.2\%$. This is even stronger than $\omega(782)\pi^\circ$ production (0.573±0.047% [38]), which is not so surprising, since production of vector mesons is very strong in $\bar{p}p$ annihilation. This larger rate for the heavier $\omega(1600)$ than for the $\omega(782)$ is also consistent with the phenomenological model of Vandermeulen [15], wherein mass rather than kinetic energy release is preferred in $\bar{p}p$ annihilation. (The publication in which this model was presented shows no specific prediction of a rate for $\omega(1600)\pi$ production, though.)

The decay of the $\omega(1600)$ into $b_1\pi$ is found to be stronger than into $\omega(\pi\pi)_s$:

$$\frac{\Gamma(\omega(1600) \to b_1\pi)}{\Gamma(\omega(1600) \to \omega(\pi\pi)_s)} = 1.6 \pm 0.1 \pm 0.2 \quad (\pm\sigma_{systematic} \pm \sigma_{statistical}).$$

In $^3P_0$ model of meson decays discussed in Section 2.2.2, the $b_1\pi$ decay mode "tags" the $1\,^3D_1$ isoscalar state, so this result adds further weight to the interpretation of the $\omega(1600)$ as the first orbital excitation of the ω.

The production of $\omega(1600)\pi^\circ$ can be confirmed in the final states $\pi^+\pi^-\pi^\circ\pi^\circ$ (with $\omega(1600) \to \rho\pi$, a known decay mode,) or, better yet, in $\omega\pi^\circ\pi^\circ\pi^\circ$ (with $\omega(1600) \to \omega\pi\pi$, also a known decay mode.) The $\omega\pi^\circ\pi^\circ\pi^\circ$ has the advantage that very few intermediate states are available, so the signal would be rather unambiguous.

13.5 $\omega(1420) \to \omega\pi\pi$

The process $\bar{p}p \to \omega(1420)\pi^\circ$, $\omega(1420) \to \omega\pi\pi$ is not needed in the PWA fits. This means that 1) $\omega(1420)\pi^\circ$ is not produced, or 2) $\omega(1420)$ does not decay to $\omega\pi\pi$. To

check for the production of $\omega(1420)\pi^\circ$, analysis of $\bar{p}p \to \pi^+\pi^-\pi^\circ\pi^\circ$ is needed, since the dominant decay mode of the $\omega(1420)$ is $\rho\pi$ [1]. Only after gaining some knowledge of this production rate can one draw conclusions concerning the $\omega\pi\pi$ decay mode.

This decay mode is predicted to be small or absent for the first radial excitation of the ω meson (the $2\,^3S_1$ state) in the meson decay models discussed in Section 2.2.2. Other experiments have found that this decay does not exist [37]. Confirmation of this would be valuable in determining the structure of this resonance.

13.6 The $\omega\pi\pi$ Decay Modes of $h_1(1170)$, $a_1(1260)$ and $a_1(1700)$

The $\omega\pi\pi$ decay mode has never been reported for the $h_1(1170)$, the $a_1(1260)$ nor the $a_1(1700)$. The $h_1(1170)$ and $a_1(1260)$ resonances are quite broad, however, with Γ of 360 and $400MeV$ respectively, and are quite close in mass. They would probably not be detected by "bump-hunting" in $\omega\pi\pi$ mass spectra, so it is not too surprising that this decay mode has not been reported for these two resonances. Evidence for the $a_1(1700)$ has only been observed in the last couple of years, and only as a result of careful, modern analysis of large data sets collected for the purpose of detecting new states; the analysis of the $a_1(1700)$ is in its infancy, and there is certainly no evidence against an $\omega\pi\pi$ decay mode for it.

Theoretical predictions for these decays are not available due to the masses of the resonances being below the $\omega\rho$ and $b_1\pi$ thresholds, but for the $a_1(1700)$, the models of meson decays discussed in Section 2.2.2 indicate that $\omega\pi\pi$ decay modes can distinguish between the $2\,^3P_1$ and hybrid states: it predicts decay widths of 41 and $15MeV$ for the $b_1\pi$ and $\omega\rho$ decay modes for the $2\,^3P_1$ $q\bar{q}$ state, and no $\omega\pi\pi$ decay modes for the hybrid state. The PWA finds that the $\omega\rho$ decay mode dominates over $b_1\pi$, so the results are not completely consistent with the model, but the existence of the $\omega\rho$ decay mode seems to be incompatible with the hybrid interpretation.

For all three resonances, the known decay mode is $\rho\pi$; in order to verify that $a_1(1700)\pi$, $a_1(1260)\pi$ and $h_1(1170)\pi$ production occur in $\bar{p}p$ annihilation, analysis of $\bar{p}p \to \pi^+\pi^-\pi^\circ\pi^\circ$ must be done. Partial wave analyses of this channel are currently in progress by members of the Crystal Barrel collaboration.

Confirmation of the $\omega\pi\pi$ decay mode of the $h_1(1170)$ can be accomplished in the analysis of $\bar{p}p \to \omega\pi^\circ\pi^\circ\pi^\circ$ Crystal Barrel data. In fact, $h_1\pi$ production is one of very few processes which can occur in this channel, making it an excellent way to confirm this result and to measure the production rate.

To confirm the $\omega\pi\pi$ decay mode of the $a_1(1260)$ and $a_1(1700)$ in Crystal Barrel data is more difficult. It would require a final state involving $\omega\pi^+\pi^-$ plus at least one additional meson; perhaps an η would be a good choice, as it would allow production of only the neutral a_1 which would simplify the analysis somewhat. Final states involving η's, however, are usually produced at a much lower rate compared to similar

channels involving π°'s. Also, with a mass of $548 MeV$, not much energy is left for production of resonances with masses greater than $1400 MeV$. A search for this decay mode is more readily carried out in a πp production experiment such as E852 at Brookhaven National Laboratory. In this experiment, production of $a_1(1260)$ and $a_1(1700)$ has been observed, in their $\rho\pi$ decay mode, and an analyses of $\omega\pi\pi$ systems is in progress [63, 64].

13.7 Production of $\omega + \rho\pi$ Resonances

About a third of the $\pi^+\pi^-\pi^\circ\omega$ final state is fitted as proceeding via ω plus heavy $\rho\pi$ resonances: $\omega h_1(1170)$, $\omega a_1(1260)$, $\omega a_2(1320)$ and $\omega\omega(1420)$, with corresponding rates of 0.33 to 2.5% of all annihilations. Only the low-mass tails of the $\rho\pi$ resonances are available to the $\pi^+\pi^-\pi^\circ$ mass spectrum (which cuts off at $< 1100 MeV$,) so one may suspect that these four decay chains in the PWA are fitting decay chains which occurred but are not included in the fit. The contributions of these channels are rather stable, however, and the production of $\omega a_2(1320)$ is corroborated by a measurement in the $\omega\eta\pi^\circ$ final state. It seems unlikely that $\omega a_2(1320)$ would be measured consistently in two different final states if it were mimicking some other process. This corroboration lends credibility to the measurement of the other three channels. The $h_1(1170)$ and $a_1(1260)$ are quite broad, and their central masses lie within $1 \cdot \Gamma$ of the maximum 3π mass available, but production of $\omega\omega(1420)$ is harder to believe, as the $\omega(1420)$ lies far above the available phase space and is not very broad ($M = 1419 \pm 31 MeV$ and $\Gamma = 174 \pm 60 MeV$ [1].) However, production of ω mesons is very strong in $\bar{p}p$ annihilation ($\omega\omega$ is the strongest measured two-body mode.)

This trend is discussed further in the following section.

13.8 Production of Vector + P-wave Mesons

In the $\omega\pi^\circ\pi^\circ$ final state, the process $\bar{p}p \to \omega f_2(1270)$ was found to contribute strongly, with a measured rate $BR(\bar{p}p \to \omega f_2(1270)) = 0.57 \pm 0.07\%$ [58]. This is also kinematically suppressed like those channels discussed above. The relatively strong rate for these processes suggests a trend: $f_2(1270)$, $h_1(1170)$, $a_1(1260)$ and $a_2(1320)$ are all thought to be P-wave mesons (mesons in which the $q\bar{q}$ pair are in an $L = 1$ state.) (See Figure 2.1.) Perhaps production of $\omega + (q\bar{q})_{P-\text{wave}}$ is favored in $\bar{p}p$ annihilation. The strong rate for production of $b_1\rho$ suggests a generalization to (vector meson) + $(q\bar{q})_{P-\text{wave}}$.

There should also be a_0 and f_0 P-wave mesons, but which observed resonances correspond to the $(q\bar{q})_{P-\text{wave}}$ states is unclear. Their decay modes should be the same as those available to the $a_0(980)$ and $f_0(980)$, though. If a pattern is established concerning the production of vector + P-wave mesons, the observed production rates of vector + 0^{++} resonances could add one more piece to the puzzle of determining

what states are the $1\,^3P_0$ $q\bar{q}$ mesons.

The following sections discuss the final states in which vector + $(q\bar{q})_{P-wave}$ productions can be observed.

13.8.1 $\omega + (q\bar{q})_{P-wave}$

Below, short discussions of the observations of $\bar{p}p \to \omega + (q\bar{q})_{P-wave}$ are presented, including existing measurements, and other final states in which such observations may be made.

- $f_0\omega$: In the $\omega\pi^\circ\pi^\circ$ final state, the following measurement was made: $BR(\bar{p}p \to \omega(\pi\pi)_s) = 0.51 \pm 0.07\%$. The interpretation of the $(\pi\pi)_s$ system is unclear, though, especially in how it relates to the $1\,^3P_0$ isoscalar $q\bar{q}$ state. Such production may also be seen in the following final states: $\omega\pi\pi\pi\pi$, $\omega\eta\eta$ and $\omega\bar{K}K$. The latter two of these have very little phase space available to them, and are therefore not likely to be studied soon.

- $f_1\omega$: The $f_1(1285)$ has strong branching fractions into 4π and $\eta\pi\pi$, making $\omega\pi\pi\pi\pi$ and $\omega\eta\pi\pi$ the best final states for study of this channel.

- $f_2\omega$: As stated above, this was seen in the $\omega\pi^\circ\pi^\circ$ final state. Other final states in which it may be seen and confirmed are $\omega\pi^+\pi^-$, $\omega\pi\pi\pi\pi$ and $\omega\bar{K}K$.

- $a_0\omega$: Which observed resonance corresponds to the $1\,^3P_0$ isovector $q\bar{q}$ state is not determined. Such a state could decay to $\eta\pi$, $\bar{K}K$ or $\omega\pi\pi$. Production of $\omega a_0(980)$ was observed in the $\omega\eta\pi^\circ$ final state, with a rate of $BR(\bar{p}p \to \omega a_0(980)) = 0.354 \pm .011 \pm .026\%)$ [48]. The $\omega\eta\pi^\circ$ final state is currently being analyzed again, in a data sample with a much greater number of events. This will allow more precise measurements, and since the $a_0(1470)$ resonance was discovered after the first analysis in the $\eta\pi$ decay mode, a search for $\bar{p}p \to a_0(1470)\omega$ may be conducted.

- $a_1\omega$: The $a_1(1260)$ appears to the $1\,^3P_1$ meson. Production of $\omega a_1(1260)$ was consistently fit as a significant ($\sim 15\%$) fraction of the $\pi^+\pi^-\pi^\circ\omega$ final state, or $2.5\pm0.2\%$ of all annihilations.

- $a_2\omega$: The $a_2(1320)$ is widely regarded as the $1\,^3P_2$ meson. The production rate of $\omega a_2(1320)$ was measured here as $1.4\pm0.2\%$ (correcting for the branching fraction of $a_2 \to \rho\pi$,) in rough agreement with the previous measurement in $\bar{p}p \to \omega\eta\pi^\circ$: $BR(\bar{p}p \to \omega a_2(1320)) = 1.88 \pm 0.22\%$.

- $h_1\omega$: Production of $\omega h_1(1170)$ was consistently fit at a level of 2.5% of $\pi^+\pi^-\pi^\circ\omega$, corresponding to $0.39\pm0.04\%$ of all annihilations (with $h_1 \to \rho\pi$.)

- $b_1\omega$: This would be most readily observed in the final state $\omega\omega\pi^\circ$. In a preliminary report on an analysis of this channel in the 8γ mode, $b_1\omega$ was not needed for a satisfactory fit to the data [65].

In summary, the following table lists final states in which ω+P-wave intermediate states may be observed:

Final state	a_0	a_1	a_2	f_0	f_1	f_2	b_1	h_1
$\omega\eta\pi^\circ$	x		x					
$\omega\pi\pi$				x		x		
$\omega\pi\pi\pi\pi$				x	x	x		
$\omega\omega\pi$							x	
$\omega\omega\pi\pi$	x		x					
$\omega\eta\pi\pi$					x			
$\omega\bar{K}K$	x		x	x		x		

13.8.2 $\rho + (q\bar{q})_{P-wave}$

The obvious generalization of ω+P-wave production is vector meson + P-wave production. The $\rho(770)$ is the isospin 1 partner of the $\omega(782)$. Its mass is similar to that of the ω, and has a width of $\Gamma \simeq 150MeV$, perhaps making it kinematically more attractive for production with the P-wave mesons (as smaller total masses are available.) The following table lists final states in which ρ+P-wave intermediate states may be observed:

Final state	a_0	a_1	a_2	f_0	f_1	f_2	b_1	h_1
$\pi^+\pi^-\pi^\circ\eta$	x		x					
$\pi^+\pi^-\pi\pi$				x		x		
$\pi^+\pi^-\pi^\circ\pi\pi$		x	x					x
$\pi^+\pi^-\pi\pi\omega$		x	x					x
$\pi^+\pi^-\bar{K}K$	x		x	x				

Of these final states, $\pi^+\pi^-\pi^\circ\pi^\circ\pi^\circ$, $\pi^+\pi^-\pi^\circ\pi^\circ$ and $\pi^+\pi^-\pi^\circ\eta$ are currently under study by members of the Crystal Barrel collaboration.

13.9 Production of ω in $\bar{p}p$ Annihilation

The large rate of production of $\pi^+\pi^-\pi^\circ\omega$ (16.1±1.0%) in $\bar{p}p$ annihilation at rest firmly establishes a trend: that ω mesons are produced copiously. In fact, it is now known that ω's are produced in at least 30% of annihilations at rest (see Table 13.2.)

It will be interesting to see if this trend is observed in the analysis of other final states, especially those involving high pion multiplicities, as these have high rates of production, and the strongest decay mode for ω's is $\pi^+\pi^-\pi^\circ$, so they are most easily observed in such final states.

Channel	Rate (%)	Reference
$\pi^+\pi^-\pi^\circ\omega$	16.1 $\pm$1.0	[This work]
$\omega\pi^\circ\pi^\circ$	2.57 $\pm$0.17	[17]
$\omega\pi^+\pi^-$	6.6 $\pm$0.6	[4]
$\omega 2\pi^+ 2\pi^-$	1.3$\pm$0.3	[18]
$\omega\eta\pi^\circ$	0.68 $\pm$0.05	[48]
$\omega\omega$	3.23 $\pm$0.25	[This work]
$\omega\pi^\circ$	0.573$\pm$0.047	[38]
$\omega\eta$	1.51 $\pm$0.12	[38]
$\omega\eta'$	0.78 $\pm$0.08	[38]

Table 13.2: Measured production rates of various final states which involve ω's, from $\bar{p}p$ annihilation at rest.

13.10 Suggestions for Further Study

The $\pi^+\pi^-\pi^\circ$ decay of the ω meson gives complete information on its polarization. (Because the pions have no spin, the polarization information is carried solely in the orientation of the decay plane. In the $\pi^\circ\gamma$ decay mode, information is lost because the photon carries spin, and its polarization is not measured in the Crystal Barrel apparatus.) Final states in which the ω is observed in this decay mode would be interesting for this reason. This final state is more difficult to extract cleanly, though, because of the greater charged multiplicity and because of a larger combinatorical background in some final states. A study of $\pi^+\pi^-\pi^\circ\omega$, but with $\omega \to \pi^+\pi^-\pi^\circ$, would suffer from this increased combinatorical background. It is possible, though, that the additional information on the ω polarization would offset the increased difficulty in extraction of the data set. This final state would result in four charged tracks and four photons in the final state. Data from the Crystal Barrel experiment have been collected with a 4-prong trigger, but analysis of these data is in an early stage, and expertise in extracting data sets is not widespread in the collaboration.

To confirm production of the two-meson states observed here, to confirm a new decay mode observed here, and to establish the vector + P-wave pattern, analysis of the following final states would be useful:

- $\omega\pi^\circ\pi^\circ\pi^\circ$: This is an all neutral final state, so C-parity is a good quantum number. This imposes restrictions on the decay chains which can occur. Additionally, no intermediate states involving ρ mesons can occur, since $\rho \not\to \pi^\circ\pi^\circ$, so production of $b_1\rho$ is prohibited, as is production of states which decay to $\rho\pi$ and $\omega\rho$. Production of $a_1(1260)$ and $\pi(1300)$, along with an ω is allowed, but they would have to decay to $\pi(\pi\pi)_s$, which appears to be a very weak decay mode for both of these resonances [33]. This final state is likely to be dominated by $\bar{p}p \to \omega(1600)\pi^\circ$ and $\bar{p}p \to h_1(1170)\pi^\circ$. This would constrain the levels of

those processes in $\pi^+\pi^-\pi^\circ\omega$. This state could be observed as 9γ or as $\pi^+\pi^-8\gamma$; the combinatorics actually favor the $\pi^+\pi^-\pi^\circ$ decay mode of the ω over the $\pi^\circ\gamma$ decay mode because of the smaller number of π°'s to form from γ pairs.

- $\pi^+\pi^-\pi^\circ\pi^\circ$: This final state has many possible decay chains available. The PWA for it is likely to contain many components, as in $\pi^+\pi^-\pi^\circ\omega$. However, in this channel one can observe five types of resonances in their known $\rho\pi$ decay modes, which may also be present in $\omega\pi\pi$ decay modes in $\pi^+\pi^-\pi^\circ\omega$:
  - $h_1(1170)\pi^\circ,\ h_1() \to \rho\pi$
  - $a_1(1260, 1700)\pi,\ a_1() \to \rho\pi$
  - $a_2(1320, 1650)\pi^\circ,\ a_2() \to \rho\pi$
  - $\omega(1600)\pi^\circ,\ \omega() \to \rho\pi$
  - $\pi_2(1670)\pi,\ \pi_2 \to \rho\pi$

  As these are established resonances, and $\rho\pi$ is their known decay mode, this channel can confirm or deny that they are produced with a π in $\bar{p}p$ annihilation.

- $\omega\eta\pi^\circ$: The knowledge gained since the first analysis of this final state will influence the re-analysis which is currently underway. In particular, a search for production of $\omega a_0(1470)$ may be conducted. Additionally, production of $a_2(1320)\omega$ intermediate state can be confirmed and measured more precisely.

- $\omega\omega\pi\pi$: Recall that four heavy resonances (decaying to $\rho\pi$) appear to be produced with an ω in $\pi^+\pi^-\pi^\circ\omega$, and are also seen to decay to $\omega\pi\pi$ after production with a π: $h_1(1170)$, $a_1(1260)$, $a_2(1320)$ and $\omega(1420)$. This channel could allow production of these with an ω in their $\omega\pi\pi$ decay modes. The large final state particle multiplicity and the presence of two ω's could make this channel difficult to cleanly select, but the number of possible decay chains should not be large, as not very many light resonances are known to decay to $\omega\pi$ and $\omega\omega$. Unfortunately, there is not much phase space for this channel, as the sum of the masses of the final state mesons is $1834 MeV$, and only $1876 MeV$ of energy is available to $\bar{p}p$ annihilation at rest.

- $\pi^+\pi^-\pi^\circ\pi^\circ\pi^\circ$ and $\pi^+\pi^-\pi^+\pi^-\pi^\circ$: In these final states, one may observe production of ρ mesons along with three P-wave mesons: a_1, a_2 and h_1; these can help to establish a pattern concerning production of vector + P-wave mesons.

- $\pi^+\pi^-\pi^\circ\eta$: Production of ρ plus a_0 or a_2 may be observed in this final state, again establishing the pattern for production of vector + P-wave mesons.

- $\omega\pi^+\pi^-\pi^+\pi^-$ and $\omega\pi^+\pi^-\pi^\circ\pi^\circ$: Again, ρ + P-wave mesons can be observed, but here the P-wave mesons could be observed in their $\omega\pi\pi$ decay modes. Such a decay mode is well known for the $a_2(1320)$, and the analysis of $\pi^+\pi^-\pi^\circ\omega$ indicates that this mode may exist for $a_1(1260)$ and $h_1(1170)$.

- $\pi^+\pi^-\bar{K}K$: A $\bar{K}K$ mode has been observed for a_0, a_2 and f_0 mesons. In this final state, one may observe their production with ρ's, helping to establish a pattern concerning production of vector + P-wave mesons.

13.10.1 Possible Improvements on this Analysis

13.10.1.1 Phase Space Factor for $\omega\pi\pi$ Decays

The problem with modeling the mass-dependent width of the Breit-Wigner function for $\omega\pi\pi$ resonances was discussed in Section 12.4. This is probably of great importance, and should be addressed again here.

The phase space factor, $\rho(m)$, in $\Gamma(m)$ is computed using the rest masses of the three decay products of the $\omega\pi\pi$ resonances. This results in $\rho(m)$ rising rapidly around 1000 to $1100MeV$, and rising slowly in the mass range in which most $\omega\pi\pi$ resonances are found. These resonances are actually decaying (in the model used) to heavier objects, such as $\omega(782)\rho(770)$ and $b_1(1235)\pi$, the sums of whose central masses are several hundred MeV greater that their decay products'. The significant effects on $\Gamma(m)$ probably occur around $1500MeV$, where there are obvious problems with the PWA. Several methods of accounting for this effect were considered: using weighted average phase space factors and using a running normalization for $\rho(m)$ among them, but some of the methods were physically unintuitive, while others yielded results which were difficult to interpret and justify. Even the way that the phase space factor is to be included in the Breit-Wigner formula came under suspicion. In the end, it seemed better to have a known weakness in the model than to have an elaborate, unfamiliar description which would produce questionable results.

A better way of handling this effect may have strong effects on the conclusions of the PWA. A model which is based on physically sound fundamental principles may soon be developed which will be acceptable for further analysis of the $\omega\pi\pi$ system.

13.10.1.2 Many Small Contributions

One of the initial motivations for study of the $\pi^+\pi^-\pi^\circ\omega$ final state was the hope of observing the exotic $\hat{\rho}$ meson decaying to $b_1\pi$. This decay mode was (and still is) favored in many models for the lowest lying 1^{-+} hybrid mesons. Assuming that the overall rate for $\bar{p}p \to \pi^+\pi^-\pi^\circ\omega$ was small, a small rate of production for $\hat{\rho}\pi$ might still comprise a significant proportion of the final state. The overall rate for $\bar{p}p \to \pi^+\pi^-\pi^\circ\omega$ is not small, however (see Section 10.2), at $16.1 \pm 1.0\%$ of all annihilations. This makes all but the strongest of intermediate states difficult to detect for two reasons: 1) Many parameters are required in the mathematical description of the data. This requires a great deal of computing time, and it is therefore difficult and time consuming to try a wide variety of combinations of decay chains. Some small contributions are inevitably neglected in the analysis. 2) If a decay chain is fitted as a 1% contribution to the final state, it's difficult to know if it's an actual signal, or

if it's mimicking a background or another small signal which has not been accounted for in the fit.

Using information from other final states can constrain the fits to $\pi^+\pi^-\pi^\circ\omega$. All intermediate states seen in the $\omega\pi^\circ\pi^\circ\pi^\circ$ final state should also be present in $\pi^+\pi^-\pi^\circ\omega$, for example. The $\omega\pi^\circ\pi^\circ\pi^\circ$ final state is produced far less copiously than is $\pi^+\pi^-\pi^\circ\omega$ [66], and probably contains far fewer intermediate states. Analysis of this final state can measure the rates for production and decays of the h_1 and ω resonances. The rates for those processes could then be fixed in the more complicated $\pi^+\pi^-\pi^\circ\omega$ analysis. Also, for resonances being observed in new decay modes in $\pi^+\pi^-\pi^\circ\omega$, observation of their production and decay into *known* decay modes can allow for more confidence in observation. Suggestions for study of channels which can constrain the analysis of $\pi^+\pi^-\pi^\circ\omega$ were made in Section 13.10.

Bibliography

[1] R.M.Barnett *et al.*, *Phys. Rev.*, **D54**, 1–720 (1996).

[2] C.Batty, *Rep. Prog. Phys.*, **52**, 1165 (1989).

[3] D.Bugg, *personal communication.*

[4] R.Bizzari *et al.*, *Nucl. Phys.* **B14**, 169 (1969).

[5] S.Godfrey and N.Isgur, *Phys. Rev.*, **D32**, 189 (1985).

[6] A.Ostrovidov, Hadron Spectroscopy: Seventh International Conference, Chung and Willutzki, eds. 1998.

[7] R.Kokoski and N.Isgur, *Phys. Rev.*, **D35**, 907 (1987).

[8] N.Isgur and J.Paton, *Phys. Rev.*, **D31**, 2910 (1985).

[9] T.Barnes *et al.*, *Phys. Rev.*, **D55**, 4157 (1997).

[10] F.Close and P.Page, *Nucl. Phys.*, **B443**, 233 (1995).

[11] E.S.Ackleh, T.Barnes, E.S.Swanson, *Phys. Rev.*, **D54**, 6811 (1996).

[12] V.Mull, J.Haidenbauer, T.Hippenchen, K.Holinde, *Phys Rev.*, **C44**, 1337 (1991).

[13] U.Hartmann, E.Klempt, J.Körner, *Z. Phys.*, **A331**, 217 (1988).

[14] A.Cieplý, M.P.Locher, B.S.Zou, *Z. Phys.*, **A345**, 41 (1993).

[15] J.Vandermeulen, *Z. Phys.*, **C37**, 563 (1988).

[16] H.Genz, M.Martinis, S.Tatur, *Z. Phys.*, **A335**, 87 (1990).

[17] C.Amsler *et al.*, *Phys. Lett.*, **B322**, 431 (1996).

[18] C.Ghesquiere, Symp. on $\bar{N}N$ Interactions, Liblice, CERN 74-18, 436 (1974).

[19] J.Diaz *et al.*, *Nucl. Phys.*, **B16**, 239 (1970).

[20] C.Baltay *et al.*, *Phys. Rev.*, **140**, B1042 (1965).

[21] C. Amsler *et al.*, *Nucl. Instrum. Methods.* **A321** 69 (1992).

[22] R. Veenhof, CERN Program Library W5050 (1989).

[23] C.J.Batty, *Rep. Prog. Phys.*, **52**, 1165 (1989).

[24] E.B.Hughes *et al.*, *IEEE Trans. Nucl. Sci.*, **NS-19 #3**, 126 (1972).

[25] E.Bloom, C.Peck, *Ann. Rev. Nucl. and Part. Sci.*, **33**, 143 (1983).

[26] N.P.Hessey, CB Note 161, (1992), Unpublished.

[27] N.P.Hessey, CB Note 199, (1992), Unpublished.

[28] C.A.Meyer, CB Note 191, (1995), Unpublished.

[29] M.Benayoun, *et al.*, CB Note 280, (1995), Unpublished.

[30] C.A.Meyer, CB Note 93, (1992), Unpublished.

[31] C.A.Meyer, CB Note 123, (1994), Unpublished.

[32] N.Noble, CB Note 258, (1994), Unpublished.

[33] C. A. Meyer. *Personal communication.*

[34] Byron P. Roe. *Probability and Statistics in Experimental Physics.* Springer Verlag. New York. 1992.

[35] N. Djaoshvili. *Personal communication.*

[36] C.A.Meyer, CB Note 197, (1995), Unpublished.

[37] A.B.Clegg, A.Donnachie, *Z. Phys.*, **C62** 455–469 (1994).

[38] C.Amsler *et al.*, *Z. Phys.*, **C58** 175 (1993).

[39] M.L.Stevenson, L.W.Alverez, B.C.Maglić, A.H.Rosenfeld, *Phys. Rev.*, **125**, 687 (1962).

[40] M.Burchell, CB Note 185, (1992), Unpublished.

[41] J. D. Richman. *An Experimenter's Guide to the Helicity Formalism.* Caltech report CALT-68-1148. 1984.

[42] C. Amsler and J. C. Bizot, *Computer Physics Communications*, 30 (1983) 21-30

[43] F.von Hippel, C.Quigg *Phys. Rev. D*, **3**, 624, (1972).

[44] K.S.Kölbig, *Comm. ACM*, **15**, 465, (1972).

[45] W.Gautschi, *S.I.A.M. J. Numer. Anal.*, **12**, 635, (1964).

[46] C.J.Batty *et al.*, *NIM*, **137**, 179-181, (1976).

[47] R.Bizzari *et al.*, *Nucl. Phys.*, **B27**, 140-148, (1971).

[48] C.Amsler *et al.*, *Phys. Lett.*, **B327**, 425–432 (1994).

[49] J.H.Lee *et al.*, *Phys. Lett.*, **B323**, 227-232 (1994).

[50] A. Abele *et al.*, *Phys. Lett.*, **B404**, 179, (1997).

[51] A. Abele et*al.*, *Phys. Lett.*, **B385**, 425, (1996).

[52] C.Amsler *et al.*, *Phys. Lett.*, **B355**, 425, (1995).

[53] C.Amsler *et al.*, *Nucl. Phys.*, **A609**, 562, (1996).

[54] A. Abele *et al.*, *Phys. Rev.*, **D57**, 3860, (1998).

[55] D.R.Thompson *et al.*, *Phys. Rev. Lett.*, **79**, 1630, (1997).

[56] A. Abele *et al.*, *Phys. Lett.*, **B423**, 175, (1998).

[57] P.M.Eugenio. PhD. thesis, University of Massachusetts. (1998).

[58] C.Amsler *et al.*, *Phys. Lett.*, **B311**, 362, (1993).

[59] J. D. Richman. *Three-Body Decays in the Helicity Formalism.* Caltech report CALT-68-1148. 1984.

[60] Dankowych *et al.*, *Phys. Rev. Lett.*, **46**, 580 (1981).

[61] J.Diaz *et al.*, *Phys. Rev. Lett.*, **32**, 260 (1974).

[62] F.James, *MINUIT Function Minimization and Error Analysis,* CERN Program Library Long Writeup D506. (1994).

[63] M.Nozar, Hadron Spectroscopy: Seventh International Conference, Chung and Willutzki, eds. 1998.

[64] A.Popov and D.Ryabchikov, Hadron Spectroscopy: Seventh International Conference, Chung and Willutzki, eds. 1998.

[65] C.Pinder, D.Bugg, C.Hodd, CB Note 293, (1996), Unpublished.

[66] D.Bugg, *personal communication.*